

Numerical Solution of Stratified Flows



by

Khalil Ur Rehman

*Department of Mathematics
Quaid-i-Azam University
Islamabad, Pakistan
2020*

Numerical Solution of Stratified Flows



by

Khalil Ur Rehman

Supervised by

Prof. Dr. Muhammad Yousaf Malik

*Department of Mathematics
Quaid-i-Azam University
Islamabad, Pakistan
2020*

Numerical Solution of Stratified Flows



by

Khalil Ur Rehman

A THESIS SUBMITTED IN THE PARTIAL FULFILLMENT OF THE REQUIREMENT FOR THE

DEGREE OF

DOCTOR OF PHILOSOPHY

IN

MATHEMATICS

Supervised by

Prof. Dr. Muhammad Yousaf Malik

Department of Mathematics

Quaid-i-Azam University

Islamabad, Pakistan

2020

Certificate of Approval

This is to certify that the research work presented in this thesis entitled Numerical Solution of Stratified Flows was conducted by Mr. Khalil Ur Rehman under the kind supervision of Prof. Dr. Muhammad Yousaf Malik. No part of this thesis has been submitted anywhere else for any other degree. This thesis is submitted to the Department of Mathematics, Quaid-I-Azam University, Islamabad in partial fulfillment of the requirements for the degree of Doctor of Philosophy in field of Mathematics from Department of Mathematics, Quaid-I-Azam University Islamabad, Pakistan.

Student Name: Khalil Ur Rehman

Signature: 

External committee:

a) External Examiner 1:

Signature: 


Name: Dr. Rehmat Ellahi

Designation: Associate Professor

Office Address: Department of Mathematics

International Islamic University, H-10, Islamabad.

b) External Examiner 2:

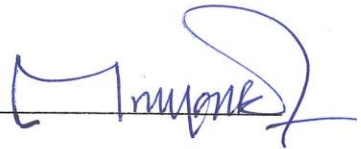
Signature: 

Name: Dr. Muhammad Mushtaq

Designation: Assistant Professor

Office Address: Department of Mathematics, COMSATS Institute of Information Technology Park Road, Chak Shahzad, Islamabad.

c) Internal Examiner

Signature: 

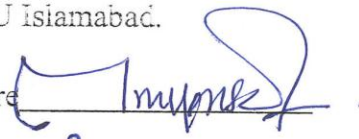
Name: Prof. Dr. Muhammad Yousaf Malik

Designation: Professor

Office Address: Department of Mathematics, QAU Islamabad.

Supervisor Name:

Prof. Dr. Muhammad Yousaf Malik

Signature: 

Name of Dean/ HOD

Prof. Dr. Sohail Nadeem

Signature: 

Numerical Solution of Stratified Flows

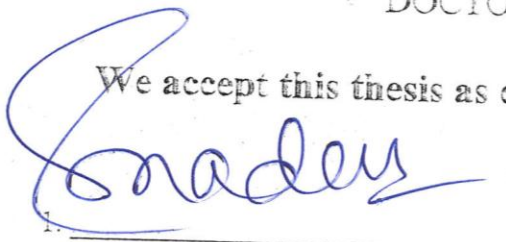
By

Khalil Ur Rehman

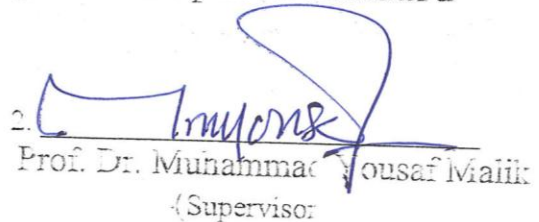
CERTIFICATE

A THESIS SUBMITTED IN THE PARTIAL FULFILLMENT OF THE
REQUIREMENTS FOR THE DEGREE OF THE
DOCTOR OF PHILOSOPHY

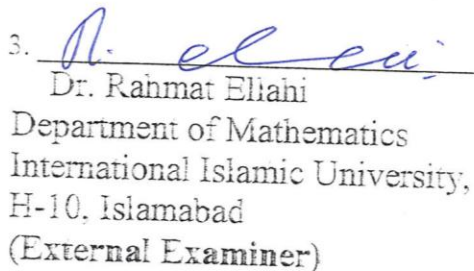
We accept this thesis as conforming to the required standard



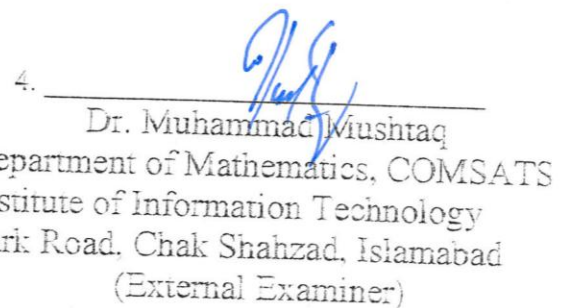
1. Prof. Dr. Sonail Nadeem
(Chairman)



2. Prof. Dr. Muhammad Yousaf Malik
(Supervisor)

3. 

Dr. Rahmat Eliahi
Department of Mathematics
International Islamic University,
H-10, Islamabad
(External Examiner)

4. 

Dr. Muhammad Mushtaq
Department of Mathematics, COMSATS
Institute of Information Technology
Park Road, Chak Shahzad, Islamabad
(External Examiner)

*Department of Mathematics
Quaid-I-Azam University
Islamabad, Pakistan*

2020

Author's Declaration

I, *Khalil Ur Rehman*, hereby state that my PhD thesis titled *Numerical Solution of Stratified Flows* is my own work and has not been submitted previously by me for taking any degree from Quaid-I-Azam University Islamabad, Pakistan or anywhere else in country/world.

At any time, if my statement is found to be incorrect even after my graduation the university has the right to withdraw my PhD degree.

Khalil Ur Rehman

Name of student: *Khalil Ur Rehman*

Dated: *15/06/2020*

Plagiarism Undertaking

I solemnly declare that research work presented in the thesis titled "Numerical Solution of Stratified Flows" is solely my research work with no significant contribution from any other person. Small contribution/help wherever taken has been duly acknowledged and that complete thesis has been written by me.

I understand the zero-tolerance policy of the HEC and Quaid-i-Azam University towards plagiarism. Therefore, I as an Author of the above titled thesis declare that no portion of my thesis has been plagiarized and any material used as reference is properly referred/cited.

I undertake that if I am found guilty of any formal plagiarism in the above titled thesis even afterward of PhD degree, the University reserves the rights to withdraw/revoke my PhD degree and that HEC and the University has the right to publish my name on the HEC/University Website on which names of students are placed who submitted plagiarized thesis.



Student/Author Signature

Name: Khalil Ur Rehman

Preface

Fluid dynamics is a branch of engineering science which deals with the analysis of different fluids flow in different geometries under their rheological behaviour. Fluids can be classified into different categories depending upon their various rheological properties. The study of interaction between heat and mass transfer regarding non-Newtonian fluids flow past a stretching surfaces along with boundary layer characteristics has a remarkable role due to its extensive use in engineering and industrial applications namely, coal-oil slurries, food stuffs or industrial thermal design equipment, metal spinning, glass blowing, metal extrusion etc. Therefore, interest of researchers and scientists immensely increased towards rheological features of non-Newtonian fluids. We have non-linear relationship between shear stress and shear rate which leads to flow diversity of non-Newtonians fluid models. Focus of present study is on rheological features of non-Newtonian fluid models. The thesis has been organized in the following manners. Introduction chapter is the literature survey about the applications of the non-Newtonian fluids flow in stratified medium along with analysis of physical effects.

Thermally stratified boundary layer flow of a tangent hyperbolic fluid induced by a stretching cylinder is considered in chapter 2. The flow field is translated in terms of differential equations along with endpoint conditions. To execute the computing scheme, the modelled partial differential equations are converted in terms of ordinary differential equations with the application of suitable symmetry transformations. A numerical study is performed to identify the effects of the flow-controlling parameters namely, curvature parameter, power law index, Weissenberg number, thermal stratification parameter and Prandtl number. The physical quantities namely, the skin friction coefficient and the local Nusselt number are calculated at the cylindrical surface and elucidated through graphs and tables. The contents of this chapter

are published in “**The European Physical Journal Plus, 132(9), (2017): 389**”. <https://doi.org/10.1140/epjp/i2017-11677-3>.

In the presence of mixed convection the temperature and concentration stratification effects on tangent hyperbolic fluid flow are exposed in chapter 3. The key objective of this chapter is to study fluid flow through no slip condition. The flow regime characteristics are modelled in terms of partial differential equations. A similarity transformation is used to transform partial differential equations into system of coupled non-linear ordinary differential equations. A computational algorithm is executed to predict its numerical results. The effects of flow controlling parameters namely, mixed convection parameter, thermal stratification and solutal stratification parameters on velocity, temperature and concentration are examined and offered by means of graphical outcomes. The contents of this chapter are published in “**Results in Physics 7(2017): 3659-3667**”. <https://doi.org/10.1016/j.rinp.2017.09.032>.

The flow characteristics of tangent hyperbolic fluid in the presence of thermal and solutal stratification effects are explored in chapter 4. The fluid flow is due to an inclined stretching cylindrical surface along with some pertinent effects, namely, heat generation, mixed convection and chemically reactive species. To be more specific, the researchers considered stratification effects, “either it is single stratification or double stratification” on flat surfaces. Numerical solution is obtained to visualize the effects of involved parameters on dimensionless quantities through graphs. Further, the skin friction coefficient, heat transfer rate and mass transfer rate are also computed and presented with the help of tables. The contents of this chapter are published in “**The European Physical Journal Plus 132(12) (2017): 550**”. <https://doi.org/10.1140/epjp/i2017-11822-0>.

In various attempts mostly researchers identified Eyring-Powell fluid flow towards flat surfaces supported with different physical effects but as yet few exploration are reported

subject to cylindrical stretching surfaces. Chapter 5 is dedicated to explore the physical aspects of magneto-hydrodynamic Eyring-Powell nanofluid flow both by flat and cylindrical inclined stretching surfaces along with chemically reactive species in vicinity of stagnation point manifested with mixed convection, thermal radiation, heat generation, temperature and concentration stratification effects. The strength of both fluid temperature and concentration adjacent to both surfaces is supposed to be higher as compared to ambient fluid. A mathematically modelled flow conducting differential equations are fairly transformed into system of coupled non-linear ordinary differential equations with the aid of suitable transformation. The numerical algorithm is developed to compute temperature, fluid velocity and concentration results. The compatibility of boundary conditions is validated by providing stream lines patterns subject to velocities ratio parameter. The impact of pertinent flow controlling parameters on dimensionless velocity, temperature and nanoparticle concentration profiles are discussed through graphical outcomes. Further, the influence of thermophoresis parameter and Brownian motion parameter are identified on heat and mass transfer rates by means of straight line curve fitting approximations. The contents of this chapter are published in “**AIP Advances 7(6), (2017): 065103**”. <https://doi.org/10.1063/1.4985061>.

Thermophysical aspects of magnetohydrodynamic double stratified mixed convection nanofluid flow by assuming Eyring-Powell model over an inclined stretching cylinder is proposed in chapter 6. In this study, concentration equations admit the role of solutal stratification and chemical reaction effects. The system of ODE's transformed from modelled PDE's is solved numerically through shooting scheme in support with Runge–Kutta-Fehlberg technique. The effects of involved physical parameters on dimensionless velocity, temperature, and nanoparticle concentration distributions are identified by graphs and tables. The compatibility of boundary conditions is verified by plotting stream lines for different

values of velocities ratio parameter. At the end the work is justified by providing comparison with literature and an excellent agreement is observed. The contents of this chapter are published in "**Journal of the Brazilian Society of Mechanical Sciences and Engineering 39(9), (2017): 3669-3682**". <https://doi.org/10.1007/s40430-017-0860-3>.

An analyse for mixed convection thermally stratified flow of Casson fluid in the presence of heat generation effects on stretching cylinder is explored in chapter 7. The flow problem narrated through partial differential equations is converted into system of non-linear ordinary differential equations through suitable transformation. The numerical solution is obtained by using shooting method with the aid of fifth order Runge-Kutta algorithm. The effects of controlling parameters on velocity and temperature profiles are depicted graphically. The numeric values for local skin friction coefficient and Nusselt number are reported with the aid of tables. Further, the obtained results are validated through table which leads to benchmark the quality of numerical communication. The contents of this chapter are published in "**Chinese Journal of Physics 55(4), (2017): 1605-1614**". <https://doi.org/10.1016/j.cjph.2017.05.002>.

The novelty of chapter 8 is to highlight the characteristics of the Casson nanofluid flow due to an inclined stretching cylinder manifested with various physical effects namely, magnetic field, mixed convection, heat generation, thermal radiations, temperature and concentration stratification along with chemical reaction. A mathematical model is developed in terms of differential equations. A self-constructed computational algorithm is executed to obtain the numerical solution of flow narrating equations. The dimensionless fluid velocity, temperature and nanoparticle concentration on varying physical parameters are demonstrated by means of graphical and tabular outcomes. The contents of this chapter are published in "**The European Physical Journal E 41(3) (2018): 37**". <https://doi.org/10.1140/epje/i2018-11641-8>.

Both Newtonian and non-Newtonian nanofluids with stagnation point flow towards an inclined cylindrical surface are considered in chapter 9. The flow field is manifested with physical effects, namely thermal radiation, mixed convection, chemical reaction, temperature and concentration stratification, heat generation/absorption, magnetic field. The reduced system of ODE's is obtained by transforming flow narrating PDE's with the aid of appropriate transformation. A computational algorithm is executed to trace out the solution of an initial value problem. The influence of Brownian motion and thermophoresis parameters are reported on mass and heat transfer rates by way of both straight line and parabolic curve fitting schemes. The contents of this chapter are published in "**The European Physical Journal Plus 132(10), (2017): 427**". <https://doi.org/10.1140/epjp/i2017-11679-1>.

Chapter 10 is dedicated to observe the non-Newtonian fluid flow towards the channel having infinite circular cylinder as an obstacle. Both upper and lower walls are considered at no slip condition and the right wall as an outlet is specified with Neumann condition. The left wall as an inlet is initiated with two different velocity profiles namely, the linear (constant) and parabolic Power law velocity profiles. The Power law fluid in each case strikes with an obstacle being placed in between channels, and the bifurcation of Power law fluid occurs around circular cylinder. The obtained outcomes with the help of finite element method are offered in terms of contour and line graphs. Besides this, the results are validated by developing comparison with existing work. The contents of this chapter are published in "**Journal of the Brazilian Society of Mechanical Sciences and Engineering, 41 (2019): 176**". <https://doi.org/10.1007/s40430-019-1664-4>.

The chapter 11 reports the extended novelty of the hydrodynamics. To be more specific, the flowing fluid stream admitting Newton's law of viscosity is considered in a smooth rectangular channel. The various typical shaped cylinders are placed fixed in between rectangular channel as an obstacle. The shape of obstacles includes the triangle, square, hexagon, octagon and circle. The no-slip condition is carried at both the upper and lower

walls of the channel. The right wall as an outlet is specified with the Neumann condition. The fluid is initiated at an inlet of the channel with the two different class of velocity profiles, namely the constant velocity profile and the parabolic profile. The whole physical designed is controlled mathematically in terms of Navier-Stokes equations. The solution is proposed with the finite element method and for the discretization of flow narrating equations the LBB-stable finite element pair is utilized along with a hybrid meshing scheme. The primitive variables namely, the velocity and pressure are reported for each obstacle. The line integration around the outer surface of the triangle, square, hexagon, octagon and circular cylinders is carried for the evaluation of hydrodynamic forces. The statistical data for such hydrodynamic forces is recorded up-to nine various refinement levels. The contents of this chapter is published in “**Journal of Molecular Liquids (2019): 111953**”. <https://doi.org/10.1016/j.molliq.2019.111953>

Thesis Abstract

The focus of this thesis is on the rheological features of Newtonian and non-Newtonian fluid models in a single or double stratified medium along with the various physical belongings namely, externally applied magnetic field, stagnation point, mixed convection, thermal radiation, Joule heating, heat generation/absorption, chemical reaction, and nanofluid flow field. The considered non-Newtonian fluid models includes Tangent hyperbolic fluid model, Eyring-Powell fluid model, Casson fluid model and Williamson fluid model. The case-wise mathematical modeling of the said fluid models along with the above mentioned physical effects is developed. The obtained differential system in terms of partial differential equations is translated into system of ordinary differential equations via suitable set of transformation. For solution purpose the numerical method named “Shooting method” is adopted. The quantity of interest includes the velocity, temperature, concentration, skin friction, heat transfer rate and mass transfer rate. The impact of flow controlling parameters are examined and offered by way of both line graphs and tables. Further, thesis contains evaluation of hydrodynamic forces namely drag force and lift force experienced by various regular shaped obstacles. Such obstacles are installed towards ongoing fluid in a rectangular channel. Both the Power law and viscous fluid models are entertained in this direction. The physics is developed in terms of partial differential equations. To obtain better solution, the finite element method is used. The quantities of interest includes the primitive variables namely velocity and pressure. The obtained outcomes are shared with the help of both contour plots and line graphs. The detail analysis on examination of forces is offered. The majority of the simulated results of present thesis are validated by developing comparison with an existing literatures which leads to surety of our findings. The completion of work on this thesis brings ten (10) research publications in well reputed peer reviewed international journals.

TABLE OF CONTENTS

| | |
|--|----|
| CHAPTER 1 | 5 |
| Introduction | 5 |
| CHAPTER 2 | 13 |
| Numerical Study of Thermally Stratified Flow of Tangent Hyperbolic Fluid Yields by Stretching Cylindrical Surface | 13 |
| 2.1 Introduction | 13 |
| 2.2 Mathematical formulation | 13 |
| 2.3 Shooting scheme | 16 |
| 2.4 Results and discussion..... | 17 |
| 2.5 Graphical outcomes..... | 20 |
| 2.6 Conclusion..... | 25 |
| CHAPTER 3 | 27 |
| Temperature and Concentration Stratification Effects on Non-Newtonian Fluid Flow Past a Cylindrical Surface | 27 |
| 3.1 Introduction | 27 |
| 3.2 Mathematical formulation | 27 |
| 3.3 Stratification modelling..... | 29 |
| 3.4 Numerical treatment..... | 31 |
| 3.5 Results and discussion..... | 32 |
| 3.6 Graphical outcomes | 35 |
| 3.7 Concluding remarks | 40 |
| CHAPTER 4..... | 42 |
| Numerical Solution of Chemically Reactive Non-Newtonian Fluid Flow: Dual Stratification | 42 |
| 4.1 Introduction | 42 |
| 4.2 Mathematical formulation | 42 |
| 4.3 Numerical scheme | 45 |
| 4.4 Analysis | 46 |
| 4.5 Graphical outcomes..... | 50 |
| 4.6 Concluding remarks | 56 |

| | |
|---|------------|
| CHAPTER 5 | 58 |
| Magneto-nanofluid Numerical Modelling of Chemically Reactive Eyring-Powell Fluid Flow Towards both Flat and Cylindrical an Inclined Surfaces: A Comparative Study..... | 58 |
| 5.1 Introduction | 58 |
| 5.2 Problem illustration..... | 58 |
| 5.3 Momentum formulation | 59 |
| 5.4 Temperature and concentration formulation..... | 61 |
| 5.5 Computational scheme..... | 64 |
| 5.6 Results and discussion..... | 65 |
| 5.6.1 Velocity distributions..... | 66 |
| 5.6.2 Temperature distributions..... | 68 |
| 5.6.3 Nanoparticle concentration distributions..... | 69 |
| 5.6.4 Straight line approximations..... | 70 |
| 5.7 Results validation..... | 70 |
| 5.8 Graphical outcomes..... | 72 |
| 5.9 Straight line curve fitting analysis..... | 79 |
| 5.10 Conclusions | 83 |
| CHAPTER 6..... | 85 |
| Thermophysical Aspects of Stagnation Point Magneto-Nanofluid Flow Yields by an Inclined Stretching Cylindrical surface: A Non-Newtonian Fluid Model..... | 85 |
| 6.1 Introduction | 85 |
| 6.2 Flow field formulation | 85 |
| 6.3 Temperature and nanoconcentration formulation | 88 |
| 6.4 Computational algorithm..... | 90 |
| 6.5 Results and discussion..... | 92 |
| 6.6 Graphical outcomes..... | 96 |
| 6.7 Concluding remarks | 104 |
| CHAPTER 7 | 106 |
| Numerical Communication for MHD Thermally Stratified Dual Convection Flow of Casson Fluid Yields by Stretching Cylinder | 106 |
| 7.1 Introduction | 106 |
| 7.2 Mathematical modelling..... | 106 |

| | | |
|-------|--|------------|
| 7.3 | Shooting method | 109 |
| 7.4 | Discussion | 110 |
| 7.4.1 | Velocity profiles..... | 111 |
| 7.4.2 | Temperature profiles..... | 111 |
| 7.5 | Graphical outcomes..... | 113 |
| 7.6 | Concluding remarks | 117 |
| | CHAPTER 8..... | 118 |
| | Nanoparticles Individualities in both Newtonian and Casson Fluid Models by Way of Stratified Media: A Numerical Analysis..... | 118 |
| 8.1 | Introduction | 118 |
| 8.2 | Mathematical formulation..... | 118 |
| 8.3 | Computational scheme..... | 122 |
| 8.4 | Results and discussion..... | 124 |
| 8.4.1 | Tabular trends | 124 |
| 8.4.2 | Velocity distribution | 125 |
| 8.4.3 | Temperature distribution..... | 126 |
| 8.4.4 | Nanoparticle concentration distribution..... | 127 |
| 8.5 | Graphical results..... | 128 |
| 8.6 | Concluding remarks | 134 |
| | CHAPTER 9..... | 136 |
| | A Comparative Study of Nanofluids Flow Yields by an Inclined Cylindrical Surface in a Double Stratified Medium | 136 |
| 9.4 | Physical outcomes | 141 |
| 9.4.1 | Tabular values..... | 141 |
| 9.4.2 | Key to the graphs | 142 |
| 9.4.3 | Velocity profiles..... | 142 |
| 9.4.4 | Temperature profiles..... | 143 |
| 9.4.5 | Concentration profiles..... | 144 |
| 9.5 | Graphical outcomes..... | 145 |
| 9.6 | Straight line and parabolic curve fitting..... | 149 |
| 9.7 | Conclusion..... | 154 |

| | |
|---|------------|
| CHAPTER 10 | 156 |
| A Potential Alternative CFD Simulations for Steady Carreau-Bird Law Based Shear Thickening Model | 156 |
| 10.1 Introduction | 156 |
| 10.2 Mathematical formulation | 156 |
| 10.3 Problem description..... | 158 |
| 10.3.1 Power law linear velocity at inlet..... | 158 |
| 10.3.2 Power law parabolic velocity profile at inlet | 159 |
| 10.3.3 Benchmark quantities..... | 160 |
| 10.4 Computational scheme | 161 |
| 10.5 Analysis | 164 |
| 10.6 Graphical results..... | 167 |
| 10.7 Conclusion..... | 183 |
| Chapter 11 | 185 |
| Object Dependent Optimization of Hydrodynamic Forces in Liquid Stream: Finite Element Analysis | |
| 11.1 Introduction | 185 |
| 11.2 Problem Description..... | 185 |
| 11.3 Mathematical Model | 186 |
| 11.4 Computational Scheme | 188 |
| 11.5 Analysis | 189 |
| 11.5.1 OBSTACLE-I | 189 |
| 11.5.2 OBSTACLE-II..... | 195 |
| 11.5.3 OBSTACLE-III..... | 200 |
| 11.5.4 OBSTACLE-IV | 205 |
| 11.5.5 OBSTACLE-V | 210 |
| 11.6 Results benchmarking | 212 |
| 11.7 Conclusion..... | 219 |
| Thesis General Concluding Remarks | 220 |
| Bibliography | 221 |

CHAPTER 1

Introduction

The study of non-Newtonian fluids has received notable attention due to its practical applications in engineering and industrial processes. For instance, sugar solutions, polymers, emulsions, synthetic lubricants, paints, pulps, blood as a biological fluid, food stuffs such as marmalades, jellies and jams etc. Just a few mentioned here are the well-known fluids having non-Newtonian characteristics. In non-Newtonian fluids it is difficult to narrate the rheological features accurately because of nonlinear relation between shear stresses and deformation rate. Although, number of constitutive laws some of them namely, Ostwald–de Waele power law [1-2], Carreau, Carreau–Yasuda [3-4], Cross [5], Sisko [6], Eyring [7-8], Barus [9], Ellis [10], Seely [11], Bingham Herschel–Bulkley [12-13] are proposed to report the physical description of fluids exhibiting non-Newtonian properties. To be more specific, Ostwald–de Waele power law fluid model fits experimental data for molten chocolate, ball point pen ink and aqueous dispersion of polymer latex spheres, Carreau Carreau–Yasuda justified for experimental data for molten polystyrene, Cross fluid model suits to experimental data for aqueous limestone suspension and aqueous polyvinyl acetate dispersion, Sisko fluid model applies to experimental data for lubricating greases, Barus fluid model suits to experimental data for organic liquids and mineral oils, Ellis fluid model outfits to experimental data for poly(vynil chloride) and 0.6% w/w carboxymethyl cellulose (CMC) solution in water, Seely fluid model fits experimental data for polybutadiene solutions, Bingham Herschel–Bulkley fluid model justified for experimental data for polybutadiene solutions. As yet a tremendous work has been done by [14-19] after considering some frequently used non-Newtonian fluid models through experimental, integral and numerical treatments.

The Ellis model, Cross model, Carreaus model, and tangent hyperbolic model are the most deliberately used fluid models in the field of fluid mechanics. These fluids are quoted as fluids having pseudo-plastic features. Out of these tangent hyperbolic fluid model belongs

to the shearing thinning non-Newtonian fluids like polymers, blood and paints are the few examples obeying tangent hyperbolic (TH) constitutive relations. Owing the importance of TH fluid numerous investigators contributed their findings on flow field properties of such fluid like Akbar et al. [20] discussed the numerical solution of TH fluid flow brought by stretched sheet. The flow narrating equations are solved by the fourth and fifth order Runge-Kutta-Fehlberg method. The numerical solution of TH fluid flow towards vertical cylinder having exponentially stretching was given by Naseer et al. [21]. The thermal radiation effect on tangent hyperbolic fluid flow with stagnation point assumption was assumed by Hayat et al. [22].

The study of interaction between heat and mass transfer regarding non-Newtonian fluids flow past a stretching surfaces along with boundary layer characteristics has a remarkable role due to its extensive use in engineering and industrial applications namely, coal-oil slurries, food stuffs or industrial thermal design equipment, metal spinning, glass blowing, metal extrusion etc. Therefore, interest of researchers and scientists immensely increased towards the rheological features of non-Newtonian fluid models. The non-linear relationship between shear stress and shear rate leads to flow diversity of non-Newtonian fluid models. In general, due to uncertainty in rheological topographies of non-Newtonian fluid models the single constitutive equation is not enough to confer the relation of shear stresses and shear rate. In this context, various model are proposed namely, White-Metzner, Rolie-Poly, Blatter fluid model (1995), Eyring-Powell (1994), FENE-CR (1988), Giesekus fluid model (1982), Phan-Thien-Tanner fluid model (1978), Johnson-Tevaarwerk (1977), Johnson-Segalman fluid model (1977), Carreau-Yasuda fluid model (1972), Carreau fluid model (1972), FENE-P (1966), Cross fluid model (1965), Seely fluid model (1964), Kaye-Bernstein-Kearsley-Zapas (K-BKZ, 1963), Sisko fluid model (1958), Criminale-Ericksen-Filbey (1957), Rivlin-Ericksen (1955), Glen fluid model (1955), Oldroyd-A (1950), Oldroyd-8 constants (1950), Oldroyd-B fluid model (1950), Reiner-Rivlin fluid model (1945), Generalized Burgers (1939), Burgers fluid model (1939), Eyring fluid model (1936), Williamson fluid model (1929), Ostwald-de Waele power law model (1923), Bingham Herschel-Bulkly (1922), Barus fluid model (1893), Maxwell fluid model (1867), etc. A non-Newtonian fluid model proposed by Eyring and Powell [23] was derived from molecular theory of gases instead of empirical

formulation. The Eyring Powell has plus point in this sense that it may turn into Newtonian mode at low and high shear rates. In heat and mass diffusion, Eyring Powell model claims its key role in numerous natural, industrial, and geophysical problems like underground energy transport, temperature and moisture distribution over agricultural pitches. Therefore, Eyring-Powell fluid model as non-Newtonian fluid model remained a matter of great notice for researchers, namely, Yoon and Ghajar [24] identified the impact of an infinite and zero shear rate viscosities on Eyring Powell fluid model. It was found that Eyring Powell reflects remarkable sensitivity for small zero shear rate viscosity but moderate attitude is observed for an infinite shear rate viscosity. Patel and Timol [25] presented numerical communication on Eyring Powell fluid. The Eyring Powell fluid flow adjacent to the linearly stretched flat surface was identified by Javed et al. [26]. Besides, the work on Eyring Powell fluid flow over a stretching surfaces with different physical effects is concerned, (see [27-32]).

The Casson fluid model (1959) is one of the most commonly used rheological model and has certain advantages over non-Newtonian fluid models. When yield stress is dominant in contrast to shear stress this model exhibits solid like behaviour and deformation occurs when yield stress is less significant as compared to shear stress. The researchers admit the importance of this fluid model and identified the influence of different physical effects by considering Casson fluid flow over stretching surfaces. Like the unsteady flow field properties of Casson fluid was discussed by Mustafa et al. [33]. Nadeem et al. [34] studied the boundary layer flow of a Casson fluid along with heat transfer characteristics towards an exponentially shrinking surface in the presence of thermal radiation. Later on, the heat transfer properties of Casson fluid flow near stretching surface under stagnation point was analyse by Mustafa et al. [35]. Mukhopadhyay et al. [36] contributed extended study on Casson fluid flow regime. She further extended her work in [37] by entertaining non-linearly stretching surface. Furthermore, the magnetic field interaction and permeable effects are studied by Mukhopadhyay et al. [38] on Casson fluid model. Higher dimensional flow field of MHD Casson fluid with porous and convective assumptions was investigated by Mahanta and Shaw [39]. The study of Casson nanofluid flow field was reported in Ref. [40]. Das et al. [41] analysed unsteady Casson fluid flow. The slip effects towards Casson flow field was analytically probed by Ramesh and Devakar [42].

Animasaun et al. [43] studied Casson boundary layer flow due to exponentially stretching surface with variable hydromagnetic properties. Raju et al. [44] discussed the heat and mass transfer of Casson fluid flow over an exponentially stretching porous sheet. The modified viscosity model in line with three dimensional field for Casson fluid model was debated by Sandeep et al. [45]. The extended version of novelty subject to entropy generation, and Cattaneo-Chirstov heat flux model towards Casson fluid flow field can be assessed in Refs. [46-47].

The Williamson fluid model [48] was proposed by Williamson in 1929. He presented a rheological equation to explore the hidden characteristics of pseudoplastic fluids flow and the obtained results were also supported experimentally. The pseudoplastic fluid as a thin layer (oblique) by considering Williamson model under gravitational force was given by Lyubimov and Perminov [49]. The perturbation findings for a pulsatile flow of Williamson fluid towards rock fracture was presented by Dapra and Scarpi [50]. The peristaltic flow of Williamson fluid towards an asymmetric channel was identified by Nadeem and Akram [51]. Vajravelu et al. [52] identified the peristaltic transport in Williamson fluid by assuming channels (asymmetric) having permeable walls. In 2013, for the first time the mathematical modelling and physical narration for Williamson fluid was presented by Nadeem et al. [53]. The heat transfer properties of Williamson fluid towards flat surface in the presence of nanoparticles was deliberated by Nadeem and Hussain [54]. Blood flow characteristics of Williamson fluid through stenosed arteries subject to permeable walls was reported by Akbar et al. [55]. The numerical solution of Williamson fluid flow in the presence of pressure dependent viscosity was discussed by Zehra et al. [56]. To predict pertinent features of pseudoplastic materials the role of maximum or minimum effective viscosities is very important. This is due to their dependence yields from molecular structure of fluid. Here, in Williamson model we have both maximum and minimum viscosities subject to pseudoplastic materials due to which Williamson model provides better outcomes. The trustful literature regarding recent developments on Williamson fluid flow can be found [57-65].

The Couette flow is the viscous fluid flow in space between two surfaces one of which is moving tangentially relative to the other. This type of configuration exists either between

two parallel plates or in the gap of two concentric cylinders. The flow in this case is induced due to drag force or applied pressure gradient. The viscometry and lightly loaded journal bearing refers to the importance of Couette flow. One can assess the detail in this direction in [66-70]. The stationary fluid flow due to effective pressure gradient towards pipe having uniform cross sectional area is termed as Poiseuille flow. In this case, the relative velocity between fluid particles with surface is considered zero. In 1838, Jean Poiseuille (1797-1869) initially identified Poiseuille flow experimentally. In the presence of smooth geometry configuration both the Couette and Poiseuille flow were investigated analytically. In some recent attempts Poiseuille flow can be assessed in [71-76]. For both the Couette and Poiseuille flow manifested with various useful assumptions the exact solutions are proposed. Still it remained a challenging task for the investigators to propose exact findings when an obstacle is placed in-between fluid flow domain. Owing the importance of flow field along with an obstacle many researchers contributed their efforts towards research society. This is due to wide range of applications in the field of engineering science [77-80]. In this thesis the analysis about flow around obstacles is limited to one of the non-Newtonian fluid known as Power law or Ostwald de Waele Equation. Owing the importance of the Power law fluid model many researchers offered their findings towards various geometrical configurations [81-88].

The formation or decomposition of thermal layers in a fluid flow regime is termed as temperature stratification phenomena. Temperature stratification is also refers as thermal stratification and it arises because of combination of fluids having different densities or it occurs due to variations in temperature. The study of boundary layer flow, non-Newtonian fluids subject to heat transfer manifested with thermal stratification has received considerable attention by the researchers because of its frequent industrial application. To mention few of them are, the oxygen and hydrogen ratio is maintained by the way stratification to control the species growth rate in the case of ponds and lakes. Stratification can be temperature stratification or concentration stratification. The stratification phenomena occur due to variant of concentration and temperature differences in a concerned medium. For example in solar ponds (thermal energy storing setup), environmental and geophysical domains having heat rejection aspects such as seas, lake and rivers. Whereas oceanography, agriculture, astrophysics and various chemical

processes also enclosed both thermal and solutal stratification. Furthermore, closed containers, heated walls environmental chambers are also supported by double diffusion occurrence. In fact, stratification has widespread uses in many industrial and natural phenomena. In real situation when mass and heat transfer mechanism run simultaneously, it becomes essential to analyse the convective mode of transportation in fluids under the influence of double stratification. Thus to describe the characteristics of the mixed convection flows in a doubly prescribed frame several analytical and experimental attempts have been made. For example, Yang et al. [89] discussed the laminar flow over a non-isothermal surface in the presence of free convection through thermally stratified medium. Transition and stability of buoyancy induced stratified flow was studied by Jaluria and Gebhart [90]. Thermally stratified fluids flow with natural convection along simple bodies was identified by Chen and Eichhorn [91]. Ishak et al. [92] presented stratified boundary layer flow with dual convection normal to horizontal surface. Narayana and Murthy [93] debated dual stratified medium aspects in power law fluid model. Chen and Lee [94] considered micro-polar fluid flow parallel to vertical plate with constant and uniform heat flux in a thermally stratified medium. Cheng [95] reported double stratification in power law fluid flow towards vertical porous wavy surface. Mukhopadhyay and Ishak [96] studied the dual convection flow in viscous fluid subject to cylindrical surface through thermally stratified medium and computed its solution numerically. The suspended nanoparticles in dual stratified field was debated in Ref. [97]. The flow regime micropolar fluid manifested with stratified medium was debated, see Ref. [98]. The Jeffrey fluid model manifested with dual stratification was examined by Hayat et al. [99].

Nanofluids are those fluids which contain solid particles having dimensions approximately less than 100nm. The term nanofluids was coined most probably by Choi and Eastman [100] in 1995. The performance mode of heat transfer is remarkably effected by nanofluids having low thermal conductivity measures like water, engine and ethylene glycol and therefore, they cannot congregate for cooling requirements. Whereas, metals exhibits larger values of thermal conductivity as compared to conventional heat transfer. Furthermore, the solid particles in nanofluids are made of carbides, oxides, and different metals namely, silicon, aluminium and copper. In short, the fluid contains nano sized

particles having higher thermal conductivity as compared to regular/base fluids. This fact enhances the use of nanoparticles for the purpose of improvement in thermal conductivity of base fluids. Therefore, the existence of nano sized solid particles in the conventional fluids are foundation of enhancement in the heat transfer individualities. In a nanofluid thermal conductivity was discussed by Choi et al. [101] subject to the base fluids when solid nano size particles were entertained. After these findings, many experimental and theoretical attempts were made to explore the advantages of nano sized particles because of numerous potential applications of nano fluids in heat transfer such as refrigerator, heat exchangers, engine cooling, microelectronics, chiller, fuel cells and thermal engineering. Different researchers addressed for the improvement/development in nano-fluids [102-111]. Furthermore, magnetic nanofluid is a fluid that reflects properties of liquid and magnetic both. The optical modulators, non-linear optical substances, optical switches magneto-optical wavelength filters are few applications of magnetic nanofluids. Therefore, plenty of researchers [112-115] are attracted and motivated to look for further avenues subject to nanofluid flows past a different stretching surfaces having magnetic characteristics.

The study of magnetic properties and the behavior of electrically conducting fluids is term as magnetohydrodynamics (MHD). An analysis of MHD flow in an electrically conducting fluid has attained considerable attention by scientists and researchers due to its abundant applications in industries namely, MHD power generators, flow of ionized gases, plasma structures, geothermal energy extractions, petroleum individualities, the isolation of hot plasma in nuclear reactor, continuous strips cooling or filaments, thinning and drawing process for copper wires in desire direction. Further, the magnetic field has numerous applications in the area of metallurgy and polymer industry. The metallurgical claim comprises the continuous strips cooling or filaments in, such as, annealing, thinning and copper wires drawing process. In all these circumstances, the stuff of the final product depends up on cooling rate. Therefore, an intelligent attempt of magnetic field is required to control cooling and stretching rates. Thereby we can improve the desired claims of the final product. Pavlov [116] reported the exact solution of momentum equation having magnetic field as a body force term. In this frame, as far as cylindrical geometries are concerned, Ishak et al. [117] studied the magneto-hydrodynamic flow transported due to

stretching cylinder by way of heat transfer. The governing flow equations are solved by utilizing Keller-box method. Singh and Makinde [118-120] explored the magneto-hydrodynamic characteristics of fluid flow along an inclined plate under volumetric heat generation phenomena. Later on, they anticipated slip flow of viscous fluid by way of isothermal reactive stretching sheet and axisymmetric slip flow on a vertical cylinder. Das et al. [121] debated magnetic field aspects along with slip effect assumption. The extended novelty in this direction can be assessed in Refs. [122-124].

CHAPTER 2

Numerical Study of Thermally Stratified Flow of Tangent Hyperbolic Fluid Yields by Stretching Cylindrical Surface

2.1 Introduction

In this chapter the effects of temperature stratification on tangent hyperbolic fluid flow towards stretching cylindrical surfaces are studied. The fluid flow is achieved by taking no slip condition. The mathematical modelling of physical problem yields the nonlinear set of partial differential equations. These obtained partial differential equations are converted to a system of ordinary differential equations. Numerical investigation is done to elaborate the effects of involved physical parameters on dimensionless velocity and temperature profiles. A dimensionless number skin friction coefficient characterising the frictional force on boundary within fluid and wall is computed. Also, the local Nusselt number is computed and presented through table for further analysis. The obtained results are validated by developing comparison within existing literature which leads to justify the present developed model.

2.2 Mathematical formulation

The two dimensional thermally stratified TH fluid flow towards stretched cylindrical is considered. The surface temperature is supposed higher in strength as compared to ambient fluid. Fig. 2.1 represents the scenario of TH fluid flow brought by stretching cylindrical surface.

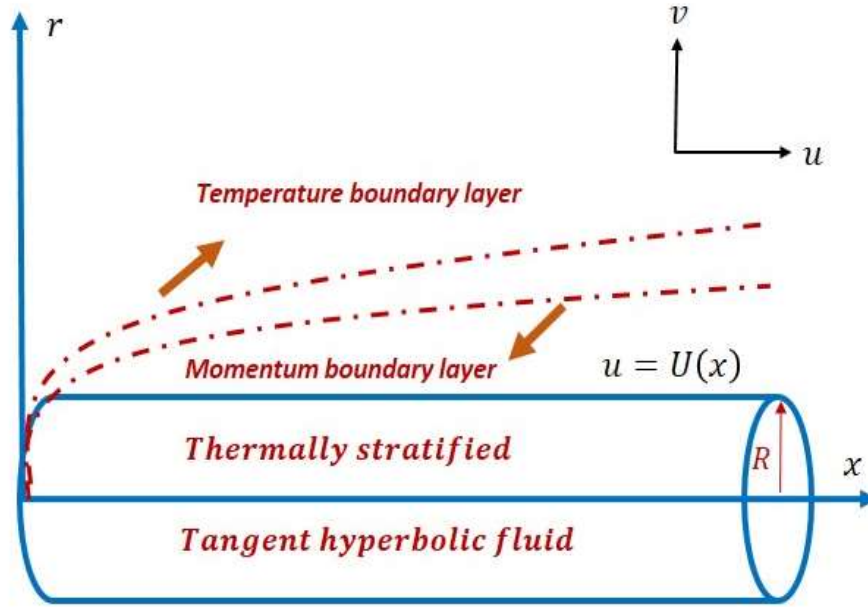


Fig. 2.1. Physical illustration.

The ultimate flow narrating differential equation for TH fluid flow can be written as:

$$\frac{\partial(rv)}{\partial r} + \frac{\partial(ru)}{\partial x} = 0, \quad (2.1)$$

$$\frac{\partial u}{\partial r} v + \frac{\partial u}{\partial x} u = v \left(\frac{1}{r} \frac{\partial u}{\partial r} (1-n) + \left(\frac{\partial u}{\partial r} \right)^2 \frac{n\Gamma}{\sqrt{2}r} + (1-n) \frac{\partial^2 u}{\partial r^2} + n\sqrt{2}\Gamma \frac{\partial^2 u}{\partial r^2} \frac{\partial u}{\partial r} \right), \quad (2.2)$$

$$\frac{\partial T}{\partial r} v + \frac{\partial T}{\partial x} u = \left(\frac{\partial^2 T}{\partial r^2} + \frac{\partial T}{\partial r} \frac{1}{r} \right) \frac{k}{\rho c_p}, \quad (2.3)$$

where $\Gamma, \nu, n, \rho, c_p$ and k denote time constant, kinematic viscosity, power law index, fluid density, specific heat at constant pressure and thermal conductivity respectively. The associated endpoint conditions are listed as follows:

$$T(x, r) = T_w(x) = T_0 + \frac{bx}{L}, \quad v(x, r) = 0, \quad u(x, r) = U(x) = \frac{U_0}{L} x, \quad \text{at } r = R, \quad (2.4)$$

$$T(x, r) \rightarrow T_\infty(x) = T_0 + \frac{cx}{L}, \quad u(x, r) \rightarrow 0, \quad r \rightarrow \infty,$$

where, ψ is the stream function, and under this relation the Eq. (2.1) holds identically.

The relation is defined as:

$$v = \frac{-1}{r} \left(\frac{\partial \psi}{\partial x} \right), \quad u = \frac{1}{r} \left(\frac{\partial \psi}{\partial r} \right). \quad (2.5)$$

To solve Eqs. (2.2)-(2.3) subject to the boundary conditions Eq. (2.4), we have used following transformations:

$$T(\eta) = \frac{T - T_\infty}{T_w - T_0}, \quad u = \frac{U_0 x}{L} F'(\eta), \quad v = -\frac{R}{r} \sqrt{\frac{U_0 \nu}{L}} F(\eta), \quad (2.6)$$

$$\psi = R F(\eta) \left(\frac{U_0 \nu x^2}{L} \right)^{\frac{1}{2}}, \quad \eta = \left(\frac{U_0}{\nu L} \right)^{\frac{1}{2}} \frac{r^2 - R^2}{2R},$$

where, $T_0, T_\infty(x), T_w(x), R, F'(\eta), F(\eta), \eta, L$ and U_0 denotes reference, ambient and surface temperatures, cylinder radius, fluid velocity, dimensionless variable, reference length and free stream velocity respectively. After incorporating Eqs. (2.5)-(2.6) into Eqs. (2.2)-(2.3) (momentum and energy equations), we have obtained following dimensionless forms:

$$(1 + 2K\eta) 2(1-n) F'''(\eta) + 2F(\eta) F''(\eta) - 2(F'(\eta))^2 + 4K(1-n) F''(\eta) \quad (2.7)$$

$$+ 3(1 + 2K\eta)^{\frac{1}{2}} K\lambda (F''(\eta))^2 + 2\lambda n (1 + 2K\eta)^{\frac{3}{2}} (F''(\eta)) F'''(\eta) = 0,$$

$$(1 + 2K\eta) T''(\eta) + 2KT'(\eta) + \text{Pr}(F(\eta)T'(\eta) - F'(\eta)T(\eta) - sF'(\eta)) = 0, \quad (2.8)$$

the reduced endpoint conditions are given as:

$$T(\eta) = 1 - s, \quad F'(\eta) = 1, \quad F(\eta) = 0, \quad \text{at } \eta = 0, \quad (2.9)$$

$$T(\eta) \rightarrow 0, \quad F'(\eta) \rightarrow 0, \quad \text{at } \eta \rightarrow \infty,$$

here, λ, K, s and Pr denotes Weissenberg number, curvature parameter, thermal stratification parameter and Prandtl number respectively. They are defined as follow:

$$\text{Pr} = \frac{\mu c_p}{\kappa}, \quad K = \frac{1}{R} \sqrt{\frac{\nu}{a}}, \quad \lambda = \Gamma \sqrt{\frac{2U_0^3}{\nu x}}, \quad s = \frac{c}{b}, \quad \text{and } a = \frac{U_0}{L}. \quad (2.10)$$

At surface the skin friction is exercised as follows

$$C_f = \frac{\tau_w}{\rho \frac{U^2}{2}}, \quad (2.11)$$

$$\tau_w = \mu \left[\frac{n\Gamma}{\sqrt{2}} \left(\frac{\partial u}{\partial r} \right)^2 + \frac{\partial u}{\partial r} (1-n) \right]_{r=R}, \quad (2.12)$$

where, shear stress and viscosity is denoted by symbols τ_w and μ . The dimensionless form is achieved as

$$C_f \sqrt{\text{Re}_x} = (F''(0))^2 n\lambda + F''(0)(1-n), \quad (2.13)$$

with $\text{Re}_x = \frac{U_0 x^2}{\nu L}$. As local Reynolds number. The local Nusselt number is carried as:

$$q_w = - \left(\frac{\partial T}{\partial r} \right)_{r=R} k, \quad Nu_x = \frac{q_w x}{(T_w - T_0)k}, \quad (2.14)$$

while the dimensionless form is:

$$\frac{Nu_x}{\sqrt{\text{Re}_x}} = -T'(0). \quad (2.15)$$

2.3 Shooting scheme

The flow Eqs. (2.7)-(2.8) with endpoint constraints Eq. (2.9) are solved numerically with the aid of shooting method having supportive fifth order Runge-Kutta algorithm. The neccessary conversion is exercised as follows:

$$\begin{aligned} p_2 &= F', \\ p_3 &= p'_3 = F'', \\ p_5 &= T', \end{aligned}$$

the alike form of Eqs. (2.7)-(2.8) under new variables is given by:

$$\left[\begin{array}{l} p'_1 = p_2 \\ p'_2 = p_3 \\ p'_3 = \frac{(p_2)^2 - p_1 p_3 - (1-n)(2K)p_3 - 0.5(1+2K\eta)^{\frac{1}{2}} \lambda K p_3^2}{(2K\eta+1)(1-n) + (2K\eta+1)^{\frac{3}{2}} p_3 n \lambda} \\ p'_4 = p_5 \\ p'_5 = \frac{\text{Pr}(p_2 p_4 + s p_2 - p_1 p_5) - 2K p_5}{1 + 2K\eta} \end{array} \right], \quad (2.16)$$

the alternative endpoint constraints are

$$\begin{aligned} p_1(0) &= 0, \\ p_2(0) &= 1, \\ p_3(0) &= \text{unknown}, \\ p_4(0) &= 1 - s, \\ p_5(0) &= \text{unknown}. \end{aligned} \quad (2.17)$$

To perform integration of Eq. (2.16), we need $p_3(0)$ reads as $F''(0)$, and $p_5(0)$ reads as $T'(0)$. The initial information $p_3(0)$ and $p_5(0)$ are not identified but we have far field information:

$$\begin{aligned} p_2(\infty) &= 0, \\ p_4(\infty) &= 0. \end{aligned} \quad (2.18)$$

It is important to note that the values of $T'(0)$ and $F''(0)$ are chosen in such a way that the Eq. (2.18) holds acceptably.

2.4 Results and discussion

The current flow analysis focuses on the physical aspects of the non-Newtonian tangent hyperbolic fluid flow over stretching cylinder through thermally stratified medium. The solution of Eqs. (2.7)-(2.8)) is calculated with the help of well-known numerical technique i.e. shooting method. The authenticity of calculated results is attained by giving comparasion with an existing work. Table 2.1 contains the evaluation of skin friction coefficient with published results (Akbar et al. [20]) via variations in Weissenberg number and power index. It is observed that the current results match with the previous one up to

significant number of digits. In Table 2.2, a comparison of local Nusselt number is established with previous trustful literature (Wang [125], Golra and Sidawi [126], Khan and Pop [127] and Hussain et al. [128]). This table ensures that computed results are accurate which gives confidence on computed results. The primitive variables namely the temperature and velocity are evaluated and offered graphically. In detail, Fig. 2.2 reflects inciting values velocity towards curvature parameter. In actual, when we increase curvature parameter, radius of cylinder decreases and hence surface contact area will reduce so that less resistance is obtainable to fluid particles which ultimately increase the fluid velocity. Fig. 2.3 paints the inverse variation of TH fluid velocity towards positive values of power law index. Fig. 2.4 depicts the attitude of fluid velocity towards Weissenberg number. It is noticed that TH fluid velocity reflects decline values for positive values of Weissenberg number. Brings enhancement in Weissenberg number cause increment in relaxation time as a result the resistance is developed and TH fluid velocity declines. Figs. 2.5-2.8 are plotted to examine the variation in temperature distribution. In detail, Fig. 2.5 shows higher values of temperature via positive variation in curvature parameter. As we know that the Kelvin temperature is an average kinetic energy so, an increase in curvature parameter causes increase in velocity particles, as a result average kinetic energy increases which reflects increase in mean temperature of fluid. Fig. 2.6 addresses the Pr impact on TH fluid temperature. Prandtl number has inverse relation with thermal conductivity of the fluid so the greater Pr values corresponds weaker diffusion of energy. That is why, significant decline in TH fluid temperature is observed towards Prandtl number. Fig. 2.7 identify that for positive values of λ the temperature profile decreases. On increasing the value of Weissenberg number the relaxation time of the fluid increases which creates resistance to the fluid particles. So, less will be the average kinetic energy which confirms the decline in fluid temperature. Fig. 2.8 shows that the higher values in stratification parameters brings decline nature in temperature. This is due to drop in convective potential difference between ambient temperature and cylindrical surface. Figs. (2.9)-(2.10) are plotted to examine the skin friction coefficient and Nusselt number with relation to flow parameters. Particularly, Fig. 2.9 is constructed for the different values of n , K and λ . It is seen that the skin friction shows decline nature for positive values of both λ and n . Fig. (2.10) depicts the behaviour of local Nusselt number towards

stratification, curvature parameters, and Prandtl number. It is seen that in absolute sense, the local Nusselt number enhances for increasing values of Prandtl number while reverse variations are noticed for positive values of thermal stratification parameter. Further, it is noticed that the skin friction coefficient (absolute sense) and Nusselt number variations are enriched for cylindrical surface as compared to flat surface.

2.5 Graphical outcomes

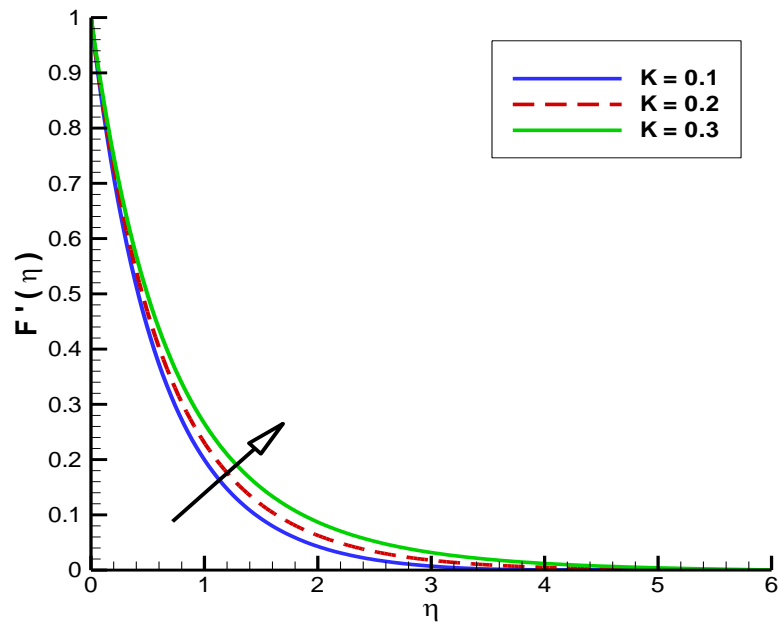


Fig. 2.2. Impact of K on fluid velocity

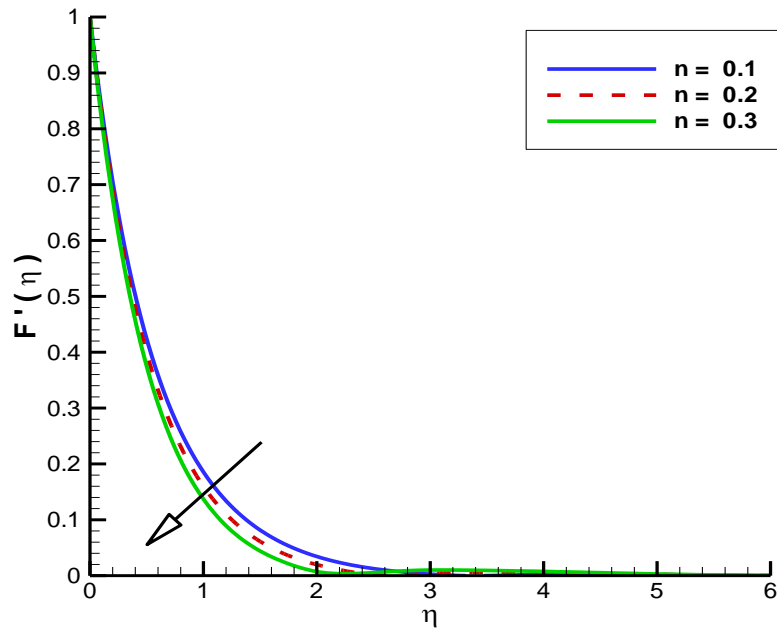


Fig. 2.3. Impact of n on fluid velocity.

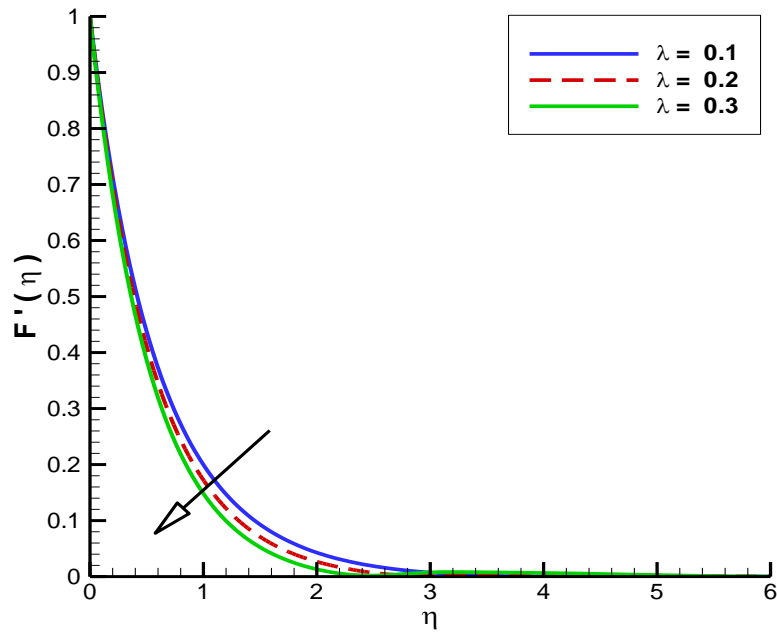


Fig. 2.4. Impact of λ on fluid velocity.

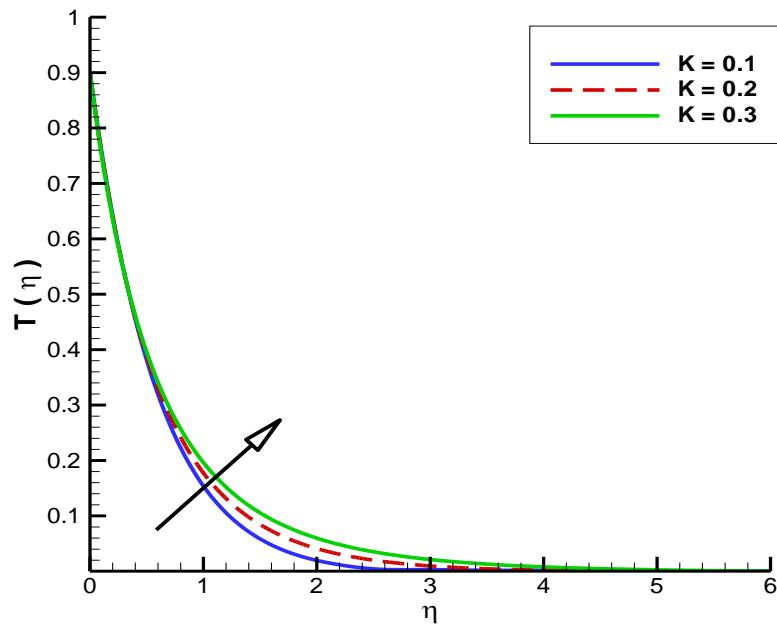


Fig. 2.5. Impact of K on fluid temperature.

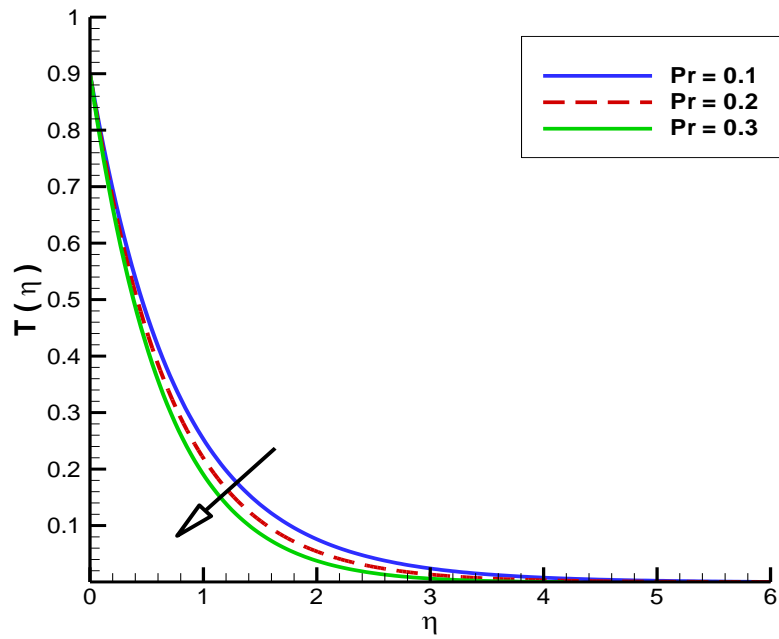


Fig. 2.6. Impact of Pr on fluid temperature.

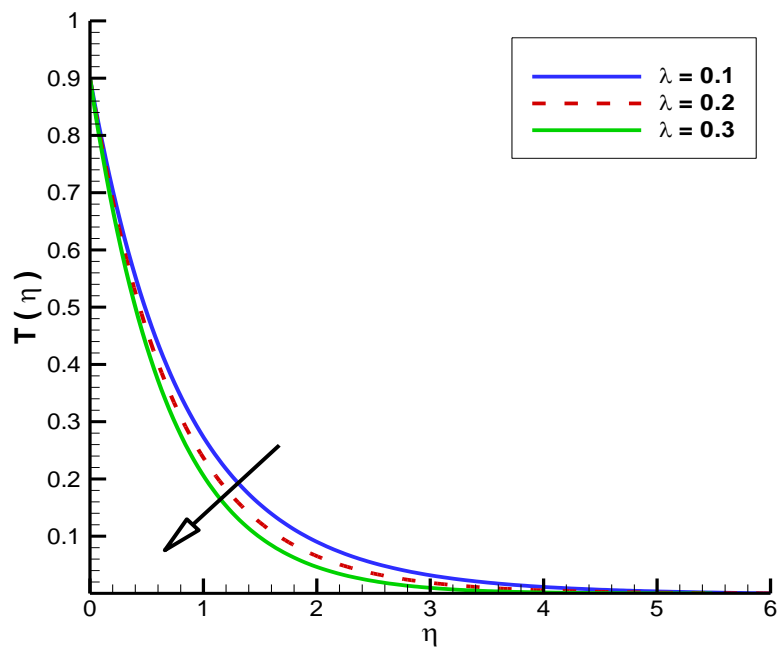


Fig. 2.7. Impact of λ on fluid temperature.

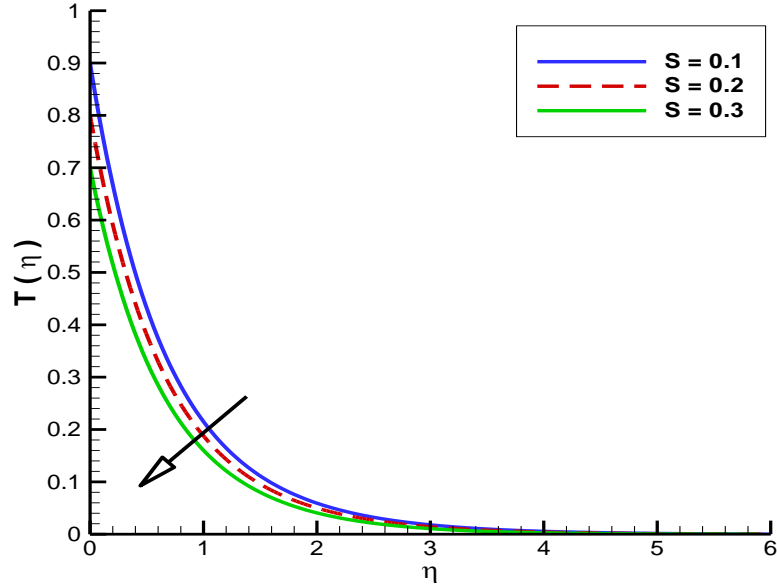


Fig. 2.8. Impact of S on fluid temperature.

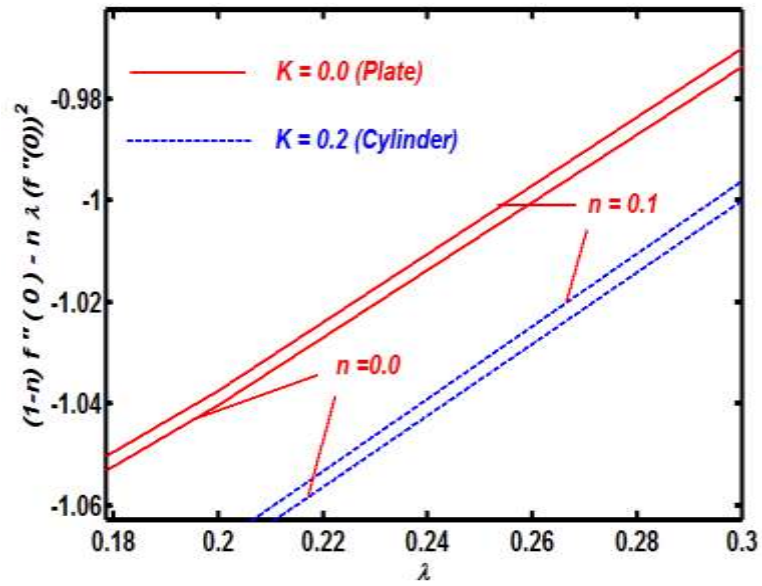


Fig. 2.9. Influence of power law index n and Weissenberg number λ on skin friction coefficient for both plate and cylinder when $Pr = 1.2$ and $S = 0.1$.

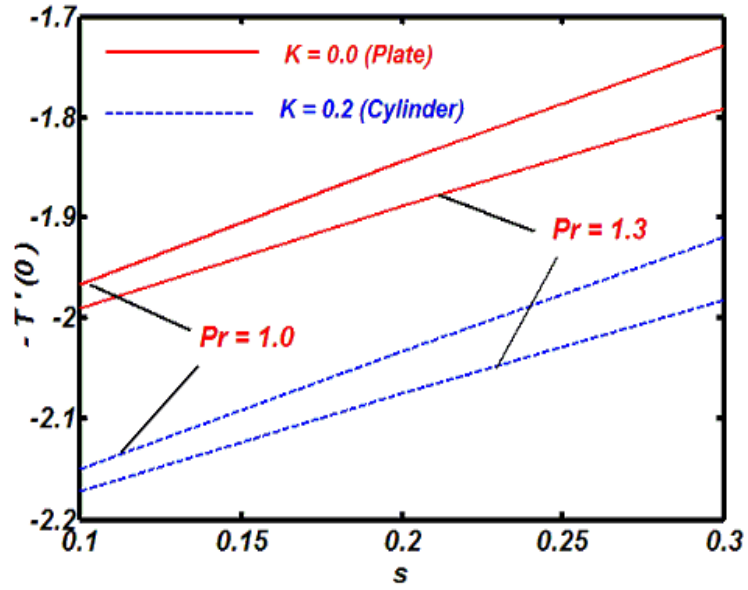


Fig. 2.10. Influence of Pr and s on heat transfer rate for both plate and cylinder when $\lambda=0.1$ and $n=0.1$.

Table 2.1: Comparison of skin friction coefficient

| n | λ | Akbar et al. [20] | Present results |
|-----|-----------|-------------------|-----------------|
| 0.0 | 0.0 | 1 | 1 |
| 0.0 | 0.3 | 1 | 1 |
| 0.0 | 0.5 | 1 | 1 |
| 0.1 | 0.0 | 0.94868 | 0.94916 |
| 0.1 | 0.3 | 0.94248 | 0.94321 |
| 0.1 | 0.5 | 0.93826 | 0.93801 |
| 0.2 | 0.0 | 0.89442 | 0.89447 |
| 0.2 | 0.3 | 0.88023 | 0.88056 |

Table 2.2: Comparison of local Nusselt number

| Pr | Hussain et al. [128] | Khan and Pop [127] | Golra and Sidawi [126] | Wang [125] | Present results |
|------|----------------------|--------------------|------------------------|------------|-----------------|
| 0.07 | 0.0656 | 0.0663 | 0.0656 | 0.0656 | 0.0661 |
| 0.2 | 0.1695 | 0.1691 | 0.1691 | 0.1691 | 0.1691 |
| 0.7 | 0.4539 | 0.4539 | 0.4539 | 0.4539 | 0.4541 |
| 2.0 | 0.9114 | 0.9113 | 0.9114 | 0.9114 | 0.9113 |
| 7.0 | 1.8954 | 1.8954 | 1.1905 | 1.1854 | 1.8945 |
| 20.0 | 3.3538 | 3.3539 | 3.3539 | 3.3539 | 3.3555 |
| 70.0 | 6.4621 | 6.4622 | 6.4622 | 6.4622 | 6.4611 |

2.6 Conclusion

The key results of present analysis are:

- The TH fluid shows an inciting velocity towards curvature parameter because larger values of curvature parameter reflects less resistance towards fluid flow.
- An increase in power law index turns to the fluid characteristics from shear thinning to shear thickening as a result fluid motion retarded.
- An enhancement in Weissenberg number brings an increase in relaxation time due to which resistance increases so that fluid velocity exhibit declined curves.
- The fluid temperature admits decline nature towards Prandtl number because of an inverse relation of Prandtl number with thermal conductivity.
- Higher values of Weissenberg number enlarge the relaxation time i.e. fluid particles takes more time to transfer heat and hence temperature reduces.
- An inciting values of thermal stratification parameter reduces the conventional potential difference due to which fluid temperature drops.
- It is seen that the skin friction coefficient (absolute sense) shows higher values for curvature parameter while opposite variations are noticed for positive values of Weissenberg number and power law index.
- It is observed that (in absolute sense) the Nusselt number admits inciting nature

towards Prandtl number and curvature parameter while opposite trend is noticed for stratification parameter.

- In absolute sense, the Nusselt number and skin friction coefficient variations are enriched for cylindrical surface as compared to flat surface.

CHAPTER 3

Temperature and Concentration Stratification Effects on Non-Newtonian Fluid Flow Past a Cylindrical Surface

3.1 Introduction

The theme of present chapter is to report the numerical solution of mixed convection tangent hyperbolic fluid flow towards stretching cylindrical surface immersed in a double stratified media. The fluid flow is attained through no slip condition. The flow regime characteristics are modelled in terms of partial differential equations. A suitable set of transformation is used to transform partial differential equations into coupled non-linear ordinary differential equations. A computational algorithm is executed to predict numerical results. The effects of flow controlling parameters namely, mixed convection parameter, thermal stratification and solutal stratification parameters on velocity, temperature and concentration are examined and offered by means of graphical outcomes.

3.2 Mathematical formulation

A steady incompressible two dimensional boundary layer flow of tangent hyperbolic fluid brought by an inclined stretching cylindrical surface is considered. Flow situation is taken with double stratification along with mixed convection effect. The ultimate mathematical formulation is as follows:

$$\frac{\partial(ru)}{\partial x} + \frac{\partial(rv)}{\partial r} = 0, \quad (3.1)$$

$$u \frac{\partial u}{\partial x} + v \frac{\partial u}{\partial r} = v \left((1-n) \frac{1}{r} \frac{\partial u}{\partial r} + (1-n) \frac{\partial^2 u}{\partial r^2} + \frac{n\Gamma}{\sqrt{2}r} \left(\frac{\partial u}{\partial r} \right)^2 + n\sqrt{2}\Gamma \frac{\partial u}{\partial r} \frac{\partial^2 u}{\partial r^2} \right) + g\beta_T(T-T_\infty)\cos\alpha + g\beta_c(C-C_\infty)\cos\alpha, \quad (3.2)$$

$$v(x,r) = 0, \quad u(x,r) = U(x) = \frac{U_0}{L}x, \quad \text{at } r=R \text{ and } u(x,r) \rightarrow 0 \text{ as } r \rightarrow \infty. \quad (3.3)$$

Here, $n, \rho, \nu, \beta_T, \beta_c, \alpha$ and g represents power law index, density of fluid, kinematic viscosity, coefficients of thermal expansion and solutal expansion, inclination of cylinder with x -axis and gravity respectively.

The ψ (stream function) fulfils the continuity Eq. (3.1) identically and can be defined as:

$$u = \left(\frac{\partial \psi}{\partial r} \right) \frac{1}{r}, \quad v = - \left(\frac{\partial \psi}{\partial x} \right) \frac{1}{r}. \quad (3.4)$$

To achieve dimensionless form we have considered the transformation given as:

$$\psi = \left(\frac{U_0 \nu x^2}{L} \right)^{\frac{1}{2}} R F(\eta), \quad u = F'(\eta) \frac{U_0 x}{L}, \quad v = - \frac{R}{r} F(\eta) \sqrt{\frac{U_0 \nu}{L}}, \quad \eta = \left(\frac{U_0}{\nu L} \right)^{\frac{1}{2}} \frac{r^2 - R^2}{2R}, \quad (3.5)$$

Once incorporating Eqs. (3.4)-(3.5) into Eq. (3.2). The dimensionless form of momentum equation can be written as:

$$(1+2K\eta)2(1-n) \frac{d^3 F(\eta)}{d\eta^3} + \frac{d^2 F(\eta)}{d\eta^2} 2F(\eta) - 2 \left(\frac{dF(\eta)}{d\eta} \right)^2 + 3(1+2K\eta)^{\frac{1}{2}} K\lambda \left(\frac{d^2 F(\eta)}{d\eta^2} \right)^2 + 4K \frac{d^2 F(\eta)}{d\eta^2} (1-n) + 2\lambda n \frac{d^2 F(\eta)}{d\eta^2} \frac{d^3 F(\eta)}{d\eta^3} (1+2K\eta)^{\frac{3}{2}} + 2(N\phi(\eta) + \theta(\eta))\lambda_m \cos\alpha = 0, \quad (3.6)$$

$$F(\eta) = 0, \quad \frac{dF(\eta)}{d\eta} = 1 \text{ at } \eta = 0 \text{ and } \frac{dF(\eta)}{d\eta} \rightarrow 0 \text{ as } \eta \rightarrow \infty, \quad (3.7)$$

The flow parameters are:

$$K = \sqrt{\frac{\nu}{a}} \frac{1}{R}, \quad \lambda = \Gamma \sqrt{\frac{2U_0^3}{\nu x}}, \quad \lambda_m = \frac{Gr}{\text{Re}_x^2}, \quad N = \frac{Gr^*}{Gr}, \quad a = \frac{U_0}{L}, \quad (3.8)$$

here, Gr^* and Gr are Grashof number due to concentration and temperature respectively

and defined as:

$$Gr^* = \frac{g\beta_T(C_w - C_0)x^3}{\nu^2}, \quad Gr = \frac{g\beta_T(T_w - T_0)x^3}{\nu^2}. \quad (3.9)$$

The skin coefficient at cylindrical surface is

$$C_f = \frac{\tau_w}{\rho \frac{U^2}{2}}, \quad (3.10)$$

$$\tau_w = \mu \left[\frac{\partial u}{\partial r} (1-n) + \left(\frac{\partial u}{\partial r} \right)^2 \frac{n\Gamma}{\sqrt{2}} \right]_{r=R}, \quad (3.11)$$

The dimensionless expression is given by

$$Re_x^{1/2} C_f = (1-n)F''(0) + \lambda n(F''(0))^2. \quad (3.12)$$

3.3 Stratification modelling

The mutual interaction of temperature and concentration stratification is considered on tangent hyperbolic fluid model. The surface temperature as well as concentration are hypothetical greater in strength as compared to ambient fluid. The reduced energy and concentration equations under boundary layer approximation are given by:

$$\frac{\partial T}{\partial r} v + \frac{\partial T}{\partial x} u = \left(\frac{\partial^2 T}{\partial r^2} + \frac{1}{r} \frac{\partial T}{\partial r} \right) \frac{k}{\rho c_p}, \quad (3.13)$$

$$\frac{\partial C}{\partial r} v + \frac{\partial C}{\partial x} u = \left(\frac{\partial^2 C}{\partial r^2} + \frac{1}{r} \frac{\partial C}{\partial r} \right) D, \quad (3.14)$$

where k, c_p , and D denotes thermal conductivity, specific heat at constant pressure and mass diffusivity respectively. Both temperature and concentration boundary conditions for the double stratified tangent hyperbolic fluid flow are given as:

$$\begin{aligned} C(x, r) = C_w(x) = C_0 + \frac{dx}{L}, \quad T(x, r) = T_w(x) = T_0 + \frac{bx}{L}, \quad \text{at } r = R, \\ C(x, r) = C_\infty(x) = C_0 + \frac{ex}{L}, \quad T(x, r) = T_\infty(x) = T_0 + \frac{cx}{L}, \quad \text{as } r \rightarrow \infty, \end{aligned} \quad (3.15)$$

where, $C_0, T_0, C_\infty(x), T_\infty(x), C_w(x)$ and $T_w(x)$, represents concentration and reference temperature, ambient concentration and temperature, surface concentration and temperature respectively. For dimensionless form we used:

$$\eta = \frac{r^2 - R^2}{2R} \left(\frac{U_0^2}{\nu L} \right), \phi(\eta) = \frac{C - C_\infty}{C_w - C_0}, \theta(\eta) = \frac{T - T_\infty}{T_w - T_0}, \quad (3.16)$$

by using Eq. (3.16) in Eqs. (3.13)-(3.14), we obtained:

$$\frac{d^2\theta(\eta)}{d\eta^2}(1+2K\eta) + 2K \frac{d\theta(\eta)}{d\eta} + \text{Pr}(F(\eta) \frac{d\theta(\eta)}{d\eta} - \frac{dF(\eta)}{d\eta} \theta(\eta) - k_1 \frac{dF(\eta)}{d\eta}) = 0, \quad (3.17)$$

$$\frac{d^2\phi(\eta)}{d\eta^2}(1+2K\eta) + 2K \frac{d\phi(\eta)}{d\eta} + \text{Sc}(F(\eta) \frac{d\phi(\eta)}{d\eta} - \frac{dF(\eta)}{d\eta} \phi(\eta) - k_2 \frac{dF(\eta)}{d\eta}) = 0, \quad (3.18)$$

the transformed boundary conditions are

$$\theta(\eta) = 1 - k_1, \quad \phi(\eta) = 1 - k_2, \quad \text{at } \eta = 0, \quad (3.19)$$

$$\theta(\eta) \rightarrow 0, \quad \phi(\eta) \rightarrow 0, \quad \text{when } \eta \rightarrow \infty,$$

while involved variables are defined as:

$$\text{Pr} = \frac{\mu c_p}{k}, \quad k_1 = \frac{c}{b}, \quad \text{Sc} = \frac{\nu}{D}, \quad k_2 = \frac{e}{d}. \quad (3.20)$$

Both Nusselt and Sherwood numbers are defined as follows:

$$\begin{aligned} Nu_x &= \frac{xq_w}{(T_w - T_0)k}, \quad q_w = - \left(\frac{\partial T}{\partial r} \right)_{r=R} k, \\ Sh &= \frac{xj_w}{(C_w - C_0)D}, \quad j_w = - \left(\frac{\partial C}{\partial r} \right)_{r=R} D. \end{aligned} \quad (3.21)$$

In dimensionless form, these quantities can be written as:

$$\begin{aligned}
Nu_x \text{Re}_x^{-\frac{1}{2}} &= -\theta'(0), \\
Sh \text{Re}_x^{-\frac{1}{2}} &= -\phi'(0).
\end{aligned}
\tag{3.22}$$

3.4 Numerical treatment

The problem given by Eqs. (3.6), (3.17) and (3.18) along with (3.7) and (3.19) is solved by shooting method. The computational algorithm is prepared as:

$$\begin{aligned}
p_2 &= F'(\eta), \\
p_3 &= p'_3 = F''(\eta), \\
p_5 &= \theta'(\eta), \\
p_7 &= \phi'(\eta),
\end{aligned}$$

the alike form of Eqs. (3.6), (3.17) and (3.18) is prearranged as:

$$\begin{aligned}
& \left[\begin{array}{l} p_2 \\ p_3 \\ p'_1 \\ p'_2 \\ p'_3 \\ p'_4 \\ p'_5 \\ p'_6 \\ p'_7 \end{array} \right] = \left[\begin{array}{l} p_2 \\ p_3 \\ \frac{(p_2)^2 - p_3 p_1 - (1-n)(2K)p_3 - \frac{3}{2}(1+2K\eta)^{\frac{1}{2}} \lambda K p_3^2 - \lambda_m(p_4 + Np_6) \cos \alpha}{(2K\eta+1)(1-n) + (2K\eta+1)^{\frac{3}{2}} n \lambda p_3} \\ p_5 \\ \frac{\text{Pr}(p_2 p_4 + k_1 p_2 - p_1 p_5) - 2Kp_5}{1+2K\eta} \\ p_7 \\ \frac{\text{Sc}(p_2 p_6 + k_2 p_2 - p_1 p_7) - 2Kp_7}{1+2K\eta} \end{array} \right] \tag{3.23}
\end{aligned}$$

and the corresponding end conditions are given as follows:

$$\begin{aligned}
p_1(0) &= 0, \\
p_2(0) &= 1, \\
p_3(0) &= \text{unknown}, \\
p_4(0) &= 1 - k_1, \\
p_5(0) &= \text{unknown}, \\
p_6(0) &= 1 - k_2, \\
p_7(0) &= \text{unknown}.
\end{aligned}
\tag{3.24}$$

The additional endpoint conditions are given by

$$\begin{aligned}
p_2(\infty) &= 0, \\
p_4(\infty) &= 0, \\
p_6(\infty) &= 0.
\end{aligned}
\tag{3.25}$$

3.5 Results and discussion

Tables (3.1)-(3.3) are assembled to examine the surface quantities. Table (3.1) depicts the skin friction coefficient variations (in absolute sense) for positive values of Weissenberg number, power law index and curvature parameter. It is seen that the skin friction coefficient near the cylindrical surface is an increasing function of curvature parameter, while opposite attitude is perceived for power law index and Weissenberg number. In addition, the negative sign subject to skin friction coefficient values remarks the drag force exerted by cylindrical surface to fluid particles. Table (3.2) is constructed to offer the variations in Nusselt number. It is found that Nusselt number shows higher values towards both Prandtl number and curvature parameter while opposite trends are noticed for higher values of thermal stratification parameter. The influence of curvature parameter, solutal stratification parameter and Schmidt number is reported on Sherwood number by way of Table. 3.3. It is observed that the Sherwood number reflects higher values for curvature parameter, solutal stratification parameter and Schmidt number. Tables. 3.4 and 3.5 provide the comparison between skin friction coefficient and local Nusselt number with existing literature. We have noticed excellent match up-to significant numerical digits which yield the surety of present work in a limiting sense. Figs. 3.1-3.6 are plotted to examine the influence of some involved physical parameters namely, curvature parameter K , inclination α , thermal stratification parameter k_1 ,

Weissenberg number λ , mixed convection parameter λ_m , and n on velocity profile. Fig. 3.1 indicate the impact of K on velocity. It is observed that for large values of K the fluid velocity exhibits an inciting nature. Here larger values of K corresponds decrease in radius of cylinder so that the interaction of fluid particles with cylindrical surface is lesser which implies the resistance towards decrease in fluid flow. As a result fluid velocity increases significantly. Fig. 3.2 report the influence of inclination α on velocity profile. It is found that there is an inverse relation between α and fluid velocity that is for large values of α the velocity profile decreases. An increase in α towards x -axis give significant rise to gravity component due to $\cos\alpha$ which drops the buoyancy force so that the driven force become weaker. As a result flow rate decreases which declines the velocity. Fig. 3.3 identify the effect of thermal stratification parameter k_1 on velocity distribution. It is noticed that the fluid velocity exhibits decreasing values for positive variations in k_1 . Fig. 3.4 incorporate the graphical trend of λ on velocity profile. It is noticed that velocity shows decreasing behavior via λ . This is due to increment in relaxation time. The effect of mixed convection parameter λ_m on velocity is depicted in Fig. 3.5. For larger values of λ_m the velocity profile increases. Physically, this is because of the larger values of buoyancy force. Fig. 3.6 point to the impact of power law index n on tangent hyperbolic fluid velocity. It is seen that there is an inverse relation between n and fluid velocity. That is, for higher values of n the tangent hyperbolic fluid velocity shows declined behaviour. Figs. 3.7-3.10 reflect the impact of flow controlling parameters namely, K , α , k_1 , and Pr on temperature profiles. In detail, Fig. 3.7 indicate that the influence of curvature parameter K on temperature distribution. It is observed that the temperature shows an inciting trend via K . An increase in K reduces the surface contact area subject to fluid particles and hence less resistance is faced by particles due to which their average velocity enhances. Since, the Kelvin temperature is defined by an average kinetic energy therefore temperature increases. Fig. 3.8 painted the impact of inclination α on temperature. It is noticed that there is an inverse relation between inclination α and fluid temperature, i.e., for large values of α the temperature profile decreases. The impact of thermal stratification

parameter k_1 on temperature distribution is examined and offered in Fig. 3.9. It is seen that for the positive values of k_1 yield decline nature of temperature because higher values of k_1 means convective potential between ambient temperature and cylindrical surface drops. Fig. 3.10 is plotted to examine the influence of Prandtl number Pr on temperature. It is clear from graphical trend that the temperature profile reflects an inverse nature for higher values of Prandtl number Pr . This fact is due to inverse relation of Pr with thermal diffusivity and it is well-known fact that the fluid with higher values of Pr has weaker thermal diffusion so that the temperature declines. Figs. 3.11 and 3.12 illustrate concentration variations towards both solutal stratification parameter k_2 and Schmidt number Sc . To be more specific, Fig. 3.11 depicts the decline trend of concentration distribution for positive values of solutal stratification parameter k_2 . For higher values of k_2 the potential difference between cylindrical surface and ambient fluid concentration drops down so that the related concentration boundary layer thickness decreases. Fig. 3.12 shows the impact of Sc on fluid concentration. It is noticed that for larger values of Sc the fluid concentration decreases. This fact is quite similar to Prandtl number's impact on temperature. Actually, mass diffusivity own inverse relation with Sc therefore, larger values of Sc corresponds thinner concentrated boundary layer. Figs. 3.13-3.15 are provided to inspect the flow pattern of tangent hyperbolic fluid in a double stratified media. The stream lines pattern claims the movement of fluid particles due to stretching of cylindrical surface so that the compatibility of endpoint conditions is attained. Further, it is clear from Figs. 3.13-3.15 that on increasing curvature parameter values, fluid momentum increases which is due to positive alteration in the fluid velocity.

3.6 Graphical outcomes

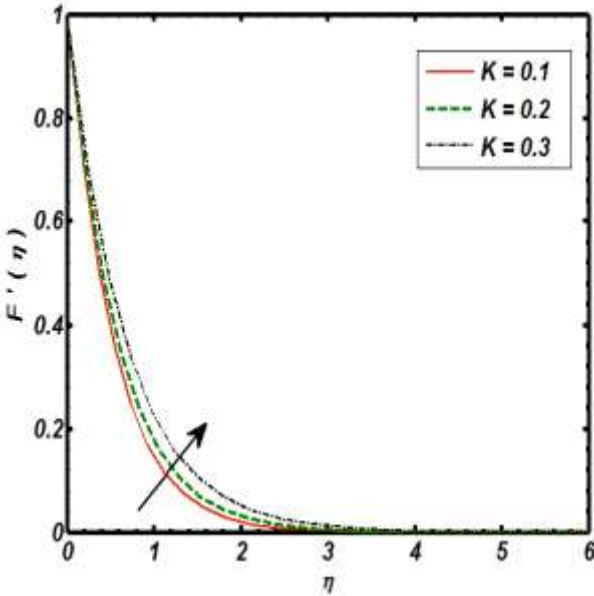


Fig. 3.1. Effect of curvature parameter on velocity profile.

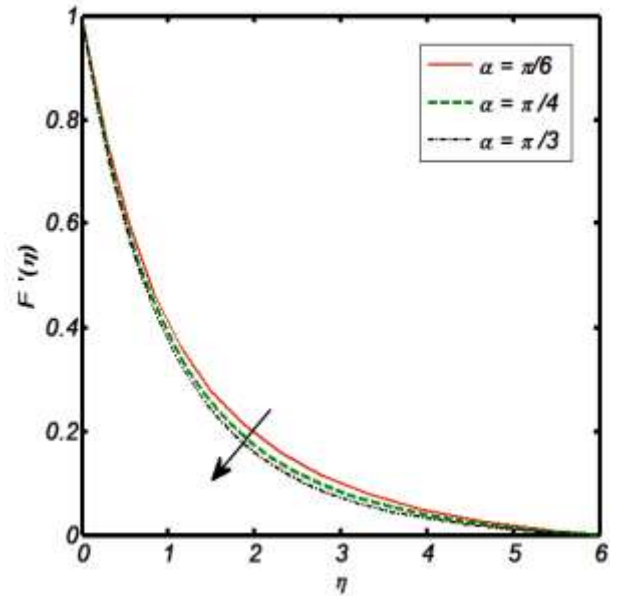


Fig. 3.2. Effect of an inclination on velocity profile.

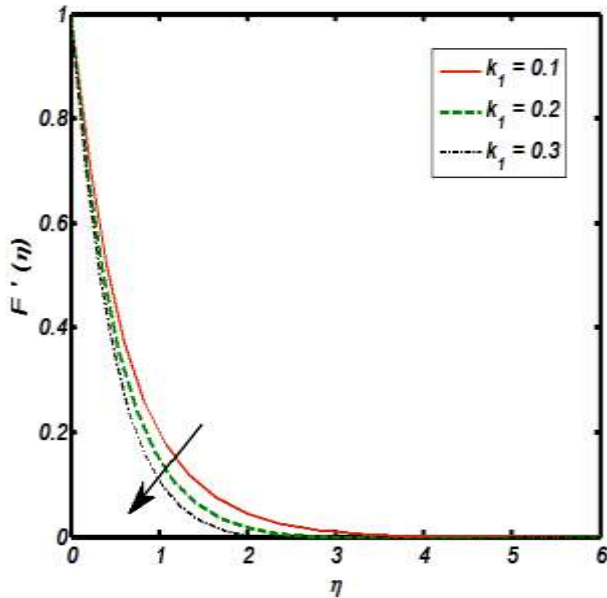


Fig. 3.3. Effect of thermal stratification parameter on velocity profile.

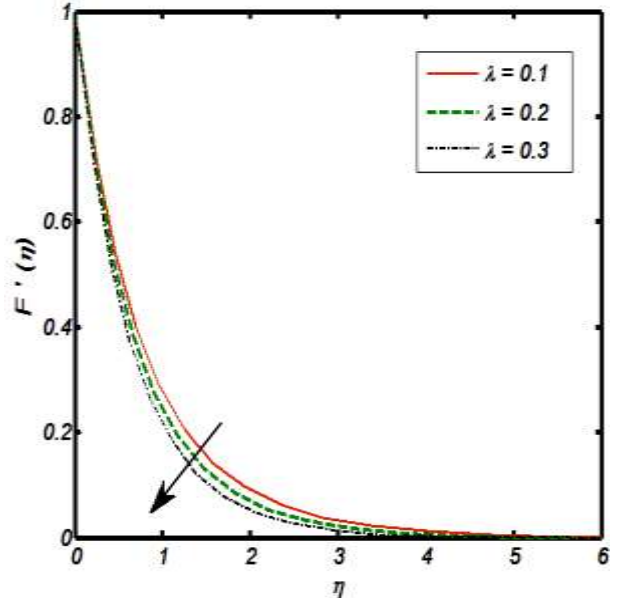


Fig. 3.4. Effect of Weissenberg number on velocity profile.

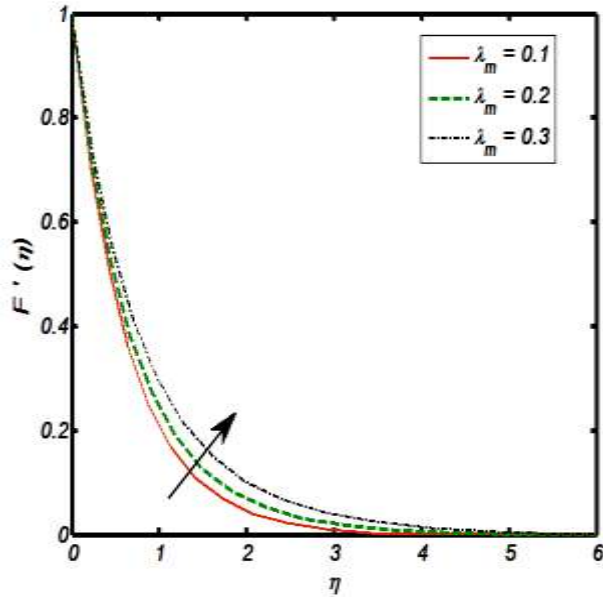


Fig. 3.5. Effect of mixed convection parameter on velocity profile.

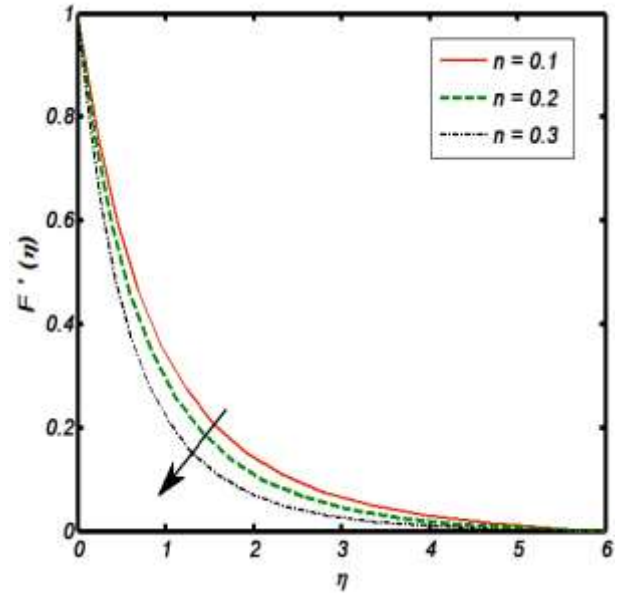


Fig. 3.6. Effect of power law index on velocity profile.

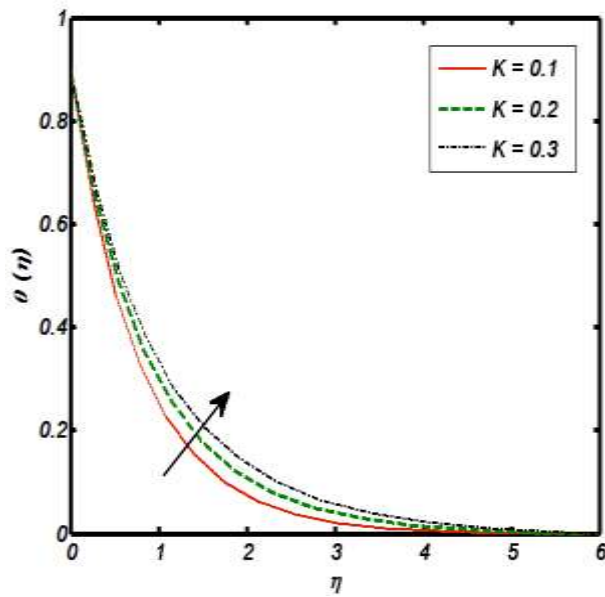


Fig. 3.7. Effect of curvature parameter on temperature profile.

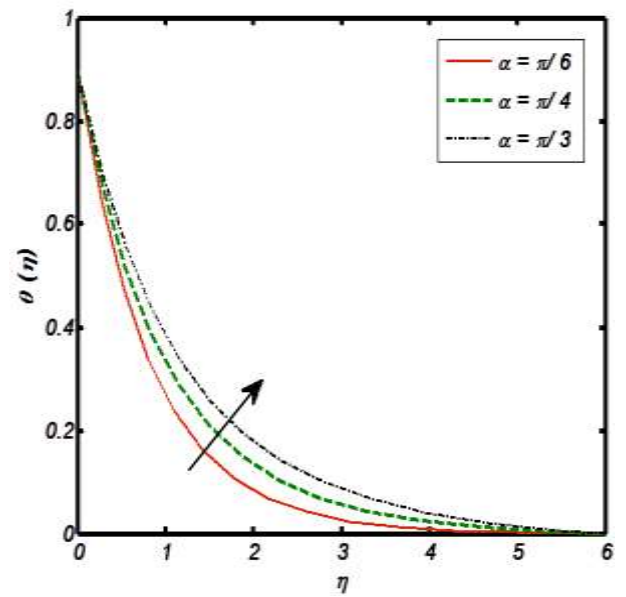


Fig. 3.8. Effect of an inclination on temperature profile.

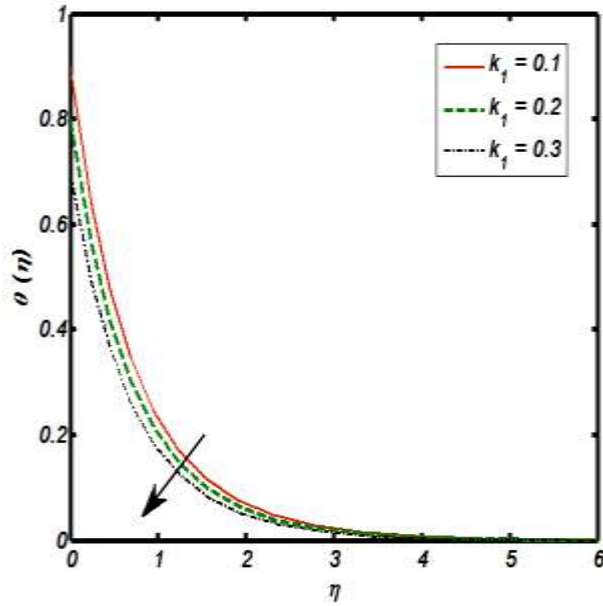


Fig. 3.9. Effect of thermal stratification parameter on temperature profile.

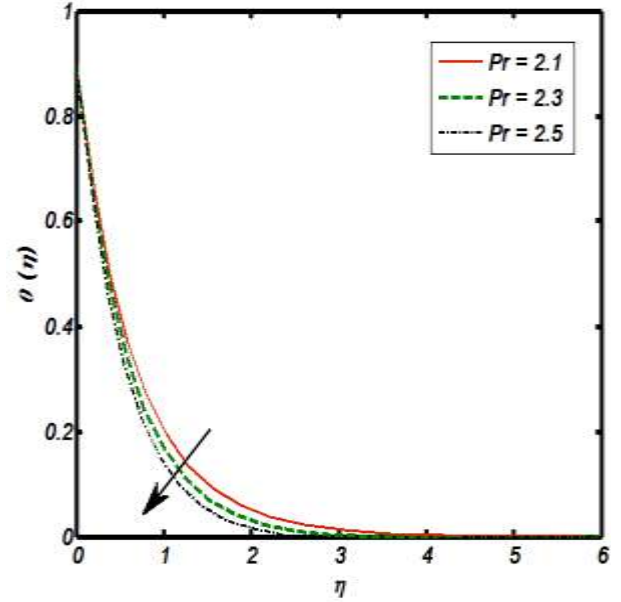


Fig. 3.10. Effect of Prandtl number on temperature profile.

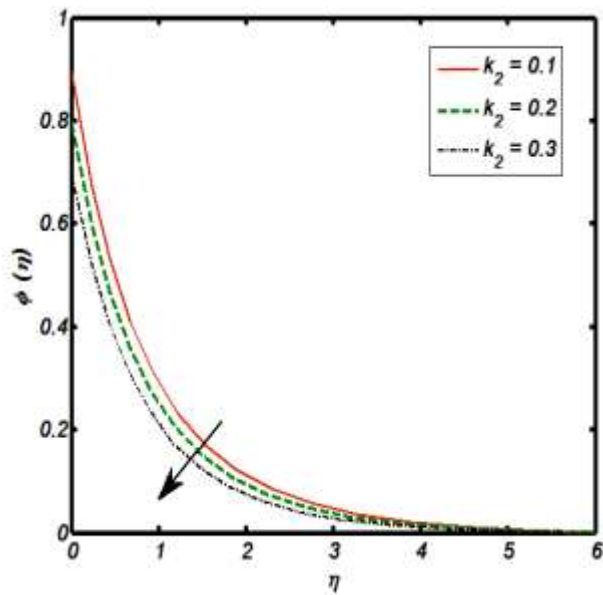


Fig. 3.11 Effect of solutal stratification parameter on concentration profile.

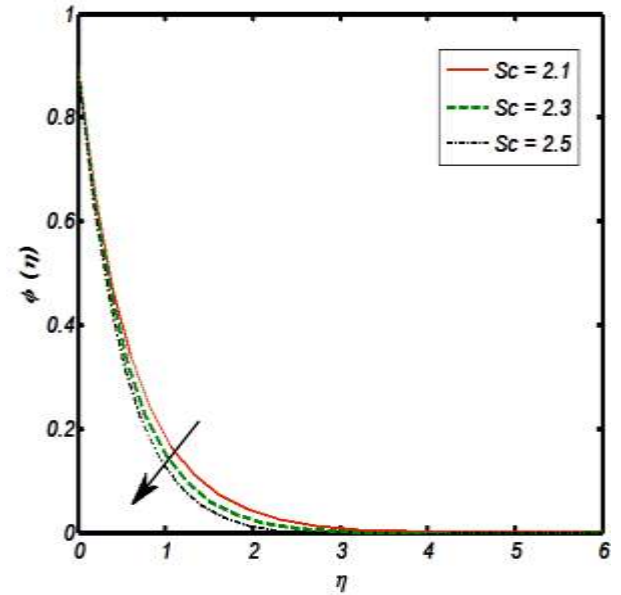


Fig. 3.12 Effect of Schmidt number on concentration profile.

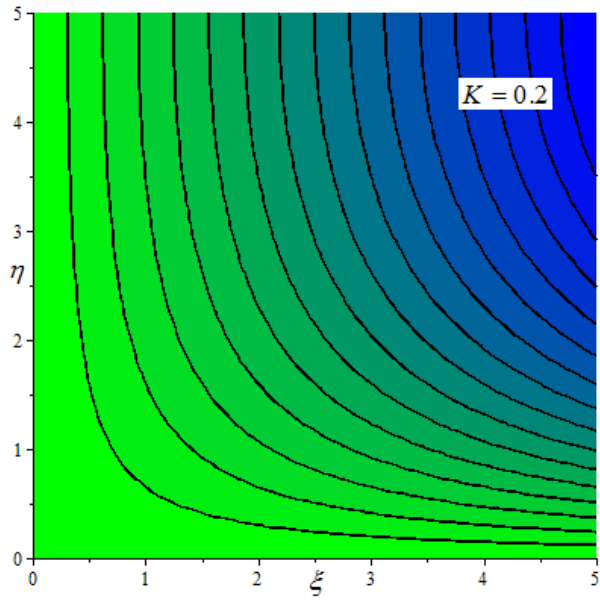


Fig. 3.13. Stream lines pattern when $K = 0.2$.

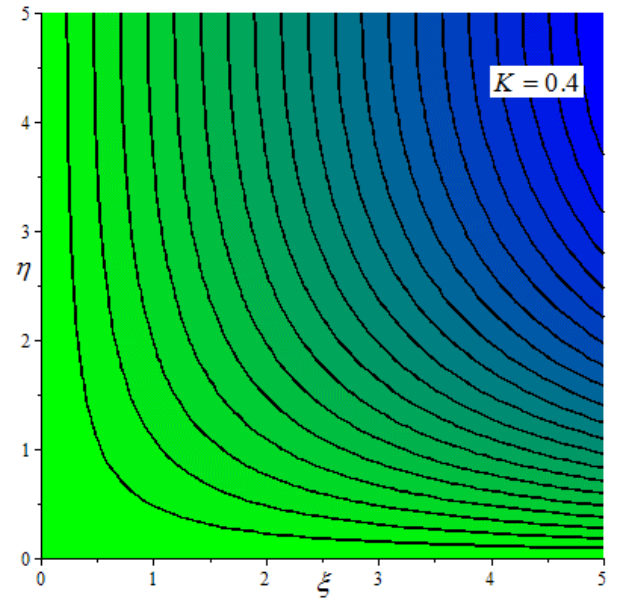


Fig. 3.14. Stream lines pattern when $K = 0.4$.

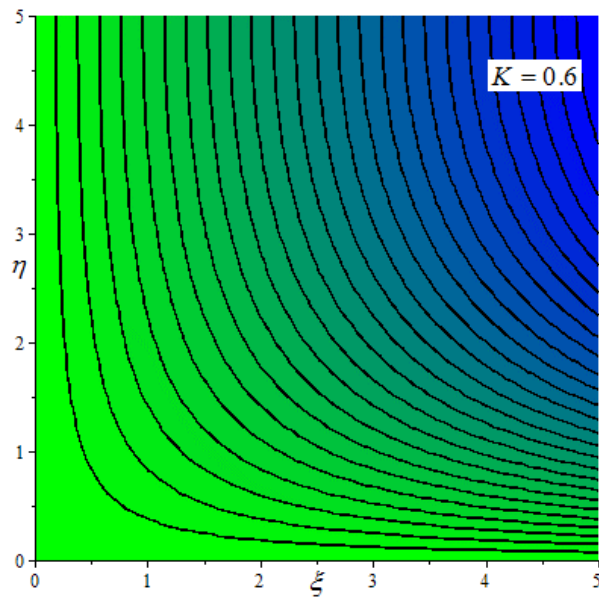


Fig. 3.15. Stream lines pattern when $K = 0.6$.

Table 3.1. Variation in $C_f\sqrt{\text{Re}_x}$ towards K, n and λ .

| K | n | λ | $-F''(0)$ | $C_f\sqrt{\text{Re}_x}$ |
|-----|-----|-----------|-----------|-------------------------|
| 0.1 | 0.1 | 0.1 | 0.4358 | -1.1613 |
| 0.2 | - | - | 0.5160 | -1.2138 |
| 0.3 | - | - | 0.5940 | -1.2702 |
| 0.1 | 0.1 | 0.1 | 0.4358 | -1.1613 |
| - | 0.2 | - | 0.4717 | 1.1022 |
| - | 0.3 | - | 0.5022 | -1.0130 |
| 0.1 | 0.1 | 0.1 | 0.4358 | -1.1613 |
| - | - | 0.2 | 0.4410 | -1.1610 |
| - | - | 0.3 | 0.4513 | -1.1591 |

Table 3.2. Variation in Nusselt number towards K, Pr and k_1 .

| K | Pr | k_1 | $-\theta'(0)$ |
|-----|-------------|-------|---------------|
| 0.1 | 1.1 | 0.1 | 1.5325 |
| 0.2 | - | - | 1.5917 |
| 0.3 | - | - | 1.6304 |
| 0.1 | 1.1 | 0.1 | 1.5325 |
| - | 1.2 | - | 1.6217 |
| - | 1.3 | - | 1.6729 |
| 0.1 | 1.1 | 0.1 | 1.5325 |
| - | - | 0.2 | 1.5012 |
| - | - | 0.3 | 1.4709 |

Table 3.3. Numerical values of Sherwood number for K, k_2 and Sc .

| K | k_2 | Sc | $-\phi'(0)$ |
|-----|-------|------|-------------|
| 0.1 | 0.1 | 2.1 | 1.7071 |
| 0.2 | - | - | 1.8802 |
| 0.3 | - | - | 2.1040 |
| 0.1 | 0.1 | 2.1 | 1.7071 |
| - | 0.2 | - | 1.8543 |
| - | 0.3 | - | 2.1006 |
| 0.1 | 0.1 | 2.1 | 1.7071 |
| - | - | 2.2 | 1.7343 |
| - | - | 2.3 | 1.7554 |

Table 3.4. Skin friction coefficient comparison via power law index n and Weissenberg number λ when $K = k_1 = 0$ and $\alpha = 0^0$.

| n | λ | Akbar et al. [20] | Rehman et al. [129] | Present outcomes |
|-----|-----------|-------------------|---------------------|------------------|
| 0.0 | 0.0 | 1 | 1 | 1 |
| 0.0 | 0.3 | 1 | 1 | 1 |
| 0.0 | 0.5 | 1 | 1 | 1 |
| 0.1 | 0.0 | 0.94868 | 0.94916 | 0.94916 |
| 0.1 | 0.3 | 0.94248 | 0.94321 | 0.94321 |
| 0.1 | 0.5 | 0.93826 | 0.93801 | 0.93801 |
| 0.2 | 0.0 | 0.89442 | 0.89447 | 0.89447 |
| 0.2 | 0.3 | 0.88023 | 0.88056 | 0.88056 |

Table 3.5. Local Nusselt number comparison via Pr when $\lambda = K = k_1 = 0$ and $\alpha = 0^0$.

| Pr | Wang [125] | Golra and Sidawi [126] | Khan and Pop [127] | Rehman et al. [129] | Present outcomes |
|------|------------|------------------------|--------------------|---------------------|------------------|
| 0.07 | 0.0656 | 0.0656 | 0.0663 | 0.0661 | 0.0661 |
| 0.20 | 0.1691 | 0.1691 | 0.1691 | 0.1691 | 0.1691 |
| 0.70 | 0.4539 | 0.4539 | 0.4539 | 0.4541 | 0.4541 |
| 2.00 | 0.9114 | 0.9114 | 0.9113 | 0.9113 | 0.9113 |
| 7.00 | 1.1854 | 1.1905 | 1.8954 | 1.8945 | 1.8945 |
| 20.0 | 3.3539 | 3.3539 | 3.3539 | 3.3555 | 3.3555 |
| 70.0 | 6.4622 | 6.4622 | 6.4622 | 6.4611 | 6.4611 |

3.7 Concluding remarks

In this chapter tangent hyperbolic fluid flow yield by cylindrical stretched surface (acutely inclined) is considered. A mathematical formulation is developed in terms of partial differential equations. A numerical solution is obtained by means of computational algorithm. The summary of present study is itemized as follows:

- The compatibility of tangent hyperbolic fluid flow regime endpoint conditions is certified through stream lines patterns.

- The tangent hyperbolic fluid velocity increases on both mixed convection parameter (λ_m) and curvature parameter (K), while it shows an inverse relation towards power law index (n), Weissenberg number (λ), an inclination (α), and thermal stratification parameter (k_1).
- The temperature of tangent hyperbolic fluid is an increasing function of curvature parameter (K), and an inclination (α), but opposite nature is notified for thermal stratification parameter (k_1) and Prandtl number (Pr).
- The tangent hyperbolic fluid concentration reflects declined trend for both solutal stratification parameter (k_2) and Schmidt number (Sc).
- In absolute sense, the skin friction coefficient is an increasing function of curvature parameter (K), while an inverse relation is observed in case of both power law index (n) and Weissenberg number (λ).
- Heat transfer rate enhances via Prandtl number (Pr), and curvature parameter (κ), whereas an inverse relation is found for thermal stratification parameter (k_1).
- Mass transfer rate enhances for solutal stratification parameter (k_2), curvature parameter (K), and Schmidt number (Sc).

CHAPTER 4

Numerical Solution of Chemically Reactive Non-Newtonian Fluid Flow: Dual Stratification

4.1 Introduction

The focus of the present chapter is to study the tangent hyperbolic fluid flow induced by acutely inclined cylindrical surface in the presence of both temperature and concentration stratification effects. To be more specific, fluid flow is attained by considering no slip condition, which implies bulk motion of fluid particles. The flow field situation is manifested with heat generation, mixed convection and chemical reaction. The flow field arising is modelled through partial differential equations which narrate complete description of the present problem. To trace out the solution, a set of suitable transformation is introduced which convert these modelled partial differential equations into ordinary differential equations. In addition, self-coded computational algorithm is executed to inspect the numerical solution of these reduced equations. The effect logs of involved parameters are elaborated by way of graphical trends. Further, the variations of physical quantities are examined and given with the aid of tables.

4.2 Mathematical formulation

Two dimensional flow of tangent hyperbolic fluid (THF) is considered due to stretching inclined cylindrical surface. The flow field is manifested with thermal and solutal stratification. Moreover, the role of chemical reaction, heat generation and mixed convection is also considered. The boundary layer approximation reduces the continuity, momentum, heat and mass equations to:

$$\frac{\partial(rv)}{\partial r} + \frac{\partial(ru)}{\partial x} = 0, \quad (4.1)$$

$$u \frac{\partial u}{\partial x} + v \frac{\partial u}{\partial r} = v \left((1-n) \frac{\partial^2 u}{\partial r^2} + \frac{n\Gamma}{\sqrt{2}r} \left(\frac{\partial u}{\partial r} \right)^2 + (1-n) \frac{1}{r} \frac{\partial u}{\partial r} + n\sqrt{2}\Gamma \frac{\partial u}{\partial r} \frac{\partial^2 u}{\partial r^2} \right) \quad (4.2)$$

$$+ g\beta_T(T - T_\infty) \cos \alpha + g\beta_c(C - C_\infty) \cos \alpha,$$

$$u \frac{\partial T}{\partial x} + v \frac{\partial T}{\partial r} = \frac{k}{\rho c_p} \left(\frac{\partial^2 T}{\partial r^2} + \frac{1}{r} \frac{\partial T}{\partial r} \right) + \frac{Q_0}{\rho c_p} (T - T_\infty), \quad (4.3)$$

$$v \frac{\partial C}{\partial r} + u \frac{\partial C}{\partial x} = D \left(\frac{\partial^2 C}{\partial r^2} + \frac{1}{r} \frac{\partial C}{\partial r} \right) - R_0(C - C_\infty). \quad (4.4)$$

The x -axis is supposed as axial direction of cylinder while r -axis is perpendicular to it. Whereas, $\Gamma > 0$, $g, \rho, Q_0, n, k, \beta_T, \nu, \beta_c, \alpha, D$ and c_p denotes time constant, gravity, fluid density, heat generation coefficient, power law index, thermal conductivity, coefficient of thermal expansion, kinematic viscosity, coefficient of solutal expansion, an inclination, mass diffusivity and specific heat respectively. The endpoint conditions are given as:

$$T(x, R) = T_w(x) = T_0 + \frac{b x}{L}, \quad v(x, R) = 0, \quad u(x, R) = U(x) = \frac{U_0}{L} x, \quad (4.5)$$

$$T(x, \infty) \rightarrow T_\infty(x) = T_0 + \frac{c x}{L}, \quad C(x, R) = C_w(x) = C_0 + \frac{dx}{L}, \quad u(x, \infty) \rightarrow 0,$$

$$C(x, \infty) \rightarrow C_\infty(x) = C_0 + \frac{e x}{L},$$

the stream function is prescribed as:

$$u = \left(\frac{\partial \psi}{\partial r} \right) \frac{1}{r}, \quad v = - \left(\frac{\partial \psi}{\partial x} \right) \frac{1}{r}. \quad (4.6)$$

To attain dimensionless form we used:

$$u = \frac{U_0 x}{L} f'(\eta), \quad v = - \frac{R}{r} \sqrt{\frac{U_0 \nu}{L}} f(\eta), \quad \eta = \frac{r^2 - R^2}{2R} \left(\frac{U_0}{\nu L} \right)^{\frac{1}{2}}, \quad (4.7)$$

$$C(\eta) = \frac{C - C_\infty}{C_w - C_0}, \quad T(\eta) = \frac{T - T_\infty}{T_w - T_0}, \quad \psi = \left(\frac{U_0 \nu x^2}{L} \right)^{\frac{1}{2}} R f(\eta),$$

Owing Eq. (4.7) one can obtained:

$$\begin{aligned}
& (1+2K\eta)2(1-n)\frac{d^3f(\eta)}{d\eta^3} + 2f(\eta)\frac{d^2f(\eta)}{d\eta^2} - 2\left(\frac{d^2f(\eta)}{d\eta^2}\right)^2 + 4\frac{d^2f(\eta)}{d\eta^2}K(1-n) \\
& + 3(1+2K\eta)^{\frac{1}{2}}\left(\frac{d^2f(\eta)}{d\eta^2}\right)^2 K\lambda + (1+2K\eta)^{\frac{3}{2}}2\lambda n\frac{d^3f(\eta)}{d\eta^3}\left(\frac{d^2f(\eta)}{d\eta^2}\right)^2 \\
& + \lambda_m(T(\eta) + NC(\eta))\cos\alpha = 0,
\end{aligned} \tag{4.8}$$

$$\begin{aligned}
& \frac{d^2T(\eta)}{d\eta^2}(1+2K\eta) + 2K\frac{dT(\eta)}{d\eta} + \text{Pr}(f(\eta)\frac{dT(\eta)}{d\eta} - \frac{df(\eta)}{d\eta}T(\eta) \\
& - k_1\frac{df(\eta)}{d\eta} + D_H T(\eta)) = 0,
\end{aligned} \tag{4.9}$$

$$\begin{aligned}
& \frac{d^2C(\eta)}{d\eta^2}(1+2K\eta) + 2K\frac{dC(\eta)}{d\eta} + Sc(f(\eta)\frac{dC(\eta)}{d\eta} - \frac{df(\eta)}{d\eta}C(\eta) \\
& - k_2\frac{df(\eta)}{d\eta} + R_c C(\eta)) = 0,
\end{aligned} \tag{4.10}$$

with the modified boundary conditions

$$f(\eta) = 0, \frac{df(\eta)}{d\eta} = 1, T(\eta) = 1 - k_1, C(\eta) = 1 - k_2, \text{ as } \eta \rightarrow 0, \tag{4.11}$$

$$\frac{df(\eta)}{d\eta} \rightarrow 0, T(\eta) \rightarrow 0, C(\eta) \rightarrow 0, \text{ as } \eta \rightarrow \infty,$$

where, $R_c, k_2, Sc, D_H, k_1, \text{Pr}, N, \lambda_m, \lambda$, and K denotes chemical reaction parameter, solutal stratification parameter, Schmidt number, heat generation parameter, thermal stratification parameter, Prandtl number, ratio of concentration to thermal buoyancy forces, mixed convection parameter, Weissenberg number and curvature parameter respectively and given as follows:

$$K = \frac{1}{R}\sqrt{\frac{v}{a}}, \quad \lambda = \Gamma\sqrt{\frac{2U^3}{vx}}, \quad \lambda_m = \frac{Gr}{\text{Re}_x^2}, \quad N = \frac{Gr^*}{Gr}, \quad \text{Pr} = \frac{\mu c_p}{K}, \tag{4.12}$$

$$k_1 = \frac{c}{b}, \quad D_H = \frac{LQ_0}{U_0\rho c_p}, \quad Sc = \frac{\nu}{D}, \quad k_2 = \frac{e}{d}, \quad R_c = \frac{R_0L}{U_0},$$

and:

$$Gr^* = \frac{g\beta_T(C_w - C_0)x^3}{\nu^2} \text{ and } Gr = \frac{g\beta_T(T_w - T_0)x^3}{\nu^2}. \quad (4.13)$$

The skin friction coefficient (SFC) is prescribed as:

$$C_f = \frac{\tau_w}{\rho \frac{U^2}{2}}, \quad \tau_w = \mu \left[\frac{\partial u}{\partial r} (1-n) + \left(\frac{\partial u}{\partial r} \right)^2 \frac{n\Gamma}{\sqrt{2}} \right]_{r=R}, \quad (4.14)$$

The dimensionless form of SFC is given by

$$\sqrt{Re_x} C_f = (1-n)f''(0) + n\lambda (f''(0))^2, \quad (4.15)$$

with $Re_x = \frac{U_0 x^2}{\nu L}$ denotes local Reynolds number.

Surface quantities are given by:

$$Nu_x = \frac{xq_w}{(T_w - T_0)k}, \quad q_w = -k \left(\frac{\partial T}{\partial r} \right)_{r=R}, \quad Sh = \frac{xj_w}{(C_w - C_0)D}, \quad j_w = -D \left(\frac{\partial C}{\partial r} \right)_{r=R}, \quad (4.16)$$

in dimensionless practice we have:

$$\frac{Nu_x}{\sqrt{Re_x}} = -T'(0), \quad \frac{Sh}{\sqrt{Re_x}} = -C'(0). \quad (4.17)$$

For instance in the absence of concentration equation if we neglect mixed convection and heat generation effects the Eqs. (4.8)-(4.9) reduces to problem reported by Rehman et al. [129].

4.3 Numerical scheme

To implement shooting method the system given by Eqs. (4.8)-(4.10) with endpoint conditions given by Eqs. (4.11) is firstly converted into first order system of differential equations. For this purpose the useful substitution is prescribed as:

$$\begin{aligned} p_2 &= f', \\ p_3 &= p'_3 = f'', \\ p_5 &= T', \\ p_7 &= C', \end{aligned}$$

one can get:

$$\left[\begin{array}{l}
p'_1 = p_2 \\
p'_2 = p_3 \\
p'_3 = \frac{(p_2)^2 - p_1 p_3 - (1-n)(2K)p_3 - 1.5\lambda K(2K\eta+1)^{\frac{1}{2}} p_3^2 - \lambda_m(p_4 + Np_6)\cos\alpha}{(1+2K\eta)(1-n) + (1+2K\eta)^{\frac{3}{2}} n\lambda p_3} \\
p'_4 = p_5 \\
p'_5 = \frac{\text{Pr}(p_2 p_4 + k_1 p_2 - p_1 p_5 - D_H p_4) - 2K p_5}{1+2K\eta} \\
p'_6 = p_7 \\
p'_7 = \frac{\text{Sc}(p_2 p_6 + k_2 p_2 - p_1 p_7 + R_c p_6) - 2K p_7}{1+2K\eta}
\end{array} \right] \quad (4.18)$$

$$\begin{aligned}
p_1(0) &= 0, \\
p_2(0) &= 1, \\
p_3(0) &= \text{unknown}, \\
p_4(0) &= 1 - k_1, \\
p_5(0) &= \text{unknown}, \\
p_6(0) &= 1 - k_2, \\
p_7(0) &= \text{unknown}.
\end{aligned} \quad (4.19)$$

The reduced system Eqs. (4.18)-(4.19) is an IVP. To integrate we need numeric values for $p_3(0)$ i.e. $f''(0)$, $p_5(0)$ i.e. $T'(0)$ and $p_7(0)$ implies $C'(0)$. Moreover, the initial conditions $p_3(0)$, $p_5(0)$ and $p_7(0)$ are missing but we have additional endpoint conditions:

$$\begin{aligned}
p_2(\infty) &= 0, \\
p_4(\infty) &= 0, \\
p_6(\infty) &= 0.
\end{aligned} \quad (4.20)$$

The integration is carried in this way the Eq. (4.20) hold fairly.

4.4 Analysis

Tables. 4.1-4.3 are constructed to examine the impact of involved physical parameters on SFC, HTR and MTR. In detail, Table. 4.1 depicts the SFC variations (in absolute sense) for positive values of K , n , λ and Pr. It is seen that the SFC near the cylindrical surface is an increasing function of both K and Pr while opposite trend is seen for n and λ . The

negative sign with the values of skin friction coefficient physically shows that the cylindrical surface exerts drag force on fluid particles. Table. 4.2 is design to provide the variations of HTR towards K , Pr , k_1 and λ . It is found that when we increase the values of both K and Pr the HTR show an inciting nature but opposite trends are noticed for higher values of k_1 and λ . The influence of K , k_2 and Sc is reported on MTR by way of Table. 4.3. The mass transfer rate reflects higher values for K , k_2 and Sc . It is noticed that in the absence of concentration equation, thermal stratification, mixed convection and heat generation effects retraced the problem reported by Akbar et al. [20]. Table. 4.4 provide the comparative values of skin friction coefficient towards both power law index and Weissenberg number. An excellent match is found with the existing values which confirm the execution of computational algorithm. Figs. 4.1(a-d) are used to examine the stream lines patterns towards curvature parameter. It is seen that for higher values of curvature parameter the fluid velocity enhances. The accelerated magnitude is witness from stream lines because for large curvature parameter the adjacent distance among stream lines decreases. The Figs. 4.2-4.7 are plotted to identify that how $f'(\eta)$ is effected via flow controlling parameters namely, curvature, mixed convection, thermal stratification parameter, an inclination, Weissenberg number and power law index. In detail, Fig. 4.2 is plotted to report the impact of K on $f'(\eta)$. It is noticed that the THF velocity varies directly, that is, for lager values of K the THF velocity enhances. Actually, large variation in K implies decrease in radius of curvature. The contact surface area reduces and less resistance is faced by THF particles as a result fluid flow accelerates. Fig. 4.3 paint the impact of α on $f'(\eta)$. It is seen that for inciting values of α , $f'(\eta)$ decreases. The fact behind is that for large values of α along x -axis, the effect of gravity reduces which cause decline in $f'(\eta)$ and within a momentum boundary layer. The effect of λ_m on $f'(\eta)$ is shown in Fig. 4.4. It is found that for higher values of λ_m , $f'(\eta)$ increases with in a boundary layer. Physically, this is due to increase in the buoyancy force. Fig. 4.5 identify that there exist an inverse relation between k_1 and $f'(\eta)$ because for positive values of k_1 the THF velocity decreases and also concerned momentum boundary layer. Fig. 4.6 portrait the impact of λ on $f'(\eta)$. It is seen that for

λ , $f'(\eta)$ shows decline trend because on increasing values of λ the relaxation time of the THF fluid increases which offers resistance to the THF fluid particles as a result the $f'(\eta)$ decreases. Fig. 4.7 discloses the impact of n on $f'(\eta)$. It is concluded that there exist an inverse relation between n and $f'(\eta)$ because for positive large values of n the THF velocity curve declines. Figs. 4.8-4.13 are plotted to envision the impact of K, D_H, k_1, Pr, α , and λ on THF temperature. In detail, the influence of K on $T(\eta)$ is examined and elaborated through Fig. 4.8. It is noticed that for higher values of K the THF temperature increases. The Kelvin temperature is evaluated as an average kinetic energy of fluid particles. Therefore, on increasing K , the velocity incites. This is due to an increase in kinetic energy, corresponding to increase in THF temperature. Fig. 4.9 illustrate the effect of D_H on $T(\eta)$. It is observed that an increase in D_H results an increase in $T(\eta)$. This fact is due to significant amount of heat produced via inciting values of D_H so the temperature of THF increases. Fig. 4.10 depicts the impact of Pr on $T(\eta)$. It is seen that there exist an inverse relation between Pr and $T(\eta)$. Moreover, fluids with high Pr corresponds weaker diffusion energy. So, an increase in Pr , results a strong reduction in $T(\eta)$ which is due to thinner thermal boundary layer. Fig. 4.11 report the inverse relation between α and $T(\eta)$ because for higher values of α the $T(\eta)$ decreases. The fact behind is that on increasing α about x -axis, the effect of gravity is less which results decrease in $T(\eta)$. Fig. 4.12 paint the impact of k_1 on $T(\eta)$ and it is seen that an increase in k_1 the temperature of THF decreases because for higher values of k_1 the convective potential between cylindrical surface and ambient fluid drops. The drop of convective potential, results in decreasing $T(\eta)$ and related thermal boundary layer also. Fig. 4.13 is used to examine the effect of λ on $T(\eta)$. We found direct relation between λ and $T(\eta)$ because large values of λ claims increase in relaxation time of THF particles due to which the resistance increases. An increase in resistance causes decrease in velocity. The drop in average kinetic energy leads to decline trend in THF temperature. Figs. 4.14-4.16 illustrate the influence of Sc, k_2 and R_c on THF concentration. In detail, Fig. 4.14 is plotted to inspect the impact of Sc on $C(\eta)$. The

mass diffusivity varies inversely via Sc so larger values of Sc results concentration boundary layer decline, as a result $C(\eta)$ decreases. Fig. 4.15 identify that an increase in κ_2 , the concentration distribution decreases. This fact is similar to the relation of κ_1 towards $T(\eta)$. Fig. 4.16 is used to examine the impact of R_c on $C(\eta)$. It is clearly seen that for large values of R_c the concentration profile shows declined trend.

4.5 Graphical outcomes

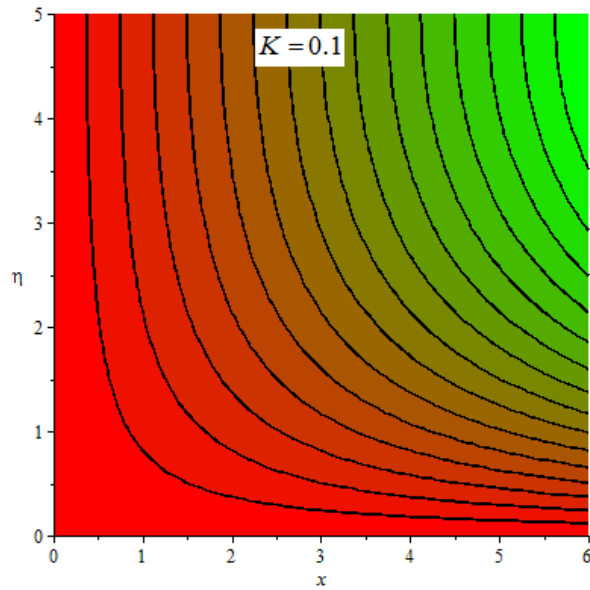


Fig. 4.1(a). Stream lines pattern for $K=0.1$.

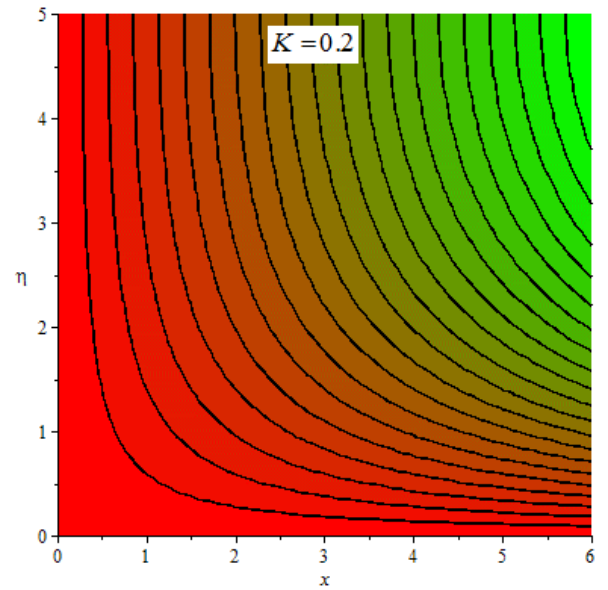


Fig. 4.1(b). Stream lines pattern for $K=0.2$.

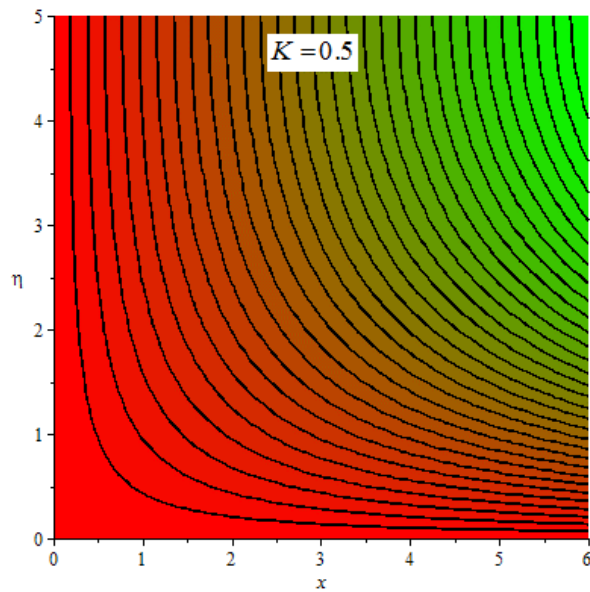


Fig. 4.1(c). Stream lines pattern for $K=0.5$.

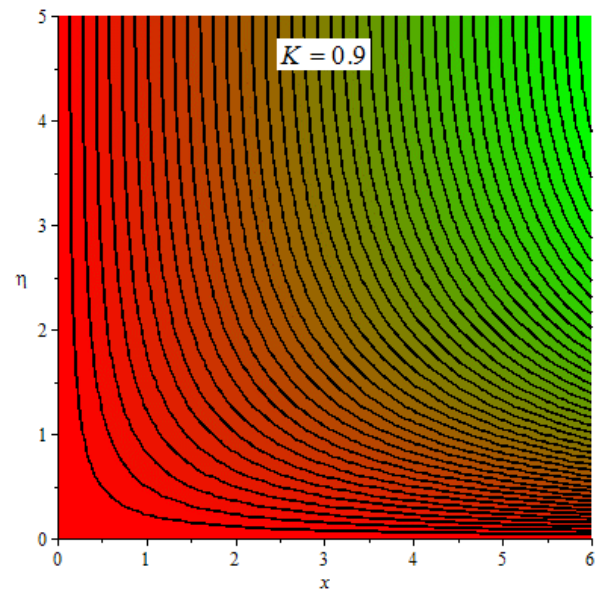


Fig. 4.1(d). Stream lines pattern for $K=0.9$.

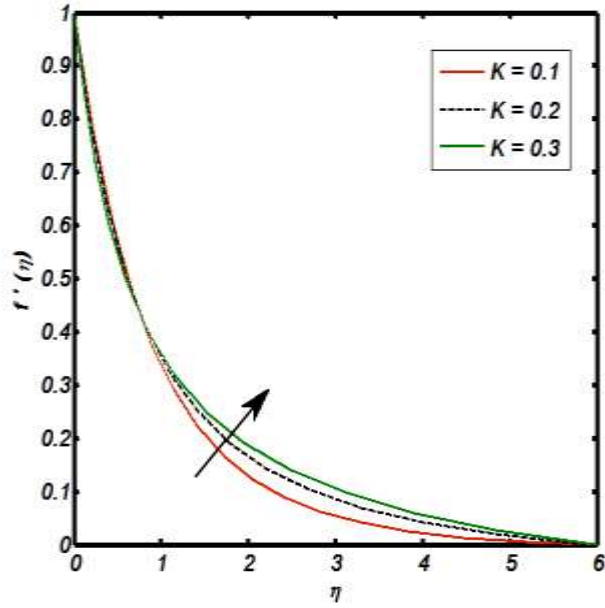


Fig. 4.2. Effect of K on $f'(\eta)$.

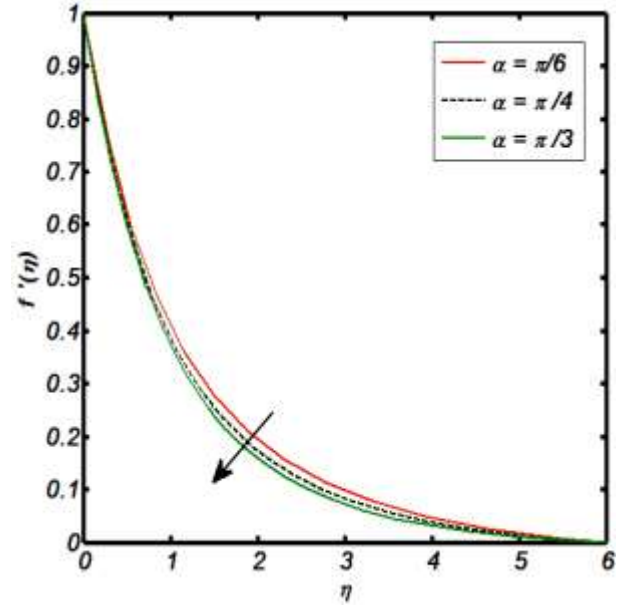


Fig. 4.3. Effect of α on $f'(\eta)$.

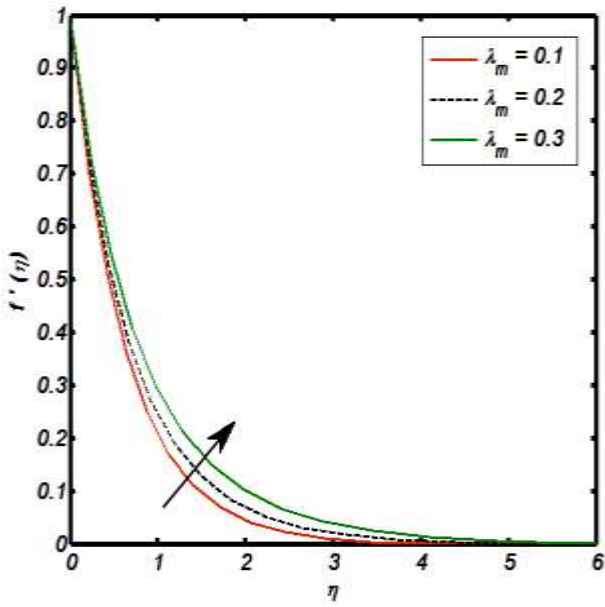


Fig. 4.4. Effect of λ_m on $f'(\eta)$.

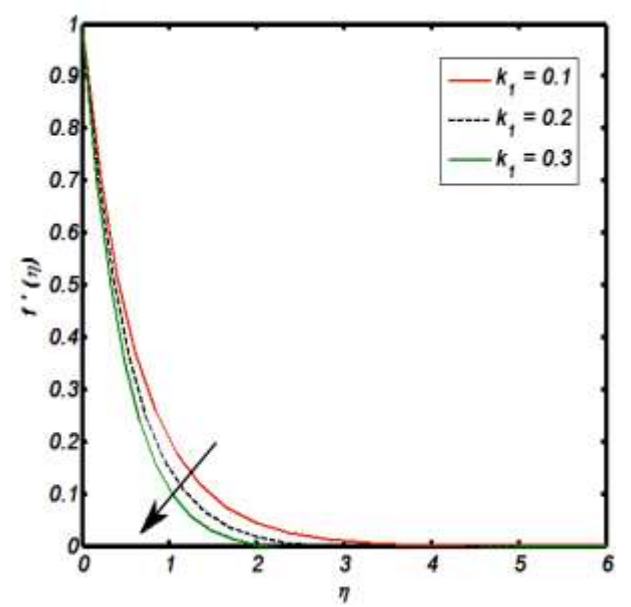


Fig. 4.5. Effect of k_1 on $f'(\eta)$.

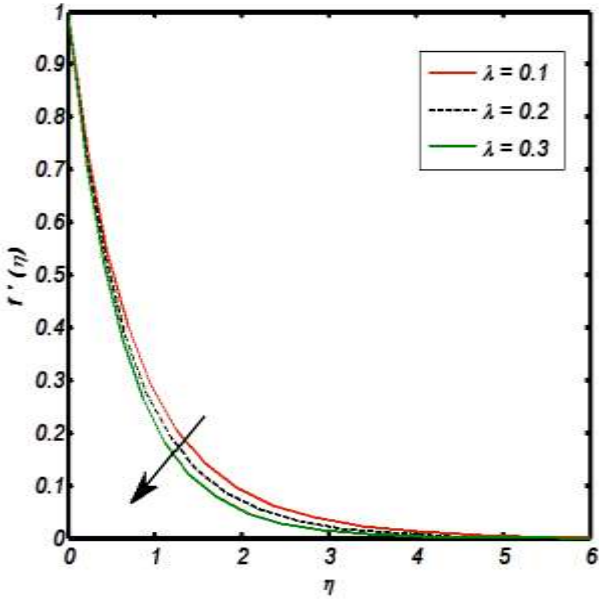


Fig. 4.6. Effect of λ on $f'(\eta)$.

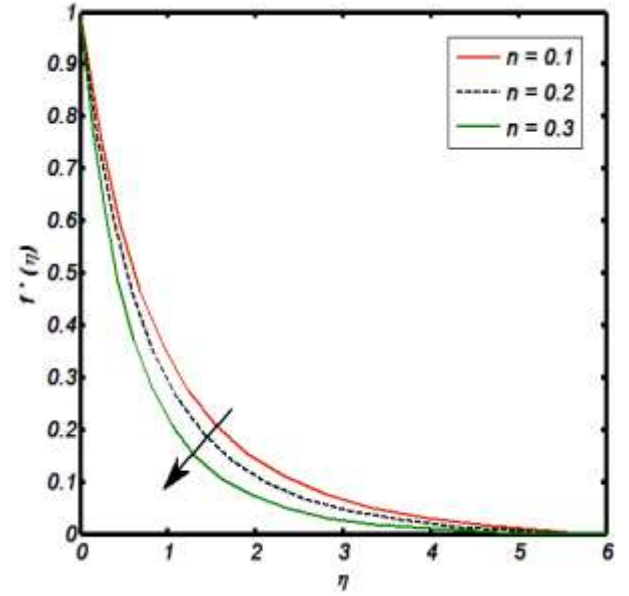


Fig. 4.7. Effect of n on $f'(\eta)$.

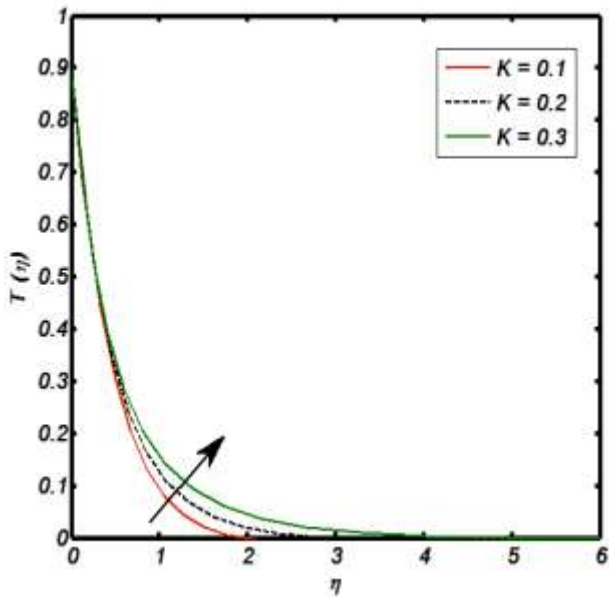


Fig. 4.8. Effect of K on $T(\eta)$.

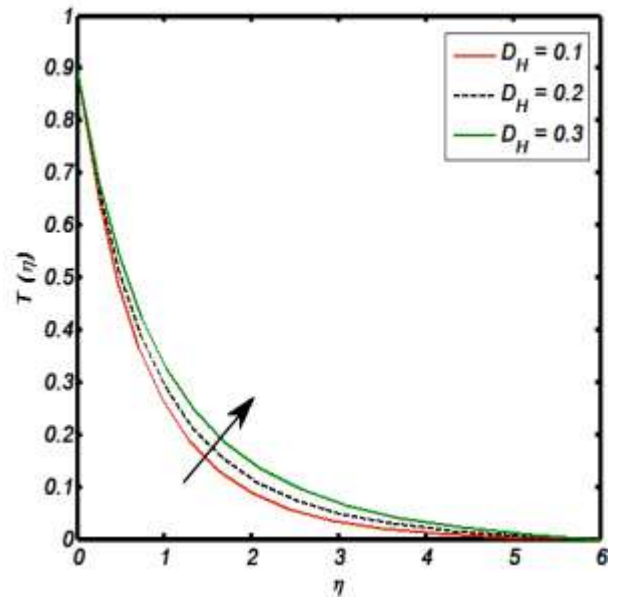


Fig. 4.9. Effect of D_H on $T(\eta)$.

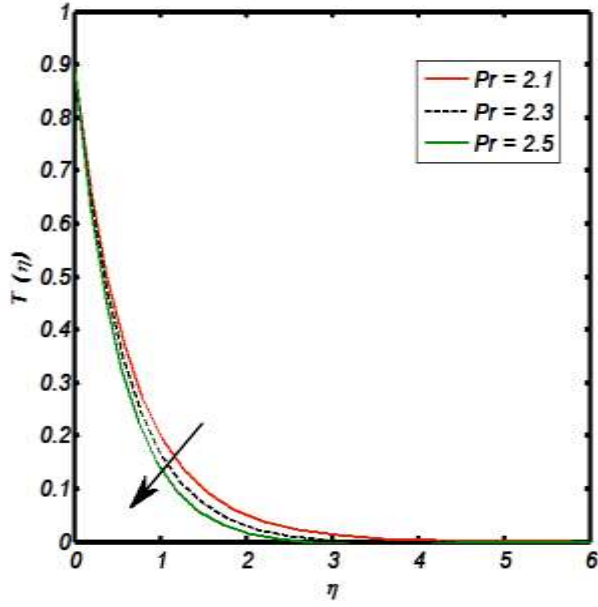


Fig. 4.10. Effect of Pr on $T(\eta)$.

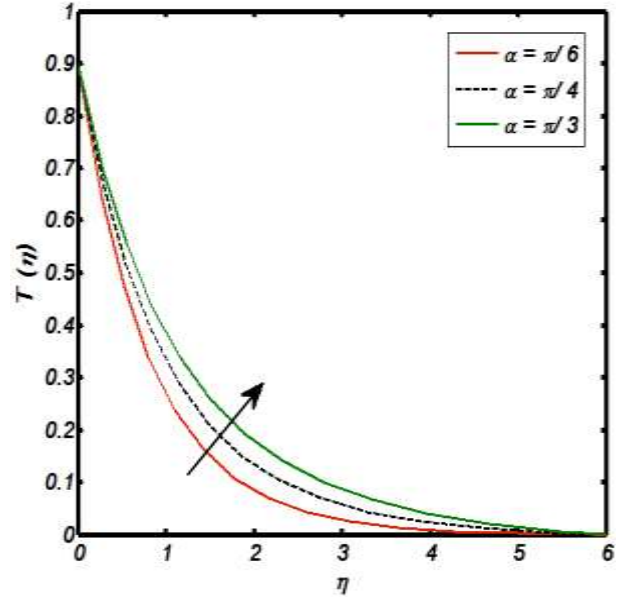


Fig. 4.11. Effect of α on $T(\eta)$.

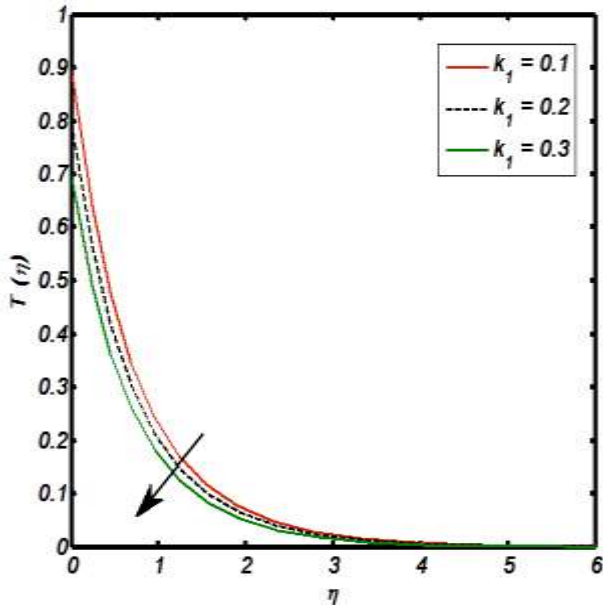


Fig. 4.12. Effect of κ_1 on $T(\eta)$.

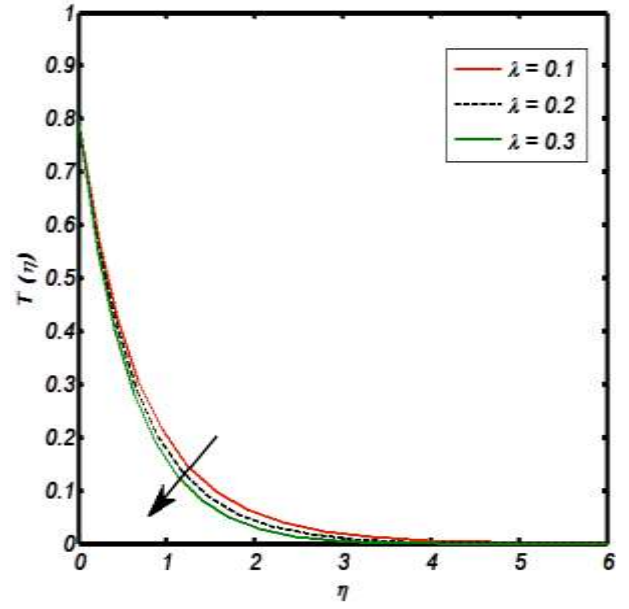


Fig. 4.13. Effect of λ on $T(\eta)$.

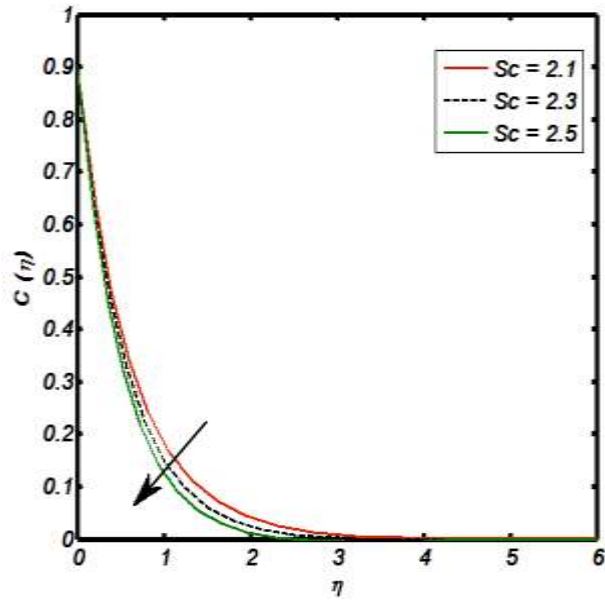


Fig. 4.14. Effect of Sc on $C(\eta)$.

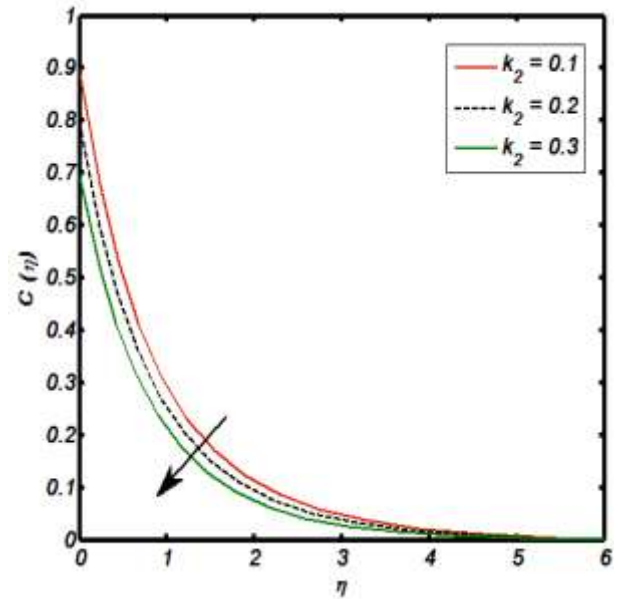


Fig. 4.15. Effect of k_2 on $C(\eta)$.

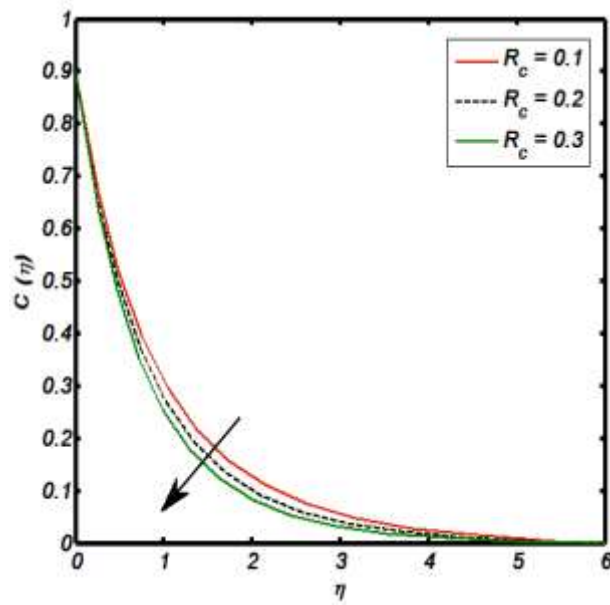


Fig. 4.16. Effect of R_c on $C(\eta)$.

Table 4.1. Variation in SFC via K, n, λ and Pr.

| K | n | λ | Pr | $C_f \sqrt{\text{Re}_x}$ |
|-----|-----|-----------|-----|--------------------------|
| 0.4 | 0.1 | 0.1 | 2.0 | -1.2108 |
| 0.6 | - | - | - | -1.9104 |
| 0.8 | - | - | - | -1.9443 |
| - | 0.1 | - | - | -1.2108 |
| - | 0.3 | - | - | 1.1017 |
| - | 0.5 | - | - | -1.0023 |
| - | - | 0.1 | - | -1.2108 |
| - | - | 0.3 | - | -1.1710 |
| - | - | 0.5 | - | -1.1083 |
| - | - | - | 2.0 | -1.2108 |
| - | - | - | 2.2 | -1.2129 |
| - | - | - | 2.4 | -1.2147 |

Table 4.2. Variation in HTR via K, Pr, k_1 and λ .

| K | Pr | k_1 | λ | $-T'(0)$ |
|-----|-----|-------|-----------|----------|
| 0.4 | 2.0 | 0.1 | 0.1 | 0.8350 |
| 0.6 | - | - | - | 0.9625 |
| 0.8 | - | - | - | 1.0444 |
| - | 2.0 | - | - | 0.8345 |
| - | 2.2 | - | - | 0.9015 |
| - | 2.4 | - | - | 0.9824 |
| - | - | 0.1 | - | 0.8350 |
| - | - | 0.3 | - | 0.7892 |
| - | - | 0.5 | - | 0.6905 |
| - | - | - | 0.1 | 0.8350 |
| - | - | - | 0.3 | 0.7108 |
| - | - | - | 0.5 | 0.6012 |

Table 4.3. Variation in MTR via K, k_2 and Sc .

| K | k_2 | Sc | $-C'(0)$ |
|-----|-------|------|----------|
| 0.4 | 0.1 | 0.1 | 1.8081 |
| 0.6 | - | - | 1.9901 |
| 0.8 | - | - | 2.015 |
| - | 0.1 | - | 1.8081 |
| - | 0.3 | - | 1.9655 |
| - | 0.5 | - | 2.0008 |
| - | - | 0.1 | 1.8081 |
| - | - | 0.3 | 1.8252 |
| - | - | 0.5 | 1.8434 |

Table 4.4. Comparison of SFC with existing work when $K = 0$.

| n | λ | Akbar et al. [20] | Rehman et al. [129] | Present |
|-----|-----------|-------------------|---------------------|---------|
| 0.0 | 0.0 | 1.00000 | 1.00000 | 1.0000 |
| 0.0 | 0.3 | 1.00000 | 1.00000 | 1.0000 |
| 0.0 | 0.5 | 1.00000 | 1.00000 | 1.0000 |
| 0.1 | 0.0 | 0.94868 | 0.94916 | 0.9491 |
| 0.1 | 0.3 | 0.94248 | 0.94321 | 0.9432 |
| 0.1 | 0.5 | 0.93826 | 0.93801 | 0.9380 |
| 0.2 | 0.0 | 0.89442 | 0.89447 | 0.8944 |
| 0.2 | 0.3 | 0.88023 | 0.88056 | 0.8805 |

4.6 Concluding remarks

The key findings of present analysis are itemized as follows:

- THF velocity increases via λ_m and K while it shows inverse behaviour for k_1, α, n and λ .
- Temperature of THF is an increasing function of K, D_H and α but it reflects opposite trend towards k_1, Pr and λ .
- Concentration of THF declines for positive values of k_2, R_c and Sc .

- In absolute sense, the SFC increases for large values of K and Pr , while an opposite behaviour is observed in that case of n and λ .
- The HTR enhance via Pr and K while an inverse relation is seen for both k_1 and λ .
- The MTR enhances towards K , Pr and Sc .
- Stream lines pattern of THF flow due to stretching cylindrical surface (see Figs. 4.1(a-d)) are offer for positive values of K .

CHAPTER 5

Magneto-nanofluid Numerical Modelling of Chemically Reactive Eyring-Powell Fluid Flow Towards both Flat and Cylindrical an Inclined Surfaces: A Comparative Study

5.1 Introduction

In this chapter the combined effects of both chemical reaction and dual stratification on boundary layer magneto-hydrodynamic Eyring Powell nanofluid flow both for flat and cylindrical inclined stretching surfaces under the region of stagnation point along with heat and mass transfer characteristics are investigated. The flow situation is carried out by considering physical effects namely, thermal radiation and heat generation. To be more specific, the fluid flow is entertained through no slip condition i-e the velocity of particles is directly related to velocity of surface due to stretching. The physical situation within the real concerned constraints is translated in terms of differential equations as a boundary value problem. To make implementation of possible computational algorithm, firstly the intricate PDE's are transformed into ODE's by using suitable transformation; secondly resulting BVP is converted into an IVP. These constructed ordinary differential equations are solved numerically by shooting technique charted with Runge-Kutta scheme. The effects of involved physical parameters are explored with the aid of graphical outcomes and tabular values. A straight line curve fitting way of communication is executed to inspect the impact of both thermophoresis parameter and Brownian motion parameter on heat and mass transfer rates.

5.2 Problem illustration

A steady laminar magneto-hydrodynamic and incompressible boundary layer stagnation point flow of non-Newtonian (Eyring Powell nanofluid-model) fluid with zero pressure gradient as shown in Fig. 5.1 is considered. The nanofluid flow yields an inclined

stretching cylinder undergoing with first order chemical reaction. Further, both the heat and mass transfer characteristics are identified by incorporating, thermal radiation, temperature and concentration stratification.

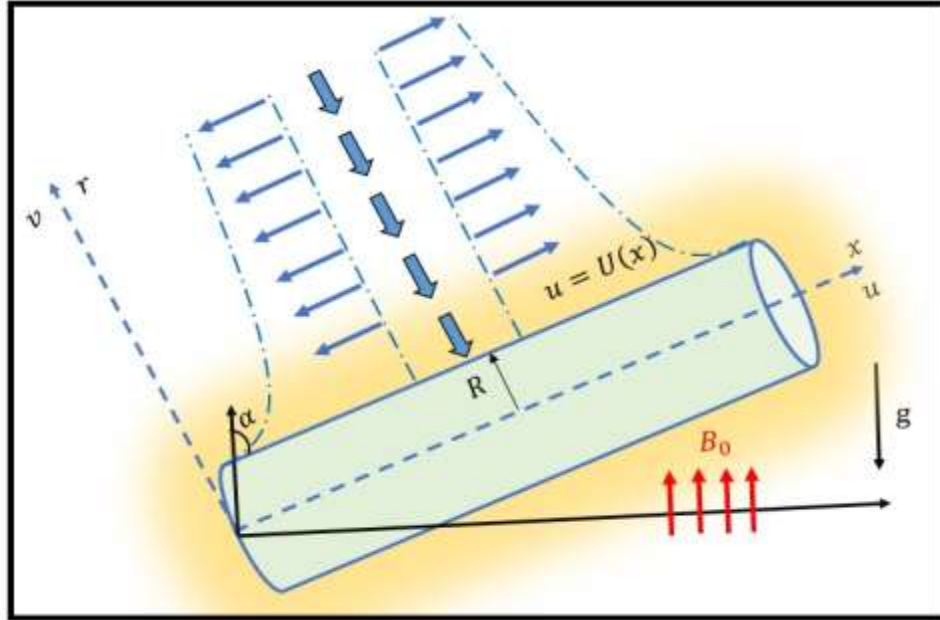


Fig. 5.1 Physical geometry of the fluid model.

The strength of temperature and concentration near the cylindrical surface are assumed to be higher than the ambient fluid. In addition, the magnetic field is applied perpendicular to the fluid flow and impact of an induced magnetic field is neglected due to low Reynolds number assumption. Moreover, the radial direction is considered perpendicular to x -axis (i.e. taken as r -axis). The axial direction of cylinder is aligned with the x -axis.

5.3 Momentum formulation

The flow characteristics of Eyring Powell nano model is explained through the generally accepted differential equation (in the absence of magnetic field and stagnation point we have basic equations, see Ref. [30]) i-e continuity and momentum equations in a two dimensional frame of reference. The simplified differential equations are:

$$\frac{\partial(r\hat{u})}{\partial x} + \frac{\partial(r\hat{v})}{\partial r} = 0, \quad (5.1)$$

$$\begin{aligned} \frac{\partial \hat{u}}{\partial r} \hat{v} + \frac{\partial \hat{u}}{\partial x} \hat{u} &= \frac{\partial^2 \hat{u}}{\partial r^2} \left(\frac{1}{\beta \rho c} + \nu \right) - \frac{1}{2\beta c^3 \rho} \left(\frac{\partial \hat{u}}{\partial r} \right)^2 \frac{\partial^2 \hat{u}}{\partial r^2} + \frac{1}{r} \left(\nu + \frac{1}{\beta \rho c} \right) \frac{\partial \hat{u}}{\partial r} - \frac{1}{6\beta r \rho c^3} \left(\frac{\partial \hat{u}}{\partial r} \right)^3 \quad (5.2) \\ + \hat{u}_e \frac{\partial \hat{u}_e}{\partial x} - \frac{\sigma B_0^2}{\rho} (\hat{u} - \hat{u}_e) &+ g((\hat{T} - \hat{T}_\infty) \beta_T + (\hat{C} - \hat{C}_\infty) \beta_c) \cos \alpha, \end{aligned}$$

and the corresponding boundary conditions are:

$$\hat{u} = U(x) = ax, \quad \hat{v} = 0, \quad \text{at } r = R, \quad \hat{u} \rightarrow \hat{u}_e = a'x, \quad \text{when } r \rightarrow \infty, \quad (5.3)$$

where ν, ρ, β and $c, \hat{u}_e, \sigma, B_0, g, \beta_T, \beta_c$, and α , denotes kinematic viscosity, fluid density, Eyring-Powell fluid parameters, free stream velocity, electrical conductivity, uniform magnetic field, gravity, thermal expansion coefficient, concentration expansion coefficient, and an inclination respectively. We incorporate transformation of the form (Ref. [30]):

$$\begin{aligned} \eta &= \frac{r^2 - R^2}{2R} \left(\frac{U_0}{\nu L} \right)^{\frac{1}{2}}, \quad \psi = \left(\frac{U_0 \nu x^2}{L} \right)^{\frac{1}{2}} R f(\eta), \quad (5.4) \\ \hat{u} &= \frac{U_0 x}{L} f'(\eta), \quad \hat{v} = -\frac{R}{r} \sqrt{\frac{U_0 \nu}{L}} f(\eta), \end{aligned}$$

here, $U_0, R, f(\eta), f'(\eta)$, and ψ denotes reference velocity, radius of cylinder, dimensionless variable, velocity of fluid past a stretching cylinder, and stream function respectively. The relation in terms of stream function can be written as:

$$\hat{u} = \frac{\psi_r}{r}, \quad \hat{v} = \frac{-\psi_x}{r}, \quad (5.5)$$

by incorporating transformation given by Eq. (5.4) into Eq. (5.2), the resulting reduced differential equations are given as:

$$(1 + 2K\eta)(1 + M) f''' + ff'' + 2K(1 + M) f'' - (f')^2 - \frac{4}{3} \lambda MK (1 + 2K\eta) (f'')^3 - \quad (5.6)$$

$$M \lambda (1 + 2K\eta)^2 (f'')^2 f''' - (f' - A) \gamma^2 + A^2 + (N\phi(\eta)\theta + (\eta)) \lambda_m \cos \alpha = 0,$$

$$f'(\eta) = 1, \quad f(\eta) = 0, \quad \text{at } \eta = 0, \quad (5.7)$$

$$f'(\eta) \rightarrow A, \quad \text{when } \eta \rightarrow \infty,$$

and:

$$K = \frac{1}{R} \sqrt{\frac{\nu}{a}}, \quad a = \frac{U_0}{L}, \quad M = \frac{1}{\mu\beta c}, \quad \lambda = \frac{a^3 x^2}{2c^2 \nu}, \quad (5.8)$$

$$\gamma = \sqrt{\frac{\sigma\beta_0^2}{\rho a}}, \quad A = \frac{a'}{a}, \quad \lambda_m = \frac{Gr}{Re_x^2}, \quad \text{and } N = \frac{Gr^*}{Gr},$$

with:

$$Gr^* = \frac{(\hat{C}_w - \hat{C}_0)g\beta_c x^3}{\nu^2}, \quad Gr = \frac{(\hat{T}_w - \hat{T}_0)g\beta_T x^3}{\nu^2}. \quad (5.9)$$

The surface quantity is:

$$C_f = \frac{\tau_w}{\rho \frac{U_e^2}{2}}, \quad \tau_w = \left[\mu \left(\frac{\partial \hat{u}}{\partial r} \right) + \frac{1}{\beta c} \frac{\partial \hat{u}}{\partial r} - \frac{1}{6\beta c^3} \left(\frac{\partial \hat{u}}{\partial r} \right)^3 \right]_{r=R}, \quad (5.10)$$

here, μ and τ_w denotes fluid viscosity and shear stress respectively. In non-dimensional form the skin friction coefficient is prearranged as:

$$Re_x^{1/2} C_f = 2f''(0)(M+1) - (f''(0))^3 \frac{2\lambda M}{3}. \quad (5.11)$$

5.4 Temperature and concentration formulation

Here the Eyring-Powell nanofluid flow towards both flat and cylindrical stretching surfaces is considered. The flow narrating differential equations (in the absence heat generation and chemical reaction we have fundamental equations, see Ref. [29]) i-e energy and concentration under boundary layer assumption reduces to:

$$\hat{v} \frac{\partial \hat{T}}{\partial r} + \hat{u} \frac{\partial \hat{T}}{\partial x} = \frac{\alpha^*}{r} \frac{\partial}{\partial r} \left(r \frac{\partial \hat{T}}{\partial r} \right) - \frac{1}{\rho c_p r} \frac{\partial}{\partial r} (r q_r) \quad (5.12)$$

$$+ \tau \left(D_B \frac{\partial \hat{T}}{\partial r} \frac{\partial \hat{C}}{\partial r} + \frac{D_T}{T_\infty} \left(\frac{\partial \hat{T}}{\partial r} \right)^2 \right) + \frac{Q_0}{c_p \rho} (\hat{T} - \hat{T}_\infty),$$

$$\hat{u} \frac{\partial \hat{C}}{\partial x} + \hat{v} \frac{\partial \hat{C}}{\partial r} = D_B \left(\frac{\partial^2 \hat{C}}{\partial r^2} + \frac{1}{r} \frac{\partial \hat{C}}{\partial r} \right) + \frac{D_T}{T_\infty} \left(\frac{\partial^2 \hat{T}}{\partial r^2} + \frac{1}{r} \frac{\partial \hat{T}}{\partial r} \right) - R_o (\hat{C} - \hat{C}_\infty), \quad (5.13)$$

here, $q_r = -\left(\frac{4}{3}\right) \frac{\sigma^*}{k^*} \frac{\partial \hat{T}^4}{\partial r}$ represents Rosseland radiative heat flux, therefore Eq. (5.12) can

be written as:

$$\begin{aligned} \hat{u} \frac{\partial \hat{T}}{\partial x} + \hat{v} \frac{\partial \hat{T}}{\partial r} &= \frac{\alpha}{r} \frac{\partial}{\partial r} \left(r \frac{\partial \hat{T}}{\partial r} \right) + \frac{1}{\rho c_p r} \left(\frac{4}{3} \right) \frac{\sigma^*}{k^*} \frac{\partial}{\partial r} \left(r \frac{\partial \hat{T}^4}{\partial r} \right) \\ + \tau \left(D_B \frac{\partial \hat{T}}{\partial r} \frac{\partial \hat{C}}{\partial r} + \frac{D_T}{T_\infty} \left(\frac{\partial \hat{T}}{\partial r} \right)^2 \right) &+ \frac{Q_0}{c_p \rho} (\hat{T} - \hat{T}_\infty), \end{aligned} \quad (5.14)$$

subjected to endpoint conditions:

$$\begin{aligned} \hat{T}(x, r) = \hat{T}_w(x) = \hat{T}_0 + \frac{b x}{L}, \quad \hat{C}(x, r) = \hat{C}_w(x) = \hat{C}_0 + \frac{d x}{L} \quad \text{at } r = R, \\ \hat{T}(x, r) \rightarrow \hat{T}_\infty(x) = \hat{T}_0 + \frac{c x}{L}, \quad \hat{C}(x, r) \rightarrow \hat{C}_\infty(x) = \hat{C}_0 + \frac{e x}{L} \quad \text{as } r \rightarrow \infty, \end{aligned} \quad (5.15)$$

where, α^* , c_p , D_B , D_T , \hat{T} , \hat{T}_∞ , Q_0 , \hat{C} , \hat{C}_∞ , and R_0 stands for thermal diffusivity, specific heat capacity at constant pressure, Brownian diffusion coefficient, thermophoretic diffusion coefficient, fluid temperature, ambient temperature, heat generation coefficient, fluid concentration, ambient concentration and rate of chemical reaction respectively. Further,

$\tau = \frac{(\rho c)_p}{(\rho c)_f}$, $T_w(x)$, $C_w(x)$, L , b , c , d , and e represents the ratio of nanoparticles heat

capacity to the base fluid heat capacity, prescribed surface temperature, prescribed surface concentration, reference length and dimensionless constants respectively. To find out the solution of Eqs. (5.13)-(5.14) under endpoint conditions Eq. (5.15), we considered following transformation of the form and given as:

$$\begin{aligned} \hat{u} = \frac{U_0 x}{L} f'(\eta), \quad \hat{v} = -\frac{R}{r} \sqrt{\frac{U_0 \nu}{L}} f(\eta), \quad \eta = \frac{r^2 - R^2}{2R} \left(\frac{U_0}{\nu L} \right)^{\frac{1}{2}}, \\ \psi = \left(\frac{U_0 \nu x^2}{L} \right)^{\frac{1}{2}} R f(\eta), \quad \theta(\eta) = \frac{\hat{T} - \hat{T}_\infty}{\hat{T}_w - \hat{T}_0}, \quad \phi(\eta) = \frac{\hat{C} - \hat{C}_\infty}{\hat{C}_w - \hat{C}_0}, \end{aligned} \quad (5.16)$$

here, \hat{T}_0 , \hat{C}_0 , and ψ denotes reference temperature, reference concentration and stream function respectively. By incorporating transformation given by Eq. (5.16) into Eqs. (5.13)-(5.14), the resulting reduced differential equations are given as:

$$(1+2K\eta)\left(1+\frac{4}{3}R_T\right)\theta''(\eta)+2K\left(1+\frac{4}{3}R_T\right)\theta'(\eta) \quad (5.17)$$

$$+\text{Pr}Nb(1+2K\eta)\left(\theta'\phi'+\frac{Nt}{Nb}\theta'^2\right)+\text{Pr}\left(\begin{matrix} f(\eta)\theta'(\eta)-f'(\eta)\theta(\eta) \\ -f'(\eta)m_1+Q\theta(\eta) \end{matrix}\right)=0,$$

$$(1+2K\eta)\left(\phi''(\eta)+\frac{Nt}{Nb}\theta''(\eta)\right)+\text{Pr}Le\left(f(\eta)\phi'(\eta)-f'(\eta)\phi(\eta)-f'(\eta)m_2\right) \quad (5.18)$$

$$+2K\left(\phi'(\eta)+\frac{Nt}{Nb}\theta'(\eta)\right)-Rc\phi(\eta)=0,$$

the transformed endpoint conditions are given as:

$$\theta(\eta)=1-m_1, \phi(\eta)=1-m_2, \text{ at } \eta=0, \quad (5.19)$$

$$\theta(\eta)\rightarrow 0, \phi(\eta)\rightarrow 0, \text{ when } \eta\rightarrow\infty.$$

here, R_T , Pr , Nb , Nt , m_1 , Q , Le , m_2 , and Rc denotes, thermal radiation parameter, Prandtl number, Brownian motion parameter, thermophoresis parameter, thermal stratification parameter, heat generation parameter, Lewis number, solutal stratification parameter and chemical reaction parameter, respectively and are defined as follows:

$$R_T = \frac{4\sigma^*T_\infty^3}{k^*k}, \text{Pr} = \frac{\nu}{\alpha^*}, Nt = \frac{(\hat{T}_w - \hat{T}_\infty)\tau D_T}{\nu T_\infty}, Nb = \frac{(\hat{C}_w - \hat{C}_\infty)\tau D_B}{\nu}, \quad (5.20)$$

$$m_1 = \frac{c}{b}, Q = \frac{LQ_0}{U_0\rho c_p}, Le = \frac{\alpha^*}{D_B}, m_2 = \frac{e}{d}, Rc = \frac{R_o L}{U_o}.$$

The expressions of local Nusselt and Sherwood number are defined as:

$$Nu = \frac{xq_w}{k(\hat{T}_w - \hat{T}_o)}, q_w = -k\left(\frac{\partial\hat{T}}{\partial r}\right)_{r=R} + (q_r)_{r=R}, \quad (5.21)$$

$$Sh = \frac{xj_w}{D(\hat{C}_w - \hat{C}_0)}, j_w = -D\left(\frac{\partial\hat{C}}{\partial r}\right)_{r=R},$$

the non-dimensional form of these expressions are well-defined and given as:

$$Nu Re_x^{-1/2} = -\left(1 + \frac{4}{3} R_d\right) \theta'(\eta), \text{ at } \eta \rightarrow 0, \quad (5.22)$$

$$Sh Re_x^{-1/2} = -\phi'(\eta), \text{ at } \eta \rightarrow 0.$$

5.5 Computational scheme

The system is solved by using computational algorithm. Order reduction is done by entertaining:

$$p_2 = f'(\eta), \quad p_3 = p'_2 = f''(\eta), \quad p_5 = \theta'(\eta), \quad p_7 = \phi'(\eta), \quad (5.23)$$

and we have:

$$p'_1 = p_2, \quad (5.24)$$

$$p'_2 = p_3,$$

$$p'_3 = \frac{\left\{ \begin{array}{l} (p_2)^2 - p_1 p_3 - (2K)(1+M)p_3 + \frac{4}{3} \lambda MK(1+2K\eta)p_3^3 + \gamma^2(p_2 - A) - A^2 \\ -\lambda_m(p_4 + Np_6) \cos \alpha, \end{array} \right\}}{(1+2K\eta)(1+M) - M\lambda(1+2K\eta)^2 p_3^2},$$

$$p'_4 = p_5,$$

$$p'_5 = \frac{\left\{ \begin{array}{l} \text{Pr}(p_2 p_4 + m_1 p_2 - p_1 p_5 - Q p_4) - 2K(1 + \frac{4}{3} R_T) p_5 \\ -\text{Pr} Nb(1+2K\eta)(p_5 p_7 + \frac{Nt}{Nb} p_5^2) \end{array} \right\}}{(1+2K\eta)(1 + \frac{4}{3} R_T)},$$

$$p'_6 = p_7,$$

$$p'_7 = \frac{\text{Pr} Le(p_2 p_6 + m_2 p_2 - p_1 p_7) - (1+2K\eta) \frac{Nt}{Nb} p'_5 - 2K(p_7 + \frac{Nt}{Nb} p_5) + Rcp_6}{1+2K\eta}.$$

and:

$$\begin{aligned}
p_1(0) &= 0, \\
p_2(0) &= 1, \\
p_3(0) &= \text{First guess value}, \\
p_4(0) &= 1 - m_1, \\
p_5(0) &= \text{Second guess value}, \\
p_6(0) &= 1 - m_2, \\
p_7(0) &= \text{Third guess value}.
\end{aligned} \tag{5.25}$$

For integration purpose of system of equations given by Eq. (5.24) as a initial value problem (IVP) we need

$$p_3(\eta) = f''(\eta), p_5(\eta) = \theta'(\eta) \text{ and } p_7(\eta) = \theta'(\eta) \text{ when } \eta \rightarrow 0, \tag{5.26}$$

Further, we observed that the three initial conditions namely, $p_3(\eta)$, $p_5(\eta)$ and $p_7(\eta)$ when $\eta \rightarrow 0$ are stated but we own:

$$p_2(\eta) = A, p_4(\eta) = 0, \text{ and } p_6(\eta) = 0, \text{ when } \eta \rightarrow \infty. \tag{5.27}$$

The numerical computation up-to four decimal precision as convergence standards are achieved by maintaining $\Delta\eta = 0.025$ as a step size.

5.6 Results and discussion

The adopted parameter values for present study are given as an inclination $\alpha = 45^\circ$, magnetic field parameter $\gamma = 0.1$, curvature parameter $K = 0.1$, Prandtl number $Pr = 1.3$, thermal radiation parameter $R_T = 0.1$, mixed convection parameter $\lambda_m = 0.1$, thermophoresis parameter $N_t = 0.1$, Eyring-Powell fluid parameters $\lambda = M = 0.1$, Brownian motion parameter $N_b = 0.1$, velocities ratio parameter $A = 0.1$, ratio of concentration to thermal buoyancy forces $N = 0.1$, heat generation parameter $Q = 0.1$, thermal stratification parameter $m_1 = 0.1$, solutal stratification parameter $m_2 = 0.1$, chemical reaction parameter $Rc = 0.1$ and Lewis number $Le = 0.1$. The results are obtained by maintaining these values otherwise indicated on graphs where needed. Tables 5.1-5.4 are presented to inspect the influence of pertinent flow controlling parameters namely, curvature parameter, Prandtl number, Eyring-Powell fluid parameters, thermal stratification parameter, solutal stratification parameter and Lewis number on skin friction

coefficient, local Nusselt and Sherwood numbers. In detail, Tables 5.1-5.2, in absolute sense reflects that skin friction coefficient is an increasing function of curvature parameter, thermal stratification parameter, solutal stratification parameter and Prandtl number while decreasing function of fluid parameter. Table 5.3 shows that local Nusselt number shows an inciting nature for positive values of curvature parameter and Prandtl number but it has opposite attitude towards thermal stratification parameter. The impact of curvature parameter, solutal stratification parameter, Lewis and Prandtl numbers is presented with the aid of Table 5.4. It is observed that local Sherwood number shows an inciting nature towards curvature parameter, Lewis number and Prandtl number while it reflects decline behavior for the positive values of solutal stratification parameter.

5.6.1 Velocity distributions

The influence of physical parameters namely, velocities ratio parameter, magnetic field parameter, mixed convection parameter, and Eyring-Powell fluid parameters on Eyring-Powell fluid flow towards both flat and cylindrical surface embedded in double stratified medium is presented with the aid of Figs. 5.2-5.12. In detail, Figs. 5.2-5.6 are plotted to identified the movement of particles towards a cylindrical surface for velocities ratio parameter i-e $A = 0.0, 0.5, 1.0, 1.5, 2.0$. To be more specific, Fig. 5.2 scrutinizes the stream lines for $A = 1$, which implies equal values of free stream velocity and stretching velocity because the velocities ratio parameter (A) is defined as the ratio of free stream velocity to the stretching velocity. Further it was found that stream lines are symmetric about radial direction. Figs. 5.3-5.4 are constructed to examine the stream lines for $A < 1$, in other words when stretching velocity exceeds against free stream velocity. Physically, the boundary layer thickness increases largely when stretching velocity is dominant as compare to free stream velocity. Further, Fig. 5.3 is plotted for $A = 0$, which mean the free stream velocity is absolutely zero and from Fig. 5.3. It is also observed that the disturbance of particles is only due to stretching velocity. Fig. 5.4 is plotted for $A = 0.5$. It is worth mentioning that the involvement of free stream velocity is little significant as compared to $A = 0$. But still lesser then stretching velocity i.e at cylindrical surface the particle disturbance is significant as compared to far away from surface. In Figs. 5.5-5.6 stream lines are switches accordingly to the velocities ratio parameter $A > 1$. In this case free

stream velocity exceeds stretching velocity. The thickness of boundary layer decreases when A increases. In actual when A increases, we yields increase in free stream velocity for fixed values of stretching velocity, ultimately straining motion adjacent to the stagnation region brings inciting acceleration of free stream as a result thinning of boundary layer is observed. The effects of velocities ratio parameter on velocity of fluid for flat and cylindrical geometry are identified by means of Fig. 5.7. It was observed that the frequent fluctuations in momentum occurred for altering values of velocities ratio parameter. The increasing values of velocities ratio parameter reflects positive attitude in the velocities of fluids towards flat and cylindrical surface. It can be seen that momentum boundary layer is formed for $A > 1$ but an inverted boundary layer is emerged for the case of $A < 1$. When velocities ratio parameter achieve unity that is $A = 1$, at this stage free stream velocity and stretching velocity becomes equal so that momentum boundary layer do not appear. Fig. 5.8 is plotted to examine the influence of magnetic field parameter on velocity of fluid towards both flat and cylindrical surface. As expected, the inciting values of magnetic parameter brings decline in velocity profiles. In actual, when we enhance magnetic field parameter a resistive force named as Lorentz force actively participate to offer resistance against fluid particles as a result horizontal velocity decreases. Fig. 5.9 depicts the attitude of velocity distributions for both surfaces towards mixed convection parameter and it is noticed that by increasing values of mixed convection parameter the velocity profile shows inciting nature for both cases. Physically, this is due to enhancement of thermal buoyancy force. So the higher values of mixed convection parameter lead to increase in velocity within boundary layer. The impact of Eyring-Powell fluid parameter is presented for both flat and cylindrical surfaces through Fig. 5.10. It is noticed that an increase in Eyring-Powell fluid parameter cause decrease in velocity of fluid. This fact is due to inverse relation of fluid parameter with fluid viscosity while increase in fluid parameter values reflects decrease in fluid viscosity due to which motion of fluid particles enhances and collectively the fluid velocity shows higher values. Fig. 5.11 is plotted to examine the impact of fluid parameter on velocity profile. It is noticed that for positive values of fluid parameter the velocity exhibits decline nature. Fig. 5.12 depicts the fluid velocity variations against an inclination α . It is noticed that there is an inverse relation between an inclination α and velocity profile. For large values of an inclination α the

velocity profile decreases. When we increase an inclination α about x -axis the effect of gravity is reduced which brings decline in fluid velocity with in a boundary layer.

5.6.2 Temperature distributions

The impact of involved physical parameters namely, Brownian motion parameter, thermophoresis parameter, Prandtl number, Lewis number, curvature parameter, thermal radiation parameter, heat generation parameter and thermal stratification parameter on temperature distributions both for flat and cylindrical surface is elaborated in Figs. 5.13-5.21. The temperature variations for both cases against Brownian motion parameter are given by Fig. 5.13. It is seen that temperature distributions are found to be increasing function of Brownian motion parameter. The positive values of Brownian motion parameter corresponds random motion and collision among nano size particles in the flow regime which leads to production of plenty of heat and of course temperature distribution in absolute sense. The influence of thermophoresis parameter over a temperature is illustrated with the help of Fig. 5.14. It is seen that temperature distributions for both cases are mount function of thermophoresis parameter. This fact is due to huge amount of pulled nanoparticles towards cold surface from hot one, as a result temperature increases. From Fig. 5.15, we noticed inverse relation of temperature with Pr because inciting values of Prandtl number corresponds less diffusion of energy due to which temperature profile decreases. The impact of Lewis number is given through Fig. 5.16. It is evident from figure, for higher values of Lewis number the temperature distributions for geometries shows decline behaviour. Fig. 5.17 paints the temperature variation against curvature parameter towards cylindrical geometry. It is clearly seen that temperature distribution increases for increasing values of curvature parameter. Since Kelvin temperature is defined as an average kinetic energy so increase in curvature of cylinder, velocity of the fluid increases, that results in increase of kinetic energy which increases temperature. Note that the temperature of fluid starts decreasing near the cylindrical surface and increases far away from surface. Fig. 5.18 witnessed that the temperature profiles of both cases show an inciting attitude towards thermal radiation parameter. This fact is due to sufficient heat transfer into the fluid. Because by increasing thermal radiation parameter more heat is produced and hence this heat transfers to the fluid. The influence of heat generation parameter on temperature profiles for both cases is given by Fig. 5.19. It is observed that

the fluid temperature remarkably increased against heat generation parameter. In actual, during heat generation process energy is produced which consequently brings enhancement in temperature profile. Fig. 5.20 depicts the attitude of temperature distribution towards thermal stratification parameter for both flat and cylindrical surfaces. It is noticed that the temperature profile decreases for increase in thermal stratification parameter. This is because of decline in temperature difference between surface of cylinder and ambient fluid therefore, temperature profile decreases. Fig. 5.21 identify that there is direct relation between an inclination α and temperature of the fluid. We have noticed that for large values of an inclination α the temperature profile increases because an increase in inclination α about x -axis the effectiveness of gravity is significant which cause increase in temperature profile.

5.6.3 Nanoparticle concentration distributions

The influence of physical parameters named as Brownian motion parameter, thermophoresis parameter, chemical reaction parameter, Lewis number and solutal stratification parameter towards both the flat and cylindrical geometry is portrayed through Figs. 5.22-5.26. Particularly, the impact of both thermophoresis and Brownian motion parameters are identified by means of Fig. 5.22 and Fig. 5.23 respectively. The effect of chemical reaction parameter on fluid concentration is explored with the aid of Fig. 5.24. The physical illustration of Lewis number towards fluid concentration is shown in Fig. 5.25. The influence of positive alterations of solutal stratification parameter on concentration distribution is given in Fig. 5.26. In detail, Fig. 5.22 portrays the variation in nanoparticles concentration for both cases against positive values of thermophoresis parameter. It is observed that the nanoparticles concentration field of both cases shows inciting nature towards thermophoresis parameter. This fact is due to huge transfer of nanoparticles from cold region to hot one which yields an increment in concentration distributions. The influence of Brownian motion parameter for both cases in nanoparticles concentration is depicted through Fig. 5.23. It shows that with gradual growth in Brownian motion parameter, nanoparticles concentration distribution shows the tendency to decline. The effect of chemical reaction parameter for both flat and cylinder is illustrated in Fig. 5.24 and it is perceived that the nanoparticle concentration field for both cases is diminishing function of chemical reaction parameter. Furthermore, decline in solute

nanoparticle concentration is noticed due to remarkable disturbance in fluid molecules. The impact of Lewis number on nanoparticle concentration distribution is examined for flat and cylindrical geometry and justified through Fig. 5.25. The upsurge in Lewis number yields a thin nanoparticle concentration boundary layer along with frail diffusivity of molecules towards each fluid. Fig. 5.26 is plotted to inspect the variation of nanoparticle concentration towards positive values of solutal stratification parameter for plate and cylindrical surface. It is observed that there is a decline in fluid concentration within a boundary layer with increment in solutal parameter. Essentially, this effect is due convective potential drop between both ambient and surface concentration.

5.6.4 Straight line approximations

The straight line curve fitting approach is entertained to inspect the impact of both thermophoresis and Brownian motion parameters towards both heat and mass transfer rate. To be more specific, the effect of both thermophoresis parameter (variation encountered through red color) and Brownian motion parameter (variation encountered through blue color) on heat transfer rate are explained via Fig. 5.27. It is observed that heat transfer rate shows decline nature for both thermophoresis and Brownian motion parameter. The mass transfer rate variations towards both thermophoresis parameter (variation encountered through blue color) and Brownian motion parameter (variation encountered through red color) are identified by Fig. 5.28. Here, we observed that mass transfer rate enhances for Brownian motion parameter but opposite trend is noticed for thermophoresis parameter.

5.7 Results validation

Tables 5.5-5.6 are constructed for comparison of both skin friction coefficient and heat transfer rate with existing values. An excellent agreement is found for both physical quantities (skin friction coefficient and heat transfer rate) which lead to surety of present work. In detail, we have considered a steady MHD laminar boundary stagnation point flow of Eyring-Powell nano fluid brought by an inclined stretching cylindrical surface. In the absence of both heat and mass transfer, after incorporating $A = K = \lambda_m = 0$, we obtained the case (see Ref. [130]) in which Eyring-Powell fluid flow yields by flat stretching surface manifested with magnetic field effects. Further, these results are verified by developing comparison (when $M = \lambda = 0$) with Fathizedeh et al. [131] for skin friction coefficient towards different values of magnetic field parameter. We compare our findings

with both of them by substituting $A = K = \lambda_m = M = \lambda = 0$ and it is seen from Table 5.5 that the current values are in an excellent match with existing values for skin friction coefficient via various values of magnetic field parameter. In addition, in the absence of mass transfer characteristics if we substitute $\lambda_m = \lambda = M = m_1 = m_2 = Q = 0$ and $\alpha^o = 0$, Eq. (5.6) and Eq. (5.17) reduces to the flow problem given by Ishak and Nazar [132]. Further, if we incorporate $K = 0$ along with $\lambda_m = \lambda = M = m_1 = m_2 = Q = 0$ and $\alpha^o = 0$, Eq. (5.6) and Eq. (5.17) reduces to flow problem reported in Ref. [133]. Particularly, Table 5.6 presents the comparison of our findings with existing results regarding heat transfer rate for different values of Pr in a limited sense. From Table 5.5 we found an excellent match which guarantees the present work.

5.8 Graphical outcomes

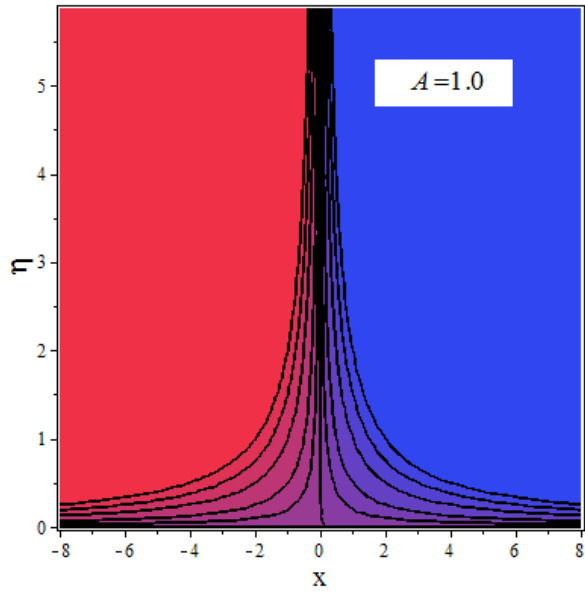


Fig. 5.2. Stream lines pattern for $A=1.0$.

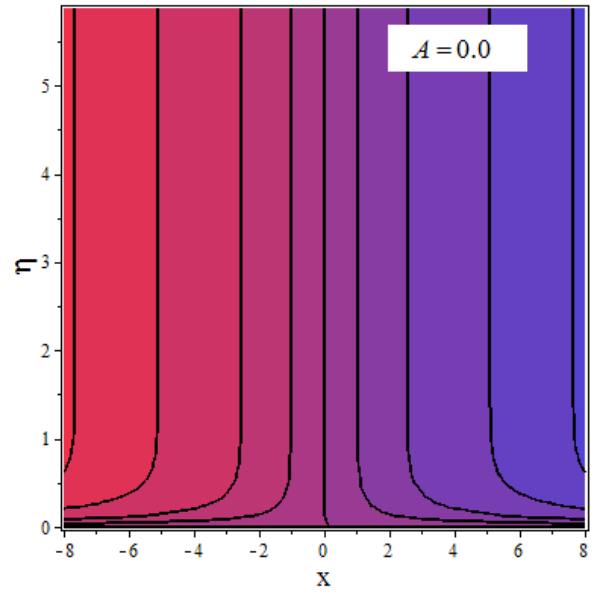


Fig. 5.3. Stream lines pattern for $A=0.0$.

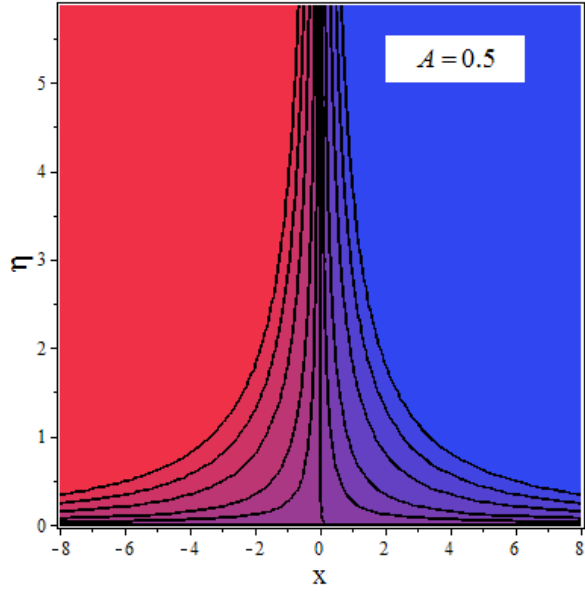


Fig. 5.4. Stream lines pattern for $A=0.5$.

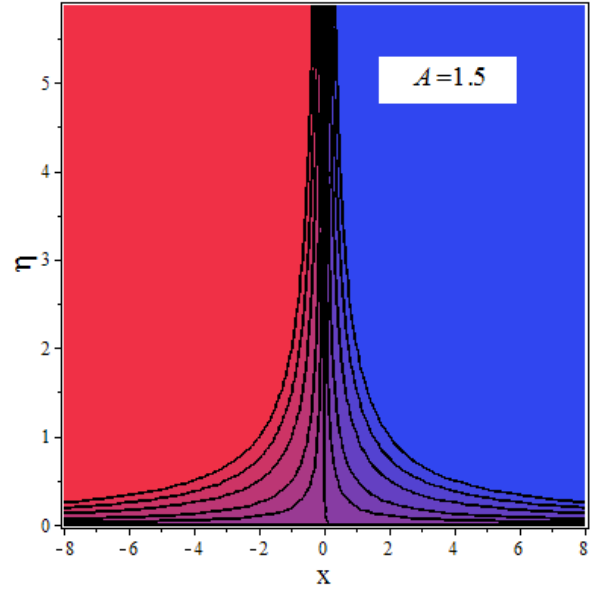


Fig. 5.5. Stream lines pattern for $A=1.5$.

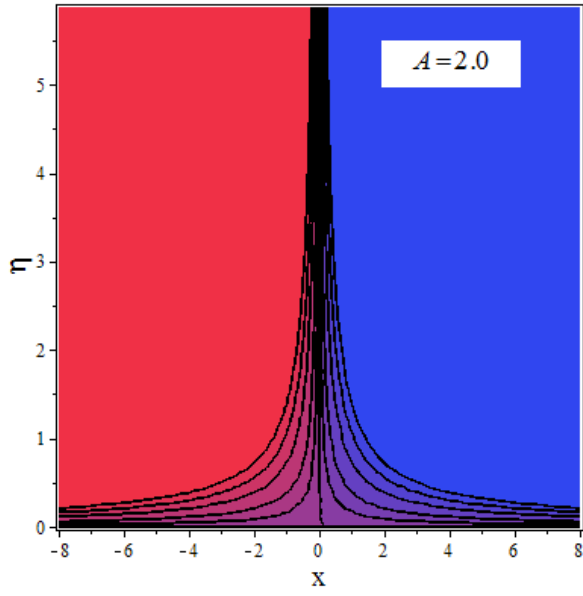


Fig. 5.6. Stream lines pattern for $A=2.0$.

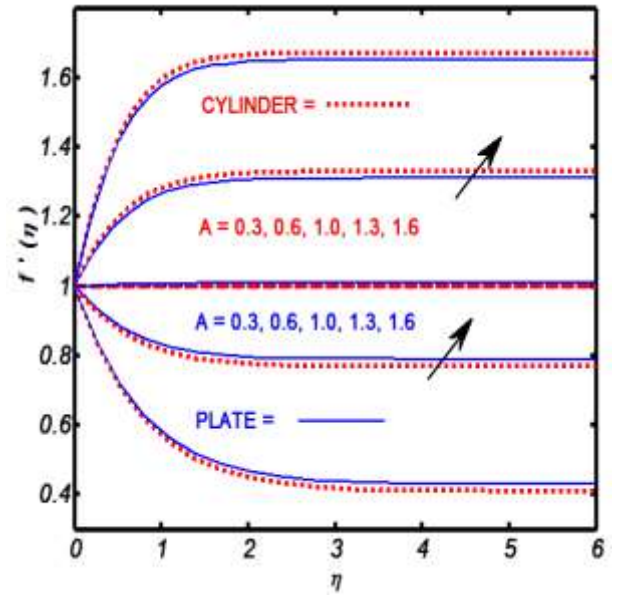


Fig. 5.7. Impact of velocities ratio parameter on velocity profile.

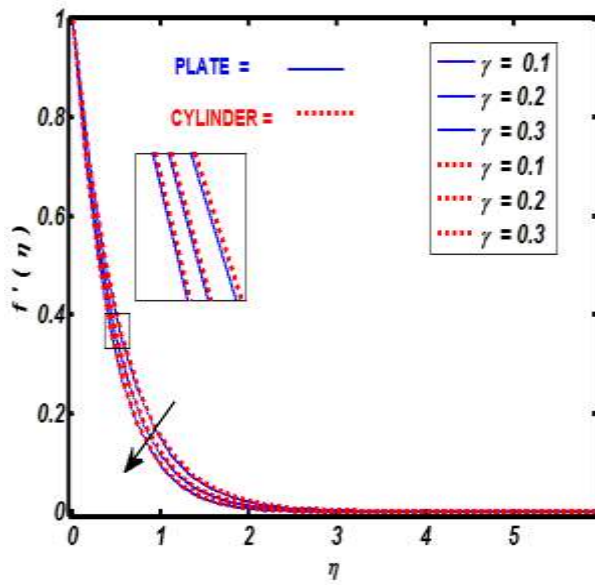


Fig. 5.8. Impact of magnetic field parameter on velocity profile.

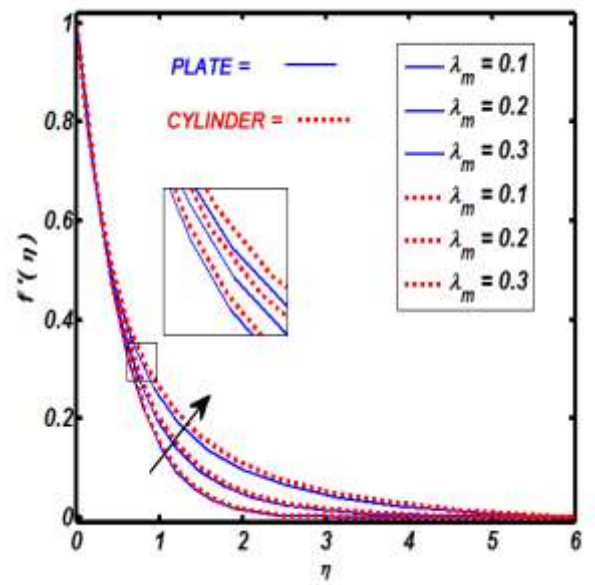


Fig. 5.9. Impact of mixed convection parameter on velocity profile.

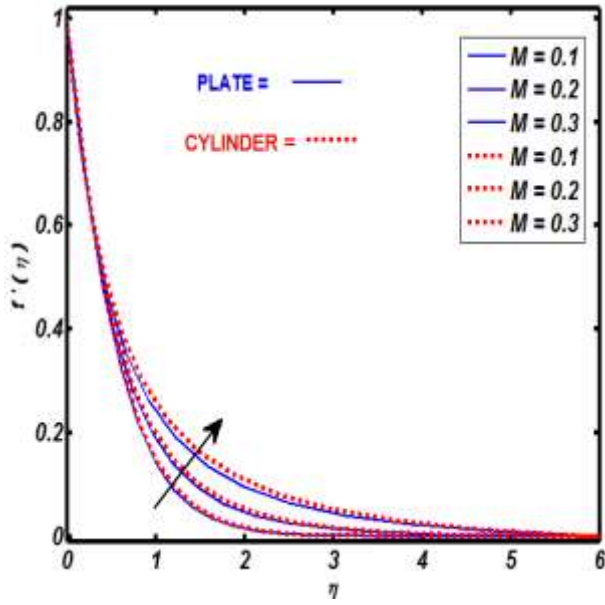


Fig. 5.10. Impact of Eyring Powell fluid parameter (M) on velocity profile.

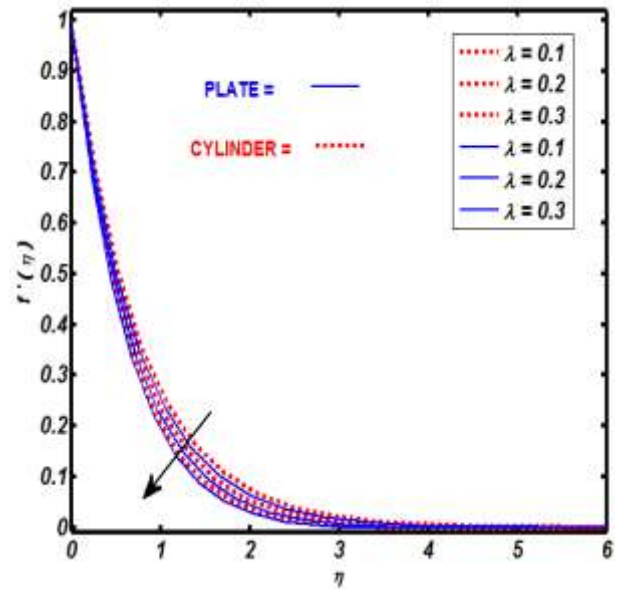


Fig. 5.11. Impact of Eyring Powell parameter (λ) on velocity profile.

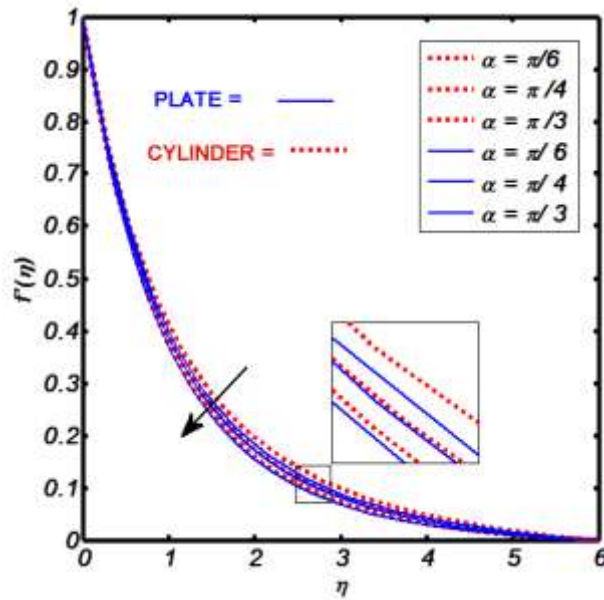


Fig. 5.12. Impact of an inclination on velocity profile.

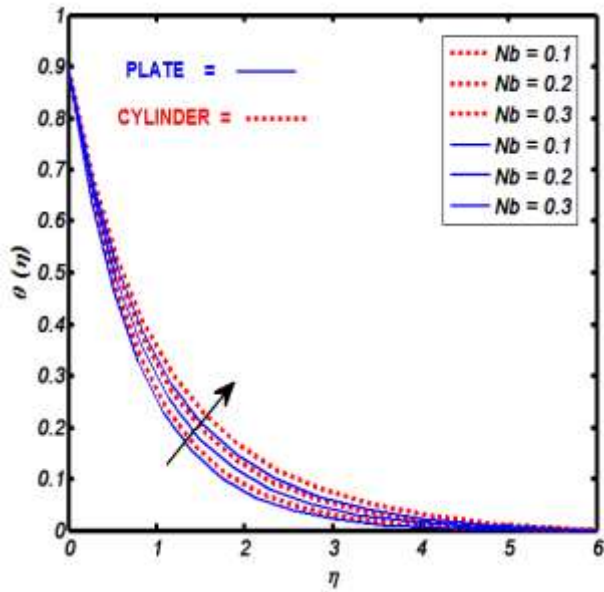


Fig. 5.13. Impact of Brownian motion parameter on temperature profile.

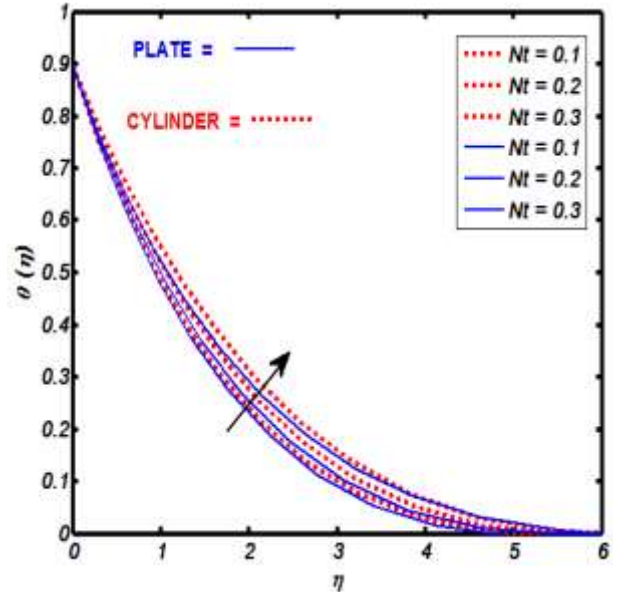


Fig. 5.14. Impact of thermophoresis parameter on temperature profile.

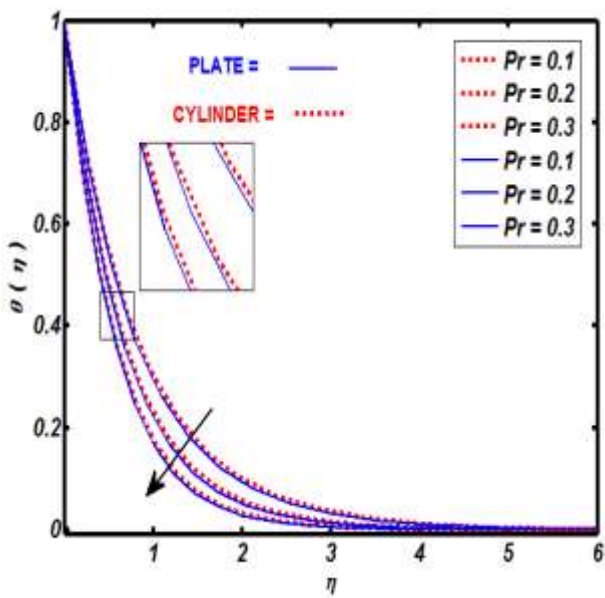


Fig. 5.15. Impact of Prandtl number on temperature profile.

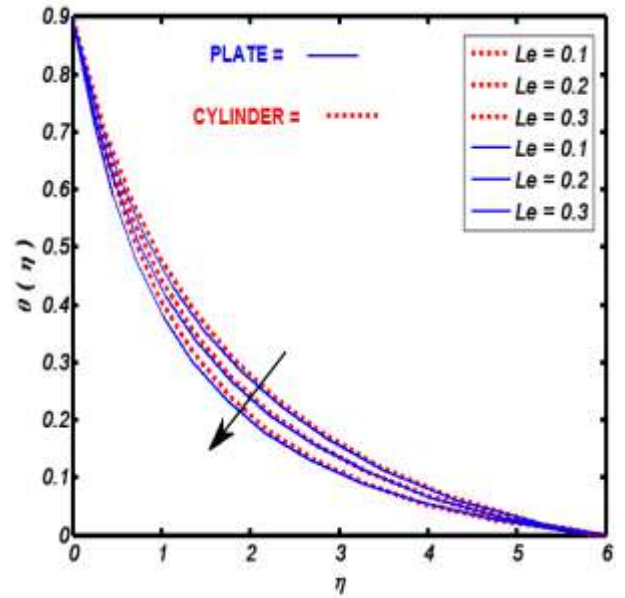


Fig. 5.16. Impact of Lewis number on temperature profile.

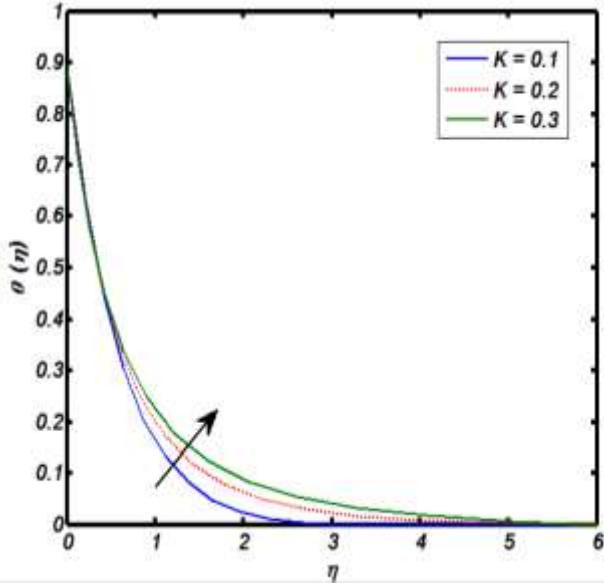


Fig. 5.17. Impact of curvature parameter on temperature profile.

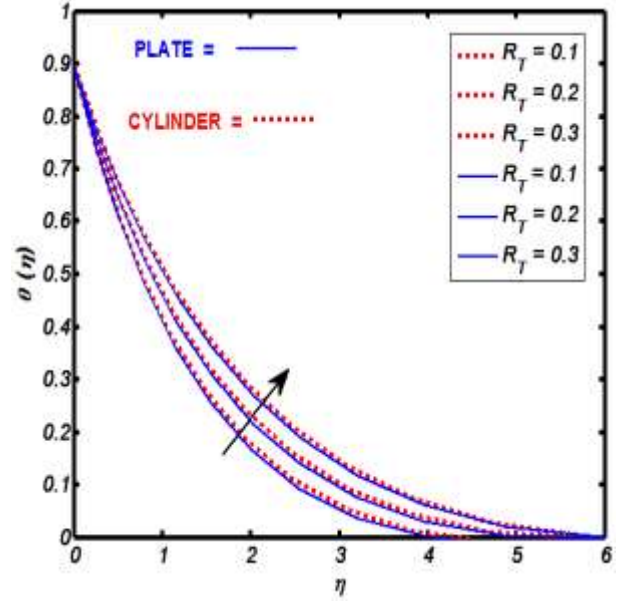


Fig. 5.18. Impact of thermal radiation parameter on temperature profile.

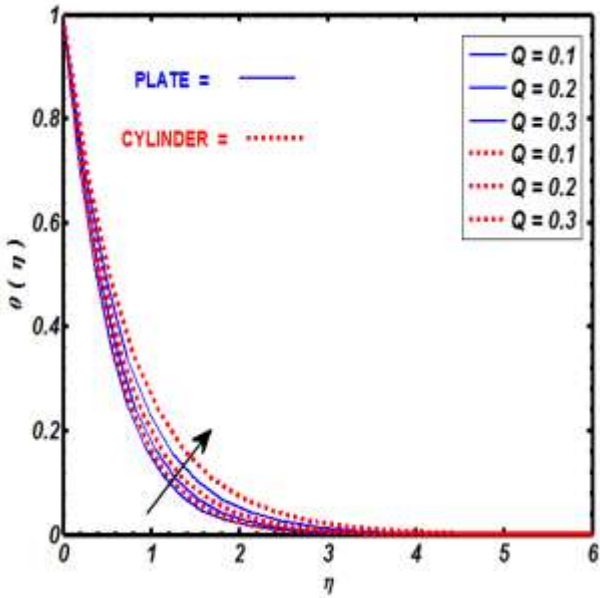


Fig. 5.19. Impact of heat generation parameter on temperature profile.

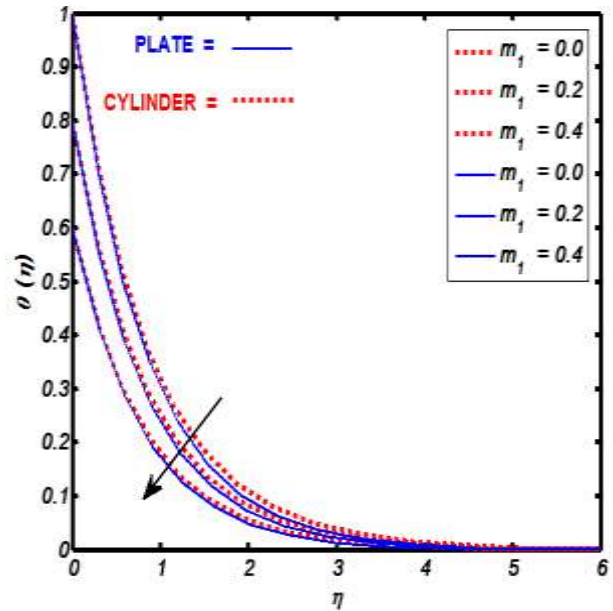


Fig. 5.20. Impact of thermal stratification parameter on temperature profile.

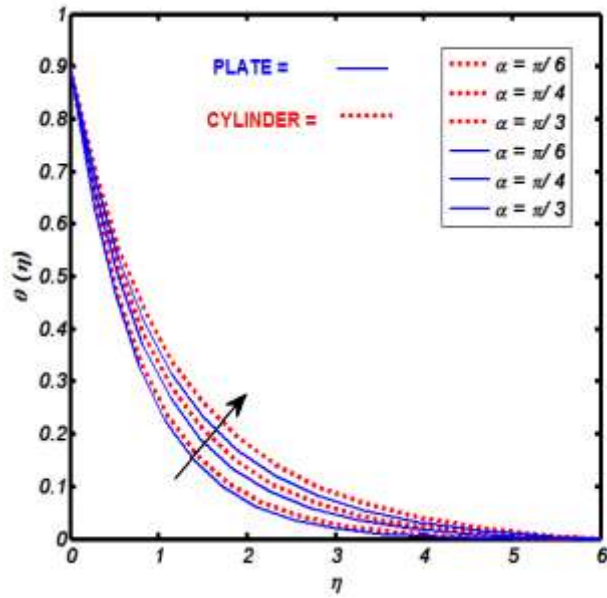


Fig. 5.21. Impact of an inclination on temperature profile.

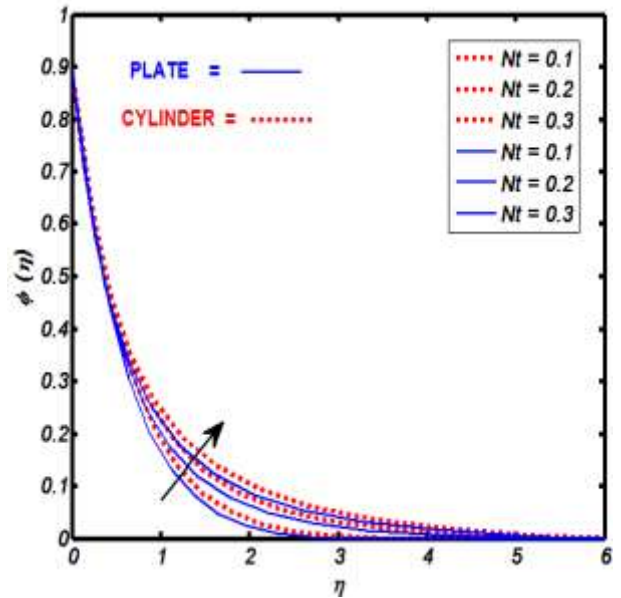


Fig. 5.22. Impact of thermophoresis parameter on concentration profile.

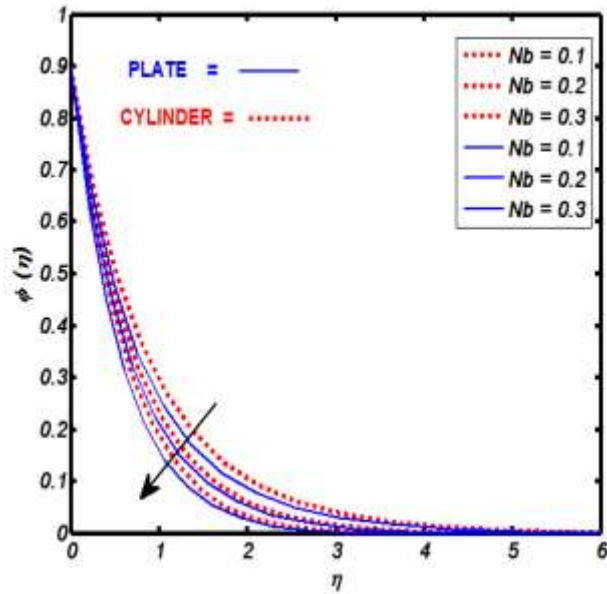


Fig. 5.23. Impact of Brownian motion parameter on concentration profile.

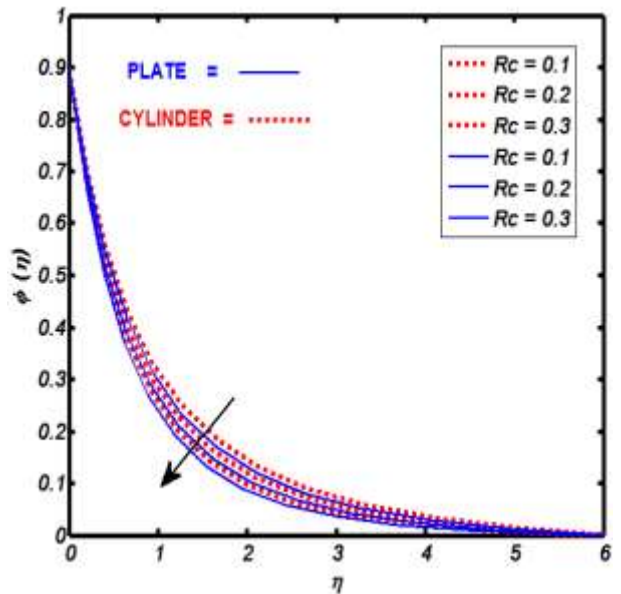


Fig. 5.24. Impact of chemical reaction parameter on concentration profile.

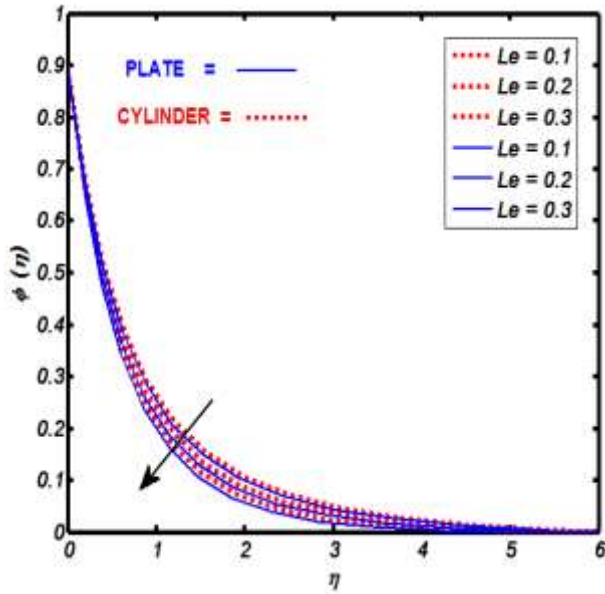


Fig. 5.25. Impact Lewis number on concentration profile.

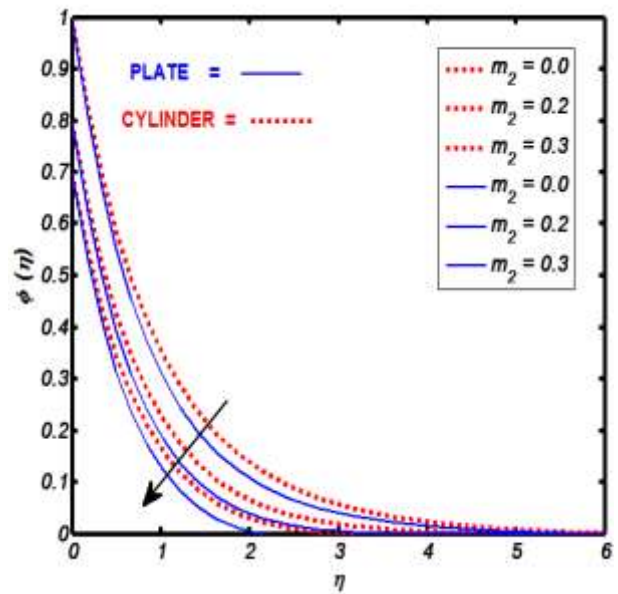


Fig. 5.26. Impact of solutal stratification parameter on concentration profile.

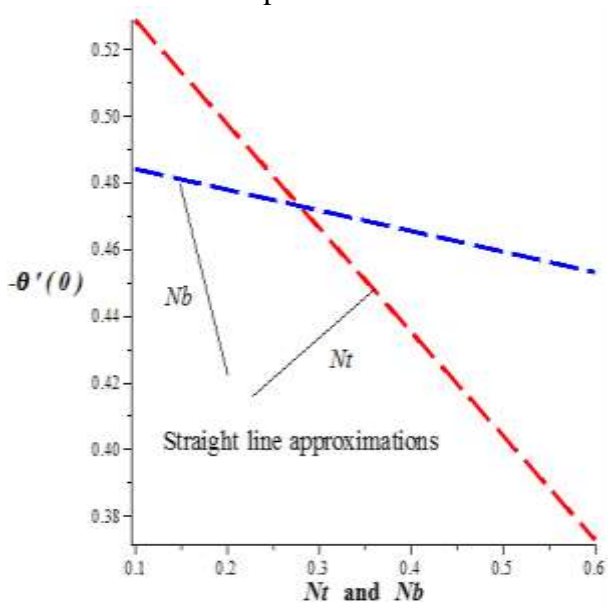


Fig. 5.27 Impact of both thermophoresis and Brownian motion parameter on heat transfer rate.

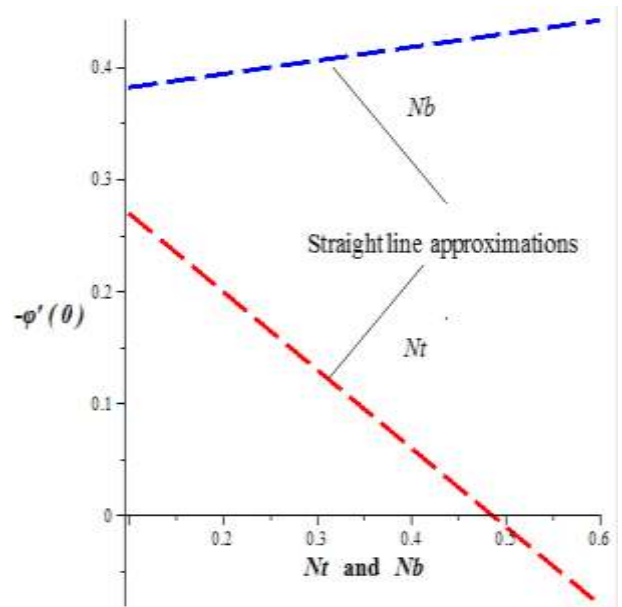


Fig. 5.28 Influence of both thermophoresis and Brownian motion parameter on mass transfer rate.

5.9 Straight line curve fitting analysis

The influence of both thermophoresis and Brownian motion parameters on heat and mass transfer rates are evaluated in this section by means of straight line curve fitting approximation. The least square method proposed by Gauss and Legendre is utilized. The normal equations for quadratic approximations can be written as:

$$na_1 + a_2 \sum X_i = \sum Y_i, \quad (5.28)$$

$$a_1 \sum X_i + a_2 \sum X_i^2 = \sum X_i Y_i.$$

To trace out straight line approximation for heat transfer rate towards thermophoresis and Brownian motion parameters i-e Nt and Nb . Let $X_i = (Nt)_i$ and $Y_i = (-\theta'(0))_i$ we get,

$$\begin{aligned} \sum (Nt)_i &= 0.3, \quad \sum (Nt)_i^2 = 0.05, \\ \sum (-\theta'(0))_i &= 1.0536, \quad \sum (Nt)_i (-\theta'(0))_i = 0.1761, \end{aligned}$$

by incorporating these values in Eq. (5.28) for straight line, we have

$$\begin{aligned} 2a_1 + 0.3a_2 &= 1.0311, \\ 0.3a_1 + 0.05a_2 &= 0.1531, \end{aligned} \quad (5.29)$$

by solving system of equations given by (5.29), we get

$$-\theta'(0) = a_1 + a_2 Nt \quad (5.30)$$

here, $a_1 = 0.56249$, and $a_2 = -0.31299$ Similarly, line curve fitting for heat transfer rate for Brownian motion parameter is entertained as follows

$$\begin{aligned} \sum (Nb)_i &= 0.4, \quad \sum (Nb)_i^2 = 0.10, \\ \sum (-\theta'(0))_i &= 0.9996, \quad \sum (Nb)_i (-\theta'(0))_i = 0.19746, \\ 2a_3 + 0.4a_4 &= 0.9996, \\ 0.4a_3 + 0.1a_4 &= 0.19746, \end{aligned} \quad (5.31)$$

then the straight line approximations towards Brownian motion parameter is given by:

$$-\theta'(0) = P(Nb) = a_3 + a_4 Nb, \quad (5.32)$$

where, $a_3 = 0.4998$ and $a_4 = -0.00062$.

Straight line curve fitting approximations for mass transfer rate towards thermophoresis and Brownian motion parameters are processed as follows:

$$\begin{aligned}\sum (Nt)_i &= 0.3, \sum (Nt)_i^2 = 0.05, \\ \sum (-\phi'(0))_i &= 0.4861, \sum (Nt)_i(-\phi'(0))_i = 0.0694, \\ 2a_5 + 0.3a_6 &= 0.4861, \\ 0.3a_5 + 0.05a_6 &= 0.0694,\end{aligned}\tag{5.33}$$

after solving this system we obtained

$$-\phi'(0) = a_5 + a_6 Nt\tag{5.34}$$

here, $a_5 = 0.3485$ and $a_6 = -0.70299$.

In similar fashion, straight line for mass transfer rate towards Brownian motion parameter are evaluated as follows;

$$\begin{aligned}\sum (Nb)_i &= 0.4, \sum (Nb)_i^2 = 0.10, \\ \sum (-\phi'(0))_i &= 0.7569, \sum (Nb)_i(-\phi'(0))_i = 0.1989, \\ 2a_7 + 0.4a_8 &= 0.7569, \\ 0.4a_7 + 0.1a_8 &= 0.1989,\end{aligned}\tag{5.35}$$

solution of this system corresponds

$$-\phi'(0) = P(Nb) = a_7 + a_8 Nb,\tag{5.36}$$

here, $a_7 = 0.37664$ and $a_8 = 0.012060$.

Table. 5.1. The variation skin friction coefficient number for K , Pr and M .

| K | Pr | M | $f''(0)$ | $\frac{1}{2}C_f Re_x^{\frac{1}{2}} = (1+M)f''(0) - \frac{M\lambda}{3}(f''(0))^3$ |
|-----|------|-----|----------|--|
| 0.2 | - | - | -0.4014 | -0.4413 |
| 0.4 | - | - | -0.4193 | -0.4616 |
| 0.6 | - | - | -0.4368 | -0.4802 |
| - | 1.2 | - | -0.4014 | -0.4413 |
| - | 1.4 | - | -0.4029 | -0.4429 |
| - | 1.6 | - | -0.4044 | -0.4445 |
| - | - | 0.2 | -0.4014 | -0.4413 |
| - | - | 0.4 | -0.3839 | -0.4603 |
| - | - | 0.6 | -0.3549 | -0.4609 |

Table. 5.2. The variation skin friction coefficient number for λ, m_1 and m_2 .

| λ | m_1 | m_2 | $f''(0)$ | $\frac{1}{2}C_f Re_x^{\frac{1}{2}} = (1+M)f''(0) - \frac{M\lambda}{3}(f''(0))^3$ |
|-----------|-------|-------|----------|--|
| 0.2 | - | - | -0.6176 | -0.6786 |
| 0.4 | - | - | -0.6170 | -0.6779 |
| 0.6 | - | - | -0.6163 | -0.6771 |
| - | 0.2 | - | -0.6163 | -0.6771 |
| - | 0.4 | - | -0.6186 | -0.6797 |
| - | 0.6 | - | -0.6208 | -0.6821 |
| - | - | 0.2 | -0.6163 | -0.6771 |
| - | - | 0.4 | -0.6196 | -0.6808 |
| - | - | 0.6 | -0.6214 | -0.6827 |

Table. 5.3. The variation Nusselt number for K, Pr and m_1 .

| K | Pr | m_1 | $-\theta'(0)$ | $\frac{Nu}{\sqrt{Re_x}} = -(1 + \frac{4}{3})\theta'(0)$ |
|-----|------|-------|---------------|---|
| 0.2 | - | - | 0.5029 | 0.5699 |
| 0.4 | - | - | 0.6268 | 0.7104 |
| 0.6 | - | - | 0.7312 | 0.8287 |
| - | 0.2 | - | 0.5029 | 0.5699 |
| - | 0.4 | - | 0.5667 | 0.5716 |
| - | 0.6 | - | 0.6252 | 0.5733 |
| - | - | 0.2 | 0.5029 | 0.5699 |
| - | - | 0.4 | 0.4934 | 0.5672 |
| - | - | 0.6 | 0.4831 | 0.5645 |

Table. 5.4. The variation Sherwood number for K, m_2, Le and Pr .

| K | m_2 | Le | Pr | $\frac{Sh}{\sqrt{Re_x}} = -\phi'(0)$ |
|-----|-------|------|------|--------------------------------------|
| 0.2 | - | - | - | 0.5295 |
| 0.4 | - | - | - | 0.6228 |
| 0.6 | - | - | - | 0.7075 |
| - | 1.2 | - | - | 0.6665 |
| - | 1.4 | - | - | 0.5980 |
| - | 1.6 | - | - | 0.5295 |
| - | - | 0.2 | - | 0.5295 |
| - | - | 0.4 | - | 0.5538 |
| - | - | 0.6 | - | 0.5781 |
| - | - | - | 1.2 | 0.5295 |
| - | - | - | 1.4 | 0.5340 |
| - | - | - | 1.6 | 0.5385 |

Table 5.5 Skin friction coefficient comparison for various values of magnetic field parameter γ .

| γ | Fathizadeh et al. [131] | Akbar et al. [20] | Present outcomes |
|----------|-------------------------|-------------------|------------------|
| 0.0 | -1 | -1 | -1 |
| 0.5 | - | -1.11803 | -1.1180 |
| 1.0 | -1.41421 | -1.41421 | -1.4142 |
| 5.0 | -2.44948 | -2.44949 | -2.4494 |
| 10 | -3.31662 | -3.31663 | -3.3166 |

Table 5.6 Comparison of heat transfer rate for various value of Prandtl number Pr .

| Pr | Ishak and Nazar [132] | Grubka and Bobba [133] | Present outcomes |
|------|-----------------------|------------------------|------------------|
| 0.72 | 0.8086313 | 0.8086 | 0.8089 |
| 1.00 | 1.0000000 | 1.000 | 1.0000 |
| 3.00 | 1.9236825 | 1.9237 | 1.9239 |
| 10.0 | 3.7206739 | 3.7207 | 3.7208 |

5.10 Conclusions

In this attempt a simultaneous way of study is executed to envision the characteristics of magneto-nano stagnation point Eyring-Powell fluid flow yields by inclined stretching surfaces (i-e flat and cylindrical surfaces). The flow analysis is encountered with pertinent physical effects namely, dual convection, chemical reactive species, heat generation, temperature stratification, and nanoparticle concentration stratification. The physical situation within the real concerned constraints is translated into of boundary value problem. To be more specific, a computational algorithm (shooting method charted with Runge-Kutta scheme) is successfully applied to obtain numerical results both for flat and cylindrical surfaces. The concluding key points of present analysis are itemized as follows:

- The compatibility of boundary conditions subject to stagnation point flow is validated through stream lines pattern (see Figs. 5.2-5.6) for concerned values of

velocities ratio parameter. Further, the obtained results are compared with existing values which yield the surety of present work.

- It is noticed that the impacts of physical parameters are significantly enriched for cylindrical surface as compared to flat surface.
- The mutual influence of both thermophoresis and Brownian motion parameters on heat and mass transfer rate is deliberated via straight line curve fitting approach for cylindrical surface and it seems to be first step in this direction.
- It is found that heat transfer normal to the cylindrical surface shows decline nature towards both thermophoresis and Brownian motion parameters while mass transfer rate shows an inciting attitude for Brownian motion parameter but inverse relation is observed for thermophoresis parameter.
- It is noticed that the velocity distributions show inciting attribute towards both mixed convection parameter, Eyring Powell fluid parameter (M) and velocities ratio parameter while opposite trends is found in the case of Eyring Powell fluid parameter (λ) and magnetic field parameter.
- The fluid temperature reflects an increasing behaviour for thermal radiation, heat generation, curvature, thermophoresis, Brownian motion parameters and inclination but opposite attribute is noticed for thermal stratification parameter, Lewis and Prandtl numbers.
- The nanoparticle concentration distribution enhances for thermophoresis parameter while opposite nature is observed for solutal stratification, chemical reaction, Brownian motion parameters and Lewis number.

CHAPTER 6

Thermophysical Aspects of Stagnation Point Magneto-Nanofluid Flow Yields by an Inclined Stretching Cylindrical surface: A Non-Newtonian Fluid Model

6.1 Introduction

In this chapter, we have considered magneto-hydrodynamic Eyring-Powell nanofluid flow brought by an included stretching cylindrical surface under the region of stagnation point. To report thermophysical aspects, Joule heating, thermal radiations, mixed convection, temperature stratification and heat generation effects are considered. The flow conducting differential equation is fairly converted into a non-linear ordinary differential equation by means of appropriate transformation. A numerical scheme is made against the obtained equations through shooting method supported with fifth order Runge-Kutta scheme. The trend of fluid temperature after varying Eckert number, thermophoresis parameter, Brownian motion parameter, thermal radiation parameter, heat generation parameter, Lewis number and thermal stratification parameter will be observed. Further, the obtained results are validated by providing comparison with existing values which sets a benchmark of quality of computational algorithm.

6.2 Flow field formulation

An incompressible magnetohydrodynamic boundary layer flow of Eyring- Powell nanofluid is considered under the region of stagnation point. The fluid flow is brought by an inclined cylindrical surface due to no slip condition. To inspect thermophysical properties imperative effects namely, Joule heating, thermal radiations, mixed convection, temperature stratification and heat generation are incorporated. In addition, concentration equation admits the role of chemical reaction and solutal stratification. The strength of both temperature and concentration near the cylindrical surface are assumed to be higher than

the ambient fluid values. The radial direction is considered perpendicular to x -axis and taken as r -axis. The axial line of cylinder is aligned parallel to x -axis.

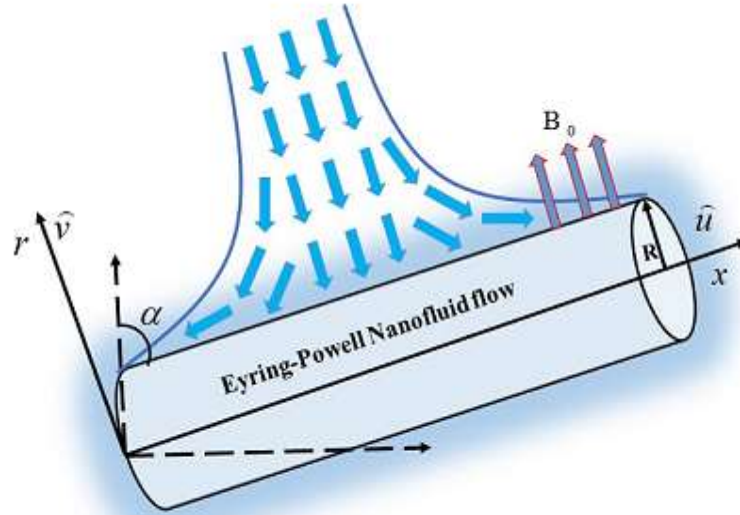


Fig. 6.1. Physical illustration of flow model.

The simplified momentum differential equation (in the absence of magnetic field and stagnation point we have basic equations [30]) are:

$$\frac{\partial(r\hat{u})}{\partial x} + \frac{\partial(r\hat{v})}{\partial r} = 0, \quad (6.1)$$

$$\begin{aligned} \frac{\partial\hat{u}}{\partial r}\hat{v} + \frac{\partial\hat{u}}{\partial x}\hat{u} &= \frac{\partial^2\hat{u}}{\partial r^2}\left(\frac{1}{\beta\rho c} + \nu\right) - \frac{\partial^2\hat{u}}{\partial r^2}\left(\frac{\partial\hat{u}}{\partial r}\right)^2 \frac{1}{2\beta c^3\rho} \\ &+ \frac{1}{r}\left(\frac{1}{\beta\rho c} + \nu\right)\frac{\partial\hat{u}}{\partial r} - \frac{1}{6\beta r\rho c^3}\left(\frac{\partial\hat{u}}{\partial r}\right)^3 + \hat{u}_e\frac{\partial\hat{u}_e}{\partial x} - \frac{\sigma B_0^2}{\rho}(\hat{u} - \hat{u}_e) \\ &+ g(\beta_T(\hat{T} - \hat{T}_\infty) + \beta_c(\hat{C} - \hat{C}_\infty))\cos\alpha, \end{aligned} \quad (6.2)$$

the corresponding boundary conditions are:

$$\hat{u} = U(x) = ax, \hat{v} = 0, \text{ at } r = R, \hat{u} \rightarrow \hat{u}_e = a'x, \text{ when } r \rightarrow \infty, \quad (6.3)$$

where, $\nu, \rho, \beta, c, \hat{u}_e, \sigma, Ec, B_0, g, \beta_T, \beta_c$, and α , denotes kinematic viscosity, fluid density, Eyring-Powell fluid parameters, free stream velocity, electrical conductivity, Eckert number, uniform magnetic field, gravity, thermal expansion coefficient, concentration expansion coefficient, and an inclination respectively. For solution we own:

$$\eta = \frac{r^2 - R^2}{2R} \left(\frac{U_0}{\nu L} \right)^{\frac{1}{2}}, \quad \psi = \left(\frac{U_0 \nu x^2}{L} \right)^{\frac{1}{2}} R F(\eta), \quad (6.4)$$

$$\hat{u} = \frac{U_0 x}{L} F'(\eta), \quad \hat{v} = -\frac{R}{r} \sqrt{\frac{U_0 \nu}{L}} F(\eta),$$

here, U_0 , R , $F(\eta)$, $F'(\eta)$, and ψ denotes reference velocity, radius of cylinder, dimensionless variable, velocity of fluid past a stretching cylinder and stream function, respectively. The relations via stream function are:

$$\hat{u} = \frac{\psi_r}{r}, \quad \hat{v} = \frac{-\psi_x}{r}, \quad (6.5)$$

by incorporating transformation given by Eq. (6.4) into Eq. (6.2), the resulting reduced differential equation is given as:

$$3(1+2K\eta)(1+M)F''' + 3FF'' + 6K(1+M)F'' - 3(F')^2 - 4\lambda MK(1+2K\eta)(F'')^3 - 3M\lambda(1+2K\eta)^2 F'''(F'')^2 - 3\gamma^2(F' - A) + 3A^2 + 3\lambda_m(T(\eta) + NC(\eta))\cos\alpha = 0, \quad (6.6)$$

$$F'(\eta) = 1, F(\eta) = 0, \quad \text{at } \eta = 0, \quad (6.7)$$

$$F'(\eta) \rightarrow A, \quad \text{when } \eta \rightarrow \infty,$$

here,:

$$K = \frac{1}{R} \sqrt{\frac{\nu}{a}}, \quad a = \frac{U_0}{L}, \quad M = \frac{1}{\mu\beta c}, \quad \lambda = \frac{a^3 x^2}{2c^2 \nu}, \quad \gamma = \sqrt{\frac{\sigma\beta_0^2}{\rho a}}, \quad A = \frac{a'}{a}, \quad (6.8)$$

$$\lambda_m = \frac{Gr}{Re_x^2}, \quad \text{and } N = \frac{Gr^*}{Gr},$$

and:

$$Gr = \frac{(\hat{T}_w - \hat{T}_0)g\beta_T x^3}{\nu^2}, \quad Gr^* = \frac{(\hat{C}_w - \hat{C}_0)g\beta_C x^3}{\nu^2}. \quad (6.9)$$

The skin friction coefficient at the surface of cylinder is defined as:

$$C_f = \frac{\tau_w}{\rho \frac{U_0^2}{2}}, \quad \tau_w = \left[\mu \left(\frac{\partial \hat{u}}{\partial r} \right) + \frac{1}{\beta c} \frac{\partial \hat{u}}{\partial r} - \frac{1}{6\beta c^3} \left(\frac{\partial \hat{u}}{\partial r} \right)^3 \right]_{r=R}, \quad (6.10)$$

here, μ and τ_w denotes fluid viscosity and shear stress respectively. In non-dimensional form the skin friction coefficient is prearranged as:

$$\text{Re}_x^{1/2} C_f = 2F''(0)(M+1) - (F''(0))^3 \frac{2\lambda M}{3}. \quad (6.11)$$

6.3 Temperature and nanoconcentration formulation

The flow field is manifested with Joule heating, temperature stratification, concentration stratification, thermal radiation, heat generation and chemical reaction effects. The strength of both temperature and concentration is supposed to be greater as compared to ambient temperature and concentration respectively. Both the energy and concentration equations (in the absence of Joule heating, heat generation and chemical reaction we consider fundamental equations [29]) under boundary layer assumption reduces to:

$$\begin{aligned} \hat{u} \frac{\partial \hat{T}}{\partial x} + \hat{v} \frac{\partial \hat{T}}{\partial r} = \frac{\alpha^*}{r} \frac{\partial}{\partial r} \left(r \frac{\partial \hat{T}}{\partial r} \right) - \frac{1}{\rho c_p r} \frac{\partial}{\partial r} (r q_r) + \tau \left(D_B \frac{\partial \hat{T}}{\partial r} \frac{\partial \hat{C}}{\partial r} + \frac{D_T}{T_\infty} \left(\frac{\partial \hat{T}}{\partial r} \right)^2 \right) \\ + \frac{\sigma B_0^2 \hat{u}^2}{\rho c_p} + \frac{Q_0}{c_p \rho} (\hat{T} - \hat{T}_\infty), \end{aligned} \quad (6.12)$$

$$\hat{u} \frac{\partial \hat{C}}{\partial x} + \hat{v} \frac{\partial \hat{C}}{\partial r} = D_B \left(\frac{\partial^2 \hat{C}}{\partial r^2} + \frac{1}{r} \frac{\partial \hat{C}}{\partial r} \right) + \frac{D_T}{T_\infty} \left(\frac{\partial^2 \hat{T}}{\partial r^2} + \frac{1}{r} \frac{\partial \hat{T}}{\partial r} \right) - R_o (\hat{C} - \hat{C}_\infty), \quad (6.13)$$

here, $q_r = -\left(\frac{4}{3}\right) \frac{\sigma^*}{k^*} \frac{\partial \hat{T}^4}{\partial r}$ represents Roseland radiative heat flux, therefore Eq. (6.12) can

be written as:

$$\begin{aligned} \hat{u} \frac{\partial \hat{T}}{\partial x} + \hat{v} \frac{\partial \hat{T}}{\partial r} = \frac{\alpha}{r} \frac{\partial}{\partial r} \left(r \frac{\partial \hat{T}}{\partial r} \right) + \frac{1}{\rho c_p r} \left(\frac{4}{3} \right) \frac{\sigma^*}{k^*} \frac{\partial}{\partial r} \left(r \frac{\partial \hat{T}^4}{\partial r} \right) + \tau \left(D_B \frac{\partial \hat{T}}{\partial r} \frac{\partial \hat{C}}{\partial r} + \frac{D_T}{T_\infty} \left(\frac{\partial \hat{T}}{\partial r} \right)^2 \right) \\ + \frac{\sigma B_0^2 \hat{u}^2}{c_p \rho} + \frac{Q_0}{c_p \rho} (\hat{T} - \hat{T}_\infty), \end{aligned} \quad (6.14)$$

subject to the endpoint conditions:

$$\begin{aligned} \hat{C}(x, r) = \hat{C}_w(x) = \hat{C}_0 + \frac{d x}{L}, \quad \hat{T}(x, r) = \hat{T}_w(x) = \hat{T}_0 + \frac{b x}{L}, \quad \text{at } r = R, \\ \hat{T}(x, r) \rightarrow \hat{T}_\infty(x) = \hat{T}_0 + \frac{c x}{L}, \quad \hat{C}(x, r) \rightarrow \hat{C}_\infty(x) = \hat{C}_0 + \frac{e x}{L} \quad \text{as } r \rightarrow \infty, \end{aligned} \quad (6.15)$$

where, $\alpha^*, c_p, D_B, D_T, \hat{T}, \hat{T}_\infty, Q_0, \hat{C}, \hat{C}_\infty$, and R_o stands for thermal diffusivity, specific heat capacity at constant pressure, Brownian diffusion coefficient, thermophoretic diffusion coefficient, fluid temperature, ambient temperature, heat generation/absorption coefficient, fluid concentration, ambient concentration and rate of chemical reaction respectively.

Further, $\tau = \frac{(\rho c)_p}{(\rho c)_f}$, $T_w(x)$, $C_w(x)$, L , b , c , d , and e represents the ratio of nanoparticles

heat capacity to the base fluid heat capacity, prescribed surface temperature, prescribed surface concentration, reference length and dimensionless constants respectively. To find out the solution of Eqs. (6.13)-(6.14) under endpoint conditions Eq. (6.15), we have considered following transformations:

$$\begin{aligned} \hat{u} &= \frac{U_0 x}{L} F'(\eta), \quad \hat{v} = -\frac{R}{r} \sqrt{\frac{U_0 \nu}{L}} F(\eta), \quad \eta = \frac{r^2 - R^2}{2R} \left(\frac{U_0}{\nu L} \right)^{\frac{1}{2}}, \\ \psi &= \left(\frac{U_0 \nu x^2}{L} \right)^{\frac{1}{2}} R F(\eta), \quad T(\eta) = \frac{\hat{T} - \hat{T}_\infty}{\hat{T}_w - \hat{T}_0}, \quad C(\eta) = \frac{\hat{C} - \hat{C}_\infty}{\hat{C}_w - \hat{C}_0}, \end{aligned} \quad (6.16)$$

here, \hat{T}_0 , \hat{C}_0 , and ψ denotes reference temperature, reference concentration and stream function respectively. By incorporating transformation given by Eq. (6.16) into Eqs. (6.13)-(6.14), the resulting reduced differential equations are given as:

$$\begin{aligned} (1+2K\eta) \left(1 + \frac{4}{3} R_p \right) T''(\eta) + 2K \left(1 + \frac{4}{3} R_p \right) T'(\eta) \\ + \text{Pr} Nb (1+2K\eta) \left(T' C' + \frac{Nt}{Nb} T'^2 \right) + \text{Pr} \begin{pmatrix} F(\eta) T'(\eta) - F'(\eta) T(\eta) \\ -F'(\eta) \alpha_1 + QT(\eta) \\ +Ec\gamma^2 F^2(\eta) \end{pmatrix} = 0, \\ (1+2K\eta) \left(C''(\eta) + \frac{Nt}{Nb} T''(\eta) \right) + \text{Pr} Le (F(\eta) C'(\eta) - F'(\eta) C(\eta) - F'(\eta) \alpha_2) \\ + 2K \left(C'(\eta) + \frac{Nt}{Nb} T'(\eta) \right) - Rc C(\eta) = 0, \end{aligned} \quad (6.17)$$

the transformed endpoint conditions are given as:

$$T(\eta) = 1 - \alpha_1, \quad C(\eta) = 1 - \alpha_2, \quad \text{at } \eta = 0, \quad (6.19)$$

$$T(\eta) \rightarrow 0, \quad C(\eta) \rightarrow 0, \quad \text{when } \eta \rightarrow \infty.$$

here, R_p , Pr , Nb , Nt , α_1 , Q , Le , α_2 , Ec and Rc denotes, thermal radiation parameter, Prandtl number, Brownian motion parameter, thermophoresis parameter, thermal stratification parameter, heat generation parameter, Lewis number, solutal stratification parameter, Eckert number and chemical reaction parameter, respectively and are defined as

follows:

$$R_p = \frac{4\sigma^* T_\infty^3}{k^* k}, \text{Pr} = \frac{\nu}{\alpha^*}, Nb = \frac{\tau D_B (\widehat{C}_w - \widehat{C}_\infty)}{\nu}, Nt = \frac{\tau D_T (\widehat{T}_w - \widehat{T}_\infty)}{\nu T_\infty}, \quad (6.20)$$

$$\alpha_1 = \frac{c}{b}, Q = \frac{LQ_0}{U_0 \rho c_p}, Le = \frac{\alpha^*}{D_B}, \alpha_2 = \frac{e}{d}, Rc = \frac{R_o L}{U_o}, Ec = \frac{u_0 x}{cp(T_w - T_0)}$$

The surface quantities are defined as:

$$Nu_x = \frac{xq_w}{(\widehat{T}_w - \widehat{T}_0)k}, q_w = -\left(\frac{\partial \widehat{T}}{\partial r}\right)_{r=R} k + (q_r)_{r=R}, \quad (6.21)$$

$$Sh = \frac{xj_w}{D(\widehat{C}_w - \widehat{C}_0)}, j_w = -D\left(\frac{\partial \widehat{C}}{\partial r}\right)_{r=R},$$

the non-dimensional form of these expressions are well-defined and given as:

$$Nu_x Re_x^{-1/2} = -\left(1 + \frac{4}{3} R_p\right) T'(\eta), \text{ at } \eta \rightarrow 0, \quad (6.22)$$

$$Sh Re_x^{-1/2} = -C'(\eta), \text{ at } \eta \rightarrow 0.$$

6.4 Computational algorithm

For order reduction we entertain

$$p_2 = F'(\eta), p_3 = p'_2 = F''(\eta), p_5 = T'(\eta), p_7 = C'(\eta), \quad (6.23)$$

equivalently:

$$p'_1 = p_2, \quad (6.24)$$

$$p'_2 = p_3,$$

$$p'_3 = \frac{\left\{ (p_2)^2 - p_1 p_3 - (2K)(1+M)p_3 + \frac{4}{3} \lambda MK(1+2K\eta)p_3^3 \right.}{\left. + \gamma^2(p_2 - A) - A^2 - \lambda_m(p_4 + Np_6) \cos \alpha \right.},$$

$$\frac{(M+1)(2K\eta+1) - M\lambda(2K\eta+1)^2 p_3^2}{},$$

$$p'_4 = p_5,$$

$$p'_5 = \frac{\left\{ \text{Pr}(p_2 p_4 + \alpha_1 p_2 - p_1 p_5 - Qp_4 - Ec\gamma^2 p_1^2) - 2K(1 + \frac{4}{3} R_p) p_5 \right.}{\left. - \text{Pr} Nb(1+2K\eta)(p_5 p_7 + \frac{Nt}{Nb} p_5^2) \right.},$$

$$\frac{(1+2K\eta)(1 + \frac{4}{3} R_p)}{}$$

$$p'_6 = p_7,$$

$$p'_7 = \frac{\text{Pr} Le(p_2 p_6 + \alpha_2 p_2 - p_1 p_7) - (1+2K\eta) \frac{Nt}{Nb} p'_5 - 2K(p_7 + \frac{Nt}{Nb} p_5) + Rcp_6^2}{2K\eta+1}.$$

and:

$$p_1(0) = 0, \quad (6.25)$$

$$p_2(0) = 1,$$

$$p_3(0) = \text{First guess value},$$

$$p_4(0) = 1 - \alpha_1,$$

$$p_5(0) = \text{Second guess value},$$

$$p_6(0) = 1 - \alpha_2,$$

$$p_7(0) = \text{Third guess value}.$$

For integration purpose of Eq. (6.24) as an initial value problem (IVP) we need

$$p_3(\eta) = F''(\eta), p_5(\eta) = T'(\eta) \text{ and } p_7(\eta) = T'(\eta) \text{ when } \eta \rightarrow 0. \quad (6.26)$$

Further, we observed that the three initial conditions namely, $p_3(\eta)$, $p_5(\eta)$ and $p_7(\eta)$ when $\eta \rightarrow 0$ are missing but some additional boundary conditions are:

$$p_2(\eta) = A, p_4(\eta) = 0, \text{ and } p_6(\eta) = 0, \text{ when } \eta \rightarrow 0 \quad (6.27)$$

The numerical computation up-to four decimal precision as convergence standards are achieved by maintaining $\Delta\eta = 0.025$ as a step size.

6.5 Results and discussion

Tables 6.1-6.4 are presented to depict the significance of admissible flow controlling parameters namely, Eckert number, Eyring-Powell fluid parameter, Prandtl number, curvature parameter, thermal stratification parameter, solutal stratification parameter, chemical reaction parameter and Lewis number on skin friction coefficient, local Nusselt and Sherwood numbers numerically. In detail, Tables 6.1-6.2 represents skin friction coefficient against various values of curvature parameter, Prandtl number, Eyring-Powell fluid parameter, magnetic field parameter, thermal stratification parameter and solutal stratification parameter. Physically, the numerical values of skin friction coefficient means the amount of drag force offered by cylindrical surface to fluid particles. It is observed that the drag force increases on increasing values of Eyring-Powell fluid parameter, curvature parameter, Prandtl number, thermal stratification parameter and solutal stratification parameter while opposite behaviour is noticed for magnetic field parameter. Tables 6.3-6.4 indicate the impacts of various physical parameters on Nusselt and Sherwood numbers. The numerical values of Nusselt number and Sherwood number corresponds to the transfer of heat and mass respectively from cylindrical surface to the fluid (normal to the surface). It is revealed that heat transfer rate shows remarkable increase for curvature parameter and Prandtl number but inverse attitude is observed for both thermal stratification parameter and Eckert number. As far as mass transfer at cylindrical surface is concerned it is found that mass transfer rate shows an inciting nature for positive values of curvature parameter, Schmidt number. The present findings are validated by developing comparison in a limiting sense towards skin friction coefficient. In detail, in the absence of both heat and mass transfer characteristics if $M = \lambda = A = K = \lambda_m = 0$ and $\alpha = 0^0$, the present case reduces to a problem given by Fathizedeh et al. [131] and if we incorporate $A = K = \lambda_m = 0$ and $\alpha = 0^0$, our problem matches with Akbar et al. [20]. An excellent agreement is found (see Table 6.5) with both studies which leads to justify the present work. Fig. 6.1 provides the physical illustration of flow model while Fig. 6.2 and Fig. 6.3 are plotted to examine the stream lines for $A < 1$, in other words when stretching velocity exceeds free stream velocity. Physically, the boundary layer thickness increases largely when stretching velocity is dominant as compared to free stream velocity. To be more

specific, Fig. 6.2 paints when $A=0$, which mean the free stream velocity is absolutely zero and from Fig. 6.2, it is seen that the disturbance of particles is only due to stretching velocity. Whereas, Fig. 6.3 is plotted for the value of $A=0.5$ and it means the involvement of free stream velocity is little significant as compare to $A=0$ but still is lesser then stretching velocity so that the particle disturbance is significant at cylindrical surface as compared to far away from surface. In Fig. 6.4 and Fig. 6.5 stream lines are switches accordingly to the velocities ratio parameter $A > 1$. In this case free stream velocity exceeds stretching velocity. The thickness of boundary layer decreases when A increases. In actual when A increases, we yield increase in free stream velocity for fixed values of stretching velocity, ultimately straining motion adjacent to the stagnation region brings inciting acceleration of free stream as a result thinning of boundary layer is observed. In Fig. 6.2- 6.5 greenish color shows how much the streamlines are close to each other for several values of velocities ratio parameter A . Fig. 6.6-6.9 illustrates that how velocity profile are affected by varying involved flow controlling parameters. To be more specific, Fig. 6.6 reveals that there is an inverse relationship between inclination and velocity profile because for large values of an inclination the velocity profile decreases. The reason behind is when we increase an inclination about x -axis the effect of gravity is lesser which causes decreasing in velocity profile within boundary layer. Fig. 6.7 classifies the effect of mixed convention parameter over velocity profile. It is seen that for larger values of mixed convention parameter the velocity profile increases with in a boundary layer. Physically, this is because of the large buoyancy force. Fig. 6.8 specifies that by an increasing magnetic field parameter the velocity profile decreases. The fact behind is that on increasing values of magnetic field parameter the resistive force known by Lorentz force starts actively participate and offer resistance to fluid particles and hence velocity decreases. Fig. 6.9 suggests that there exist direct relation between Eyring-Powell fluid parameter and velocity distribution i-e an increase in Eyring-Powell fluid parameter the velocity profile increase. Specifically, Eyring-Powell fluid parameter has inverse relation with viscosity of fluid. On increasing fluid parameter the fluid viscosity decreases and particles are free to move and hence average velocity of fluid increases. Fig. 6.10-6.19 are plotted to examine the influence of pertinent flow controlling parameters over temperature profile. In detail, Fig. 6.10 examines the impact of Eckert number on temperature profile. It

is seen that for high values of Eckert number the temperature distribution increases. Fig. 6.11 indicates that for large values of curvature parameter the temperature distribution shows an inciting nature. Kelvin temperature is proportional to average kinetic energy so, an increase in curvature parameter, velocity profile of the fluid increases which causes increase in kinetic energy and due to which temperature profile increases. Fig. 6.12 paints the impact of Prandtl number and as expected by increasing Prandtl number temperature profile decreases because for higher values of Prandtl number less will be the diffusion of energy. So, an increase in Prandtl number results a strong reduction in temperature profile of the fluid which causes thinner boundary layer. In Fig. 6.13, it is seen the fluid temperature decreases for the larger values of Lewis number while Fig. 6.14 illustrates the effect of heat generation parameter over temperature profile. It is identify that an increase in heat generation parameter results an increase in temperature profile. Here symbolic heat is produced during heat a generation phenomenon which causes increase in temperature profile. The impact of Brownian motion parameter on temperature profile is given by Fig. 6.15. It is seen that higher values of Brownian motion parameter brings an increase in fluid temperature profile within boundary layer. In actual, growth of Brownian motion increase in the random motion and collision among nanoparticles of the fluid which produces more heat and eventually temperature increases. Influence of thermophoresis parameter on temperature profile is depicted in Fig. 6.16. It is noticed that higher values of thermophoresis parameter corresponds an increase in temperature profile. Due to increasing values of thermophoresis parameter, more nanoparticles are pulled towards the cold surface from hot one which ultimately results an increase in temperature. Fig. 6.17 is used to explain the impact of thermal radiation parameter on temperature profile. For large values of thermal radiation parameter temperature profile increases. Actually, for higher values of thermal radiation parameter plenty of heat is transfer into fluid flow regime as a result temperature shows an inciting values. From Fig. 6.18, it is examined that the temperature profile decreases for an inciting values of thermal stratification parameter. Actually, this effect is due to drop of convective potential between surface of cylinder and ambient temperature. Fig. 6.19 identify that there is an inverse relation between inclination and temperature profile. For large values of inclination the temperature profile decreases. The fact is that for an inciting value of an inclination the gravity effects are actively

participated to reduce the movement of fluid particles and hence average kinetic energy decreases due to which fluid temperature drops. Figs. 6.20-6.24 are used to classify that how concentration profile are effected by Brownian motion parameter, solutal stratification parameter, thermophoresis parameter, Lewis number and chemical reaction parameter. In detail, the impact of Brownian motion parameter on nanoparticle concentration profile is depicted in Fig. 6.20. It is seen that gradual growth of Brownian motion parameter is the cause of decline in values of nanoparticle concentration distributions. Influence of thermophoresis parameter on concentration profile is depicted in Fig. 6.21. It is noticed that increasing values of thermophoresis parameter reflects an increase in concentration profile because increasing values of thermophoresis parameter corresponds lager amount of nanoparticles pulled from colder region to hotter one which brings enhancement in concentration profiles. The influence of Lewis number on nanoparticle concentration profile is given by Fig. 6.22. It is noticed that the upsurge in Lewis number yields a thin nanoparticle concentration boundary layer with frail molecular diffusivity. Fig. 6.23 indicates the relation between concentration profile for different values of chemical reaction parameter. Decline in nanoparticles concentration and its allied boundary layer thickness is noticed because of large disturbance in fluid molecules. Fig. 6.24 signals that an increase in solutal stratification parameter the concentration distribution decreases. For higher values of solutal stratification parameter we have drop of potential difference between surface conditions and ambient concentration which yields decline in values of concentration distributions.

6.6 Graphical outcomes

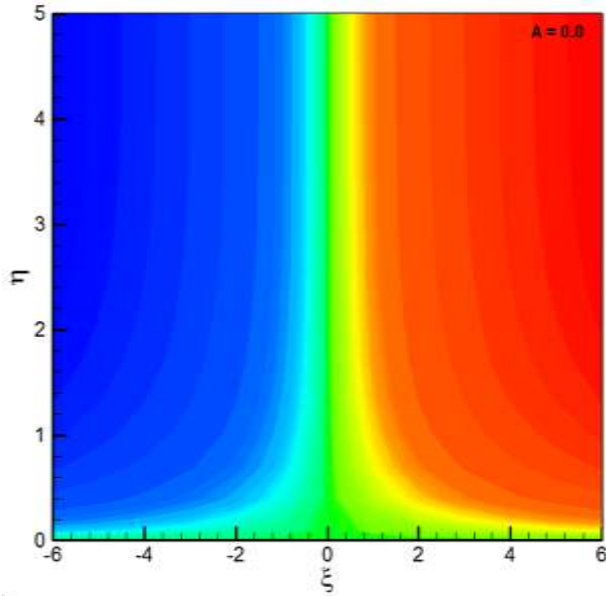


Fig. 6.2. Stream lines pattern for $A = 0.0$.

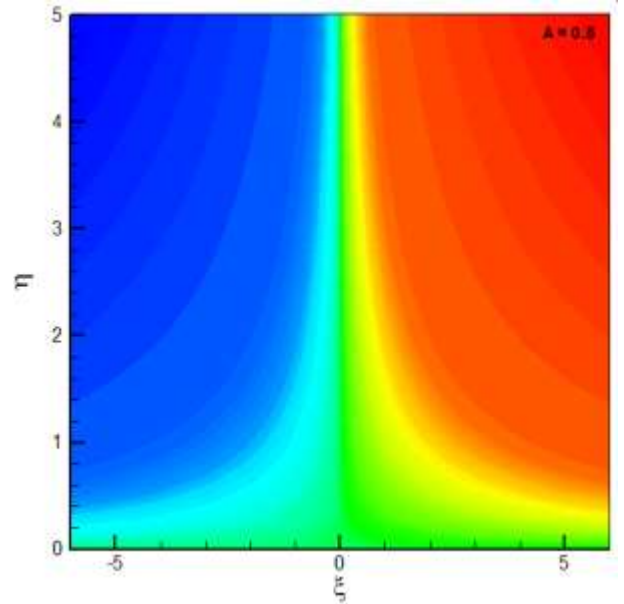


Fig. 6.3. Stream lines pattern for $A = 0.5$.

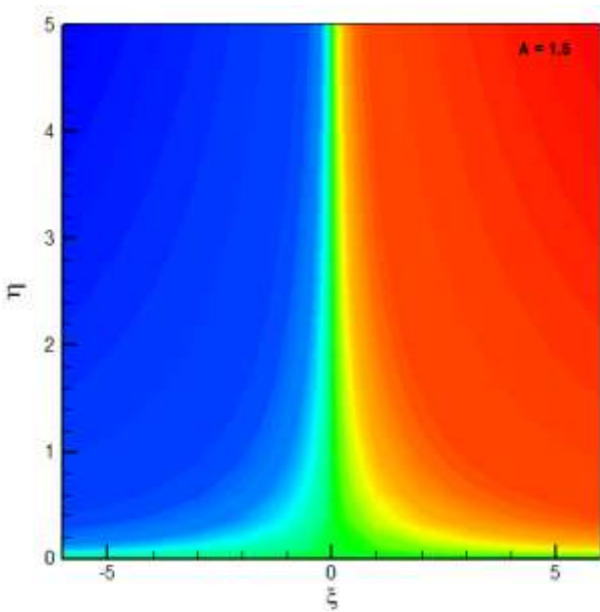


Fig. 6.4. Stream lines pattern for $A = 1.5$.

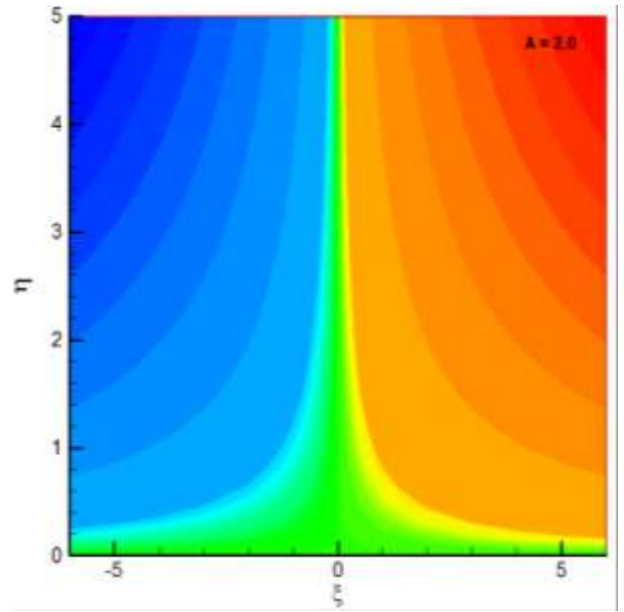


Fig. 6.5. Stream lines pattern for $A = 2.0$.

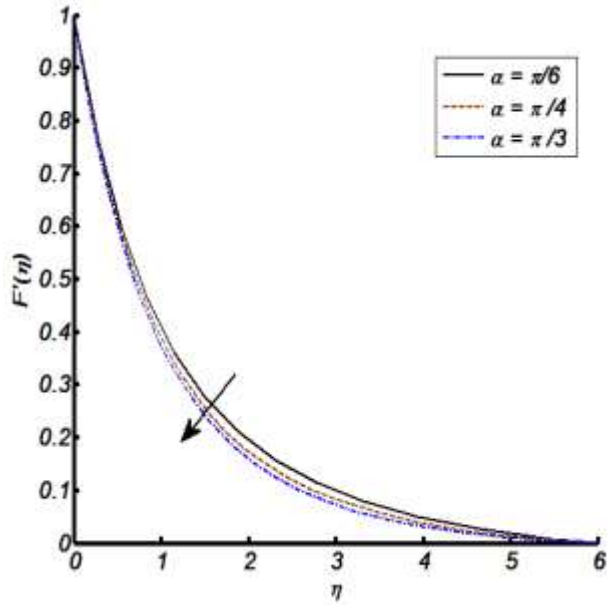


Fig. 6.6. Effect of an inclination over velocity profile.

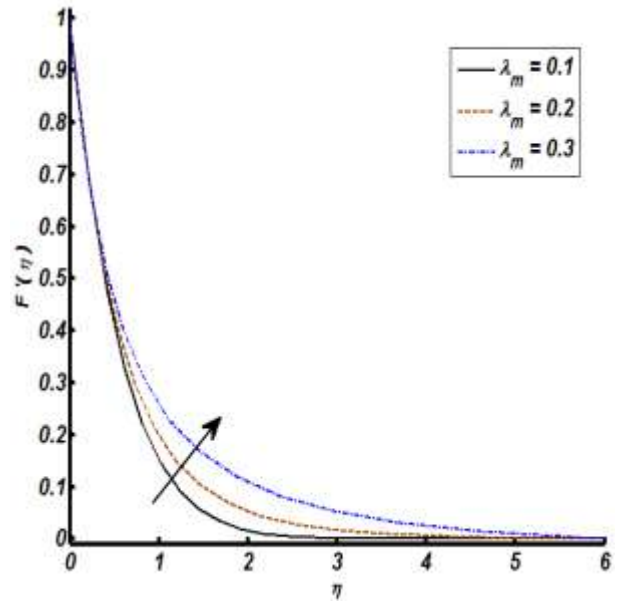


Fig. 6.7. Effect of mixed convection parameter over velocity profile.

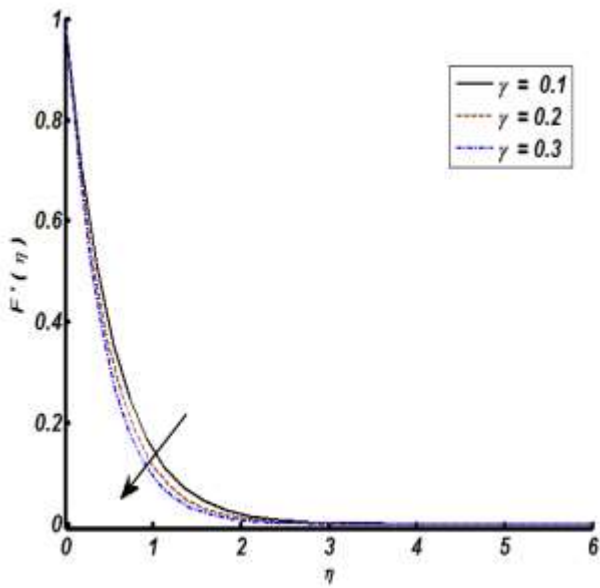


Fig. 6.8. Effect of magnetic field parameter over velocity profile.

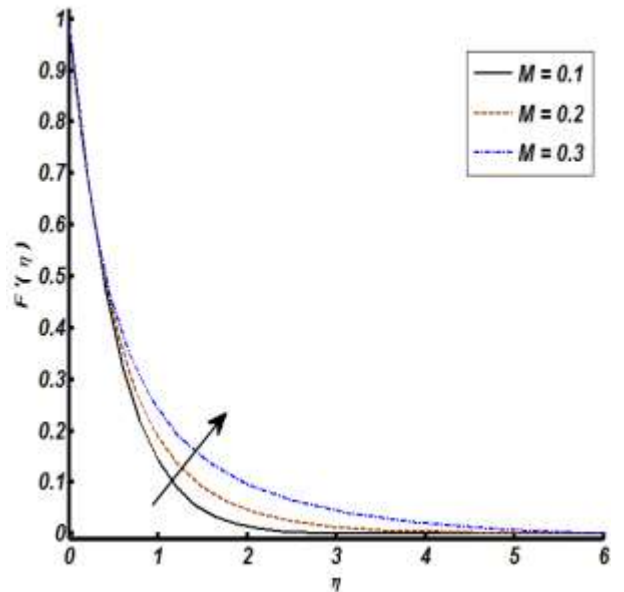


Fig. 6.9. Influence of fluid parameter over velocity profile.

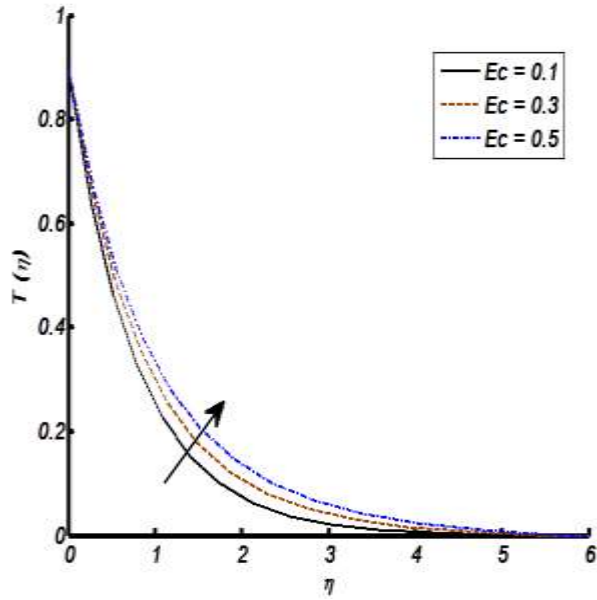


Fig. 6.10. Influence of Eckert number over temperature profile.

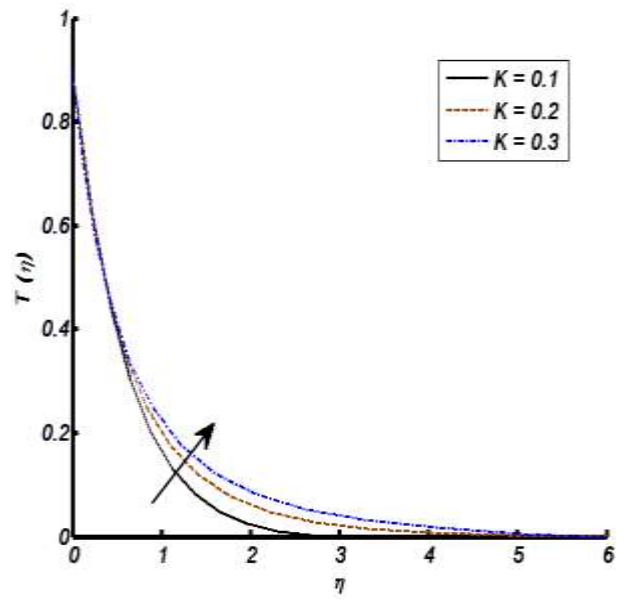


Fig. 6.11. Influence of curvature parameter over temperature profile.

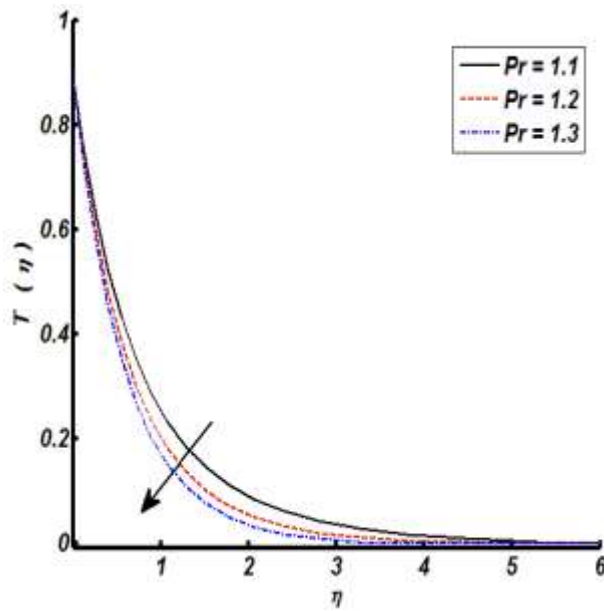


Fig. 6.12. Influence of Prandtl number over temperature profile.

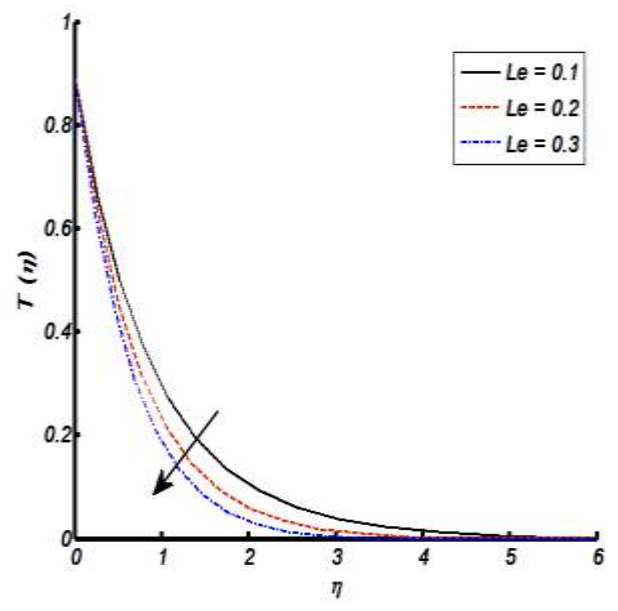


Fig. 6.13. Influence of Lewis number over temperature profile.

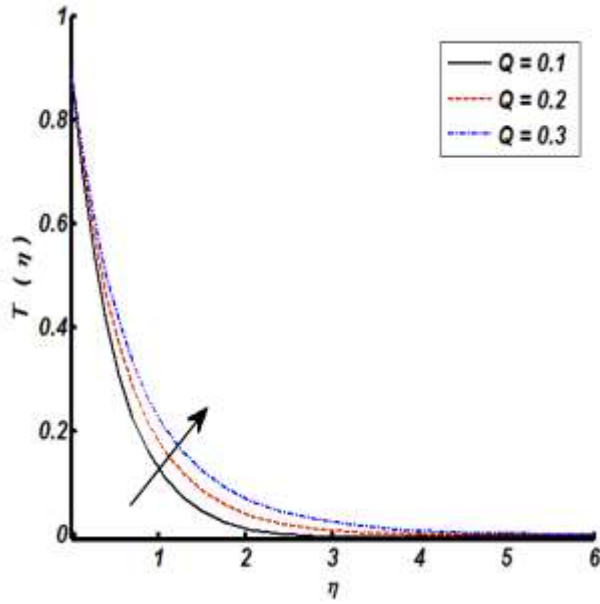


Fig. 6.14. Influence of heat generation parameter over temperature profile.

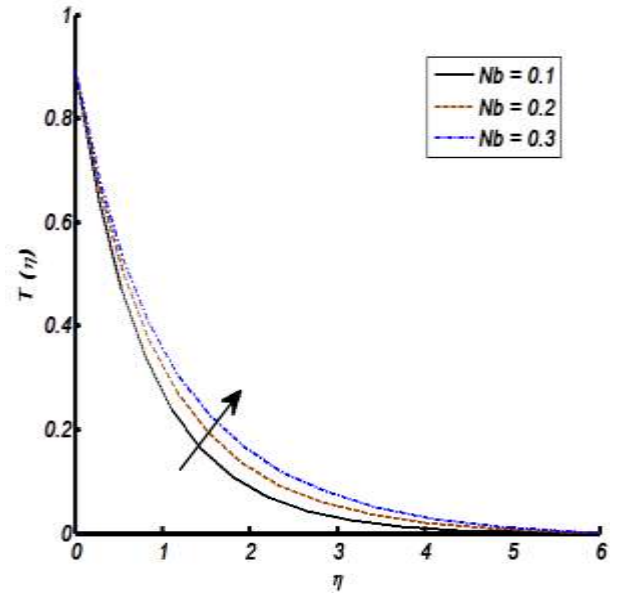


Fig. 6.15. Influence of Brownian motion parameter over temperature profile.

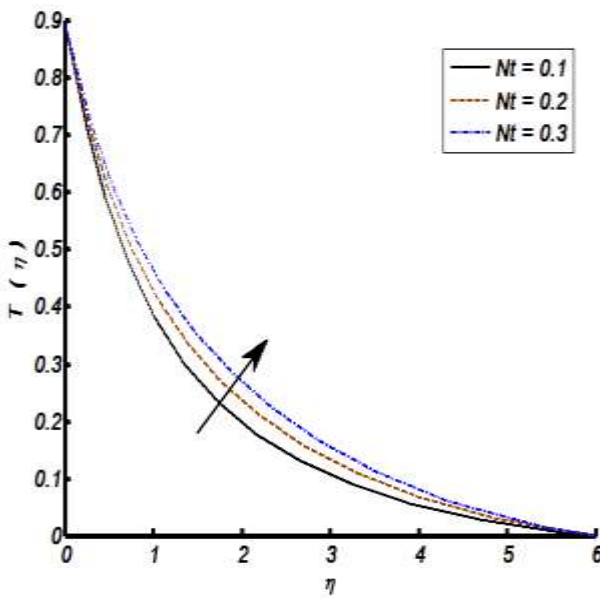


Fig. 6.16. Influence of thermophoresis parameter over temperature profile.

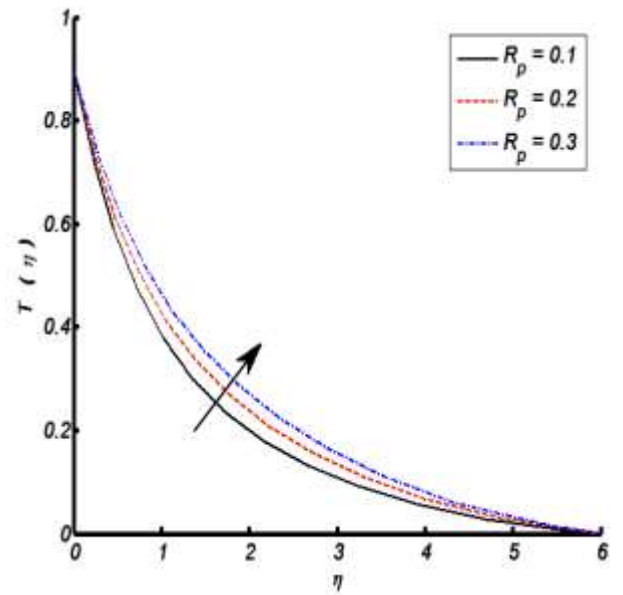


Fig. 6.17. Influence of thermal radiation parameter over temperature profile.

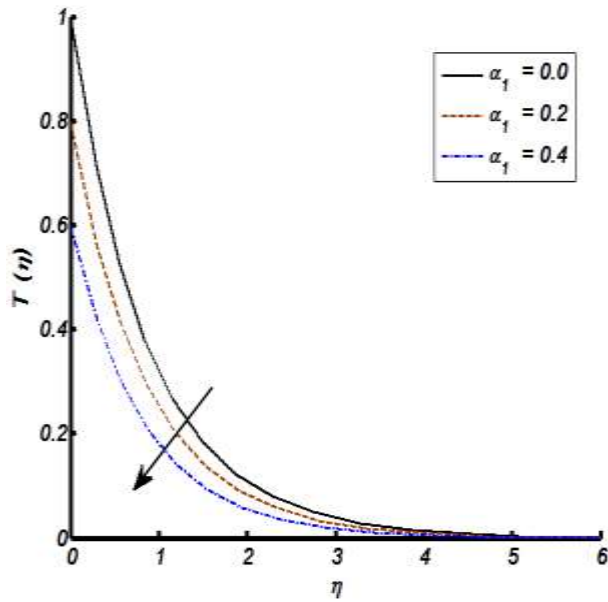


Fig. 6.18. Influence of thermal stratification parameter over temperature profile.

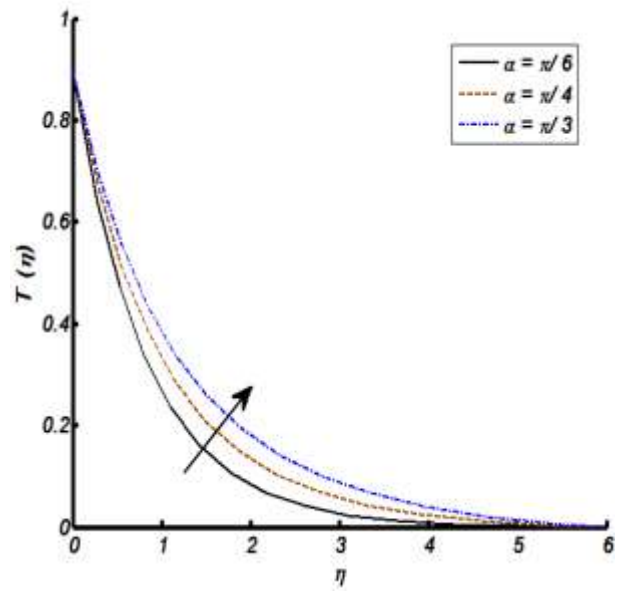


Fig. 6.19. Influence of an inclination over temperature profile.

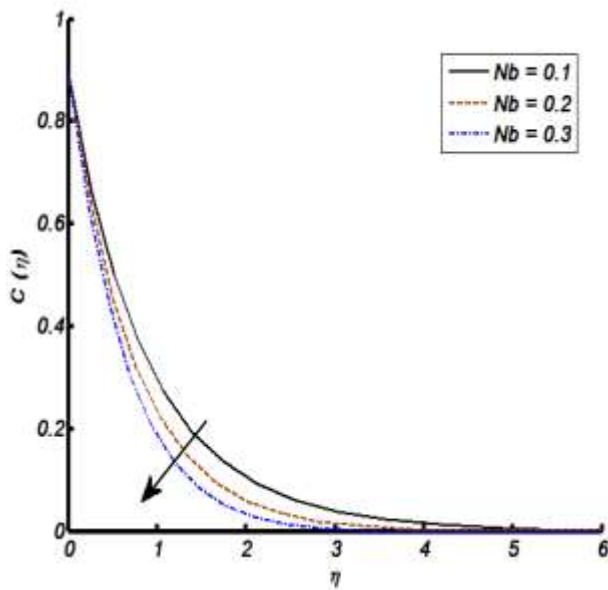


Fig. 6.20. Influence of Brownian motion parameter over concentration profile.

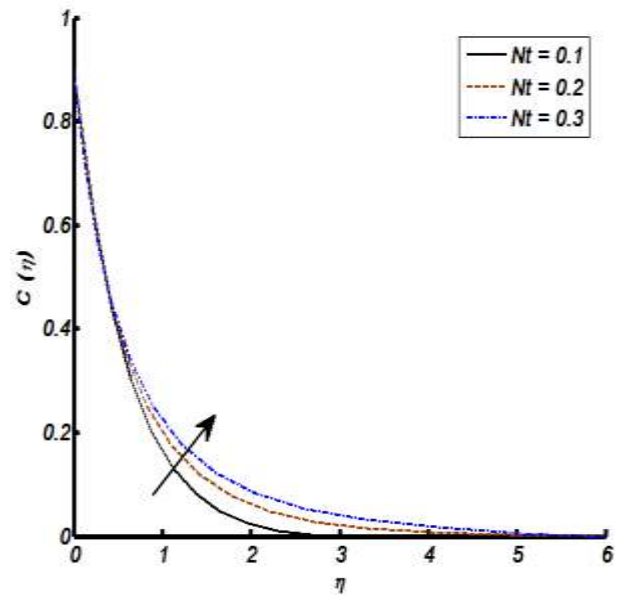


Fig. 6.21. Influence of thermophoresis parameter over concentration profile.

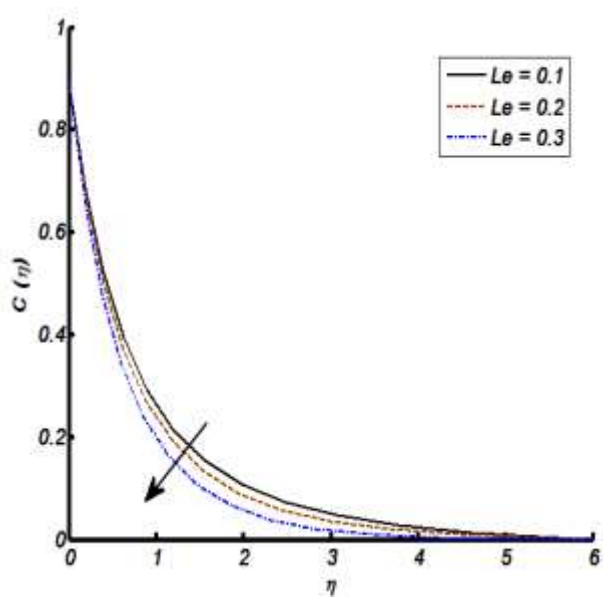


Fig. 6.22. Influence of Lewis number over concentration profile.

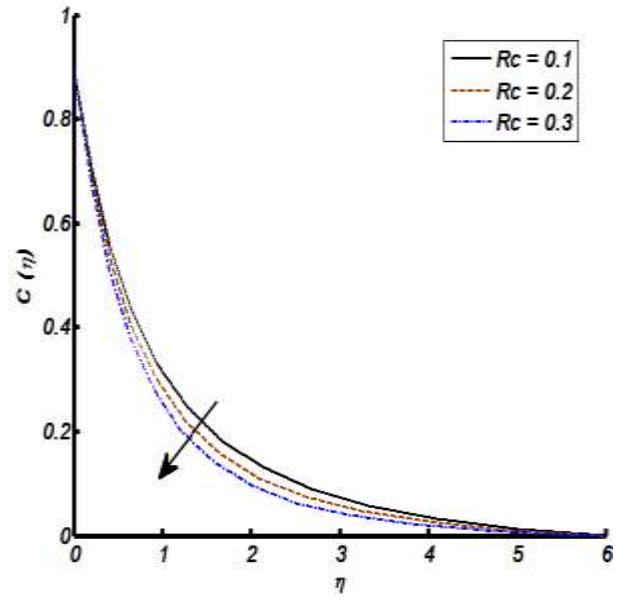


Fig. 6.23. Influence of chemical reaction parameter over concentration profile.

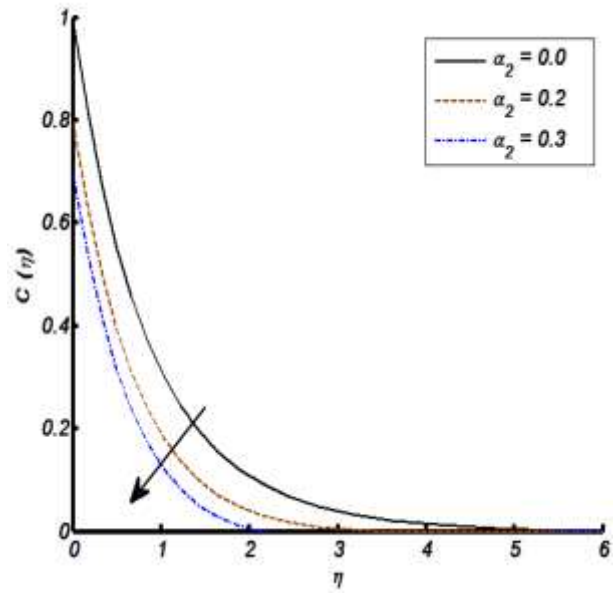


Fig. 6.24. Influence of solutal stratification parameter over concentration profile.

Table. 6.1. The variation skin friction coefficient number for K , Pr and M .

| K | Pr | M | $-F''(0)$ | $\frac{1}{2}C_f Re_x^{\frac{1}{2}} = (1+M)F''(0) - \frac{M\lambda}{3}(F''(0))^3$ |
|-----|------|-----|-----------|--|
| 0.1 | 1.1 | 0.1 | 0.3923 | 0.4322 |
| 0.3 | 1.1 | 0.1 | 0.4105 | 0.4525 |
| 0.5 | 1.1 | 0.1 | 0.4249 | 0.4713 |
| 0.1 | 1.1 | 0.1 | 0.3923 | 0.4322 |
| 0.1 | 1.3 | 0.1 | 0.3939 | 0.4338 |
| 0.1 | 1.5 | 0.1 | 0.3953 | 0.4352 |
| 0.1 | 1.1 | 0.1 | 0.3923 | 0.4322 |
| 0.1 | 1.1 | 0.3 | 0.3761 | 0.4509 |
| 0.1 | 1.1 | 0.5 | 0.3479 | 0.4791 |

Table. 6.2. The variation skin friction coefficient number for γ, α_1 and α_2 .

| γ | α_1 | α_2 | $-F''(0)$ | $\frac{1}{2}C_f Re_x^{\frac{1}{2}} = (1+M)F''(0) - \frac{M\lambda}{3}(F''(0))^3$ |
|----------|------------|------------|-----------|--|
| 0.1 | 0.1 | 0.1 | 0.5926 | 0.6576 |
| 0.3 | 0.1 | 0.1 | 0.6569 | 0.6569 |
| 0.5 | 0.1 | 0.1 | 0.6561 | 0.6561 |
| 0.1 | 0.1 | 0.1 | 0.5926 | 0.6576 |
| 0.1 | 0.3 | 0.1 | 0.5996 | 0.6609 |
| 0.1 | 0.5 | 0.1 | 0.6016 | 0.6629 |
| 0.1 | 0.1 | 0.1 | 0.5926 | 0.6576 |
| 0.1 | 0.1 | 0.3 | 0.6027 | 0.6621 |
| 0.1 | 0.1 | 0.5 | 0.6183 | 0.6657 |

Table. 6.3. The variation Nusselt number for K, Pr, Ec and α_1 .

| K | Pr | Ec | α_1 | $\frac{Nu}{\sqrt{Re_x}} = -(1 + \frac{4}{3})T'(0)$ |
|-----|------|------|------------|--|
| 0.1 | 0.1 | 0.1 | 0.1 | 0.3946 |
| 0.3 | 0.1 | 0.1 | 0.1 | 0.5101 |
| 0.5 | 0.1 | 0.1 | 0.1 | 0.6256 |
| 0.1 | 0.1 | 0.1 | 0.1 | 0.3946 |
| 0.1 | 0.3 | 0.1 | 0.1 | 0.5658 |
| 0.1 | 0.5 | 0.1 | 0.1 | 0.7355 |
| 0.1 | 0.1 | 0.1 | 0.1 | 0.3946 |
| 0.1 | 0.1 | 0.3 | 0.1 | 0.3838 |
| 0.1 | 0.1 | 0.5 | 0.1 | 0.3766 |
| 0.1 | 0.1 | 0.1 | 0.1 | 0.3946 |
| 0.1 | 0.1 | 0.1 | 0.3 | 0.3927 |
| 0.1 | 0.1 | 0.1 | 0.5 | 0.3908 |

Table. 6.4. The variation Sherwood number for K, Sc, α_2, Rc and Ec .

| K | Sc | α_2 | Rc | Ec | $\frac{Sh}{\sqrt{Re_x}} = -C'(0)$ |
|-----|------|------------|------|------|-----------------------------------|
| 0.1 | 0.1 | 0.1 | 0.1 | 0.1 | 0.3197 |
| 0.3 | 0.1 | 0.1 | 0.1 | 0.1 | 0.4571 |
| 0.5 | 0.1 | 0.1 | 0.1 | 0.1 | 0.5838 |
| 0.1 | 0.1 | 0.1 | 0.1 | 0.1 | 0.3197 |
| 0.1 | 0.3 | 0.1 | 0.1 | 0.1 | 0.5207 |
| 0.1 | 0.5 | 0.1 | 0.1 | 0.1 | 0.7217 |
| 0.1 | 0.1 | 0.1 | 0.1 | 0.1 | 0.3197 |
| 0.1 | 0.1 | 0.3 | 0.1 | 0.1 | 0.3453 |
| 0.1 | 0.1 | 0.5 | 0.1 | 0.1 | 0.3709 |
| 0.1 | 0.1 | 0.1 | 0.1 | 0.1 | 0.3197 |
| 0.1 | 0.1 | 0.1 | 0.3 | 0.1 | 0.3439 |
| 0.1 | 0.1 | 0.1 | 0.5 | 0.1 | 0.3681 |
| 0.1 | 0.1 | 0.1 | 0.1 | 0.1 | 0.3197 |
| 0.1 | 0.1 | 0.1 | 0.1 | 0.3 | 0.3089 |
| 0.1 | 0.1 | 0.1 | 0.1 | 0.5 | 0.2981 |

Table 6.5 Comparison results for skin friction coefficient towards magnetic field parameter γ .

| γ | Fathizadeh et al. [131] | Akbar et al. [20] | Present values |
|----------|-------------------------|-------------------|----------------|
| 0.0 | -1 | -1 | -1 |
| 0.5 | - | -1.11803 | -1.1182 |
| 1.0 | -1.41421 | -1.41421 | -1.4145 |
| 5.0 | -2.44948 | -2.44949 | -2.4496 |
| 10 | -3.31662 | -3.31663 | -3.3168 |

6.7 Concluding remarks

Present work is made to report thermophysical characteristics of MHD Eyring-Powell nanofluid flow brought by an inclined stretching cylindrical surface. The flow analysis carried out in the presence of Joule heating, thermal radiations, temperature stratification, heat generation, solutal stratification and chemical reaction effects. The flow situation is mathematically modelled in terms of partial differential equations. An appropriate transformation is utilized to transform partial differential equations into system of coupled non-linear ordinary differential equations. A computational algorithm is executed to offered numerical solution. The variations in fluid velocity, temperature and nanoparticle concentration towards pertinent flow controlling parameters are recorded and reported by way of graphs. Some physical quantities are calculated at cylindrical surface and demonstrated through tables. The core findings are itemized as follow:

- The compatibility of boundary conditions is attained through stream lines patterns via velocities ratio parameter.
- It is found that fluid velocity reflects an inciting attitude for positive values of mixed convection parameter, Eyring-Powell parameter and curvature parameter but opposite trends are noticed for thermal stratification parameter and inclination.
- The temperature distribution shows mounts values for Eckert number, thermophoresis parameter, thermal radiation parameter, Brownian motion parameter, an inclination, heat generation parameter. Whereas it reflects opposite trends for Prandtl number, thermal stratification parameter and Lewis number.

- The fluid nanoparticle concentration distribution increases for thermophoresis parameter while the concentration decline towards solutal stratification parameter, Brownian motion parameter, Lewis number and chemical reaction parameter.
- The physical quantity (skin friction coefficient) increases for Prandtl number, curvature parameter, thermal stratification parameter, and solutal stratification parameter but opposite trend is observed for an inclination and fluid parameter.
- The heat transfer rate exhibits positive variations due to curvature parameter, Prandtl number and an inverse relation is verified for Eckert number and thermal stratification parameter.
- An inciting nature is observed for mass transfer rate towards solutal stratification parameter, chemical reaction parameter, solutal stratification parameter and curvature parameter.
- The present findings are validated by developing comparison with existing literature. An excellent agreement is found which leads to validate the present work.

CHAPTER 7

Numerical Communication for MHD Thermally Stratified Dual Convection Flow of Casson Fluid Yields by Stretching Cylinder

7.1 Introduction

This chapter reports the comparative study of magnetohydrodynamic mixed convection boundary layer flow of Casson fluid brought by both flat and cylindrical stretching surfaces. Flow field analysis is accounted with thermal stratification phenomena. The temperature is assumed to be higher across the surface of cylinder as compared to ambient fluid. The arising mathematically modelled partial differential equations of Casson fluid flow are successfully converted into ordinary differential equations with the source of suitable transformation. The numerical solutions are computed through the application of shooting technique charted with fifth order Runge-Kutta algorithm. The effect logs of an interesting physical parameters namely, magnetic field parameter, mixed convection parameter, thermal stratification parameter, heat generation parameter, curvature parameter and Prandtl number are discussed graphically. Further, the variations of skin friction coefficient and heat transfer rate are identified by way of tables.

7.2 Mathematical modelling

In this study, we considered steady two dimensional, an incompressible magnetohydrodynamic boundary layer flow of Casson fluid brought by both flat and cylindrical stretching surfaces. Flow field analysis is taken with thermal stratification phenomena along with heat generation effects. The temperature is supposed to be higher near the cylindrical surface as compared to ambient fluid.

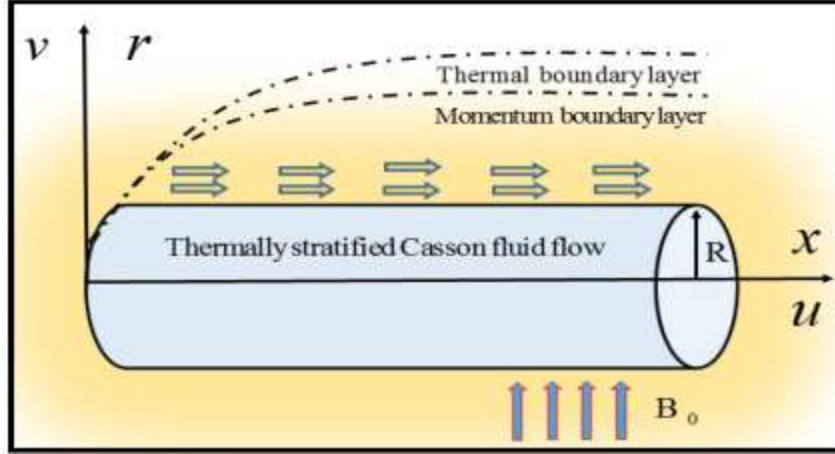


Fig. 7.1. The physical model and coordinates system.

The steady two dimensional equations under boundary layer approximation for Casson fluid model, in usual notation are given as follow:

$$\frac{\partial(rv)}{\partial r} + \frac{\partial(ru)}{\partial x} = 0, \quad (7.1)$$

$$u \frac{\partial u}{\partial x} + v \frac{\partial u}{\partial r} = \nu \left(1 + \frac{1}{\beta} \right) \left[\frac{\partial^2 u}{\partial r^2} + \frac{1}{r} \frac{\partial u}{\partial r} \right] + g \beta_T (T - T_\infty) - \frac{\sigma B_0^2}{\rho} u, \quad (7.2)$$

$$u \frac{\partial T}{\partial x} + v \frac{\partial T}{\partial r} = \frac{k}{c_p \rho} \left(\frac{\partial^2 T}{\partial r^2} + \frac{1}{r} \frac{\partial T}{\partial r} \right) + \frac{Q_0}{c_p \rho} (T - T_\infty), \quad (7.3)$$

the axial line of cylinder is considered as x -axis and radial direction perpendicular to axial line is taken as r -axis. So that, $u, v, \nu, g, c_p, \rho, \beta_T, B_0$ and Q_0 denotes velocity components in the x and r direction, kinematic viscosity, gravity, specific heat at constant pressure, fluid density, coefficient of thermal expansion, magnetic field and heat generation coefficient, respectively. The endpoint conditions are given as:

$$\begin{aligned} u(x, r) = U(x) = \frac{U_0}{L} x, \quad v(x, r) = 0 \quad \text{at } r = R, \\ u(x, r) \rightarrow 0 \quad \text{at } r \rightarrow \infty, \\ T(x, r) = T_w(x) = T_0 + \frac{b x}{L}, \quad \text{at } r = R, \\ T(x, r) \rightarrow T_\infty(x) = T_0 + \frac{c x}{L}, \quad \text{as } r \rightarrow \infty. \end{aligned} \quad (7.4)$$

For solution we own:

$$u = \frac{U_0 x}{L} F'(\eta), v = -\frac{R}{r} \sqrt{\frac{U_0 \nu}{L}} F(\eta), \eta = \frac{r^2 - R^2}{2R} \left(\frac{U_0}{\nu L} \right)^{\frac{1}{2}}, \quad (7.5)$$

$$\psi = \left(\frac{U_0 \nu x^2}{L} \right)^{\frac{1}{2}} R F(\eta), \quad T(\eta) = \frac{T - T_\infty}{T_w - T_0},$$

where, U_0 , L , $F(\eta)$, $F'(\eta)$ denotes free stream velocity, reference length, dimensionless variable, velocity of fluid towards both flat and cylindrical stretching surfaces because prime denotes differentiation with respect to η (similarity variable). Whereas, b and c are positive constants, ψ is the stream function, which identically satisfies the continuity Eq. (7.1) and is defined as:

$$u = \frac{1}{r} \left(\frac{\partial \psi}{\partial r} \right), \quad v = -\frac{1}{r} \left(\frac{\partial \psi}{\partial x} \right), \quad (7.6)$$

by substituting Eqs. (7.5)-(7.6) in Eqs. (7.2)-(7.3), one can get:

$$F''(\eta)F(\eta) - F'(\eta)^2 + \left(1 + \frac{1}{\beta} \right) \left[(1 + 2K\eta)F'''(\eta) + 2KF''(\eta) \right] + \lambda_m T(\eta) - M^2 F'(\eta) = 0, \quad (7.7)$$

$$(1 + 2K\eta)T''(\eta) + 2KT'(\eta) + \text{Pr} \left(F(\eta)T'(\eta) - F'(\eta)T(\eta) - F'(\eta)S + \delta_H T(\eta) \right) = 0, \quad (7.8)$$

the transformed endpoint conditions are:

$$F'(\eta) = 1, \quad F(\eta) = 0, \quad T(\eta) = 1 - S \quad \text{at} \quad \eta = 0, \quad (7.9)$$

$$F'(\eta) \rightarrow 0, \quad T(\eta) \rightarrow 0 \quad \text{as} \quad \eta \rightarrow \infty,$$

where, β , K , λ_m , Pr , S , δ_H , and M denotes Casson fluid parameter, curvature parameter, mixed convection parameter, Prandtl number, thermal stratification parameter, heat generation parameter and magnetic field parameter respectively and defined as follow:

$$K = \frac{1}{R} \sqrt{\frac{\nu L}{U_0}}, \quad \lambda_m = \frac{Gr}{\text{Re}_x^2}, \quad \text{Pr} = \frac{\mu c_p}{k}, \quad (7.10)$$

$$S = \frac{c}{b}, \quad \delta_H = \frac{LQ_0}{U_0 \rho c_p} \quad \text{and} \quad M = \sqrt{\frac{\sigma B_0^2 L}{\rho U_0}}.$$

Furthermore, Gr denotes thermal Grashof number which is defined as:

$$Gr = \frac{(T_w - T_0)g\beta_T x^3}{\nu^2}. \quad (7.11)$$

The surface quantity is:

$$C_f = \frac{\tau_w}{\rho \frac{U^2}{2}}, \quad \tau_w = \mu \left(1 + \frac{1}{\beta}\right) \left(\frac{\partial u}{\partial r}\right)_{r=R}, \quad (7.12)$$

where, τ_w and μ denotes shear stress and viscosity of fluid respectively. The dimensionless form of skin friction coefficient is prearranged as:

$$0.5 \text{Re}_x^{1/2} C_f = \left(1 + \frac{1}{\beta}\right) F''(0). \quad (7.13)$$

The local Nusselt number is defined as:

$$Nu_x = \frac{-xq_w}{(T_w - T_\infty)k}, \quad q_w = -\left(\frac{\partial T}{\partial r}\right)_{r=R} k, \quad (7.14)$$

in dimensionless form it can be written as:

$$Nu_x \text{Re}_x^{-1/2} = -T'(0). \quad (7.15)$$

7.3 Shooting method

For solution we let

$$\begin{aligned} y_2 &= F', \\ y_3 &= y_2' = F'', \\ y_5 &= T', \end{aligned}$$

equivalently

$$\left[\begin{array}{l} y_1' = y_2 \\ y_2' = y_3 \\ y_3' = \frac{(y_2)^2 - y_3 y_1 - \lambda_m y_4 - \left(1 + \frac{1}{\beta}\right) 2Ky_3 - M^2 y_2}{(2K\eta + 1) \left(1 + \frac{1}{\beta}\right)} \\ y_4' = y_5 \\ y_5' = \frac{\text{Pr}(y_2 y_4 - y_1 y_5 - \delta_H y_4 + S y_2) - 2Ky_5}{1 + 2K\eta} \end{array} \right], \quad (7.16)$$

and:

$$\begin{aligned}
 y_1(0) &= 0, \\
 y_2(0) &= 1, \\
 y_3(0) &= \eta_1, \\
 y_4(0) &= 1 - S, \\
 y_5(0) &= \eta_2,
 \end{aligned}
 \tag{7.17}$$

where, η_1 and η_2 are initial guessed values. For the integration of first order system i-e Eq. (7.16) as a IVP with the aid of fifth order Runge-Kutta scheme, we required values for $y_3(0)$ i.e. $F''(0)$, and $y_5(0)$ i.e. $T'(0)$. Newton's method is than used to estimate the values of $F''(0)$ and $T'(0)$ till the solution approaches to zero with the desired efficiency of 10^{-4} along step size $\Delta\eta = 0.025$ by way of additional conditions given as:

$$\begin{aligned}
 y_2(\infty) &= 0, \\
 y_4(\infty) &= 0.
 \end{aligned}
 \tag{7.18}$$

7.4 Discussion

The magnetohydrodynamic Casson fluid flow towards both flat and cylindrical stretching surfaces are considered in the presence of an important physical effects namely, thermal stratification, heat generation and mixed convection. A numerical study is executed to inspect the flow field situation. The obtained results are validated by developing comparison with existing literature. An excellent match is found which confirms the numerical treatment. To be more specific, Table. 7.1 shows the comparison of Nusselt number with previously published results. Whereas, Tables. 7.1-7.2 are used to examine the variation of physical quantities for positive values of involved flow controlling parameters like Casson fluid parameter, curvature parameter, mixed convection parameter, Prandtl number, thermal stratification parameter, heat generation parameter and magnetic field parameter. Particularly, Table 7.2 is constructed to determine the behaviour of skin friction coefficient $(0.5C_f Re_x^{1/2})$ for distinct values of physical variables namely, $\beta, K, \lambda_m, Pr, S$ and δ_H . Here, we observed that skin friction coefficient shows an

increasing behaviour for larger values of K, β, Pr and S . However, opposite situation is noticed for λ_m and δ_H . Whereas, Table 7.3 is constructed to determine the behaviour of local Nusselt number for distinct values of physical variables $\beta, K, \lambda_m, Pr, S$ and δ_H . Here, we found that local Nusselt number shows an increasing behaviour for greater values of K, λ_m and Pr . However, opposite situation is noticed for β, S and δ_H .

7.4.1 Velocity profiles

The physical illustration of Casson fluid flow is given by Fig. 7.1 while Figs. 7.2-7.5 are plotted to examine the influence of Casson fluid parameter, curvature parameter, mixed convection parameter and magnetic field parameter on dimensionless velocity profile. In detail, Fig. 7.2, depicts the influence of β on velocity profile for both flat and cylindrical geometry. It is seemed that the velocity profile decreases for higher values of Casson fluid parameter β . Fig. 7.3 represents the influence of curvature parameter K on velocity profile for cylinder. It shows that the larger values of curvature parameter K is the cause of increase in velocity profile. The curvature parameter K has inverse relation with radius of curvature. When we increase curvature parameter, the radius of cylinder decreases and hence contact surface area of cylinder with fluid reduces which offers less resistance to fluid flow. So an increase in curvature parameter K causes an increase in velocity profile. Fig. 7.4 includes the effect of mixed convection parameter λ_m on velocity profile for both flat and cylindrical surfaces. It is noticed that for higher iterations of mixed convection parameter λ_m , velocity of the fluid increases. Physically, it is due to an inciting attitude of thermal buoyancy force. The influence of magnetic field parameter on velocity profile is displayed through Fig. 7.5. It is seen that for positive values of magnetic field parameter the velocity profile decreases. In actual, when we enhance magnetic field parameter a resistive force named as Lorentz force becomes actively participate to offer resistance against fluid particles as a result horizontal velocity decreases.

7.4.2 Temperature profiles

Figs. 7.6-7.10 are plotted to inspect the impact of involved physical parameters namely, heat generation parameter, curvature parameter, Prandtl number and thermal stratification parameter on temperature profile. To be more specific, Fig. 7.6, shows the impact of δ_H

on temperature profile for both flat and cylindrical geometry. It is clearly seen that for positive values of δ_H , temperature of fluid rises. In actual, during heat generation process energy is produce which brings enhancement in temperature. In addition, sometimes for higher values of δ_H , we may have over shoot in temperature profile. Such type of over shoot can be controlled by introducing heat sink which helps to reduce temperature of fluid. Fig. 7.7 represents the effect of curvature parameter K on temperature profile for cylindrical case. It shows that the temperature distribution increases due to increase in curvature parameter K . As Kelvin temperature is define as an average kinetic energy so when we increase curvature of cylinder, velocity of fluid increases. Note that the temperature of fluid start decreasing near the cylindrical surface and increases far away with respect to surface. Fig. 7.8 identifies the influence of Prandtl number Pr on temperature profile for both sheet and cylinder and an inciting values of Pr correspond less diffusion of energy due to which temperature profile shows decline nature. Fig. 7.9 represents the impact of the stratification parameter S over the temperature gradient $T'(\eta)$ and temperature $T(\eta)$. The presence of stratification S is the cause of decrease in the temperature in a flow regime and due to this temperature gradient decrease (absolute sense). The thermal boundary layer thickness also decreases with an increase in the stratification parameter S . The buoyancy factor $(T_w - T_\infty)$ reduces within the boundary layer for positive values of stratification parameter S . The temperature distribution decays from the largest value at the wall to zero in the free stream that is temperature converges at the outer edge of the boundary layer. Fig. 7.10 paints the influence of stratification parameter S for both flat and cylindrical geometry. It is witnessed that the temperature profile decreases for increasing values of δ_H and this is because of decline in temperature difference between both surfaces and ambient fluid therefore, temperature profile decreases.

7.5 Graphical outcomes

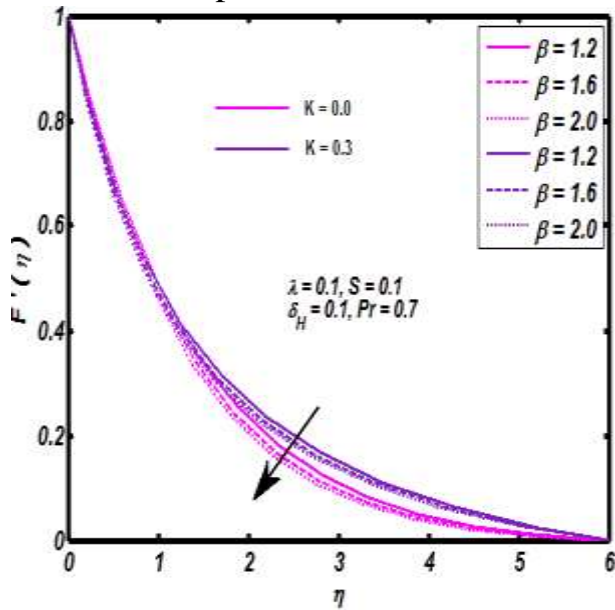


Fig. 7.2. Impact of β on $F'(\eta)$.

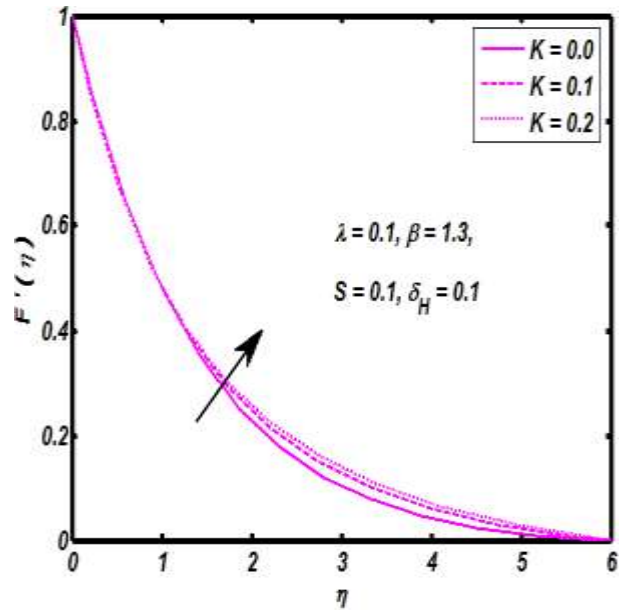


Fig. 7.3. Impact of K on $F'(\eta)$.

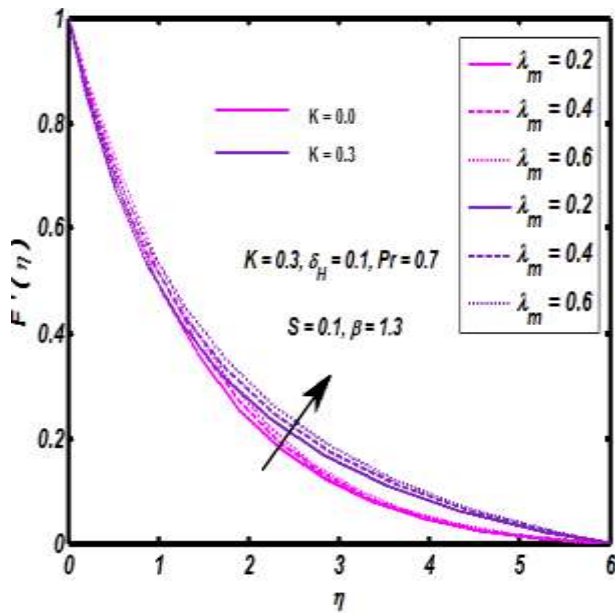


Fig. 7.4. Impact of λ_m on $F'(\eta)$.

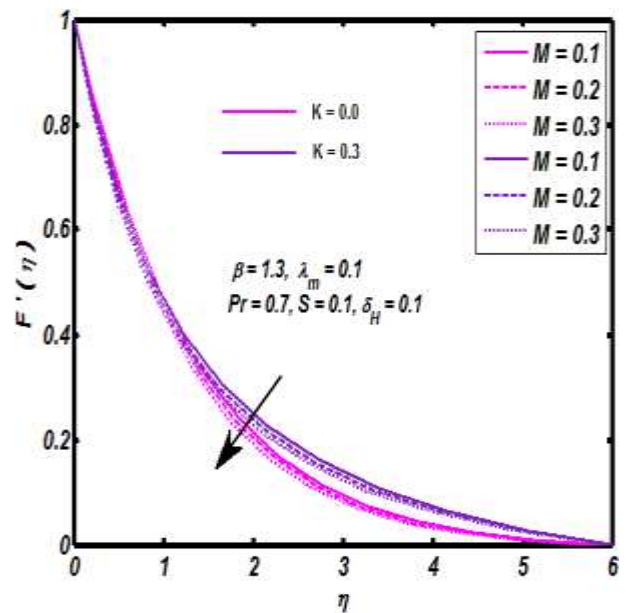


Fig. 7.5. Impact of M on $F'(\eta)$.

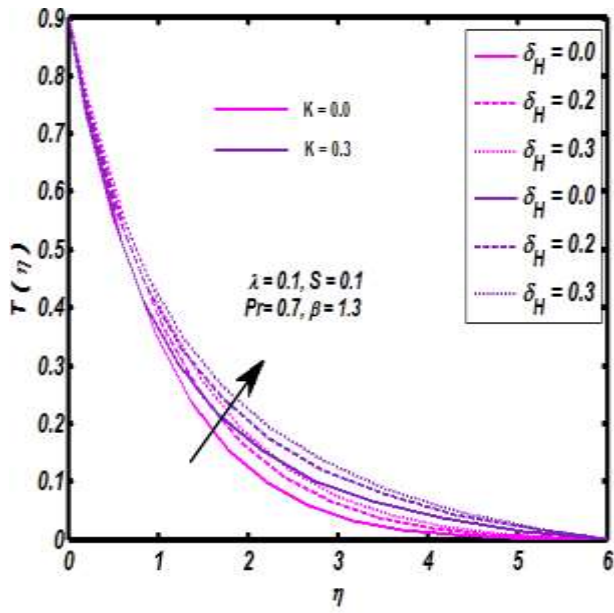


Fig. 7.6. Impact of δ_H on $T(\eta)$.

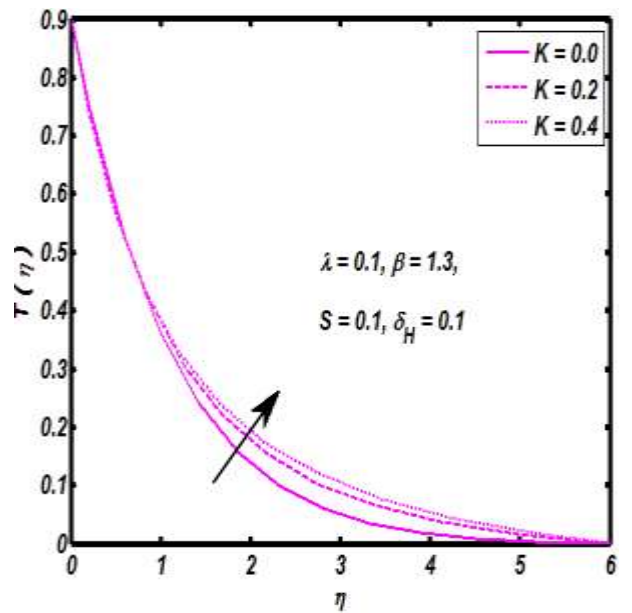


Fig. 7.7. Impact of K on $T(\eta)$.

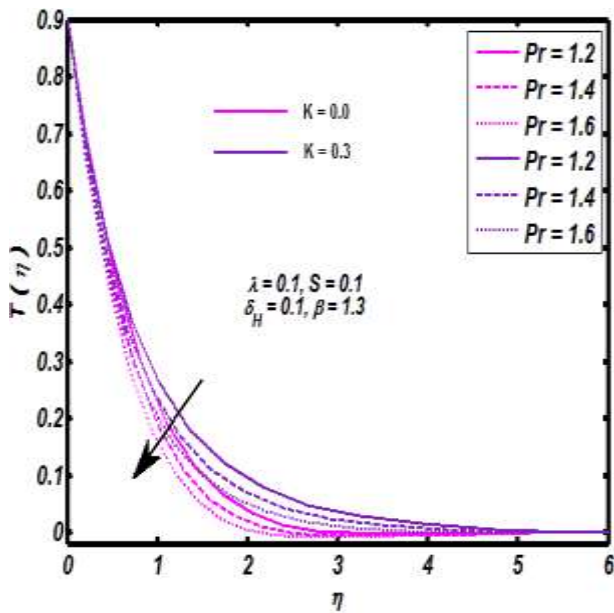


Fig. 7.8. Impact of Pr on $T(\eta)$.

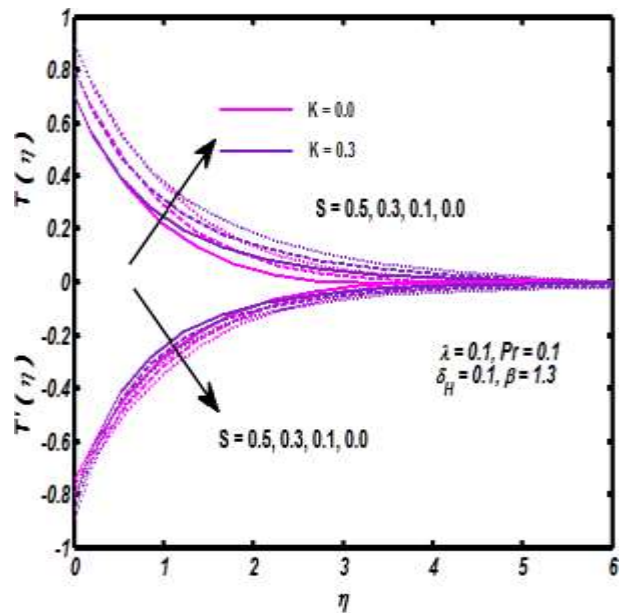


Fig. 7.9. Impact of S on $T(\eta)$ & $T'(\eta)$.

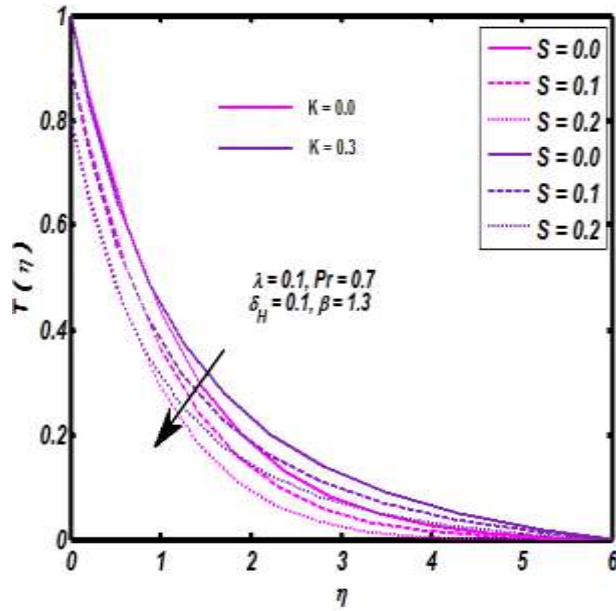


Fig. 7.10. Impact of S on $T(\eta)$.

Table. 7.1 The comparison of $Nu_x Re_x^{-1/2} = -T'(0)$ for Prandtl number.

| Pr | Bidin and Nazar [134] ($E = K = 0$) | Mukhopadhyay [135] ($St = S = M = 0$) | Present study ($\beta \rightarrow \infty, K = S = M = \delta_H = 0$) |
|-----|--|---|---|
| 1.0 | 0.9547 | 0.9547 | 0.9547 |
| 2.0 | 1.4714 | 1.4714 | 1.4714 |
| 3.0 | 1.8961 | 1.8961 | 1.8961 |

Table. 7.2. Numerical values of skin friction $0.5C_f \text{Re}_x^{1/2}$ for distinct values of $\beta, K, \lambda_m, \text{Pr}, S$ and δ_H

| K | β | λ_m | Pr | S | δ_H | $F''(0)$ | $0.5C_f \text{Re}_x^{1/2}$ |
|-----|---------|-------------|-----|-----|------------|----------|----------------------------|
| 0.1 | - | - | - | - | - | -0.7652 | -0.3826 |
| 0.2 | - | - | - | - | - | -0.8073 | -0.4036 |
| 0.3 | - | - | - | - | - | -0.8497 | -0.4248 |
| - | 1.3 | - | - | - | - | -0.7652 | -0.3826 |
| - | 1.4 | - | - | - | - | -0.7760 | -0.3884 |
| - | 1.5 | - | - | - | - | -0.7857 | -0.3928 |
| - | - | 0.1 | - | - | - | -0.7652 | -0.3826 |
| - | - | 0.2 | - | - | - | -0.7358 | -0.3679 |
| - | - | 0.3 | - | - | - | -0.7071 | -0.3535 |
| - | - | - | 0.6 | - | - | -0.7633 | -0.3816 |
| - | - | - | 0.7 | - | - | -0.7652 | -0.3826 |
| - | - | - | 0.8 | - | - | -0.7670 | -0.3835 |
| - | - | - | - | 0.1 | - | -0.7652 | -0.3826 |
| - | - | - | - | 0.2 | - | -0.7703 | -0.3851 |
| - | - | - | - | 0.3 | - | -0.7754 | -0.3877 |
| - | - | - | - | - | 0.1 | -0.7652 | -0.3826 |
| - | - | - | - | - | 0.2 | -0.7640 | -0.3821 |
| - | - | - | - | - | 0.3 | -0.7626 | -0.3813 |

Table. 7.3. Comparison value of $-T'(0)$ against the parameter.

| K | β | λ_m | Pr | S | δ_H | $-T'(0)$ |
|-----|---------|-------------|-----|-----|------------|----------|
| 0.1 | - | - | - | - | - | 0.8254 |
| 0.2 | - | - | - | - | - | 0.8599 |
| 0.3 | - | - | - | - | - | 0.8948 |
| - | 1.3 | - | - | - | - | 0.8254 |
| - | 1.4 | - | - | - | - | 0.8225 |
| - | 1.5 | - | - | - | - | 0.8200 |
| - | - | 0.1 | - | - | - | 0.8254 |
| - | - | 0.2 | - | - | - | 0.8322 |
| - | - | 0.3 | - | - | - | 0.8387 |
| - | - | - | 0.6 | - | - | 0.7542 |
| - | - | - | 0.7 | - | - | 0.8254 |
| - | - | - | 0.8 | - | - | 0.8930 |
| - | - | - | - | 0.1 | - | 0.8254 |
| - | - | - | - | 0.2 | - | 0.7958 |
| - | - | - | - | 0.3 | - | 0.7662 |
| - | - | - | - | - | 0.1 | 0.8254 |
| - | - | - | - | - | 0.2 | 0.7789 |
| - | - | - | - | - | 0.3 | 0.7275 |

7.6 Concluding remarks

The magneto-thermally stratified Casson fluid flow in the presence of mixed convection is investigated numerically. The behaviour of dimensionless velocity and temperature profiles are identified under different physical parameters. The key results of this study are summarized and itemized as follow:

- The velocity profile shows an inciting nature for higher values of mixed convection parameter λ_m and curvature parameter K , while it shows opposite behaviour for both Casson fluid parameter β and magnetic field parameter M .
- The temperature increases significantly for greater values of both δ_H and curvature parameter K , whereas it shows decline attitude via thermal stratification parameter S and Prandtl number Pr .
- In absolute sense, the skin friction coefficient shows decreasing behaviour towards mixed convection parameter λ_m and heat generation parameter δ_H but increasing via Casson fluid β , K , Pr and stratification parameter S .
- The local Nusselt number is reducing function of Casson fluid parameter β , thermal stratification parameter S and heat generation parameter δ_H but increasing via curvature parameter K , λ_m and Prandtl number Pr .
- It is seems that the obtained variations (see Figs. 7.2, 7.4-7.6, 7.8-7.10) are remarkably enormous for cylindrical geometry as compares to plane geometry i-e plate.

CHAPTER 8

Nanoparticles Individualities in both Newtonian and Casson Fluid Models by Way of Stratified Media: A Numerical Analysis

8.1 Introduction

The current chapter contains simultaneous analysis on both Newtonian and non-Newtonian nanofluid models. The fluid flow is achieved by entertaining no-slip condition subject to stretched cylindrical surface. The flow regime is manifested with pertinent physical effects, namely temperature stratification, concentration stratification, thermal radiation, heat generation, magnetic field, dual convection and chemical reaction. The strength of fluid temperature and nanoparticles concentration adjacent to an inclined cylindrical surface is assumed to be higher than the ambient flow field. A mathematical model is developed in terms of partial differential equations. A self constructed numerical algorithm is executed to report numerical solution. The resultant annotations are illustrated through both tables and graphs. Moreover, analysis is certified through comparison with existing values in a limiting sense.

8.2 Mathematical formulation

We have assumed steady laminar magneto-hydrodynamic an incompressible boundary layer stagnation point flow of both Casson ($\beta \neq 0$) and Newtonian ($\beta \rightarrow \infty$) nanofluid. The fluid flow is brought by stretching cylindrical surface. The flow field is manifested with physical effects namely, magnetic field, dual convection, temperature stratification, concentration stratification, thermal radiation, heat generation and chemical reaction. An axial line of the cylinder is taken parallel to x -axis and the radial direction is considered

perpendicular to x -axis and named as r -axis. Presently the steady two dimensional equations for the Casson nanofluid model are given as:

$$\frac{\partial(r\bar{v})}{\partial r} + \frac{\partial(r\bar{u})}{\partial x} = 0, \quad (8.1)$$

$$\begin{aligned} \frac{\partial\bar{u}}{\partial r}\bar{v} + \frac{\partial\bar{u}}{\partial x}\bar{u} = \nu\left(1 + \frac{1}{\beta}\right)\left(\frac{\partial^2\bar{u}}{\partial r^2} + \frac{1}{r}\frac{\partial\bar{u}}{\partial r}\right) + \bar{u}_e\frac{\partial\bar{u}_e}{\partial x} - \frac{\sigma B_0^2}{\rho}(\bar{u} - \bar{u}_e) \\ + g\beta_T(\bar{T} - \bar{T}_\infty)\cos\alpha + g\beta_c(\bar{C} - \bar{C}_\infty)\cos\alpha, \end{aligned} \quad (8.2)$$

$$\begin{aligned} \frac{\partial\bar{T}}{\partial r}\bar{v} + \frac{\partial\bar{T}}{\partial x}\bar{u} = \frac{\partial}{\partial r}\left(r\frac{\partial\bar{T}}{\partial r}\right)\frac{\alpha^\bullet}{r} - \frac{1}{\rho c_p r}\frac{\partial}{\partial r}(rq_r) + \tau\left(\frac{D_T}{\bar{T}_\infty}\left(\frac{\partial\bar{T}}{\partial r}\right)^2 + D_B\frac{\partial\bar{T}}{\partial r}\frac{\partial\bar{C}}{\partial r}\right) \\ + \frac{Q_0}{c_p\rho}(\bar{T} - \bar{T}_\infty), \end{aligned} \quad (8.3)$$

$$\bar{u}\frac{\partial\bar{C}}{\partial x} + \bar{v}\frac{\partial\bar{C}}{\partial r} = D_B\left(\frac{1}{r}\frac{\partial\bar{C}}{\partial r} + \frac{\partial^2\bar{C}}{\partial r^2}\right) + \frac{D_T}{\bar{T}_\infty}\left(\frac{1}{r}\frac{\partial\bar{T}}{\partial r} + \frac{\partial^2\bar{T}}{\partial r^2}\right) - R_0(\bar{C} - \bar{C}_\infty), \quad (8.4)$$

here, $q_r = -\left(\frac{4}{3}\right)\frac{\sigma^\bullet}{k^\bullet}\frac{\partial\bar{T}^4}{\partial r}$ signifies Roseland radiative heat flux. Therefore, Eq. (8.3) can

be written as:

$$\begin{aligned} \frac{\partial\bar{T}}{\partial r}\bar{v} + \frac{\partial\bar{T}}{\partial x}\bar{u} = \frac{\partial}{\partial r}\left(r\frac{\partial\bar{T}}{\partial r}\right)\frac{\alpha^\bullet}{r} + \frac{1}{\rho c_p r}\left(\frac{4}{3}\right)\frac{\sigma^\bullet}{k^\bullet}\frac{\partial}{\partial r}\left(r\frac{\partial\bar{T}^4}{\partial r}\right) \\ + \tau\left(\frac{D_T}{\bar{T}_\infty}\left(\frac{\partial\bar{T}}{\partial r}\right)^2 + D_B\frac{\partial\bar{T}}{\partial r}\frac{\partial\bar{C}}{\partial r}\right) + \frac{Q_0}{c_p\rho}(\bar{T} - \bar{T}_\infty), \end{aligned} \quad (8.5)$$

the end point conditions are given by:

$$\bar{u} = U(x) = ax, \bar{v} = 0, \text{ at } r = R, \bar{u} \rightarrow \bar{u}_e = a'x, \text{ when } r \rightarrow \infty, \quad (8.6)$$

$$\bar{T}(x, r) = \bar{T}_w(x) = \bar{T}_0 + \frac{b x}{L}, \quad \bar{C}(x, r) = \bar{C}_w(x) = \bar{C}_0 + \frac{d x}{L} \quad \text{at } r = R,$$

$$\bar{T}(x, r) \rightarrow \bar{T}_\infty(x) = \bar{T}_0 + \frac{c x}{L}, \quad \bar{C}(x, r) \rightarrow \bar{C}_\infty(x) = \bar{C}_0 + \frac{e x}{L} \quad \text{as } r \rightarrow \infty,$$

where, $\nu, \rho, \bar{u}_e, \sigma, B_0, g, \beta_T, \beta_c, \alpha, \alpha^\bullet, c_p, D_B, D_T, \bar{T}, \bar{T}_\infty, Q_0, \bar{C}, \bar{C}_\infty$ and R_0 represents the kinematic viscosity, fluid density, free stream velocity, electrical conductivity, uniform magnetic field, gravity, thermal expansion coefficient, concentration expansion

coefficient, an inclination, thermal diffusivity, specific heat capacity at constant pressure, Brownian diffusion coefficient, thermophoretic diffusion coefficient, fluid temperature, ambient temperature, heat generation/absorption coefficient, fluid concentration, ambient concentration and rate of chemical reaction respectively. Likewise, $\tau = \frac{(\rho c)_p}{(\rho c)_f}$, $T_w(x)$, $C_w(x)$, L , b , c , d and e denotes the ratio of nanoparticles heat capacity to the base fluid heat capacity, surface temperature, surface concentration, reference length and positive constants respectively. We use the following transformation to get the transformed forms of Eqs. (8.2)-(8.5):

$$\begin{aligned} \bar{u} &= \frac{U_0 x}{L} F'(\eta), \quad \bar{v} = -\frac{R}{r} \sqrt{\frac{U_0 \nu}{L}} F(\eta), \quad \eta = \frac{r^2 - R^2}{2R} \left(\frac{U_0}{\nu L} \right)^{\frac{1}{2}}, \\ \psi &= \left(\frac{U_0 \nu x^2}{L} \right)^{\frac{1}{2}} RF(\eta), \quad C(\eta) = \frac{\bar{C} - \bar{C}_\infty}{\bar{C}_w - \bar{C}_0}, \quad T(\eta) = \frac{\bar{T} - \bar{T}_\infty}{\bar{T}_w - \bar{T}_0}, \end{aligned} \quad (8.7)$$

here, U_0 , R , $F'(\eta)$, \bar{T}_0 , \bar{C}_0 and ψ denotes reference velocity, radius of cylinder, velocity of fluid over a stretching cylinder, reference temperature, reference concentration and stream function respectively. The stream function in terms of velocity components can be written as:

$$\bar{u} = \frac{1}{r} \left(\frac{\partial \psi}{\partial r} \right), \quad \bar{v} = -\frac{1}{r} \left(\frac{\partial \psi}{\partial x} \right), \quad (8.8)$$

by using the transformation given by Eq. (8.7) into Eqs. (8.2)-(8.5) the subsequent reduced differential equations are:

$$\begin{aligned} \left(1 + \frac{1}{\beta} \right) \left[(1 + 2K\eta) F'''(\eta) + 2KF''(\eta) \right] + F(\eta)F''(\eta) - F'(\eta)^2 \\ - \gamma^2 (F'(\eta) - A) + A^2 + \lambda_m (T(\eta) + NC(\eta)) \cos \alpha = 0, \end{aligned} \quad (8.9)$$

$$\begin{aligned} 2K \left(1 + \frac{4}{3} R_r \right) T'(\eta) + \text{Pr} (F(\eta)T'(\eta) - F'(\eta)\delta_1 + QT(\eta) - F'(\eta)T(\eta)) \\ + \text{Pr} Nb (1 + 2K\eta) \left(T'(\eta)C'(\eta) + \frac{Nt}{Nb} T'^2(\eta) \right) + (1 + 2K\eta) \left(1 + \frac{4}{3} R_r \right) T''(\eta) = 0, \end{aligned} \quad (8.10)$$

$$(1+2K\eta)\left(C''(\eta)+\frac{Nt}{Nb}T''(\eta)\right)+\text{Pr}Le(F(\eta)C'(\eta)-F'(\eta)C(\eta)-F'(\eta)\delta_2)+ \quad (8.11)$$

$$2K\left(C'(\eta)+\frac{Nt}{Nb}T'(\eta)\right)-R_cC(\eta)=0,$$

and the transformed end point conditions become:

$$F'(\eta)=1, \quad F(\eta)=0, \quad T(\eta)=1-\delta_1, \quad C(\eta)=1-\delta_2, \quad \text{at} \quad \eta=0, \quad (8.12)$$

$$F'(\eta) \rightarrow A, \quad T(\eta) \rightarrow 0, \quad C(\eta) \rightarrow 0, \quad \text{when} \quad \eta \rightarrow \infty,$$

where, $K, \beta, \gamma, A, \lambda_m, N, R_T, \text{Pr}, Nb, Nt, \delta_1, Q > 0, Le, \delta_2,$ and R_c denote curvature parameter, Casson fluid parameter, magnetic field parameter, velocities ratio parameter, mixed convection parameter, ratio of concentration to thermal buoyancy forces, thermal radiation parameter, Prandtl number, Brownian motion parameter, thermophoresis parameter, thermal stratification parameter, heat generation parameter, Lewis number, Solutal stratification parameter and chemical reaction parameter respectively and are well-defined as below:

$$\begin{aligned} K &= \frac{1}{R} \sqrt{\frac{\nu}{a}}, \quad a = \frac{U_0}{L}, \quad \gamma = \sqrt{\frac{\sigma B_0^2}{\rho a}}, \quad A = \frac{a^*}{a}, \quad \lambda_m = \frac{Gr}{\text{Re}_x^2}, \quad N = \frac{Gr^*}{Gr}, \\ R_T &= \frac{4\sigma^* T_\infty^3}{k^* k}, \quad \text{Pr} = \frac{\nu}{\alpha^*}, \quad Nb = \frac{(\bar{C}_w - \bar{C}_\infty)\tau D_B}{\nu}, \quad Nt = \frac{(\bar{T}_w - \bar{T}_\infty)\tau D_T}{\nu \bar{T}_\infty}, \\ \delta_1 &= \frac{c}{b}, \quad Q = \frac{LQ_0}{U_0 \rho c_p}, \quad Le = \frac{\alpha^*}{D_B}, \quad \delta_2 = \frac{e}{d}, \quad R_c = \frac{R_0 L}{U_0}, \end{aligned} \quad (8.13)$$

here, Gr and Gr^* categorized as Grashof numbers subject to temperature and concentration respectively and are defined as follow:

$$Gr = \frac{g\beta_T(\bar{T}_w - \bar{T}_0)x^3}{\nu^2}, \quad Gr^* = \frac{g\beta_C(\bar{C}_w - \bar{C}_0)x^3}{\nu^2}, \quad (8.14)$$

and the surface quantity is:

$$C_f = \frac{\tau_w}{\rho \frac{U^2}{2}}, \quad \tau_w = \mu \left(1 + \frac{1}{\beta}\right) \left(\frac{\partial u}{\partial r}\right)_{r=R}, \quad (8.15)$$

where μ and τ_w denotes the viscosity of the fluid and the shear stress respectively. In dimensionless practice, it is written as:

$$0.5C_f\sqrt{\text{Re}_x} = \left(1 + \frac{1}{\beta}\right)F''(0), \quad (8.16)$$

with $\text{Re}_x = \frac{U_0 x^2}{\nu L}$ be the local Reynolds number.

The expression for the both local Nusselt and the local Sherwood numbers are given as:

$$\begin{aligned} Nu_x &= \frac{xq_w}{k(\bar{T}_w - \bar{T}_0)}, & q_w &= -k \left(\frac{\partial \bar{T}}{\partial r} \right)_{r=R} + (q_r)_{r=R}, \\ Sh &= \frac{xj_w}{D(\bar{C}_w - \bar{C}_0)}, & j_w &= -D \left(\frac{\partial \bar{C}}{\partial r} \right)_{r=R}, \end{aligned} \quad (8.17)$$

the dimensionless form of these expressions

are pre-arranged as:

$$\frac{Nu_x}{\sqrt{\text{Re}_x}} = -\left(1 + \frac{4}{3}R_d\right)T'(\eta), \quad \text{as } \eta \rightarrow 0, \quad (8.18)$$

$$\frac{Sh_x}{\sqrt{\text{Re}_x}} = -C'(\eta), \quad \text{as } \eta \rightarrow 0.$$

8.3 Computational scheme

For the implementation of the computational algorithm, the partial differential equations are converted into ordinary differential equations and then the coupled nonlinear ordinary differential equations (8.9)-(8.11) subject to the end point conditions (8.12) are solved by using shooting scheme along with the Runge-Kutta fifth order algorithm. For order reduction:

$$\begin{aligned} Z_1 &= F(\eta), & Z_2 &= \frac{dF(\eta)}{d\eta}, & Z_3 &= \frac{dZ_2(\eta)}{d\eta} = \frac{d^2F(\eta)}{d\eta^2}, & Z_4 &= T(\eta), \\ Z_5 &= \frac{dZ_4(\eta)}{d\eta} = \frac{dT(\eta)}{d\eta}, & Z_6 &= C(\eta), & Z_7 &= \frac{dZ_6(\eta)}{d\eta} = \frac{dC(\eta)}{d\eta}, \end{aligned} \quad (8.19)$$

by taking into account these replacements, the identical appearance of Eqs. (8.9)- (8.11) with new variables is given as:

$$\begin{aligned}
\frac{dZ_1}{d\eta} &= Z_2, \\
\frac{dZ_2}{d\eta} &= Z_3, \\
\frac{dZ_3}{d\eta} &= \frac{Z_2^2 - Z_1 Z_3 + \gamma^2 (Z_2 - A) - A^2 - \lambda_m (Z_4(\eta) + NZ_6(\eta)) \cos \alpha}{\left(1 + \frac{1}{\beta}\right)(1 + 2K\eta)} - \frac{2KZ_3}{(1 + 2K\eta)}, \\
\frac{dZ_4}{d\eta} &= Z_5, \\
\frac{dZ_5}{d\eta} &= \frac{\left\{ \begin{aligned} &\Pr (Z_2 Z_4 + \delta_1 Z_2 - Z_1 Z_5 - QZ_4) - 2K \left(1 + \frac{4}{3} R_T\right) Z_5 \\ &- \Pr Nb (1 + 2K\eta) \left(Z_5 Z_7 + \frac{Nt}{Nb} Z_5^2 \right) \end{aligned} \right\}}{(1 + 2K\eta) \left(1 + \frac{4}{3} R_T\right)}, \\
\frac{dZ_6}{d\eta} &= Z_7, \\
\frac{dZ_7}{d\eta} &= \frac{\Pr Le (Z_2 Z_6 + \delta_2 Z_2 - Z_1 Z_7) - (1 + 2K\eta) \frac{Nt}{Nb} Z_5' - 2K \left(Z_7 + \frac{Nt}{Nb} Z_5 \right) + R_c Z_6}{1 + 2K\eta},
\end{aligned} \tag{8.20}$$

the end point conditions under concerning new variables are given as:

$$\begin{aligned}
Z_1(0) &= 0, \\
Z_2(0) &= 1, \\
Z_3(0) &= \text{First initial guess}, \\
Z_4(0) &= 1 - \delta_1, \\
Z_5(0) &= \text{Second initial guess}, \\
Z_6(0) &= 1 - \delta_2, \\
Z_7(0) &= \text{Third initial guess},
\end{aligned} \tag{8.21}$$

now for the integration of the system given by Eqs. (20) we need

$$Z_3(\eta) = F''(\eta), \quad Z_5(\eta) = T'(\eta) \quad \text{and} \quad Z_7(\eta) = T'(\eta) \quad \text{when} \quad \eta \rightarrow 0, \tag{8.22}$$

additionally, we have noticed that the three initial conditions namely, $Z_3(\eta)$, $Z_5(\eta)$ and $Z_7(\eta)$ when $\eta \rightarrow 0$, are missing but we have end point conditions:

$$Z_2(\eta) = A, \quad Z_4(\eta) = 0, \quad \text{and} \quad Z_6(\eta) = 0 \quad \text{when} \quad \eta \rightarrow \infty, \quad (8.23)$$

the integration of the system of first order ordinary differential equations is carried by electing complementary values for $\frac{d^2F(\eta)}{d\eta^2}$, $\frac{dT(\eta)}{d\eta}$ and $\frac{dC(\eta)}{d\eta}$ when $\eta = 0$, such that the distant conditions given by Eq. (8.23) holds satisfactory.

8.4 Results and discussion

8.4.1 Tabular trends

The variations of local skin friction coefficient, local Nusselt number and local Sherwood number are offered through Tables. 8.1-8.3. In detail, Table. 8.1 is used to inspect the impact of curvature parameter, Casson fluid parameter, mixed convection parameter and Prandtl number on local skin friction coefficient. Table. 8.2 identified the variations of Nusselt number via curvature parameter, Prandtl number and thermal stratification parameter whereas Table. 8.3 demonstrate the influence of curvature parameter, Lewis number and Solutal stratification parameter on local Sherwood number. In absolute sense, it is noticed that the skin friction coefficient is an increasing function of both K , and β . On the other hand it shows an opposite behaviour for the increasing values of λ_m . Moreover, the local skin friction coefficient is independent of Prandtl number. The negative sign of local skin friction implies the drag forced exerted by cylindrical surface towards Casson fluid particles. In context of Table 8.2 it has been observed through the local Nusselt number shows an increasing behaviour for the greater values of K and Pr. However opposite variation is observed for the increasing values of the parameter δ_1 . The negative sign in local Nusselt number relates the transfer of heat normal to the cylindrical surface. As far as the Table 8.3 is concerned it is clearly observed that the local Sherwood number depicts an increasing attitude for the increasing values of K , and Le . On the other hand, it shows a decreasing nature towards δ_2 . The Eqs. (8.2)-(8.4) narrates MHD Casson nanofluid flow induced by stretching cylindrical surface in the presence of externally applied magnetic field. The flow regime is manifested with double stratification,

heat generation and chemical reaction effects. In absence of concentration equation and by setting $A = 0, N = 0, \alpha = 0^0, R_r = 0, Nb = 0$ and $Nt = 0$ our results match with Rehman et al. [136]. Tables 8.4-8.5 are constructed in this regard. Particularly Table 8.4 shows the comparative values of the local skin friction coefficient while Table 8.5 depicts the comparative values of local Nusselt number. From both tables one can see that we found an excellent match which yields the surety of present modelled work.

8.4.2 Velocity distribution

The impact of various physical parameters namely the magnetic field parameter, mixed convection parameter, Casson fluid parameter and curvature parameter towards both Casson fluid and the Newtonian fluid are presented with the help of graphical outcomes. In detail, Fig. 8.1 shows the influence of β on the velocity profile for both the cylindrical and flat surface. It is observed that for both the flat and cylindrical surfaces the velocity profile decreases towards the positive value of the Casson fluid parameter β . Fig. 8.2 depicts the impact of the curvature parameter K on the velocity profile for both the Casson and the Newtonian fluids. It shows that the larger values of the curvature parameter K results increase in velocity profiles for both fluid models. The curvature parameter has an inverse relation towards radius of curvature. Therefore, the radius of cylinder decreases for increasing values of curvature parameter and thus it reduces the contact surface area of the cylinder with the fluid particles and hence offers less resistance to the fluid flow. Thus an increase in the curvature parameter causes an increase in the velocity distributions. Fig. 8.3 demonstrated the influence of mixed convection parameter λ_m on the velocity profile. It is observed that for higher iterations of the mixed convection parameter, the velocity profile increases. Actually, it is due to the inciting nature of the thermal buoyancy force. Fig. 8.4 is plotted to observe the impact of the magnetic field parameter on the velocity of the fluid for both the Casson and the Newtonian fluid. The stimulating values of the magnetic field parameter produces reduction in the velocity profile. In actual, when we increase the magnetic field parameter, a resistive force named as Lorentz force contribute actively and offers resistance to the fluid particles which brings decline in the horizontal velocity. From Figs. 8.1-8.4 it can be observed that for larger values of η , the fluid velocity $F'(\eta)$

asymptotically converges to zero. These reflections are justified because the endpoint condition given by Eq. (8.12) is compatible with the trends depicted in Figs. 8.1-8.4.

8.4.3 Temperature distribution

The impacts of involved physical parameters namely, the thermophoresis parameter, Lewis number, curvature parameter, thermal radiation parameter, heat generation parameter and thermal stratification parameter on temperature distribution for both fluids i.e. Casson and Newtonian fluids are provided with the aid of the graphical trends. In detail, the effect of thermophoresis parameter over the temperature distribution is examined and given in Fig. 8.5. It is observed that the temperature distributions of both fluids are increasing function of the thermophoresis parameter. This is due to large amount of nanoparticles, which are pulled from hot surface towards the cold one, so that the temperature increases. The influence of the Lewis number is illustrated through Fig. 8.6. It is seen that for the increasing values of the Lewis number, the temperature distribution for both fluids reflects decaying performance. One can conclude the graphical trend mathematically with the support of Eq. (8.12) that the large value of η , the fluid temperature for both cases asymptotically converges to zero. Fig. 8.7 depicts an increasing behavior of temperature distribution of both the fluids towards the thermal radiation parameter. This is due to transfer of huge amount of heat into the fluid because an increase the thermal radiation parameter, more heat is produced and thus transfer to the fluid. Fig. 8.8 represents the impact of heat generation parameter on temperature profile for both the Casson and the Newtonian fluid flow. It is seen that the fluid temperature increases by increasing the heat generation parameter. In real practice, increase in heat generation parameter produces heat energy which yields inciting values of fluid temperature. Fig. 8.9 represents the behaviour of temperature distribution towards thermal stratification parameter for both types of fluids. It is noticed that the temperature profile decreases due to the increase in the thermal stratification parameter. This happens due to decrease in temperature difference between surface fluid and the ambient fluid, thus the temperature profile decreases. The variation in $\delta_1 = 0.0, 0.1, 0.2$ yields $T(\eta) = 1 - \delta_1 = (1 - 0.0, 0.1, 0.2) = (1, 0.9, 0.8)$. These initial approximations of fluid temperature for both fluid models can be seen in Fig. 8.9. In addition, the graphical trends given by Figs. 8.5-8.9 are compatible with the boundary condition given in Eq. (8.12).

8.4.4 Nanoparticle concentration distribution

The graphical representation against different physical parameters namely chemical reaction parameter, Lewis Number, and Solutal stratification parameter for both fluid models is provided through Figs. 8.10-8.13. In detail, the impact of the Brownian motion parameter on nanoparticle concentration for both fluids is given with the aid of Fig. 8.10. It shows that the nanoparticle concentration distribution shows decrease with the increment in the values of Brownian motion parameter. The graphical trend reflects the asymptotic decline in concentration via positive values of Brownian motion parameter and this effect is justified mathematically, (see Eq. (8.12)). The influence of the chemical reaction parameter on fluid concentration for both Casson and the Newtonian fluid is explained in Fig. 8.11. It is observed that the nanoparticle concentration field for both fluids is decreasing function of chemical reaction parameter. This is due to the noteworthy disturbance in the fluid molecules, so that a decrease in the nanoparticle concentration is observed. The influence of the Lewis number on the nanoparticle concentration distribution for both fluids is explained with the aid of Fig. 8.12. Here, an increase in the Lewis number produces a thin nanoparticle concentration boundary layer along with a weak diffusivity of molecules to each fluid. Fig. 8.13 is designed to investigate the variation of the nanoparticle concentration towards positive values of the Solutal stratification parameter for both the Casson and the Newtonian fluids. It is witnessed that by increasing the solutal parameter, a decline in the fluid concentration within the boundary layer is recorded. This effect occurs due to the drop of the convective potential between both fluids and the ambient marks. The variation in $\delta_2 = 0.0, 0.1, 0.2$ yields $C(\eta) = 1 - \delta_2 = (1 - 0.0, 0.1, 0.2) = (1, 0.9, 0.8)$. Such initial approximation of nanoparticle concentration for both fluid models can be seen in Fig. 8.13. Further, the Figs. 8.10-8.13 are compatible with the endpoint condition given in Eq. (8.12).

8.5 Graphical results

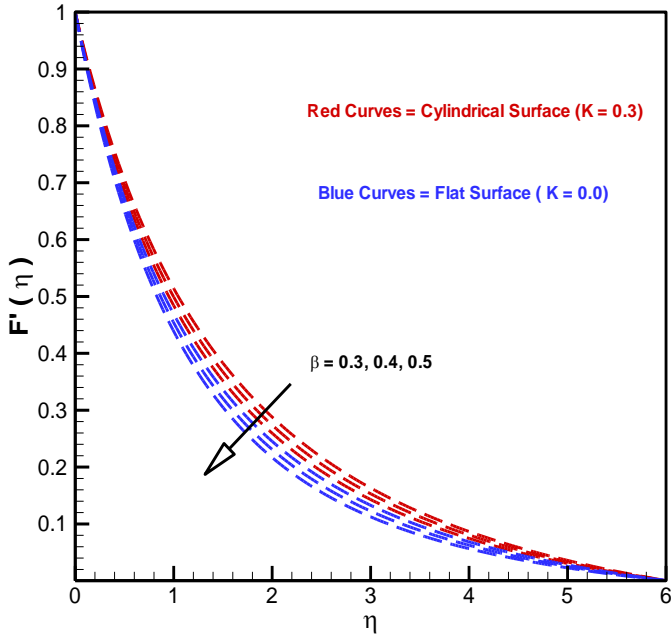


Fig. 8.1. Velocity profile towards Casson fluid parameter.

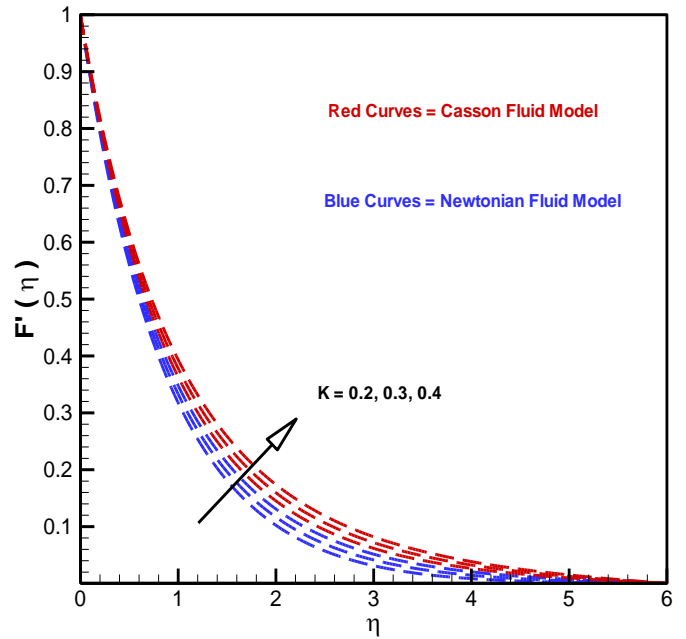


Fig. 8.2. Velocity profile towards curvature parameter.

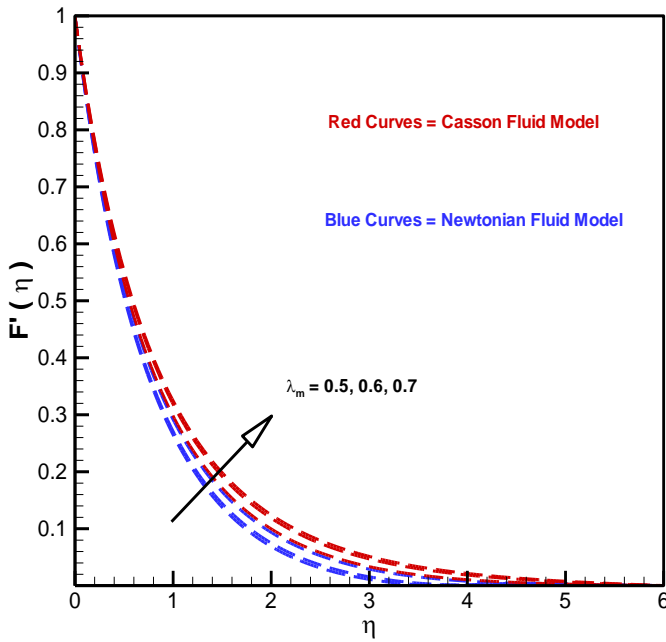


Fig. 8.3. Velocity profile towards mixed convection parameter.

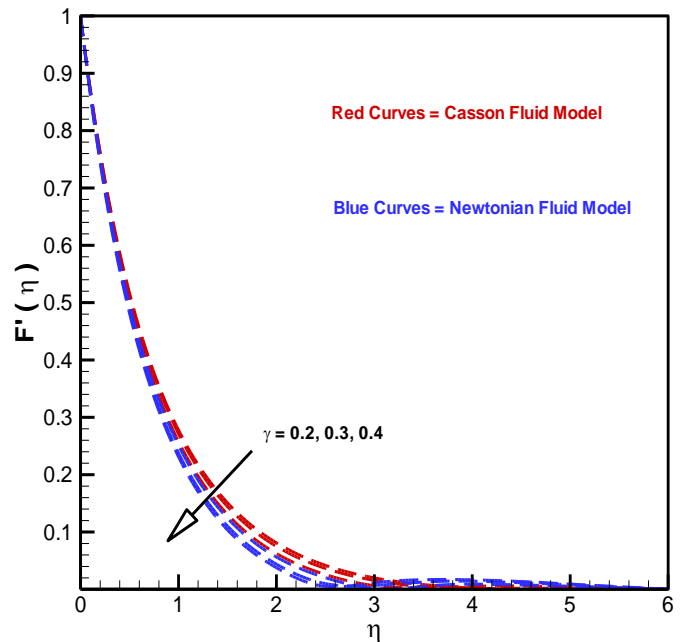


Fig. 8.4. Velocity profile towards magnetic field parameter.

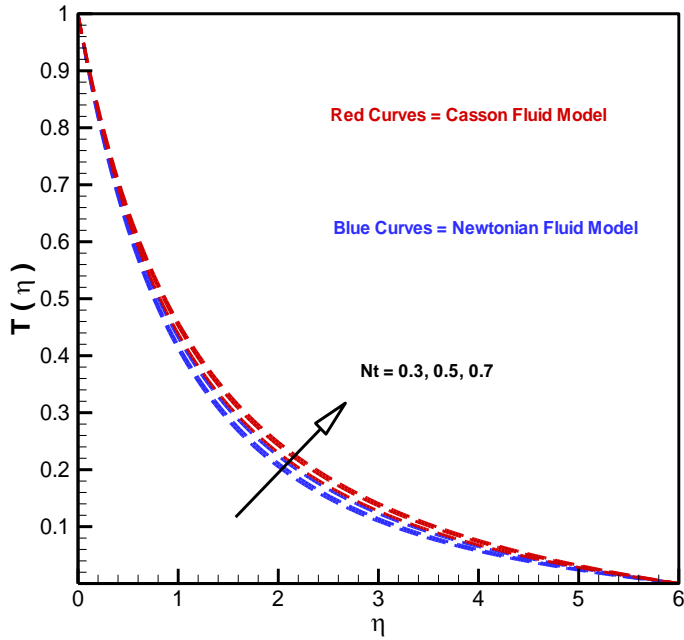


Fig. 8.5. Temperature profile towards thermophoresis parameter.

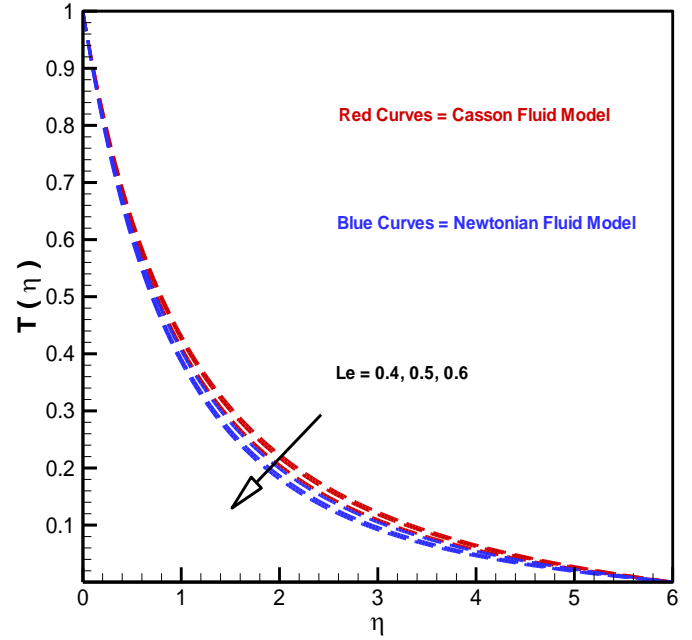


Fig. 8.6. Temperature profile towards Lewis number.

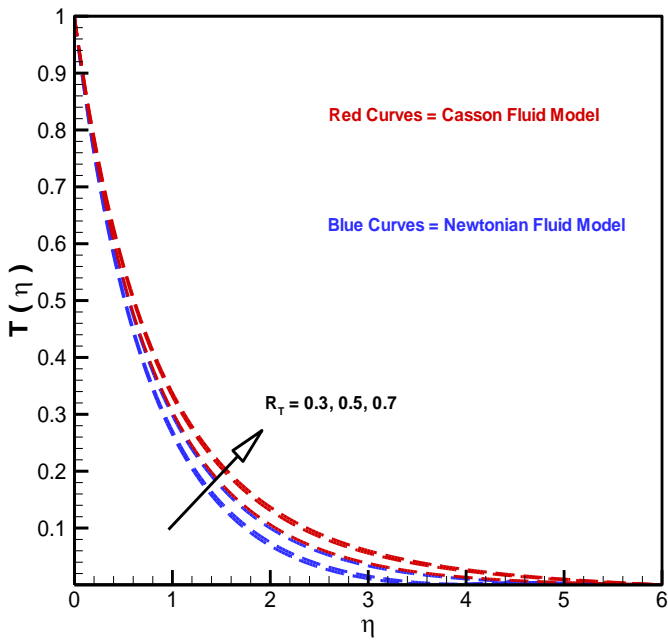


Fig. 8.7. Temperature profile towards thermal radiation parameter.

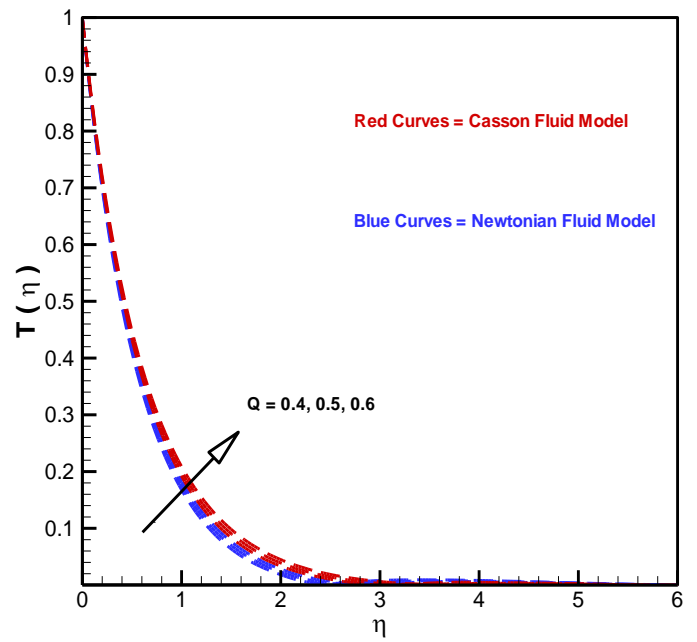


Fig. 8.8. Temperature profile towards heat generation parameter.

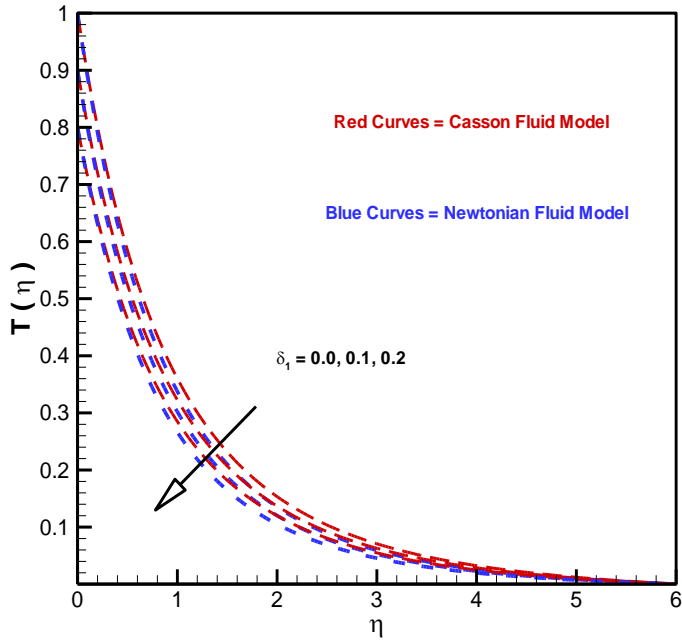


Fig. 8.9. Temperature profile towards thermal stratification parameter.

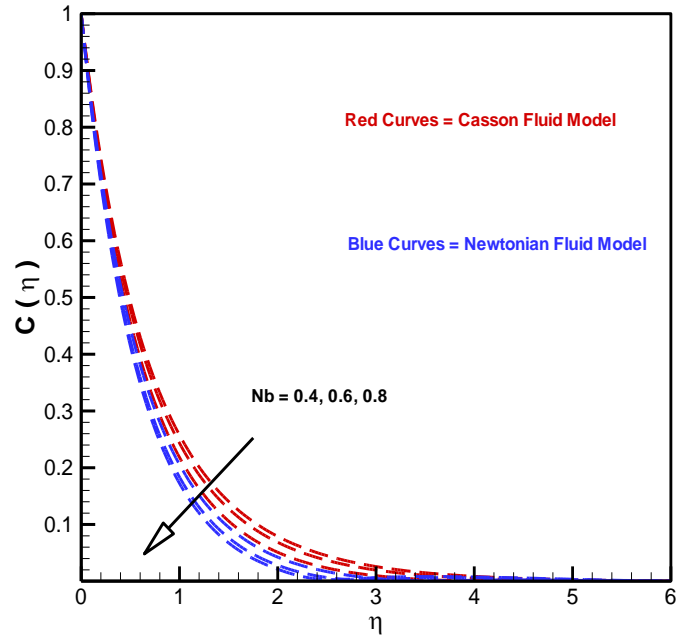


Fig. 8.10. Concentration profile towards Brownian motion parameter.

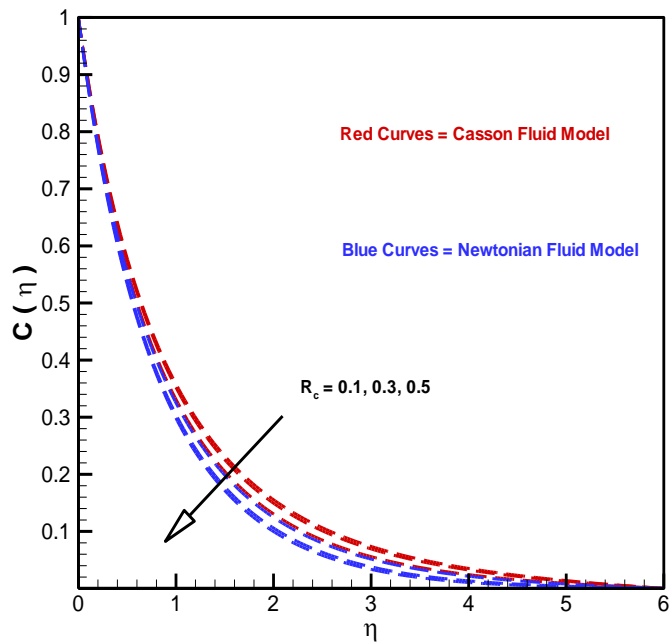


Fig. 8.11. Concentration profile towards chemical reaction parameter.

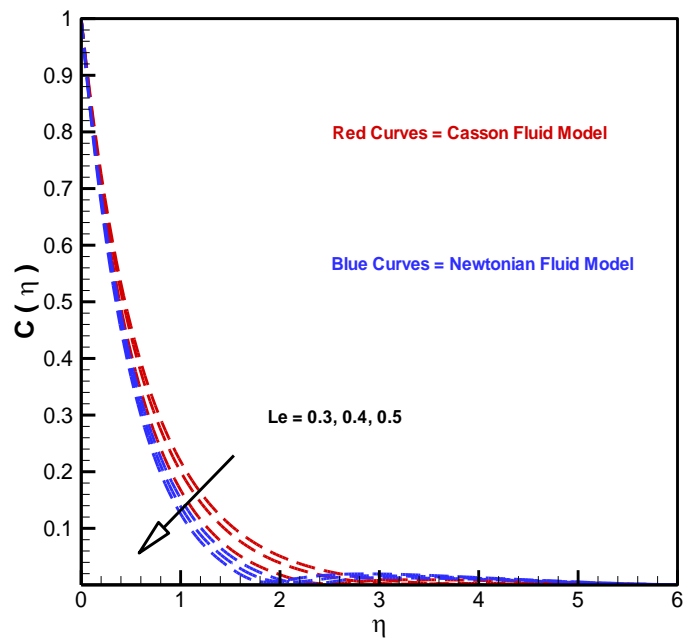


Fig. 8.12. Concentration profile towards Lewis number.

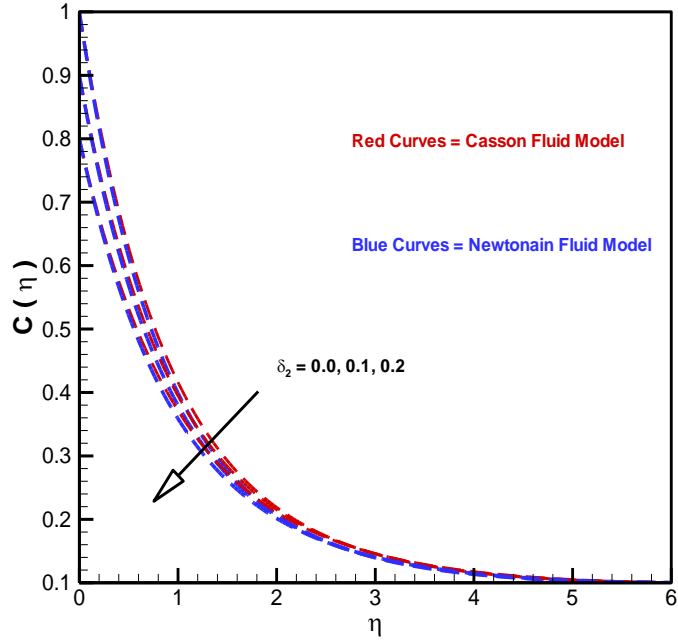


Fig. 8.13. Concentration profile towards Solutal stratification parameter.

Table. 8.1. Numerical values of local skin friction coefficient via various parameters.

| K | β | λ_m | Pr | $F''(0)$ | $0.5C_f\sqrt{\text{Re}_x} = \left(1 + \frac{1}{\beta}\right)F''(0)$ |
|-----|---------|-------------|-----|----------|---|
| 0.4 | - | - | - | -0.7863 | -2.3589 |
| 0.5 | - | - | - | -0.9204 | -2.7612 |
| 0.6 | - | - | - | -1.0539 | -3.1617 |
| - | 1.1 | - | - | -0.7969 | -2.3907 |
| - | 1.2 | - | - | -0.8110 | -2.4330 |
| - | 1.3 | - | - | -0.8236 | -2.4708 |
| - | - | 0.2 | - | -0.4064 | -1.2192 |
| - | - | 0.4 | - | -0.4008 | -1.2024 |
| - | - | 0.6 | - | -0.3953 | -1.1859 |
| - | - | - | 0.8 | -0.4092 | -1.2276 |
| - | - | - | 1.0 | -0.4092 | -1.2276 |
| - | - | - | 1.2 | -0.4092 | -1.2276 |

Table. 8.2. Numerical values of local Nusselt number via various parameters.

| K | Pr | δ_1 | $-T'(0)$ | $\frac{Nu_x}{\sqrt{Re_x}} = -\left(1 + \frac{4}{3}R_d\right)T'(0)$ |
|-----|-----|------------|----------|--|
| 0.3 | - | - | 0.7817 | 1.09438 |
| 0.5 | - | - | 1.1299 | 1.58186 |
| 0.7 | - | - | 1.4716 | 2.06024 |
| - | 1.5 | - | 1.4024 | 1.96336 |
| - | 1.7 | - | 1.4712 | 2.05968 |
| - | 1.9 | - | 1.5332 | 2.14648 |
| - | - | 0.2 | 0.2585 | 0.36190 |
| - | - | 0.4 | 0.1939 | 0.27146 |
| - | - | 0.6 | 0.1293 | 0.18102 |

Table. 8.3. Numerical values of local Sherwood number via various parameters.

| K | δ_2 | Le | Pr | $\frac{Sh_x}{\sqrt{Re_x}} = -C'(0)$ |
|-----|------------|------|-----|-------------------------------------|
| 0.2 | - | - | - | 1.4913 |
| 0.3 | - | - | - | 1.8466 |
| 0.4 | - | - | - | 2.1845 |
| - | 0.1 | - | - | 1.1297 |
| - | 0.2 | - | - | 1.0858 |
| - | 0.3 | - | - | 1.0420 |
| - | - | 0.4 | - | 1.1546 |
| - | - | 0.5 | - | 1.1627 |
| - | - | 0.6 | - | 1.1706 |
| - | - | - | 1.3 | 1.4752 |
| - | - | - | 1.5 | 1.5020 |
| - | - | - | 1.7 | 1.5271 |

Table. 8.4. Comparison with local skin friction coefficient.

| | β | λ_m | Pr | δ_1 | Q | Rehman et al. [136] | Present values |
|-----|---------|-------------|-----|------------|-----|---------------------|----------------|
| 0.1 | - | - | - | - | - | -0.3826 | -0.3826 |
| 0.2 | - | - | - | - | - | -0.4036 | -0.4036 |
| 0.3 | - | - | - | - | - | -0.4248 | -0.4248 |
| - | 1.3 | - | - | - | - | -0.3826 | -0.3826 |
| - | 1.4 | - | - | - | - | -0.3884 | -0.3884 |
| - | 1.5 | - | - | - | - | -0.3928 | -0.3928 |
| - | - | 0.1 | - | - | - | -0.3826 | -0.3826 |
| - | - | 0.2 | - | - | - | -0.3679 | -0.3679 |
| - | - | 0.3 | - | - | - | -0.3535 | -0.3535 |
| - | - | - | 0.6 | - | - | -0.3816 | -0.3816 |
| - | - | - | 0.7 | - | - | -0.3826 | -0.3826 |
| - | - | - | 0.8 | - | - | -0.3835 | -0.3835 |
| - | - | - | - | 0.1 | - | -0.3826 | -0.3826 |
| - | - | - | - | 0.2 | - | -0.3851 | -0.3851 |
| - | - | - | - | 0.3 | - | -0.3877 | -0.3877 |
| - | - | - | - | - | 0.1 | -0.3826 | -0.3826 |
| - | - | - | - | - | 0.2 | -0.3821 | -0.3821 |
| - | - | - | - | - | 0.3 | -0.3813 | -0.3813 |

Table. 8.5. Comparison with local Nusselt number.

| K | β | λ_m | Pr | δ_1 | Q | Rehman et al. [136] | Present values |
|-----|---------|-------------|-----|------------|-----|---------------------|----------------|
| 0.1 | - | - | - | - | - | 0.8254 | 0.8254 |
| 0.2 | - | - | - | - | - | 0.8599 | 0.8599 |
| 0.3 | - | - | - | - | - | 0.8948 | 0.8948 |
| - | 1.3 | - | - | - | - | 0.8254 | 0.8254 |
| - | 1.4 | - | - | - | - | 0.8225 | 0.8225 |
| - | 1.5 | - | - | - | - | 0.8200 | 0.8200 |
| - | - | 0.1 | - | - | - | 0.8254 | 0.8254 |
| - | - | 0.2 | - | - | - | 0.8322 | 0.8322 |
| - | - | 0.3 | - | - | - | 0.8387 | 0.8387 |
| - | - | - | 0.6 | - | - | 0.7542 | 0.7542 |
| - | - | - | 0.7 | - | - | 0.8254 | 0.8254 |
| - | - | - | 0.8 | - | - | 0.8930 | 0.8930 |
| - | - | - | - | 0.1 | - | 0.8254 | 0.8254 |
| - | - | - | - | 0.2 | - | 0.7958 | 0.7958 |
| - | - | - | - | 0.3 | - | 0.7662 | 0.7662 |
| - | - | - | - | - | 0.1 | 0.8254 | 0.8254 |
| - | - | - | - | - | 0.2 | 0.7789 | 0.7789 |
| - | - | - | - | - | 0.3 | 0.7275 | 0.7275 |

8.6 Concluding remarks

The present work is devoted to report numerical communication subject to both the Newtonian and Casson fluid flow brought by stretching cylindrical surface. The flow regime carry stagnation point, magnetic field, mixed convection, double stratification, heat generation and chemical reaction effects. A numerical solution is presented and the key observations are given as:

- The velocity distribution shows an increasing behaviour towards the increasing values of the mixed convection parameter λ_m and the curvature parameter K , but opposite trends are noticed for the Casson fluid parameter β and the magnetic field parameter γ .
- The temperature profile shows an inciting nature towards the positive values of the thermophoresis parameter N_t , thermal radiation parameter R_T and the heat generation parameter Q whereas it shows a decline curves towards the increasing values of the Lewis number Le , and the thermal stratification parameter δ_1 .
- For both cases the concentration distribution is a decreasing function of the Brownian motion parameter N_b , chemical reaction parameter R_c , Lewis number Le and the Solutal stratification parameter δ_2 .
- It is noticed that Casson fluid as a non-Newtonian fluid model reflects significant variations towards an involved physical parameters in contrast to Newtonian fluid model.

CHAPTER 9

A Comparative Study of Nanofluids Flow Yields by an Inclined Cylindrical Surface in a Double Stratified Medium

9.1 Introduction

In this attempt, we have considered both Newtonian and non-Newtonian nanofluids flow with stagnation point towards an inclined cylindrical surface. The flow field own thermal radiation, mixed convection, chemical reaction, temperature, concentration stratification, heat generation/absorption and magnetic field. The reduced system of ODE's is obtained by transforming flow narrating PDE's with the aid of appropriate transformation. Shooting method is used for solution. To be more specific, the effects of an involved pertinent flow parameters are discussed for both $\lambda = 0$ (Newtonian fluid) and $\lambda = 0.5$ (non-Newtonian fluid). The non-Newtonian fluid reflects considerable variations towards flow parameters as compared to Newtonian fluid. Further, the compatibility of endpoint conditions is validated by providing stream lines pattern towards velocities ratio parameter. In addition, the influence of thermophoresis and Brownian motion parameters are reported on mass and heat transfer rates by way of both straight line and parabolic curve fitting scheme.

9.2 Mathematical description

We have considered a steady laminar magneto-hydrodynamic incompressible boundary layer flow of both Newtonian and non-Newtonian (Williamson model) nanofluids with zero pressure gradient. The nanofluids flow is induced by an inclined cylinder in the presence of chemically reactive species. Further, both the heat and mass transfer characteristics are identified by an incorporating thermal radiation, temperature and concentration stratification effects. Moreover, the cylinder axial line is ranged parallel to x -axis and radial direction is aligned normal to x -axis and considered as r -axis.

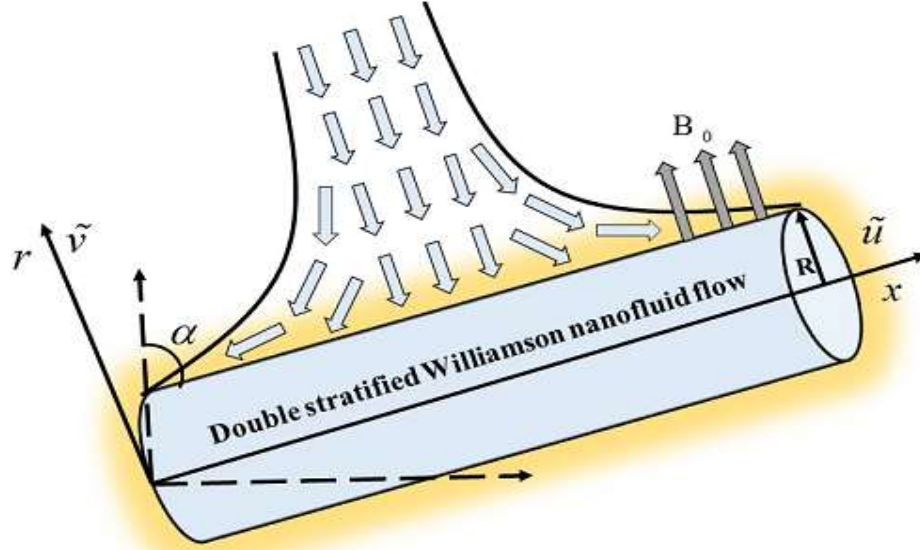


Fig. 9.1. Geometry of flow model.

The generally accepted differential equations namely, concentration, energy, and momentum are sufficient to depicts the flow fields characteristics in a two dimensional frame of reference. Therefore, the finalized form of these differential equations under boundary layer approximation is given as:

$$\frac{\partial(r\tilde{v})}{\partial r} + \frac{\partial(r\tilde{u})}{\partial x} = 0, \quad (9.1)$$

$$\begin{aligned} \frac{\partial\tilde{v}}{\partial r}\tilde{v} + \frac{\partial\tilde{u}}{\partial x}\tilde{u} = v \left(\frac{\partial^2\tilde{u}}{\partial r^2} + \frac{1}{r}\frac{\partial\tilde{u}}{\partial r} + \sqrt{2}\Gamma\frac{\partial^2\tilde{u}}{\partial r^2}\frac{\partial\tilde{u}}{\partial r} + \left(\frac{\partial\tilde{u}}{\partial r}\right)^2\frac{\Gamma}{\sqrt{2}r} \right) \\ + \tilde{u}_e\frac{\partial\tilde{u}_e}{\partial x} - \frac{\sigma B_0^2}{\rho}(\tilde{u} - \tilde{u}_e) + g(\beta_T(\tilde{T} - \tilde{T}_\infty) + \beta_c(\tilde{C} - \tilde{C}_\infty))\cos\alpha, \end{aligned} \quad (9.2)$$

$$\begin{aligned} \frac{\partial\tilde{T}}{\partial r}\tilde{v} + \frac{\partial\tilde{T}}{\partial x}\tilde{u} = \frac{\partial}{\partial r}\left(r\frac{\partial\tilde{T}}{\partial r}\right)\frac{\alpha^*}{r} - \frac{1}{\rho c_p r}\frac{\partial}{\partial r}(rq_r) \\ + \tau\left(\frac{D_T}{\tilde{T}_\infty}\left(\frac{\partial\tilde{T}}{\partial r}\right)^2 + D_B\frac{\partial\tilde{T}}{\partial r}\frac{\partial\tilde{C}}{\partial r}\right) + \frac{Q_0}{c_p\rho}(\tilde{T} - \tilde{T}_\infty), \end{aligned} \quad (9.3)$$

$$\frac{\partial\tilde{C}}{\partial r}\tilde{v} + \frac{\partial\tilde{C}}{\partial x}\tilde{u} = \left(\frac{1}{r}\frac{\partial\tilde{C}}{\partial r} + \frac{\partial^2\tilde{C}}{\partial r^2}\right)D_B + \left(\frac{1}{r}\frac{\partial\tilde{T}}{\partial r} + \frac{\partial^2\tilde{T}}{\partial r^2}\right)\frac{D_T}{\tilde{T}_\infty} - R_o(\tilde{C} - \tilde{C}_\infty), \quad (9.4)$$

here, $q_r = -\left(\frac{4}{3}\right)\frac{\sigma^*}{k^*}\frac{\partial\tilde{T}^4}{\partial r}$, therefore Eq. (9.3) can be rewritten as:

$$\begin{aligned} \tilde{u} \frac{\partial \tilde{T}}{\partial x} + \tilde{v} \frac{\partial \tilde{T}}{\partial r} &= \frac{\alpha^*}{r} \frac{\partial}{\partial r} \left(r \frac{\partial \tilde{T}}{\partial r} \right) + \frac{1}{\rho c_p r} \left(\frac{4}{3} \right) \frac{\sigma^*}{k^*} \frac{\partial}{\partial r} \left(r \frac{\partial \tilde{T}^4}{\partial r} \right) \\ &+ \tau \left(\frac{D_T}{\tilde{T}_\infty} \left(\frac{\partial \tilde{T}}{\partial r} \right)^2 + D_B \frac{\partial \tilde{T}}{\partial r} \frac{\partial \tilde{C}}{\partial r} \right) + \frac{Q_0}{c_p \rho} (\tilde{T} - \tilde{T}_\infty), \end{aligned} \quad (9.5)$$

subjected to endpoint conditions:

$$\begin{aligned} \tilde{u} &= U(x) = ax, \quad \tilde{v} = 0, \quad \text{at } r=R, \quad \tilde{u} \rightarrow \tilde{u}_e = a'x, \quad \text{as } r \rightarrow \infty, \\ \tilde{T}(x, r) &= \tilde{T}_w(x) = \tilde{T}_0 + \frac{b x}{L}, \quad \tilde{C}(x, r) = \tilde{C}_w(x) = \tilde{C}_0 + \frac{d x}{L} \quad \text{at } r=R, \\ \tilde{T}(x, r) &\rightarrow \tilde{T}_\infty(x) = \tilde{T}_0 + \frac{c x}{L}, \quad \tilde{C}(x, r) \rightarrow \tilde{C}_\infty(x) = \tilde{C}_0 + \frac{e x}{L} \quad \text{as } r \rightarrow \infty, \end{aligned} \quad (9.6)$$

For dimensionless practice of Eqs. (9.2)-(9.5) along with Eq. (9.6), we have transformation:

$$\begin{aligned} \tilde{v} &= -\frac{R}{r} \sqrt{\frac{U_0 \nu}{L}} F(\eta), \quad \tilde{u} = \frac{U_0 x}{L} F'(\eta), \quad \eta = \frac{r^2 - R^2}{2R} \left(\frac{U_0}{\nu L} \right)^{\frac{1}{2}}, \\ \psi &= \left(\frac{U_0 \nu x^2}{L} \right)^{\frac{1}{2}} R F(\eta), \quad C(\eta) = \frac{\tilde{C} - \tilde{C}_\infty}{\tilde{C}_w - \tilde{C}_0}, \quad T(\eta) = \frac{\tilde{T} - \tilde{T}_\infty}{\tilde{T}_w - \tilde{T}_0}, \end{aligned} \quad (9.7)$$

The velocity components subject to stream function can be written as:

$$\tilde{u} = \frac{1}{r} \left(\frac{\partial \psi}{\partial r} \right), \quad \tilde{v} = \frac{-1}{r} \left(\frac{\partial \psi}{\partial x} \right), \quad (9.8)$$

after utilizing Eq. (9.7) into Eqs. (9.2)-(9.5), we obtained:

$$\begin{aligned} (1 + 2K\eta) F'''(\eta) + F(\eta) F''(\eta) + 2KF''(\eta) - (F'(\eta))^2 \\ + 2\lambda (2K\eta + 1)^{\frac{3}{2}} F''(\eta) F'''(\eta) + 3\lambda K ((2K\eta + 1))^{\frac{1}{2}} F''(\eta)^2 \\ - \gamma^2 (F' - A) + A^2 + \lambda_m (T(\eta) + NC(\eta)) \cos \alpha = 0, \end{aligned} \quad (9.9)$$

$$\begin{aligned} 2K \left(1 + \frac{4}{3} R_d \right) T'(\eta) + \text{Pr} Nb (1 + 2K\eta) \left(T(\eta)' C(\eta)' + \frac{Nt}{Nb} T(\eta)^2 \right) \\ + (1 + 2K\eta) \left(1 + \frac{4}{3} R_d \right) T''(\eta) + \text{Pr} \left(\frac{F(\eta) T'(\eta) - F'(\eta) \delta_1}{+QT(\eta) - F'(\eta) T(\eta)} \right) = 0, \end{aligned} \quad (9.10)$$

$$\begin{aligned} (1 + 2K\eta) \left(C''(\eta) + \frac{Nt}{Nb} T''(\eta) \right) + \text{Pr} Le (F(\eta) C'(\eta) - F'(\eta) C(\eta) - F'(\eta) \delta_2) \\ + 2K \left(C'(\eta) + \frac{Nt}{Nb} T'(\eta) \right) - R_c C(\eta) = 0, \end{aligned} \quad (9.11)$$

the reduced endpoint conditions are given as:

$$F'(0) = 1, F(\infty) = 0, T(\eta) = 1 - \delta_1, C(\eta) = 1 - \delta_2, \text{ at } \eta = 0, \quad (9.12)$$

$$F'(\eta) \rightarrow A, T(\eta) \rightarrow 0, C(\eta) \rightarrow 0, \text{ when } \eta \rightarrow \infty.$$

here, the involved parameters are given as follow:

$$\begin{aligned} K &= \frac{1}{R} \sqrt{\frac{\nu}{a}}, \quad a = \frac{U_0}{L}, \quad \lambda = \frac{\Gamma a^{\frac{3}{2}} x}{\sqrt{2\nu L^{\frac{3}{2}}}}, \quad \gamma = \sqrt{\frac{\sigma\beta_0^2}{\rho a}}, \quad A = \frac{a'}{a}, \\ \lambda_m &= \frac{Gr}{\text{Re}_x^2}, \quad N = \frac{Gr^*}{Gr}, \quad R_d = \frac{4\sigma^* T_\infty^3}{k^* k}, \quad \text{Pr} = \frac{\nu}{\alpha^*}, \quad Nb = \frac{(\tilde{C}_w - \tilde{C}_\infty)\tau D_B}{\nu}, \\ Nt &= \frac{(\tilde{T}_w - \tilde{T}_\infty)\tau D_T}{\nu \tilde{T}_\infty}, \quad \delta_1 = \frac{c}{b}, \quad Q = \frac{LQ_0}{U_0 \rho c_p}, \quad Le = \frac{\alpha^*}{D_B}, \quad \delta_2 = \frac{e}{d}, \quad R_c = \frac{R_o L}{U_o}, \end{aligned} \quad (9.13)$$

here, thermal Grashof number Gr , and solutal Grashof number Gr^* are identified as:

$$Gr = \frac{(\tilde{T}_w - \tilde{T}_0)g\beta_T x^3}{\nu^2}, \quad Gr^* = \frac{(\tilde{C}_w - \tilde{C}_0)g\beta_C x^3}{\nu^2}. \quad (9.14)$$

The skin friction coefficient subject to Williamson fluid model is given as:

$$C_f = \frac{\tau_w}{\rho \frac{U^2}{2}}, \quad \tau_w = \mu \left[\left(\frac{\partial \tilde{u}}{\partial r} \right) + \frac{1}{\sqrt{2}} \Gamma \left(\frac{\partial \tilde{u}}{\partial r} \right)^2 \right]_{r=R}, \quad (9.15)$$

the corresponding dimensionless form is prearranged as:

$$C_f \text{Re}_x^{1/2} = F''(0) + \lambda F''(0)^2, \quad (9.16)$$

The local Nusselt and Sherwood number are written as:

$$\begin{aligned} Nu_x &= \frac{xq_w}{k(\tilde{T}_w - \tilde{T}_0)}, \quad q_w = -k \left(\frac{\partial \tilde{T}}{\partial r} \right)_{r=R} + (q_r)_{r=R}, \\ Sh &= \frac{xj_w}{D(\tilde{C}_w - \tilde{C}_0)}, \quad j_w = -D \left(\frac{\partial \tilde{C}}{\partial r} \right)_{r=R}, \end{aligned} \quad (9.17)$$

the corresponding dimensionless forms are given as:

$$\begin{aligned} Nu_x \text{Re}_x^{-1/2} &= - \left(1 + \frac{4}{3} R_d \right) T'(\eta), \text{ at } \eta \rightarrow 0, \\ Sh \text{Re}_x^{-1/2} &= -C'(\eta), \text{ at } \eta \rightarrow 0. \end{aligned} \quad (9.18)$$

9.3 Computational algorithm

The non-linear system of ODE's i-e Eqs. (9.9)-(9.11), under endpoint conditions given by Eq. (9.12) is solved with the aid of shooting scheme together with R-K algorithm. The order has been reduced by the implementing

$$w_2 = F'(\eta), \quad w_3 = w'_2 = F''(\eta), \quad w_5 = T'(\eta), \quad w_7 = C'(\eta), \quad (9.19)$$

the equivalent form of Eqs. (9.9)-(9.11) under new variables defined above can be written as:

$$\begin{aligned} w'_1 &= w_2, \\ w'_2 &= w_3, \\ w'_3 &= \frac{\left\{ \begin{aligned} &(w_2)^2 - w_1 w_3 - 2Kw_3 - 3\lambda K(1+2K\eta)^{\frac{1}{2}} w_3^3 + \gamma^2(w_2 - A) \\ &-A^2 - \lambda_m(w_4 + Nw_6) \cos \alpha \end{aligned} \right\}}{(1+2K\eta) + 2\lambda(1+2K\eta)^{\frac{3}{2}} w_3}, \\ w'_4 &= w_5, \\ w'_5 &= \frac{\left\{ \begin{aligned} &\text{Pr}(w_2 w_4 + \delta_1 w_2 - w_1 w_5 - Qw_4) - 2K(1 + \frac{4}{3}R_d)w_5 \\ &- \text{Pr} Nb(1+2K\eta)(w_5 w_7 + \frac{Nt}{Nb} w_5^2) \end{aligned} \right\}}{(1+2K\eta)(1 + \frac{4}{3}R_d)}, \\ w'_6 &= w_7, \\ w'_7 &= \frac{\left\{ \begin{aligned} &\text{Pr} Le(w_2 w_6 + \delta_2 w_2 - w_1 w_7) - (1+2K\eta) \frac{Nt}{Nb} w'_5 \\ &- 2K(w_7 + \frac{Nt}{Nb} w_5) + R_c w_6 \end{aligned} \right\}}{1+2K\eta}, \end{aligned} \quad (9.20)$$

under new variables the endpoint conditions are given as follow:

$$\begin{aligned}
w_1(0) &= 0, \\
w_2(0) &= 1, \\
w_3(0) &= \text{First initial guess}, \\
w_4(0) &= 1 - \delta_1, \\
w_5(0) &= \text{Second initial guess}, \\
w_6(0) &= 1 - \delta_2, \\
w_7(0) &= \text{Third initial guess}.
\end{aligned} \tag{9.21}$$

For integration of Eq. (9.20) we required:

$$w_3(\eta) = F''(\eta), w_5(\eta) = T'(\eta) \text{ and } w_7(\eta) = T'(\eta) \text{ when } \eta \rightarrow 0, \tag{9.22}$$

further, we observed that the three initial conditions namely,

$w_3(\eta)$, $w_5(\eta)$ and $w_7(\eta)$ when $\eta \rightarrow 0$ are not available but additional conditions are given:

$$w_2(\eta) = A, w_4(\eta) = 0, \text{ and } w_6(\eta) = 0, \text{ when } \eta \rightarrow 0. \tag{9.23}$$

The iterative solution is carried out against suitable values of $F''(0)$, $T'(0)$ and $C'(0)$ so that Eq. (9.23) holds absolutely.

9.4 Physical outcomes

9.4.1 Tabular values

Tables 9.1, 9.2 and 9.3 are constructed numerically to inspect the impact of pertinent flow controlling parameter namely, curvature parameter K , magnetic field parameter γ , Weissenberg number λ , Prandtl number Pr , solutal stratification parameter δ_2 , Lewis number Le and thermal stratification parameter δ_1 on skin friction coefficient, local Nusselt number and Sherwood number. Particularly, Table 9.1 shows that skin friction coefficient increases (in absolute sense) towards γ , λ , K and Pr . From Table 9.2, it is clearly seen that local Nusselt number increases for positive values of K and Pr but it has opposite attitude towards δ_1 . The influence of K , δ_2 , Le and Pr is presented with the aid of Table 9.3. It is observed that local Sherwood number shows significant decline for the positive values of δ_2 while opposite attitude is noticed against K , Le and Pr . In the absence of Eq. (9.10) and Eq. (9.11), when we incorporate mixed convection parameter, velocities ratio parameter, magnetic field parameter, curvature parameter and an

inclination equals to zero i-e $K=0, A=0, \gamma=0, \lambda_m=0,$ and $\alpha=0^0$, . We retrace the problems given in [53] and [137]. Therefore, Table 9.4 is constructed to validate our current results with existing literature. An excellent match has been found which confirms the accuracy of numerical algorithm.

9.4.2 Key to the graphs

Eqs. (9.9)-(9.11) subject to boundary conditions given by Eq. (9.12) represent mathematical formulation of stagnation point Williamson nanofluid (non-Newtonian fluid model) flow towards an inclined cylinder on attendance of mixed convection, magnetic field, double stratification, thermal radiation and heat generation/absorption effects. For $\lambda \neq 0$, the Eqs. (9.9)-(9.11) represents Williamson nanofluid as a non-Newtonian fluid model whereas $\lambda = 0$ narrates Newtonian nanofluid flow. The graphical results (fig. 9.2 and figs. 9.6-9.17) are offered for different physical parameters by setting $\lambda = 0.5$ (non-Newtonian fluid) and $\lambda = 0$ (Newtonian fluid). To be more specific, fig. 9.2 and figs. 9.6-9.17, the red long dashes curves represent Williamson nanofluid variations as a non-Newtonian fluid model while solid green curves represent Newtonian nanofluid variations.

9.4.3 Velocity profiles

The physical illustration of flow problem is given by fig. 9.1. The effects of velocities ratio parameter A on nanofluids flow are illustrated in fig. 9.2. It was observed that the frequent fluctuations in momentum of both Newtonian and non-Newtonian fluids are occurred for altering values of velocities ratio parameter. The increasing values of velocities ratio parameter reflects positive attitude in the velocities of both fluids. It is observed that momentum boundary layer is formed $A > 1$ but an inverted boundary layer is emerged for the case of $A < 1$. When velocities ratio parameter achieve unity that is $A = 1$, at this stage free stream and stretching velocities becomes equal so that momentum boundary layer disappears. The stream lines pattern for $A < 1$ is offered through fig. 9.3. In this case, the stretching rate overcomes the free stream condition so that the thickness of boundary layer shows inciting values in contrast to free stream velocity. Fig. 9.4 scrutinizes the stream lines for $A = 1$, which implies to equal values of free stream velocity and stretching velocity. It was found that stream lines are symmetric about radial direction.

The variation of stream lines for $A > 1$ is reported in fig. 9.5. For $A > 1$, the free stream velocity remarks greater values against stretching velocity so that the straining movement of fluid particles near stagnation region brings enhancement in fluid flow which yields decline in boundary layer. Fig. 9.6 depicts the impact of γ on velocity profile for both fluids. As expected, an inciting values of γ brings decline in velocity profiles. In actual, when we enhance the value of γ a resistive force named as Lorentz force actively participates to offer resistance towards fluid particles. As a result horizontal velocity decreases. The effects of λ_m on velocity are given by fig. 9.7 and it is noticed that by increasing values of λ_m the velocity profile shows an inciting nature for both cases.

9.4.4 Temperature profiles

Fig. 9.8 depicts the attitude of temperature distribution towards δ_1 and it is noticed that the temperature profile show decline trends in curves for increasing δ_1 . This fact is due to decline in temperature strength between ambient and cylindrical surface. The influence of both heat generation (positive values of Q) and heat absorption parameter (negative values of Q) on temperature profiles for both fluids is illustrated through Fig. 9.9 and Fig. 9.10 respectively. In Fig. 9.9 it is observed that the fluid temperature remarkably increases while opposite trend is noticed in Fig. 9.10 against heat absorption parameter. For positive variations of Q , the heat energy is generated due to which temperature rises while heat energy is released in case of heat absorption parameter and hence declines in the temperature distribution for both fluids. From Fig. 9.11, it is witnessed that the temperature of both fluids shows an inciting attitude towards R_d . This fact is due to plenty of heat transfer into the fluid because of increasing R_d , more heat is produced and hence transfer towards flow regime. Fig. 9.12 paints the temperature variation against K . It is clearly seen that fluid temperature increases for inciting values of K . The positive variations of K admits decrease in radius of cylinder so that less resistance is faced by fluid particles which confirms the acceleration generated by fluid particles and increase in average kinetic energy. The average kinetic energy is termed as Kelvin temperature therefore, an enhancement in average kinetic energy yields the positive variations of fluid temperature.

From fig. 9.13, it is evident that an inciting values of Pr corresponds less diffusion of energy due to which temperature profile decreases.

9.4.5 Concentration profiles

The influence of Nt over a temperature is illustrated with the help of Fig. 9.14. It is seen that temperature distributions for both fluids are mount function of Nt .. This fact is due to huge amount of pulled nanoparticles towards cold surface from hot one, as a result temperature increases. Fig. 9.15 is plotted to inspect the variation of nanoparticle concentration for both Newtonian and non-Newtonian fluid towards positive values of δ_2 . It is observed that there is a decline in fluid concentration within a boundary layer for increment in δ_2 . Essentially, this effect is similar as the fluid variations are noticed against δ_1 . The effect of R_c for both Newtonian and non-Newtonian fluid is illustrated in Fig. 9.16. It is perceived that the nanoparticle concentration field of both fluids is diminishing function of R_c . Further, decline in solute nanoparticle concentration is noticed due to remarkable disturbance in fluid molecules. The influence of Nb on both Newtonian and non-Newtonian is depicted through Fig. 9.17. It shows that with gradual growth in Nb nanoparticle concentration distribution shows a decline tendency. The influence of both Nt and Nb on heat transfer rate as well as on mass transfer is identified by means of straight line and parabolic approximations via Figs. 9.18-9.19. To be more specific, Fig. 9.18 portray the effect of both Nt (variation encountered through green color) and Nb (variation encountered through red color) on heat transfer rate. The heat transfer rate shows decline nature for both Nt and Nb . The mass transfer rate variation towards both Nt (variation encountered through red color) and Nb (variation encountered through green color) are identified by Fig. 9.19. Here, we observed that mass transfer rate is an increasing function of Nb but opposite trend is noticed for higher values of Nt .

9.5 Graphical outcomes

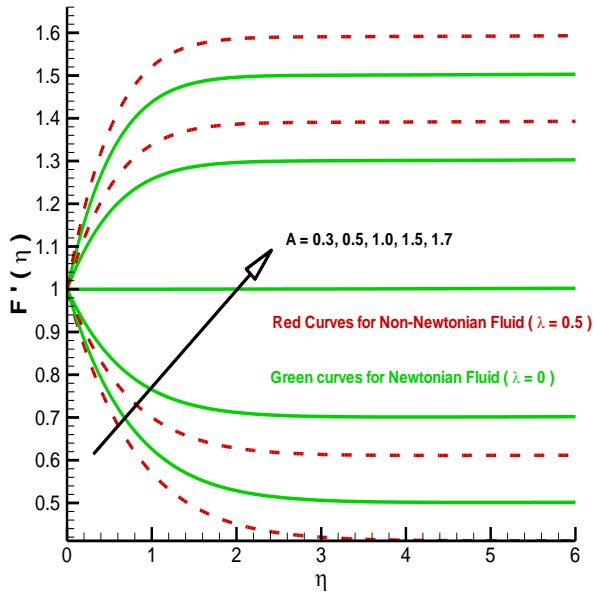


Fig. 9.2. Velocity profiles for various values of A .

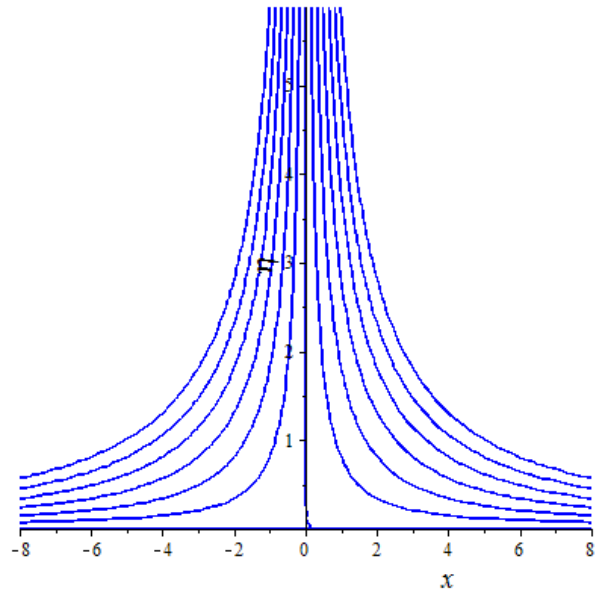


Fig. 9.3. Stream lines pattern of Williamson fluid flow for

$A < 1$.

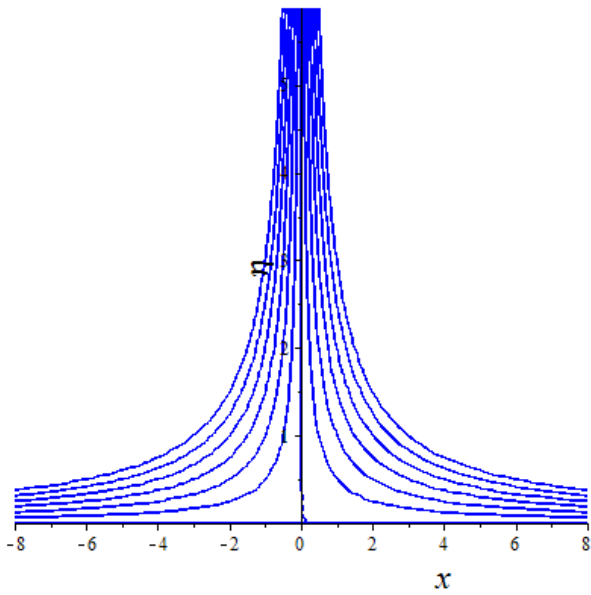


Fig. 9.4. Stream lines pattern of Williamson fluid flow
for $A = 1$.

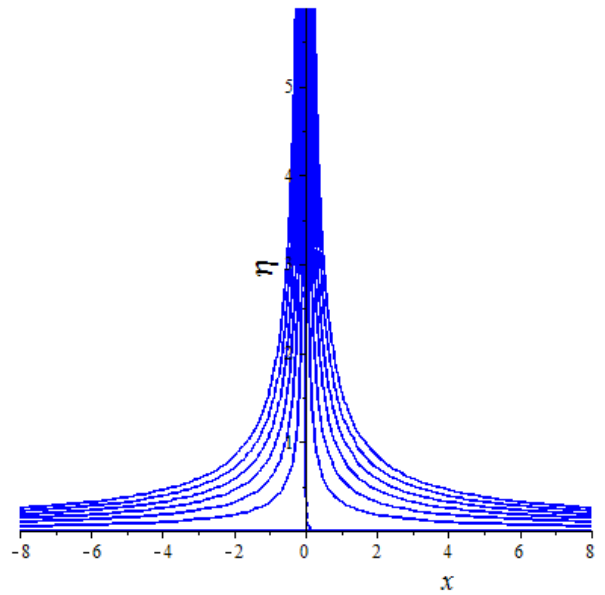


Fig. 9.5. Stream lines pattern of Williamson fluid flow for
 $A > 1$.

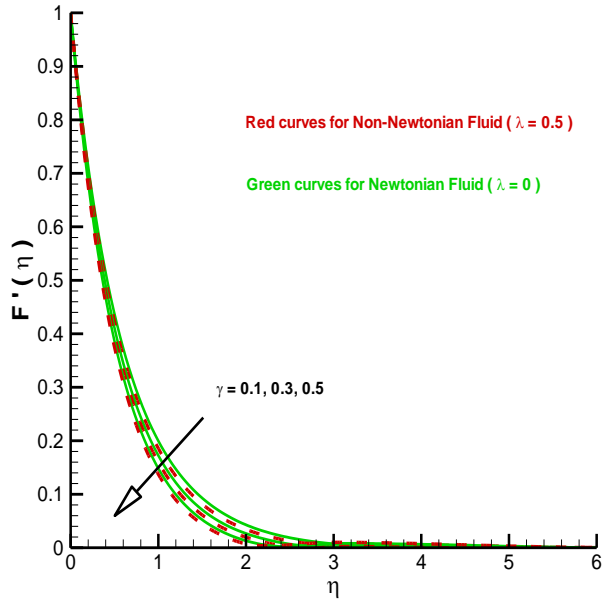


Fig. 9.6. Velocity profiles for various values of γ .

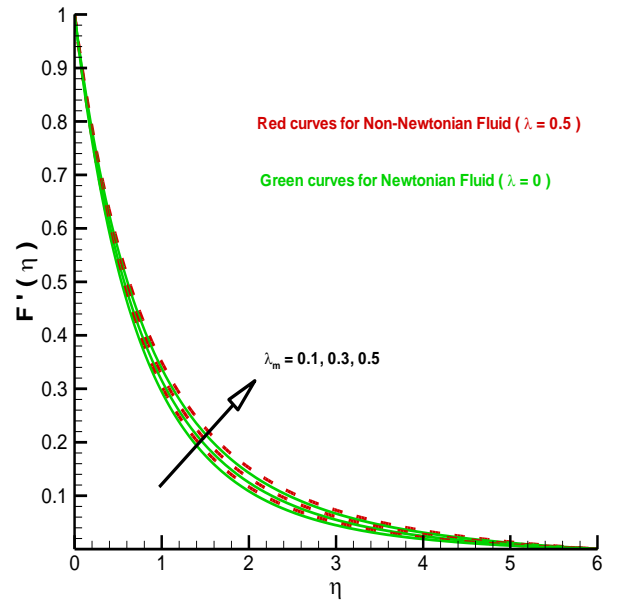


Fig. 9.7. Velocity profiles for various values of λ_m .

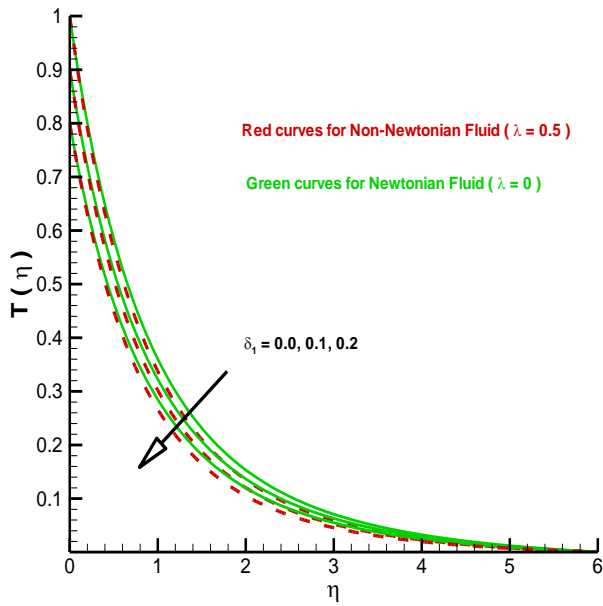


Fig. 9.8. Temperature profiles for various values of δ_1 .

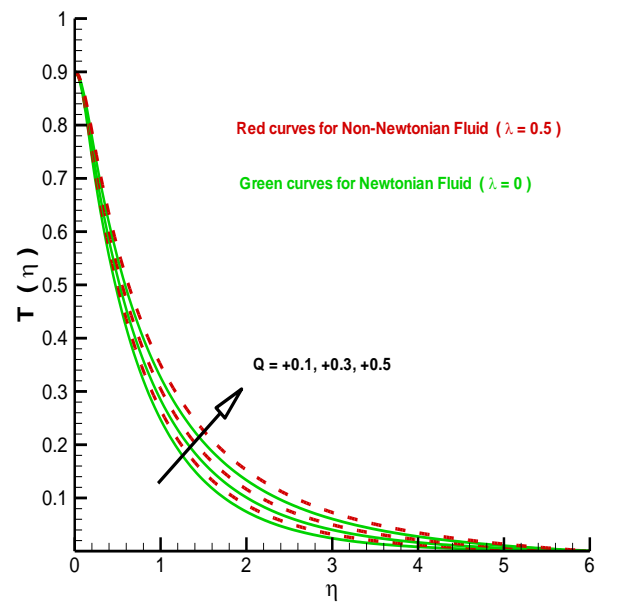


Fig. 9.9. Temperature profiles for various positive values of Q .

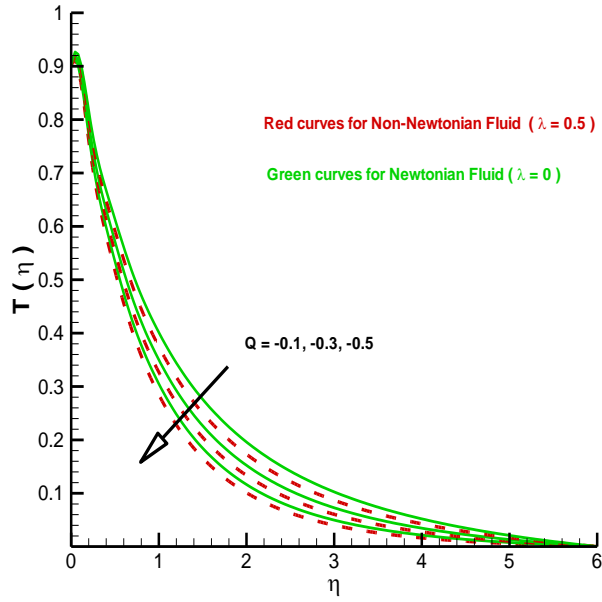


Fig. 9.10. Temperature profiles for various negative values of Q .

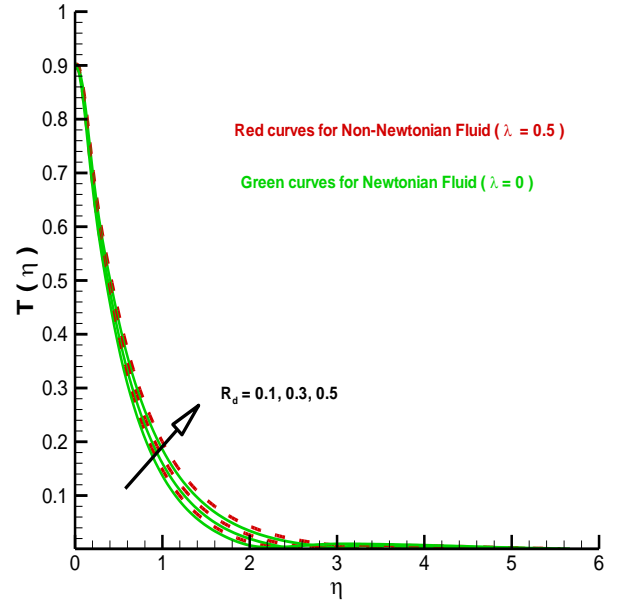


Fig. 9.11. Temperature profiles for various values of R_d .

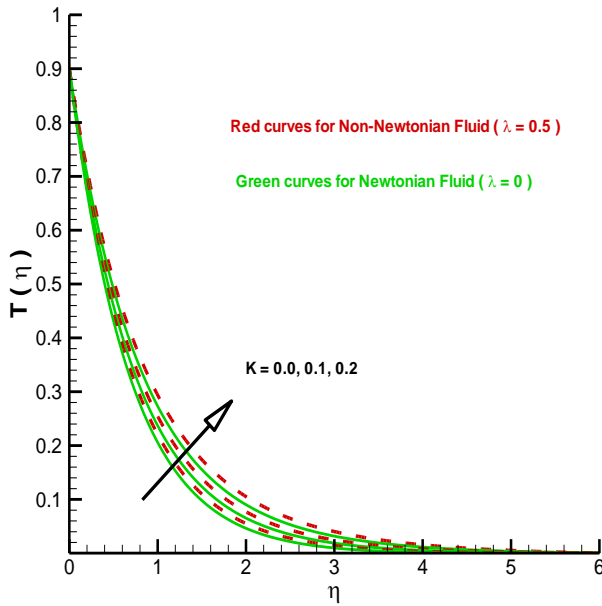


Fig. 9.12. Temperature profiles for various values of K .

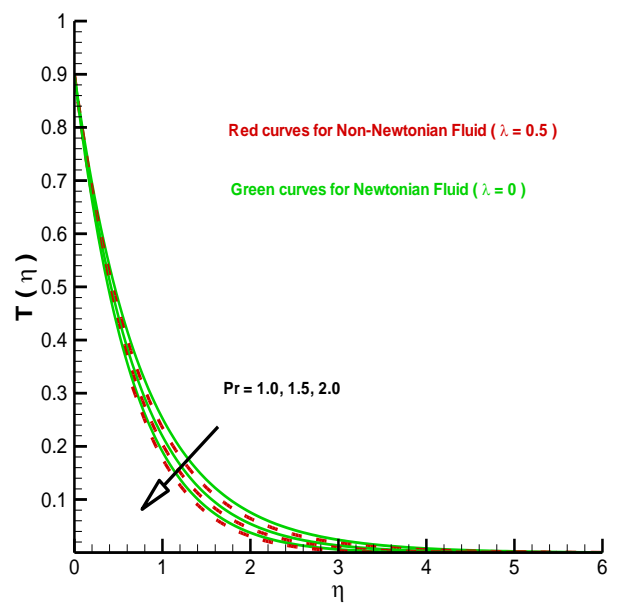


Fig. 9.13. Temperature profiles for various values of Pr .

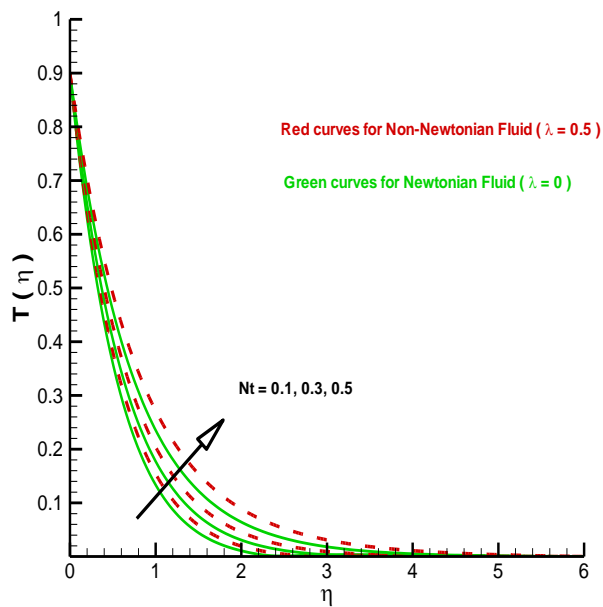


Fig. 9.14. Temperature profiles for various values of Nt .

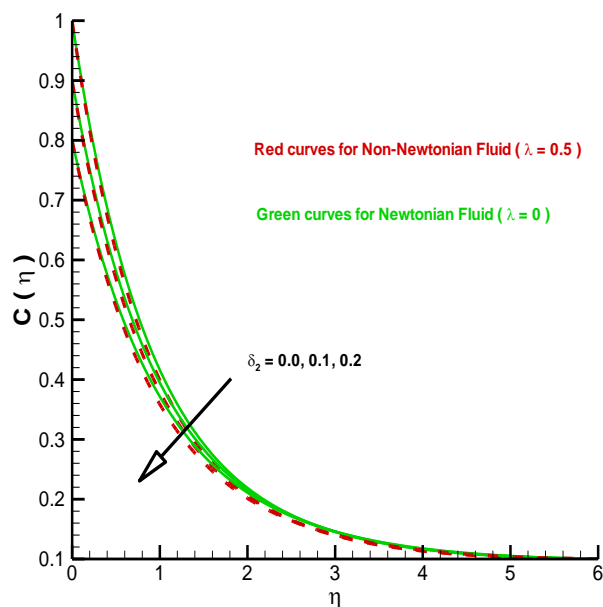


Fig. 9.15. Nanoparticle concentration profiles for various values of δ_2 .

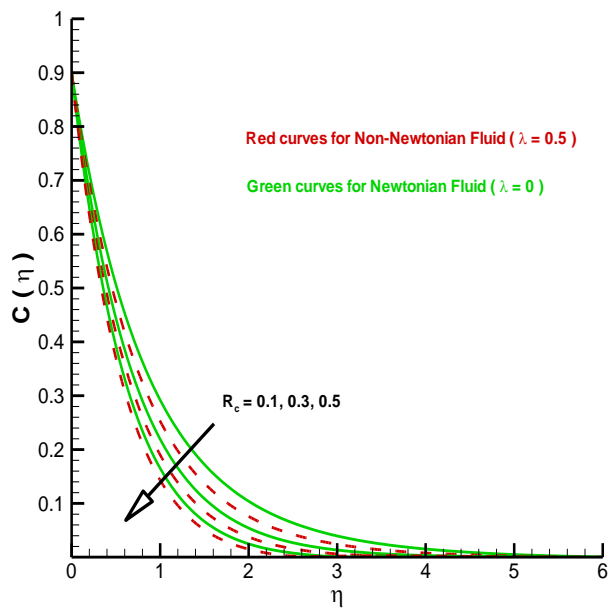


Fig. 9.16. Nanoparticle concentration profiles for various values of R_c .

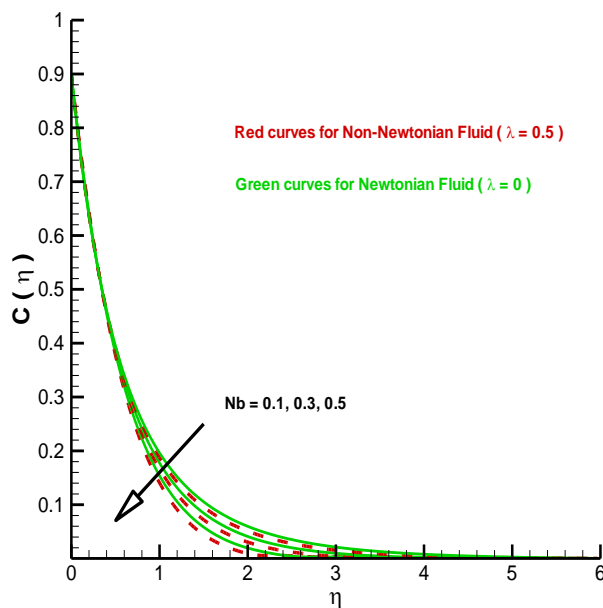


Fig. 9.17. Nanoparticle concentration profiles for various values of Nb .

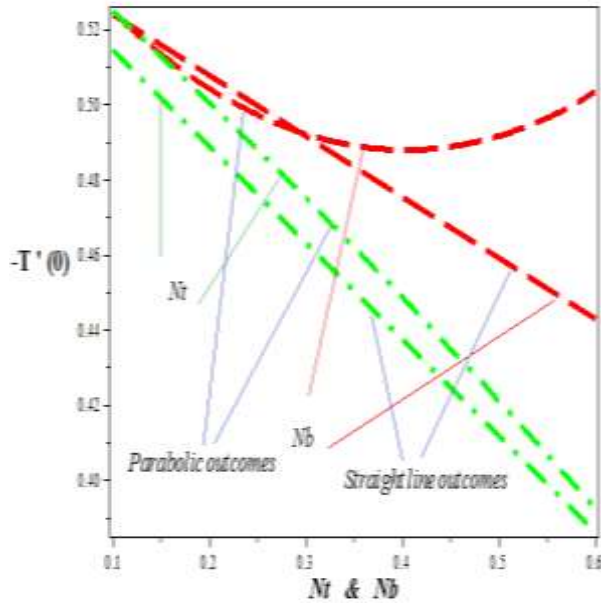


Fig. 9.18. Influence of both N_t and N_b on heat transfer rate.

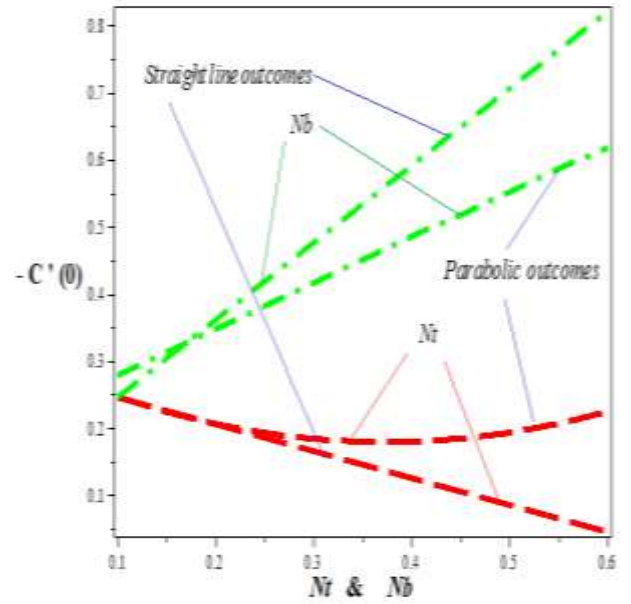


Fig. 9.19. Influence of both N_t and N_b on mass transfer rate.

9.6 Straight line and parabolic curve fitting

In this section, we have evaluated the behavior of both heat and mass transfer rates by way of straight line and parabolic curve fitting approximation towards both N_t and N_b in the absence of thermal radiation effects. The least square method was utilized here and it was proposed by Gauss and Legendre. The normal equations for quadratic approximations can be written as:

$$na_0 + a_1 \sum X_i + a_2 \sum X_i^2 = \sum Y_i,$$

$$a_0 \sum X_i + a_1 \sum X_i^2 + a_2 \sum X_i^3 = \sum X_i Y_i,$$

$$a_0 \sum X_i^2 + a_1 \sum X_i^3 + a_2 \sum X_i^4 = \sum X_i^2 Y_i,$$

where, $i = 1, 2$ for straight line and $i = 1, 2, 3$ for parabolic curve fitting approximations. To trace out straight line and parabolic approximation for heat transfer rate towards N_t and N_b . Let $X_i = (Nt)_i$ and $Y_i = (-T'(0))_i$, we get,

$$\begin{aligned}\sum (Nt)_i &= 0.3, \sum (Nt)_i^2 = 0.05, \\ \sum (-T'(0))_i &= 1.0314, \sum (Nt)_i(-T'(0))_i = 0.1539,\end{aligned}\tag{9.24}$$

by incorporating these values in Eq. (9.24) for straight line, we have

$$\begin{aligned}2a_0 + 0.3a_1 &= 1.0314, \\ 0.3a_0 + 0.05a_1 &= 0.1539,\end{aligned}\tag{9.25}$$

by solving system of equations given by (9.25), we get

$$-T'(0) = a_0 + a_1 Nt\tag{9.26}$$

here, $a_0 = 0.54000$, and $a_1 = -0.16200$. For parabolic curve fitting, we have

$$\begin{aligned}\sum (Nt)_i &= 0.6, \sum (Nt)_i^2 = 0.14, \sum (Nt)_i^3 = 0.036, \\ \sum (Nt)_i^4 &= 0.0098, \sum (-T'(0))_i = 1.5233, \\ \sum (Nt)_i(-T'(0))_i &= 0.30147, \sum (Nt)_i^2(-T'(0))_i = 0.069813,\end{aligned}\tag{9.26}$$

by incorporating these numeric values into (9.24), we obtained

$$\begin{aligned}3a_2 + 0.6a_3 + 0.14a_4 &= 1.5233, \\ 0.6a_2 + 0.14a_3 + 0.036a_4 &= 0.30147, \\ 0.14a_2 + 0.036a_3 + 0.0098a_4 &= 0.069813,\end{aligned}\tag{9.27}$$

by common algebraic practise this system gives parabolic curve fitting relation for heat transfer rate towards N_t i-e

$$-T'(0) = P(Nt) = a_2 + a_3 Nt + a_4 (Nt)^2\tag{9.28}$$

where, $a_2 = 0.55369$, $a_3 = -0.32299$, and $a_4 = 0.39999$. Similarly, line and parabolic curve fitting for heat transfer rate for N_b is entertained as follow:

$$\begin{aligned}2b_0 + 0.4b_1 &= 0.9963, \\ 0.4b_0 + 0.1b_1 &= 0.19413,\end{aligned}\tag{9.29}$$

then the straight line approximations towards N_b is given by:

$$-T'(0) = P(Nb) = b_0 + b_1 Nb,\tag{9.30}$$

where, $b_0 = 0.54945$ and $b_1 = -0.25650$. Now for parabolic curve fitting approximations, we have:

$$\begin{aligned}
\sum (Nb)_i &= 0.9, \sum (Nb)_i^2 = 0.35, \sum (Nb)_i^3 = 0.1530, \sum (Nb)_i^4 = 0.0707, \\
\sum (-T'(0))_i &= 1.4211, \sum (Nb)_i(-T'(0))_i = 0.40653, \sum (Nb)_i^2(-T'(0))_i = 0.153958, \\
3b_2 + 0.9b_3 + 0.3500b_4 &= 1.4211, \\
0.9b_2 + 0.3500b_3 + 0.1530b_4 &= 0.40653, \\
0.3500b_2 + 0.1530b_3 + 0.0707b_4 &= 0.153952,
\end{aligned} \tag{9.31}$$

than solution of system corresponds

$$-T'(0) = P(Nb) = b_2 + b_3Nb + b_4(Nb)^2 \tag{9.32}$$

here, $b_2 = 0.54817$, $b_3 = -0.22707$, and $b_4 = -0.05445$. Straight line and Parabolic curve fitting approximations for mass transfer rate towards N_t and N_b are processed as follow:

$$\begin{aligned}
\sum (Nt)_i &= 0.3, \sum (Nt)_i^2 = 0.05, \\
\sum (-C'(0))_i &= 0.4528, \sum (Nt)_i(-C'(0))_i = 0.06591, \\
2c_0 + 0.3c_1 &= 0.4528, \\
0.3c_0 + 0.05c_1 &= 0.06591,
\end{aligned} \tag{9.33}$$

after solving this system we obtained

$$-C'(0) = c_0 + c_1Nt \tag{9.34}$$

here, $c_0 = 0.28670$ and $c_1 = -0.40199$. Now for parabolic approximation we have,

$$\begin{aligned}
\sum (Nt)_i &= 0.6, \sum (Nt)_i^2 = 0.14, \sum (Nt)_i^3 = 0.036, \sum (Nt)_i^4 = 0.0098, \\
\sum (-C'(0))_i &= 0.6366, \sum (Nt)_i(-C'(0))_i = 0.12105, \\
\sum (Nt)_i^2(-C'(0))_i &= 0.02726, \\
3c_2 + 0.6c_3 + 0.14c_4 &= 0.6366, \\
0.6c_2 + 0.14c_3 + 0.036c_4 &= 0.12105, \\
0.14c_2 + 0.036c_3 + 0.0098c_4 &= 0.02726,
\end{aligned} \tag{9.35}$$

by solving this system we gain

$$-C'(0) = P(Nt) = c_2 + c_3Nt + c_4(Nt)^2, \tag{9.36}$$

here, $c_2 = 0.30489$, $c_3 = -0.67349$, and $c_4 = 0.89999$. In similar fashion, straight line and parabolic approximations for mass transfer rate towards N_b are evaluated as follow:

$$\begin{aligned}
\sum (Nb)_i &= 0.4, \sum (Nb)_i^2 = 0.10, \\
\sum (-C'(0))_i &= 0.7236, \sum (Nb)_i(-C'(0))_i = 0.1677, \\
2d_0 + 0.4d_1 &= 0.7236, \\
0.4d_0 + 0.1d_1 &= 0.1677,
\end{aligned} \tag{9.37}$$

solution of this system corresponds

$$-C'(0) = P(Nb) = d_0 + d_1 Nb, \tag{9.38}$$

here, $d_0 = 0.13200$ and $d_1 = 1.14900$. For parabolic relation, we have

$$\begin{aligned}
\sum (Nb)_i &= 0.9, \sum (Nb)_i^2 = 0.35, \sum (Nb)_i^3 = 0.1530, \sum (Nb)_i^4 = 0.0707, \\
\sum (-C'(0))_i &= 1.2465, \sum (Nb)_i(-C'(0))_i = 0.4292, \sum (Nb)_i^2(-C'(0))_i = 0.1761, \\
3d_2 + 0.9d_3 + 0.35d_4 &= 1.2465, \\
0.9d_2 + 0.35d_3 + 0.15d_4 &= 0.4292, \\
0.35d_2 + 0.153d_3 + 0.0707d_4 &= 0.1761,
\end{aligned} \tag{9.39}$$

after solving by common algebraic practise, we get

$$-C'(0) = P(Nb) = d_2 + d_3 Nb + d_4 (Nb)^2, \tag{9.40}$$

where, $d_2 = 0.20844$, $d_3 = 0.70226$, and $d_4 = -0.03102$.

Table 9.1. Impact of γ, λ, K and Pr on skin friction coefficient.

| γ | λ | K | Pr | $F''(0)$ | $C_f \sqrt{Re_x} = F''(0) + \lambda F'''(0)$ |
|----------|-----------|-----|------|----------|--|
| 0.1 | 0.1 | 0.1 | 1.1 | -1.0502 | -1.1605 |
| 0.2 | 0.1 | 0.1 | 1.1 | -1.0508 | -1.1612 |
| 0.3 | 0.1 | 0.1 | 1.1 | -1.0514 | -1.1619 |
| 0.1 | 0.1 | 0.1 | 1.1 | -1.0502 | -1.1605 |
| 0.1 | 0.2 | 0.1 | 1.1 | -1.1240 | -1.3767 |
| 0.1 | 0.3 | 0.1 | 1.1 | -1.2396 | -1.3933 |
| 0.1 | 0.1 | 0.1 | 1.1 | -1.0502 | -1.1605 |
| 0.1 | 0.1 | 0.2 | 1.1 | -1.2227 | -1.2227 |
| 0.1 | 0.1 | 0.3 | 1.1 | -1.2859 | -1.2859 |
| 0.1 | 0.1 | 0.1 | 1.1 | -1.0502 | -1.1605 |
| 0.1 | 0.1 | 0.1 | 1.2 | -1.0504 | -1.1607 |
| 0.1 | 0.1 | 0.1 | 1.3 | -1.0508 | -1.1617 |

Table 9.2. Impact of K, Pr and δ_1 on local Nusselt number.

| K | Pr | δ_1 | $-T'(0)$ | $\frac{Nu}{\sqrt{Re_x}} = -(1 + \frac{4}{3} R_d) T'(0)$ |
|-----|------|------------|----------|---|
| 0.1 | 1.1 | 0.1 | 0.3456 | 0.0806 |
| 0.2 | 1.1 | 0.1 | 0.4246 | 0.0991 |
| 0.3 | 1.1 | 0.1 | 0.5000 | 0.1167 |
| 0.1 | 1.1 | 0.1 | 0.3456 | 0.0806 |
| 0.1 | 1.2 | 0.1 | 0.3529 | 0.0823 |
| 0.1 | 1.3 | 0.1 | 0.3602 | 0.0840 |
| 0.1 | 1.1 | 0.1 | 0.3456 | 0.0840 |
| 0.1 | 1.1 | 0.2 | 0.3341 | 0.0779 |
| 0.1 | 1.1 | 0.3 | 0.3223 | 0.0752 |

Table 9.3. Impact of K, δ_2, Le and Pr on local Sherwood number.

| K | δ_2 | Le | Pr | $\frac{Sh}{\sqrt{Re_x}} = -C'(0)$ |
|-----|------------|------|------|-----------------------------------|
| 0.1 | 0.1 | 0.1 | 1.1 | 0.2478 |
| 0.2 | 0.1 | 0.1 | 1.1 | 0.2719 |
| 0.3 | 0.1 | 0.1 | 1.1 | 0.2927 |
| 0.1 | 0.1 | 0.1 | 1.1 | 0.2478 |
| 0.1 | 0.2 | 0.1 | 1.1 | 0.2809 |
| 0.1 | 0.3 | 0.1 | 1.1 | 0.2508 |
| 0.1 | 0.1 | 0.1 | 1.1 | 0.2478 |
| 0.1 | 0.1 | 0.2 | 1.1 | 0.2721 |
| 0.1 | 0.1 | 0.3 | 1.1 | 0.3005 |
| 0.1 | 0.1 | 0.1 | 1.1 | 0.2478 |
| 0.1 | 0.1 | 0.1 | 1.2 | 0.2523 |
| 0.1 | 0.1 | 0.1 | 1.3 | 0.2569 |

Table 9.4. Comparison of $-C_f \sqrt{Re_x}$ with existing work.

| λ | Nadeem et al. [53] | Bilal et al. [137] | Present values |
|-----------|--------------------|--------------------|----------------|
| 0.0 | 1.00000 | 1.00000 | 1.0000 |
| 0.1 | 0.976588 | 0.97665 | 0.9765 |
| 0.2 | 0.939817 | 0.938238 | 0.9398 |
| 0.3 | 0.88727 | 0.887147 | 0.8872 |

9.7 Conclusion

A simultaneous way of study is executed to report to the flow characteristics of both Newtonian and non-Newtonian nanofluids flow carried out by an inclined cylindrical surface in a double stratified medium. The flow regime variations are proposed for an involved pertinent parameters namely, $K, \gamma, \lambda, A, \lambda_m, \delta_1, \delta_2, R_d, Pr, Q, Nt, Nb,$ and R_c . The amplitude of heat and mass transfer rates are demonstrated by means of straight line and parabolic curve fitting approach. The key outcomes of present analysis are itemized as follow:

- The stream lines pattern towards A (see figs. 9.3-9.5) yields the compatibility of endpoint conditions.
- The impact of both Nt and Nb on both heat and mass transfer rates is presented by way of straight line and parabolic curve fitting approach.
- It was noticed that heat transfer rate shows decline nature for positive values of both Nt and Nb . Whereas, mass transfer rate is increasing function of Nb but an inverse relation is found for Nt .
- The velocity distribution shows remarkable inciting attribute for positive values of both λ_m and A while opposite trend is noticed in the case of γ .
- The temperature distribution is an increasing function of Q , R_d , K and Nt but an inverse attribute is observed for δ_1 , Q (negative values) and Pr .
- The nanoparticle concentration distribution reflects diminishing trends for positive values of δ_2 , R_c and Nb .
- It is found that the impacts of involved physical parameter are remarkably enriched for non-Newtonian (Williamson model) nanofluid as compared to Newtonian (viscous model) nanofluid.

CHAPTER 10

A Potential Alternative CFD Simulations for Steady Carreau-Bird Law Based Shear Thickening Model

10.1 Introduction

The current chapter provides the numerical investigation on an infinite length circular cylinder placed as an obstacle in the flow of non-Newtonian fluid. To be more specific, a channel of length 2.2 m and with the height 0.41 m is considered. The Power law fluid model is carried out with Carreau-Bird law as a non-Newtonian fluid model and both the Power law linear (constant) and parabolic velocity profiles are initiated simultaneously at an inlet of the channel. The right wall as an outlet is carried with Neumann condition. The relative velocity of Power law fluid particles with both the lower and upper walls is taken zero. A mathematical model is structured in terms of non-linear differential equations. A well trusted numerical technique named as finite element method is adopted commercially. The (LBB)-stable element pair is utilized to approximate the velocity and pressure. The non-linear iterations are stopped when the residual is dropped by 10^{-6} . The impact of Power law index and Reynolds number on the primitive variables is inspected. The obtained observations in this direction are provided by means of both the contour plots and line graphs. Due to circular obstacle both the drag and lift coefficients are evaluated around outer surface of an obstacle towards the higher values of the Power law index. The numerical values of drag and lift coefficients up-to various refinement mesh levels of domain are provided by way of tables.

10.2 Mathematical formulation

The physical design can be studied by means of the mathematical model. This model can be constructed by using mathematical language and concepts. The chemistry, biology, earth science, physics, electrical engineering, computer science, political science, economics, sociology and psychology to mention just a few are the subjects where the

mathematical models are constructed for the better description of system and factors effecting the various components of system. In the field of fluid dynamics, the most generally accepted laws of conservation are i) law of conservation of mass and ii) law of conservation of momentum. To develop mathematical model for our problem, the law of conservation of mass yielded an equation of continuity as follows:

$$\frac{\partial \rho(x, y, z, t)}{\partial t} + \vec{\nabla} \cdot (\rho(x, y, z, t) \vec{V}(x, y, z, t)) = 0, \quad (10.1)$$

In rectangular coordinates Eq. (10.1) can be written as:

$$\frac{\partial \rho}{\partial t} + \frac{\partial(\rho u)}{\partial x} + \frac{\partial(\rho v)}{\partial y} + \frac{\partial(\rho w)}{\partial z} = 0, \quad (10.2)$$

Here two-dimensional, incompressible, non-Newtonian steady state flow is under consideration (i.e. $\rho \neq \rho(x, y, z, t)$ and $\vec{V} \neq \vec{V}(t)$). Eq. (10.2) reduces to:

$$\frac{\partial u(x, y)}{\partial x} + \frac{\partial v(x, y)}{\partial y} = 0. \quad (10.3)$$

The law of conservation of momentum gives the flow equation as follows:

$$\rho(x, y, z, t) \frac{D\vec{V}(x, y, z, t)}{Dt} = -\vec{\nabla} p(x, y, z) + \vec{\nabla} \cdot \vec{\tau} + \rho(x, y, z, t) \vec{B}, \quad (10.4)$$

here, $\vec{\nabla}, t, \rho, \vec{V}, p, \vec{\tau}, \vec{B}$, and μ , represents Del operator, time, fluid density, fluid velocity, pressure, stress tensor for the Power law fluid model, body force and the viscosity of fluid, respectively. Since an incompressible time independent fluid flow in the absence of body force ($\vec{B} = 0$) is considered therefore, the Eq. (10.4) reduces to:

$$\rho \frac{D\vec{V}(x, y)}{Dt} = -\vec{\nabla} p(x, y) + \vec{\nabla} \cdot \vec{\tau}. \quad (10.5)$$

In both x and y components the Eq. (10.5) can be written as:

$$\rho \left(u(x, y) \frac{\partial u(x, y)}{\partial x} + v(x, y) \frac{\partial u(x, y)}{\partial y} \right) = -\frac{\partial p(x, y)}{\partial x} + \frac{\partial \tau_{xx}(x, y)}{\partial x} + \frac{\partial \tau_{xy}(x, y)}{\partial y}, \quad (10.6)$$

$$\rho \left(u(x, y) \frac{\partial v(x, y)}{\partial x} + v(x, y) \frac{\partial v(x, y)}{\partial y} \right) = -\frac{\partial p(x, y)}{\partial y} + \frac{\partial \tau_{yx}(x, y)}{\partial x} + \frac{\partial \tau_{yy}(x, y)}{\partial y}. \quad (10.7)$$

The relation between the stress tensor and the rate of strain tensor for the Power law fluid can be written as:

$$\tau_{ij} = 2\eta \left(S_{ij} = \frac{1}{2} \left(\frac{\partial u_i}{\partial x_j} + \frac{\partial u_j}{\partial x_i} \right) \right), \quad (10.8)$$

using Eq. (10.8) into Eqs. (10.6)-(10.7), we get :

$$\begin{aligned} \rho \left(u(x, y) \frac{\partial u(x, y)}{\partial x} + v(x, y) \frac{\partial u(x, y)}{\partial y} \right) &= - \frac{\partial p(x, y)}{\partial x} \\ + 2 \left(\frac{\partial}{\partial x} \left(\eta(x, y) \frac{\partial u(x, y)}{\partial x} \right) \right) &+ \frac{\partial}{\partial y} \left(\eta(x, y) \left(\frac{\partial u(x, y)}{\partial y} + \frac{\partial v(x, y)}{\partial x} \right) \right), \end{aligned} \quad (10.9)$$

$$\begin{aligned} \rho \left(u(x, y) \frac{\partial v(x, y)}{\partial x} + v(x, y) \frac{\partial v(x, y)}{\partial y} \right) &= - \frac{\partial p(x, y)}{\partial y} \\ + 2 \left(\frac{\partial}{\partial y} \left(\eta(x, y) \frac{\partial v(x, y)}{\partial y} \right) \right) &+ \frac{\partial}{\partial x} \left(\eta(x, y) \left(\frac{\partial u(x, y)}{\partial y} + \frac{\partial v(x, y)}{\partial x} \right) \right), \end{aligned} \quad (10.10)$$

the apparent viscosity via Carreau-Bird law is defined as:

$$\eta = K \left\{ 2 \left(\left(\frac{\partial u(x, y)}{\partial x} \right)^2 + \left(\frac{\partial v(x, y)}{\partial y} \right)^2 \right) + \left(\frac{\partial u(x, y)}{\partial y} + \frac{\partial v(x, y)}{\partial x} \right)^2 \right\}^{\frac{n-1}{2}}, \quad (11.10)$$

here, n is the power law index, and K is consistency coefficient.

10.3 Problem description

10.3.1 Power law linear velocity at inlet

In this section, the non-Newtonian fluid flow is introduced in channel of finite length 2.2 m with height 0.41 m. The non-Newtonian fluid model is Power law fluid model. The Power law fluid is considered in channel having circular cylinder as an obstacle. The obstacle is centred at (0.2, 0.2) m. The inlet Power law flow velocity is considered linear (constant) that is $U_{\text{mean}} = 0.2$ while the outlet is settled with Neumann condition. The upper and lower walls are considered with no slip condition which implies the relative velocity of the Power law particles and the side walls is zero in magnitude. The geometrical illustration of present problem is given in Fig. 10.1.

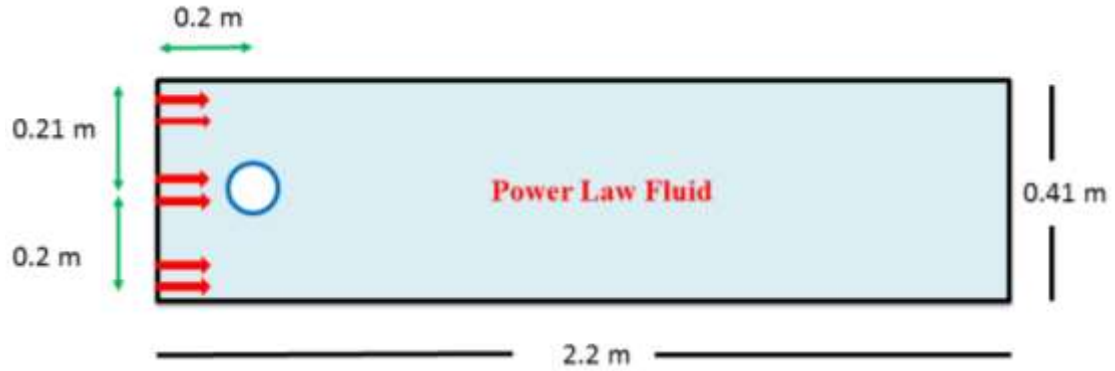


Fig. 10.1. Schematic diagram when Power law velocity is linear at inlet.

The fluid flow illustrated in Fig. 10.1 is mathematically modeled in terms of nonlinear differential equations, see Eqs. (10.9)-(10.11) along with following constraints:

$$\begin{aligned}
 \text{Inlet boundary} \quad & u = U_{\max}, v = 0, \\
 \text{Outlet boundary} \quad & \frac{\partial u}{\partial x} = \frac{\partial v}{\partial x} = 0, \\
 \text{Side walls} \quad & u = 0, v = 0, \\
 \text{Cylindrical surface} \quad & u = 0, v = 0.
 \end{aligned} \tag{10.12}$$

10.3.2 Power law parabolic velocity profile at inlet

In this section, the Power law fluid with parabolic profile at inlet of channel is considered. The outlet of channel is taken with Neumann condition. Both upper and lower walls of channel are at no slip condition. The circular cylinder is placed as an obstacle in channel. The obstacle is centered at (0.2, 0.2) m. The length and height of channel is 2.2 m and 0.41 m respectively. Fig. 10.2 is the flow diagram of present case.

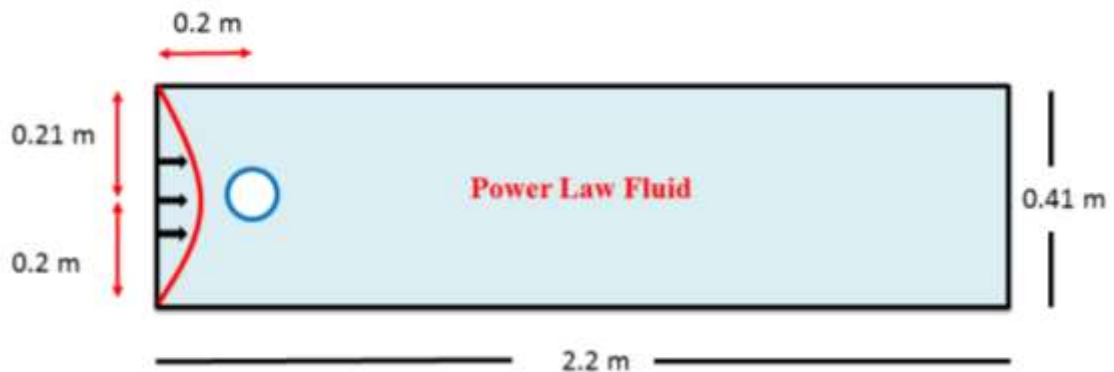


Fig. 10.2. Schematic diagram when Power law velocity is parabolic at inlet.

The flow illustration is controlled through mathematical formulation. The flow narrating differential subject to flow problem given in Fig. 10.2 can be studied through Eqs. (10.9)-(10.11) with following conditions:

$$\begin{aligned}
 \text{Inlet boundary} \quad u &= U_{\text{mean}} = \frac{2}{3} U_{\text{max}}, v = 0, \\
 \text{Outlet boundary} \quad \frac{\partial u}{\partial x} &= \frac{\partial v}{\partial x} = 0, \\
 \text{Side walls} \quad u &= 0, v = 0, \\
 \text{Cylindrical surface} \quad u &= 0, v = 0.
 \end{aligned} \tag{10.13}$$

The involved Reynolds number for Power law model is written as:

$$\text{Re} = \frac{(U_{\text{mean}})^{2-n} D^n \rho}{\mu}, \tag{10.14}$$

here, D denotes characteristic length, ρ is fluid density, μ is fluid viscosity and n stands for Power law index. The range $0 < n < 1$ implies shear thinning case while $n > 1$ implies shear thickening characteristics. In present analysis the range of Power law index is considered $1 \leq n \leq 5$ with step size $\Delta n = 0.5$.

10.3.3 Benchmark quantities

The placement of an obstacle yields two benchmark quantities namely, the drag coefficient

(C_D) and the lift coefficient (C_L). The dimensionless form of these quantities can be written as:

$$C_D = \frac{2F_D}{\rho(U_{\text{mean}})^2 D}, \tag{10.15}$$

$$C_L = \frac{2F_L}{\rho(U_{\text{mean}})^2 D}, \tag{10.16}$$

here, the drag and lift forces are represented by F_D and F_L . Further, ρ, U_{mean} and D denotes fluid density, mean velocity and the characteristic length respectively. The benchmark quantities namely, the drag and lift coefficients will appear when an obstacle is placed at right angle to oncoming fluid. It is important to note that the drag force can exist without lift force. When height of channel is 0.4m and obstacle is placed at (0.2, 0.2), the lift coefficient will vanish. Therefore, to seek the lift force the height of channel is selected 0.41m to bring obstacle little offset. The numerical values of both the drag and lift coefficients are evaluated at various refined mesh levels for better accuracy.

10.4 Computational scheme

The fluid flow in a channel without any obstacle may have an exact solution but when obstacles are accounted to ongoing fluid it becomes difficult to report exact solution. To find the numerical solution, the finite difference method, finite element method and finite volume method are prominent methods. Out of these the finite element method [138] is powerful tool to encounter boundary value problems. The conforming element pair $P_2 - P_1$ is utilized for the velocity and pressure approximation. This element is a stable element pair satisfying inf-sup condition [139]. The location of degrees of freedom for this finite element pair is shown in Fig. 10.3. This pair has 15 local degrees of freedom for two dimensional flows. The convergence criterion for the non-linear defect is set as follows:

$$\left| \frac{\xi^{n+1} - \xi^n}{\xi^{n+1}} \right| \leq 10^{-6}. \quad (10.17)$$

Here, ξ is the general solution component. The freedom regarding choice of discretization is one of the big benefits of finite element method. The discretization for computation is the preprocessing stage of finite element method. The computational domain can be discretized by way of line elements, triangular elements, rectangular elements etc. An accurate representation of complex geometry, an inclusion of dissimilar material properties, and easy representation of the total solution and capturing of local effects are the advantages of sub division of larger system into smaller. The key steps involved in this method are itemized as follows:

1. Domain discretization.

2. Establish simpler finite element equations.
3. Combine/Assemble element equations.
4. Incorporate boundary constraints or initial conditions.
5. Solve the developed equations.
6. Post processing (Visualization).

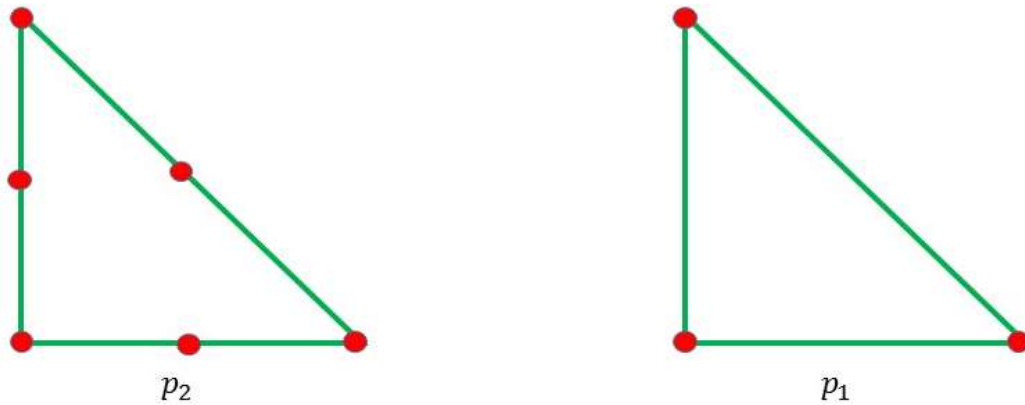
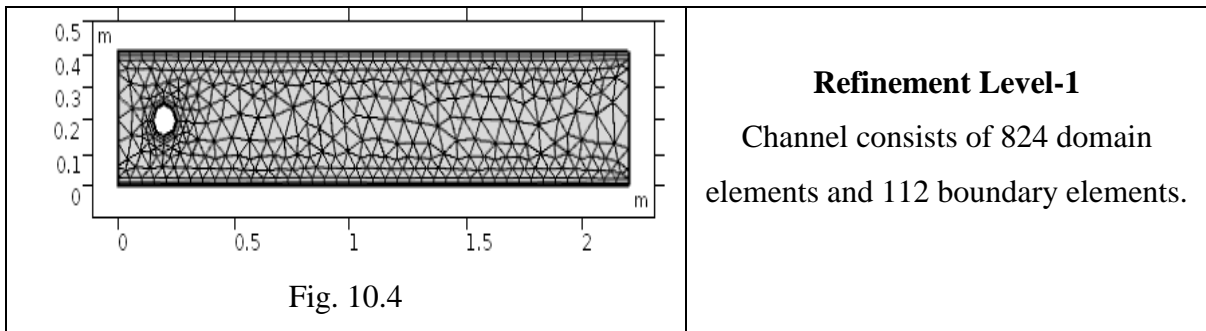
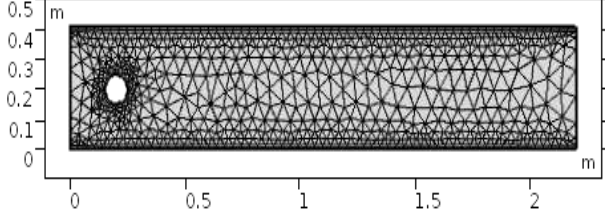
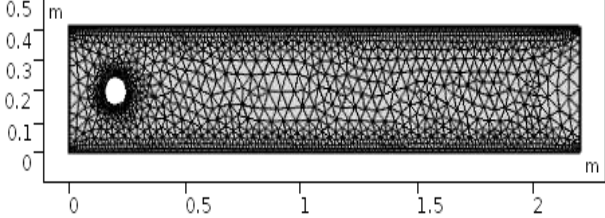
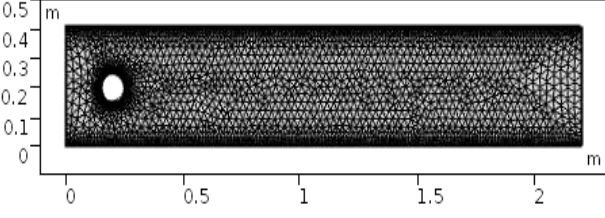
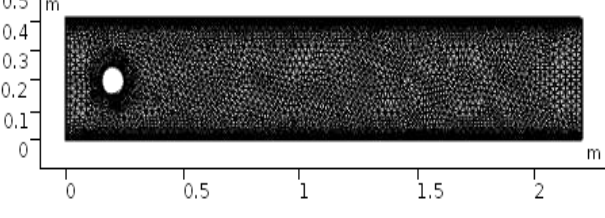
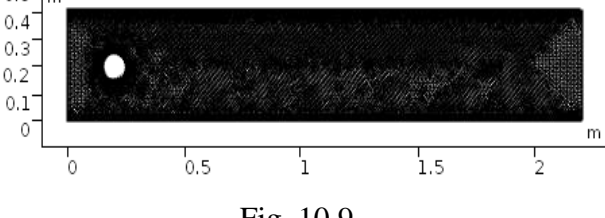
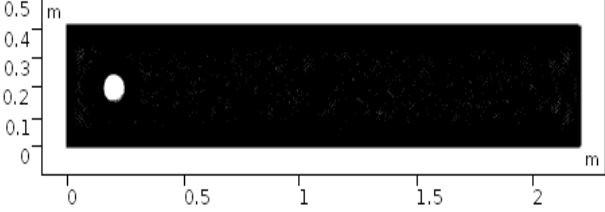
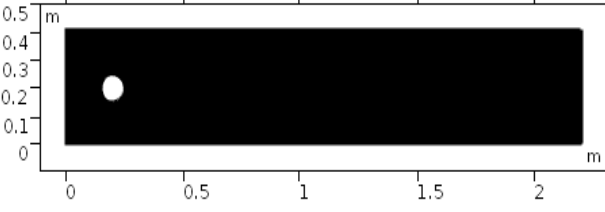


Fig. 10.3. Schematic diagram for $p_2 - p_1$ element pair.

In this attempt the channel as a computational domain is discretized via triangular and rectangular elements. For better solution, the eight various meshing levels are reported. The detail in this direction is provided by way of Figs. 10.4-10.11. The degrees of freedom (DOFs) for each refinement level is provided in Table 10.17.



| | |
|--|--|
|  <p style="text-align: center;">Fig. 10.5</p> | <p style="text-align: center;">Refinement Level-2</p> <p>Channel consists of 1365 domain elements and 159 boundary elements.</p> |
|  <p style="text-align: center;">Fig. 10.6</p> | <p style="text-align: center;">Refinement Level-3</p> <p>Channel consists of 2198 domain elements and 204 boundary elements</p> |
|  <p style="text-align: center;">Fig. 10.7</p> | <p style="text-align: center;">Refinement Level-4</p> <p>Channel consists of 4200 domain elements and 298 boundary elements.</p> |
|  <p style="text-align: center;">Fig. 10.8</p> | <p style="text-align: center;">Refinement Level-5</p> <p>Consists of 6232 domain elements and 374 boundary elements.</p> |
|  <p style="text-align: center;">Fig. 10.9</p> | <p style="text-align: center;">Refinement Level-6</p> <p>Channel consists of 11422 domain elements and 468 boundary elements.</p> |

| | |
|---|---|
|  <p style="text-align: center;">Fig. 10.10</p> | <p style="text-align: center;">Refinement Level-7</p> <p style="text-align: center;">Channel consists of 26286 domain elements and 970 boundary elements.</p> |
|  <p style="text-align: center;">Fig. 10.11</p> | <p style="text-align: center;">Refinement Level-8</p> <p style="text-align: center;">Channel consists of 63373 domain elements and 1851 boundary elements.</p> |

10.5 Analysis

The Power law fluid flow in a channel is investigated by considering both linear (constant) and parabolic profiles at an inlet. The observations in this direction are discussed section-wise namely, section –I and section-II. Simulations are performed at refinement level-8 for both linear (constant) and parabolic profiles.

- **Section -I**

The problem given by Eqs. (10.9)-(10.12) is nonlinear in character. To report numerical solution the numerical method named finite element method is utilized. The obtain outcomes are provided by way of Figs. 10.12-10.20. The flow visualization of the Power law fluid in a finite length channel towards the higher values of Power law index is examined and provided with the help of Figs. 10.12-10.14. In detail, Fig. 10.12 is devoted to present the Power law fluid flow when Power law index is taken $n = 1$. It is seen that the Power law fluid initiated with linear velocity profile as an inlet velocity strikes with circle and the stagnation point region is created at right angle to the flow direction and fluid moves around the circular cylinder with larger velocity while the fluid near the side walls admits zero velocity due to no slip condition. It is important to note that the Power law fluid model turns into viscous fluid model at $n = 1$. The impact of Power law index $n = 2$ and $n = 3$ on Power law fluid is inspected and the outcomes in this regard are identified in Fig.

10.13 and Fig. 10.14 respectively. Since the positive values of Power law index implies the shear thickening fluid therefore, iterating the Power law index $n = 2$ and $n = 3$ reflects large stagnation point region when the Power law fluid strikes with left face of circular obstacle. The speedy bifurcation in-between $0.1 < x < 0.5$ occurs as the Power law index increases. The way of line graph for velocity examination is executed to inspect the flow aspects of Power law fluid towards different iterations of Power law index that is $n=1,2,3$ at different location of channel namely, $[(0, 0), (0, 0.41)]$, $[(0.1,0), (0.1, 0.41)]$, $[(0.2,0), (0.2,0.41)]$, $[(0.3,0), (0.3,0.41)]$, $[(1,0), (1,0.41)]$ and $[(2,0), (2,0.41)]$. The inlet Power law velocity is taken $U_{\max} = 0.2$. The line graph of velocity (see Fig. 10.15) at location $x = 0$ validate the inflow velocity for all values of Power law index that is $n=1, 2$ and 3 . The line graph of velocity at location $x = 0.1$ reflects deformation of Power law fluid towards an obstacle. Such variations are reported in Fig. 10.16. The velocity line graph at location $x=0.2$ is provided in Fig. 10.17. It is noticed that at this location the Power law fluid bifurcates significantly. From, Figs. 10.15-10.16 one can see easily that for higher values of Power law index ($n = 2$ and $n = 3$) the fluid velocity is lesser in magnitude as compared to Newtonian fluid ($n = 1$) because for $n = 2$ and $n= 3$ the fluid becomes more viscous. Surprising it is noticed that the bifurcation towards higher values of Power law index ($n = 2$ and $n = 3$) is higher in strength as compared to $n = 1$, for location $x = 0.3$, see Figs. 10.18. The Fig. 10.19 and Fig. 10.20 provide the variations in velocity in terms of line graph at location $x = 1$ and $x = 2$ respectively. From these plots it can be concluded that the initial velocity profile that is linear (constant) at an inlet of channel cannot be recovered at an outlet. This is due to non-compatible assumption “the no slip condition at walls and linear (constant) velocity at an inlet”.

- **Section-II**

Analysis on the Power law fluid when parabolic velocity profile is taken at an inlet is elaborated in this section. The computational scheme is implemented. The method used in this regard is finite element method. The obtained outcomes are presented by way of graphs and tables. Figs. 10.21-10.23 are plotted to provide the impact of Power law index when parabolic inlet flow velocity of Power law fluid is considered. The iteration in Power law index that is $n = 1, 2$ and 3 implies shear thickening fluids. Fig. 10.21 is plotted when Power law index is taken $n = 1$. At this value the Power law fluid model turns into Newtonian fluid model. Further, for iteration $n = 2$ and $n = 3$ surprisingly noticed that the speedy bifurcation occurs at location $0.1 < x < 0.5$ of the channel. One can observed from the Figs. 10.21-10.23 that the stagnation point region towards left face of an obstacle increases for higher values of the Power law index. The corresponding pressure increases significantly at this zone. Higher the values of Power law index, more pressure at left face of an obstacle. Figs. 10.24-10.26 are evident for this fact. The line graphs are also provided for better description of the Power law fluid deformation due to circular obstacle. Fig. 10.27 is the line graph of velocity at location $x = 0$ (inlet of channel) for $n = 1, 2$ and 3 . The maximum velocity for the parabolic profile is taken $U_{\max} = 0.3$. Such assumption is justified in Fig. 10.27. Fig 10.28 reports the Power law fluid deformation at location $x = 0.1$. Further, the clear bifurcation of Power law fluid can be assessed in Fig. 10.29 at location $x = 0.2$. It is observed from Figs. 10.28-10.29 that the magnitude of velocity for $n = 1$ is higher as compared to $n = 2$ and $n = 3$. This is due to viscosity effects because by increasing Power law index the fluid becomes more viscous. The Fig. 10.30, Fig. 10.31 and Fig. 10.32 shows velocity line graphs at locations $x = 0.3, x = 1$ and $x = 2$ respectively. It is seen from Figs. 10.31-10.32 that the parabolic profile (inlet flow velocity assumption) is retraced at outlet of channel.

10.6 Graphical results

- Section-I

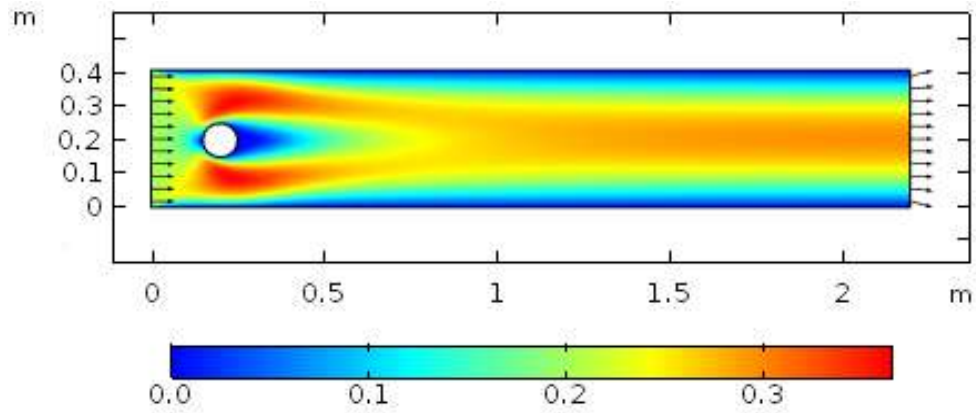


Fig. 10.12. Velocity plot when $n = 1$, $U_{\text{mean}} = 0.2$ and $Re = 20$.

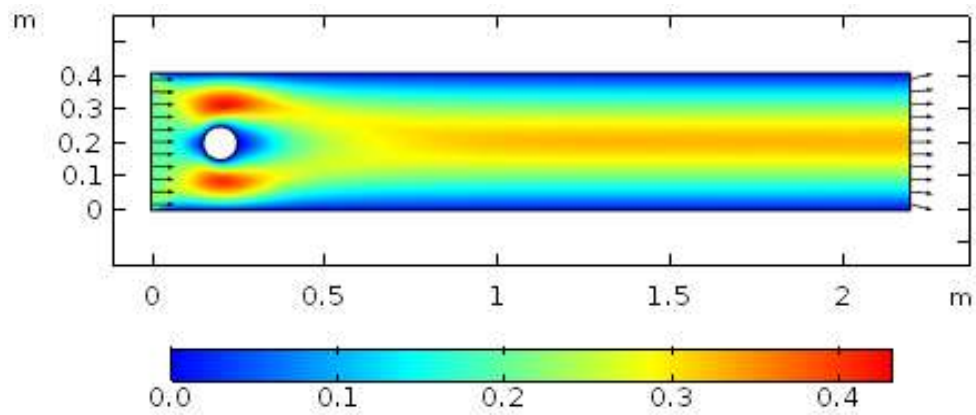


Fig. 10.13. Velocity plot when $n = 2$, $U_{\text{mean}} = 0.2$ and $Re = 10$.

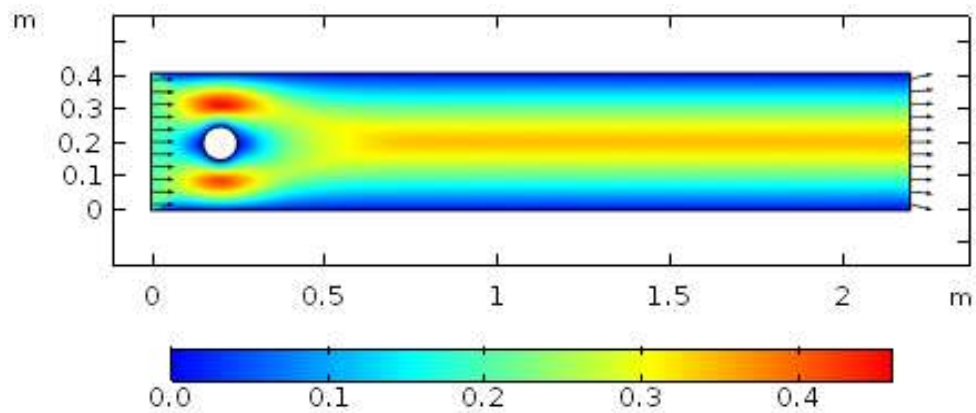


Fig. 10.14. Velocity plot when $n = 3$, $U_{\text{mean}} = 0.2$ and $Re = 5$.

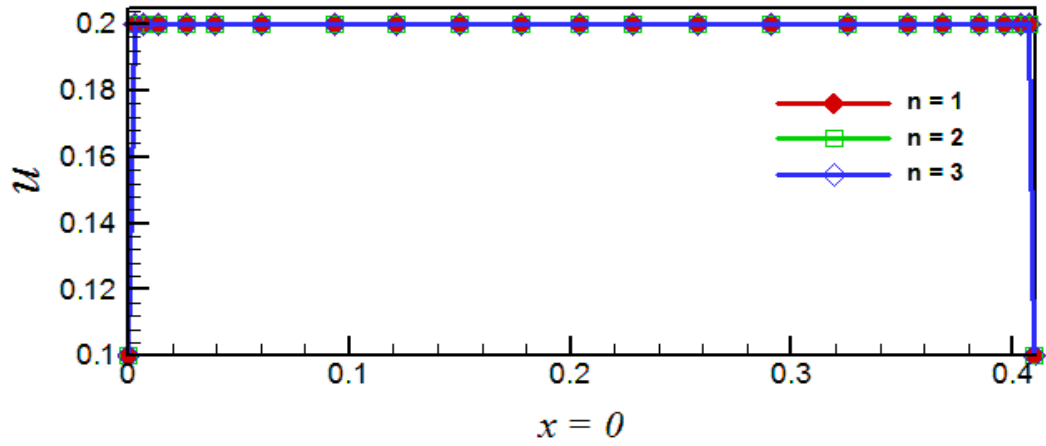


Fig. 10.15. Line graph of Power law linear velocity profile at location $x = 0$.

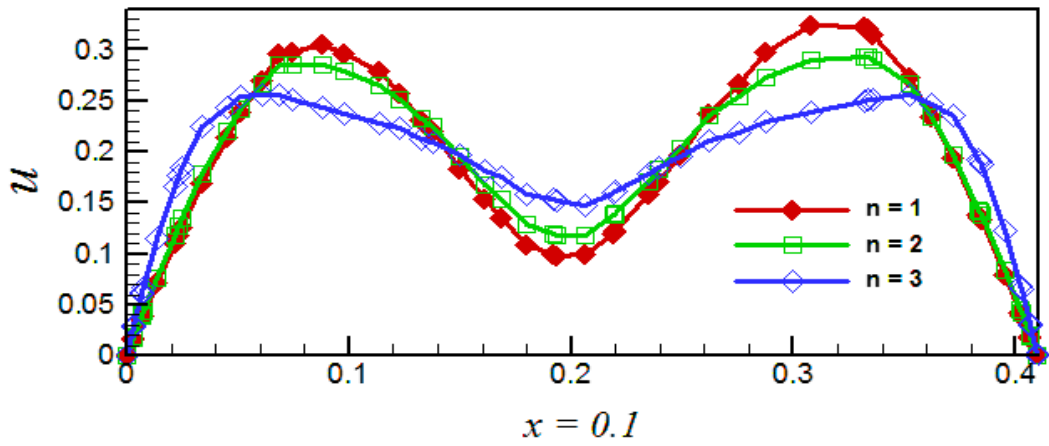


Fig. 10.16. Line graph of Power law linear velocity profile at location $x = 0.1$.

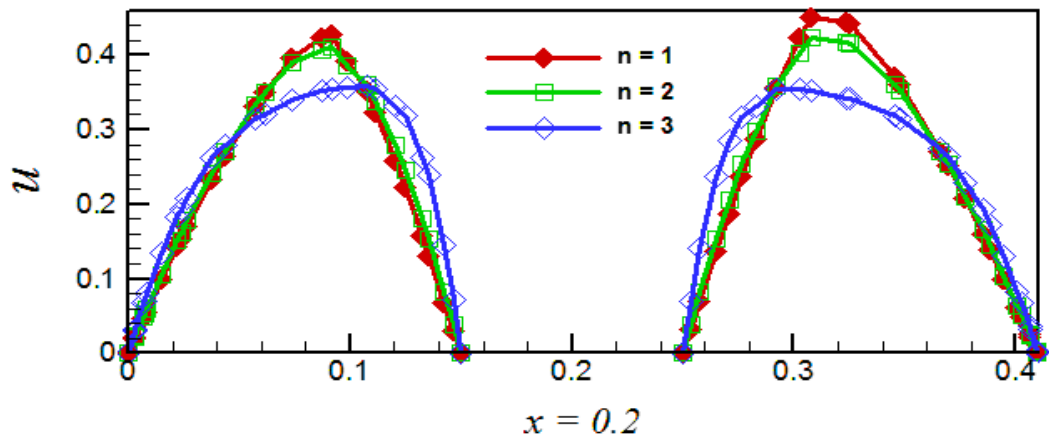


Fig. 10.17. Line graph of Power law linear velocity profile at location $x = 0.2$.

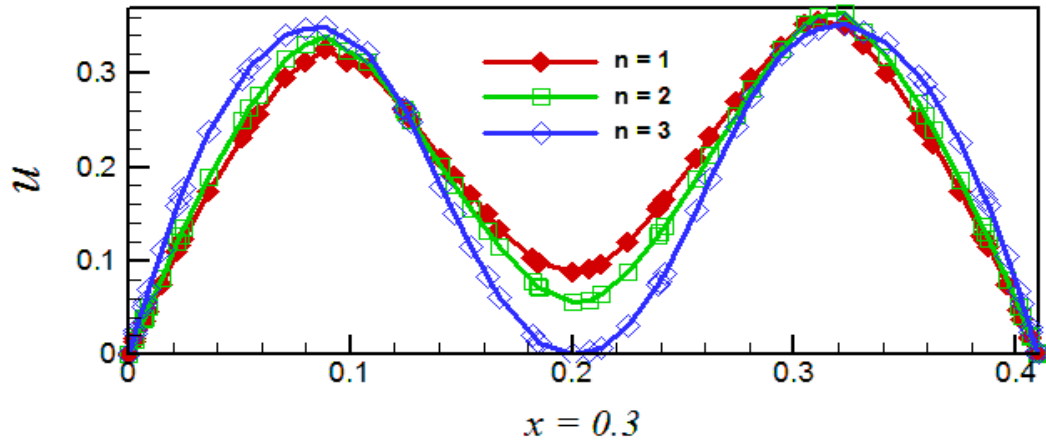


Fig. 10.18. Line graph of Power law linear velocity profile at location $x = 0.3$.

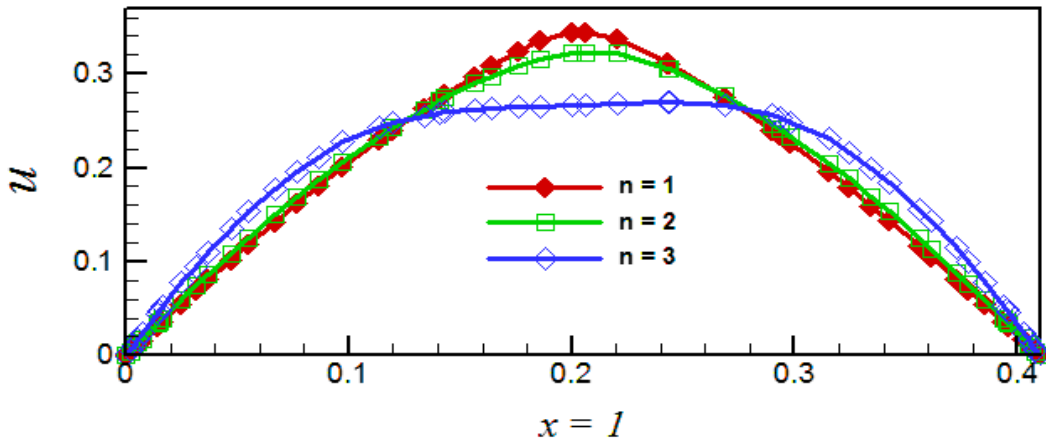


Fig. 10.19. Line graph of Power law linear velocity profile at location $x = 1$.

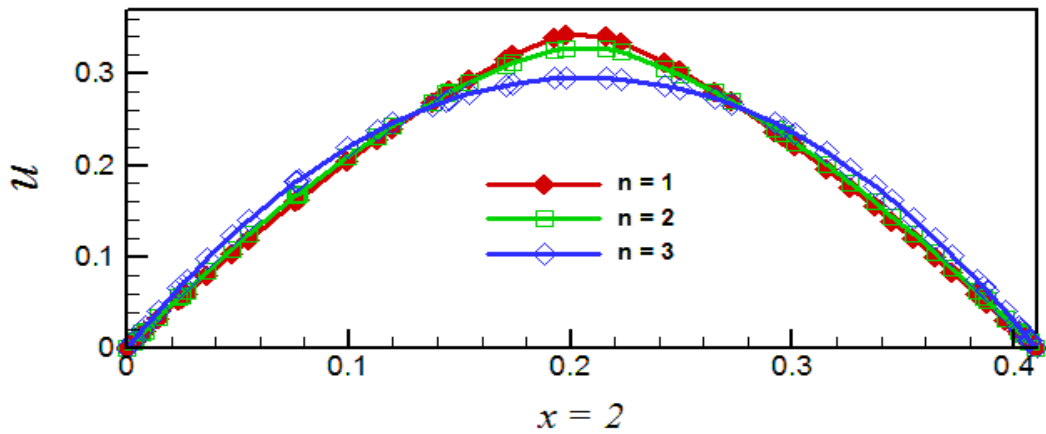


Fig. 10.20. Line graph of Power law linear velocity profile at location $x = 2$.

Table 10.1: Numerical values of drag and lift coefficients when

$$U_{\max} = 0.2 \text{ with mesh level-1.}$$

| Refinement Level-1 | n | C_D | C_L |
|-----------------------|-----|--------|-----------|
| | 1.5 | 8.6546 | -0.013507 |
| | 2 | 15.997 | -0.36968 |
| | 2.5 | 32.508 | -0.70465 |
| | 3 | 69.598 | 0.68874 |
| | 3.5 | 151.83 | 0.17555 |
| | 4 | 334.59 | 1.4553 |
| | 4.5 | 738.48 | 5.8203 |
| | 5 | 1632.5 | 16.892 |

Table 10.2: Numerical values of drag and lift coefficients when

$$U_{\max} = 0.2 \text{ with mesh level-2.}$$

| Refinement Level-2 | n | C_D | C_L |
|-----------------------|-----|--------|---------|
| | 1.5 | 8.6022 | 0.10413 |
| | 2 | 16.475 | 0.54782 |
| | 2.5 | 34.511 | 1.1245 |
| | 3 | 76.001 | 1.6229 |
| | 3.5 | 170.55 | 2.1833 |
| | 4 | 386.18 | 3.0244 |
| | 4.5 | 878.78 | 4.2750 |
| | 5 | 2005.7 | 5.9499 |

Table 10.3: Numerical values of drag and lift coefficients when

$U_{\max} = 0.2$ with mesh level-3.

| Refinement Level-3 | n | C_D | C_L |
|-----------------------|-----|--------|----------|
| | 1.5 | 8.6254 | 0.087501 |
| | 2 | 16.593 | 0.48322 |
| | 2.5 | 34.779 | 1.0173 |
| | 3 | 76.855 | 1.5238 |
| | 3.5 | 172.74 | 2.2427 |
| | 4 | 391.10 | 3.6760 |
| | 4.5 | 888.10 | 6.8543 |
| | 5 | 2021.2 | 14.585 |

Table 10.4: Numerical values of drag and lift coefficients when

$U_{\max} = 0.2$ with mesh level-4.

| Refinement Level-4 | n | C_D | C_L |
|-----------------------|-----|--------|---------|
| | 1.5 | 8.6164 | 0.13278 |
| | 2 | 16.695 | 0.57157 |
| | 2.5 | 35.497 | 1.1339 |
| | 3 | 79.341 | 1.6566 |
| | 3.5 | 181.22 | 2.4246 |
| | 4 | 416.89 | 3.8802 |
| | 4.5 | 965.05 | 6.5248 |
| | 5 | 2241.7 | 11.279 |

Table 10.5: Numerical values of drag and lift coefficients when

$$U_{\max} = 0.2 \text{ with mesh level-5.}$$

| Refinement Level-5 | n | C_D | C_L |
|-----------------------|-----|--------|---------|
| | 1.5 | 8.6281 | 0.13842 |
| | 2 | 16.741 | 0.55529 |
| | 2.5 | 35.625 | 1.0428 |
| | 3 | 79.753 | 1.3990 |
| | 3.5 | 182.47 | 1.7208 |
| | 4 | 421.23 | 2.0644 |
| | 4.5 | 977.53 | 2.3444 |
| | 5 | 2280.1 | 1.6548 |

Table 10.6: Numerical values of drag and lift coefficients when

$$U_{\max} = 0.2 \text{ with mesh level-6.}$$

| Refinement Level-6 | n | C_D | C_L |
|-----------------------|-----|--------|---------|
| | 1.5 | 8.6167 | 0.16342 |
| | 2 | 16.816 | 0.58054 |
| | 2.5 | 35.911 | 1.0819 |
| | 3 | 80.761 | 1.4588 |
| | 3.5 | 185.61 | 1.8303 |
| | 4 | 431.02 | 2.2711 |
| | 4.5 | 1007.4 | 2.7725 |
| | 5 | 2367.0 | 3.1896 |

Tables 10.1-10.6 are provided when the Power law fluid model is considered towards channel and an inlet velocity profile is considered linear (constant). The impact of Power law index namely $n = 1.5, 2, 2.5, 3, 3.5, 4, 4.5$ and 5 on drag and lift coefficients are evaluated for six different refined mesh structures for an accuracy. It is noticed that for the higher values of the Power law index both the drag and lift coefficients increases.

- Section-II

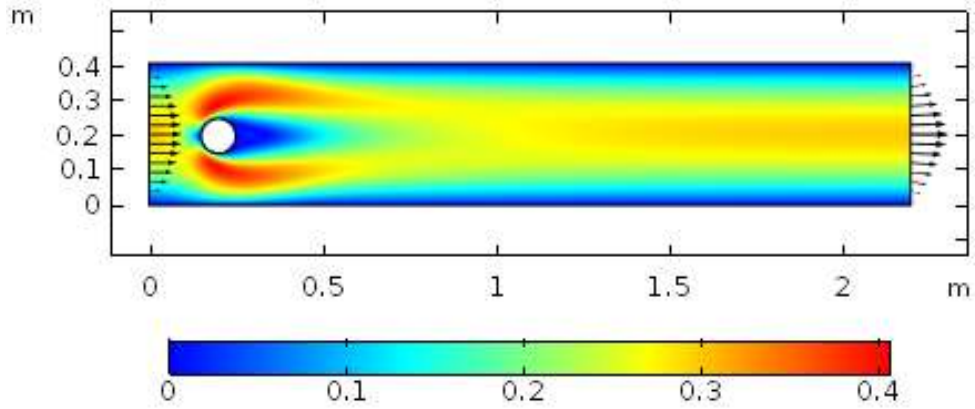


Fig. 10.21. Velocity plot when $n = 1$, $U_{\max} = 0.3$ and $Re = 20$.

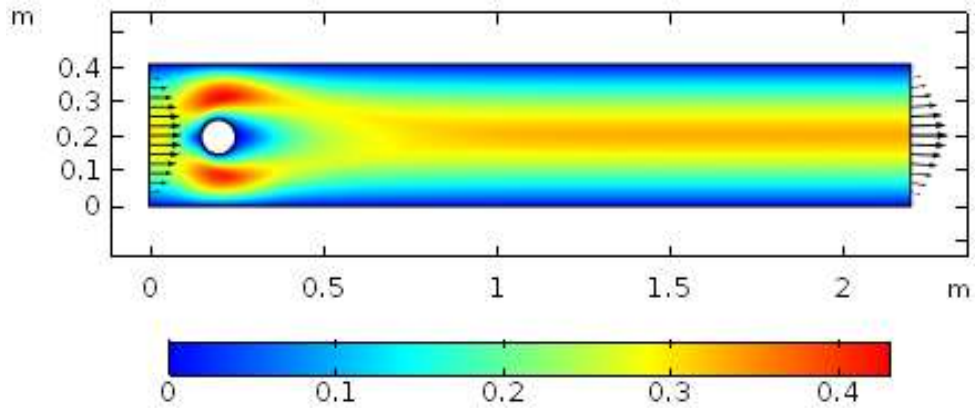


Fig. 10.22. Velocity plot when $n = 2$, $U_{\max} = 0.3$ and $Re = 10$.

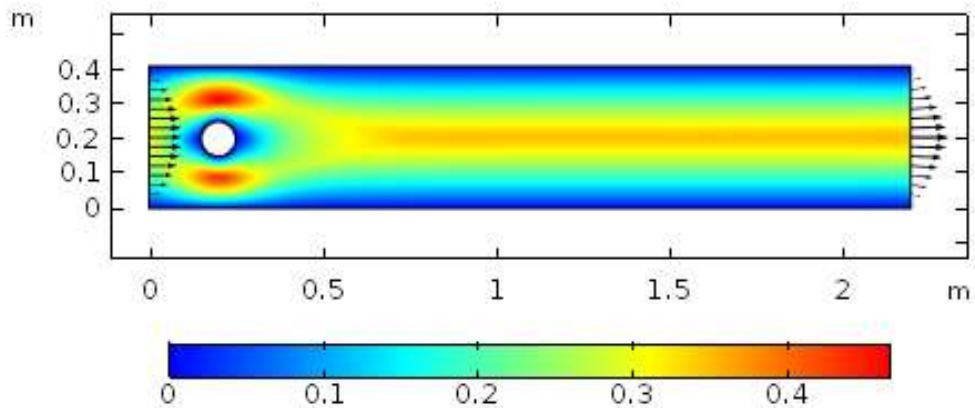


Fig. 10. 23. Velocity plot when $n = 3$, $U_{\max} = 0.3$ and $Re = 5$.

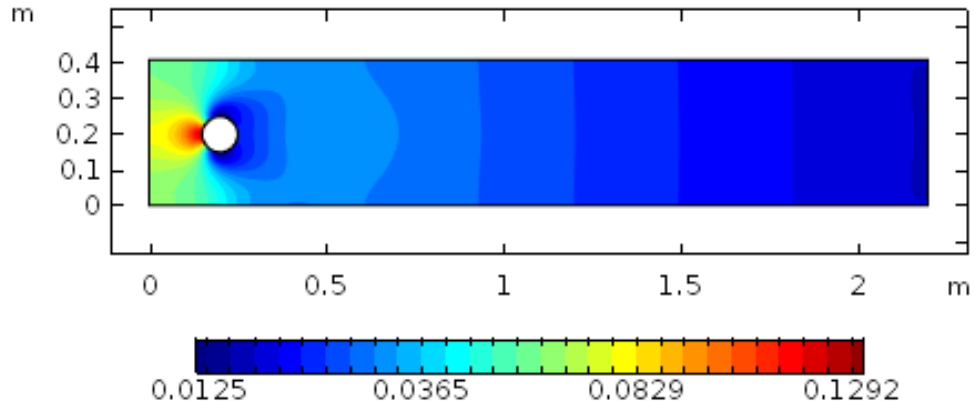


Fig. 10.24. Pressure plot when $n = 1$, $U_{\max} = 0.3$ and $Re = 20$.

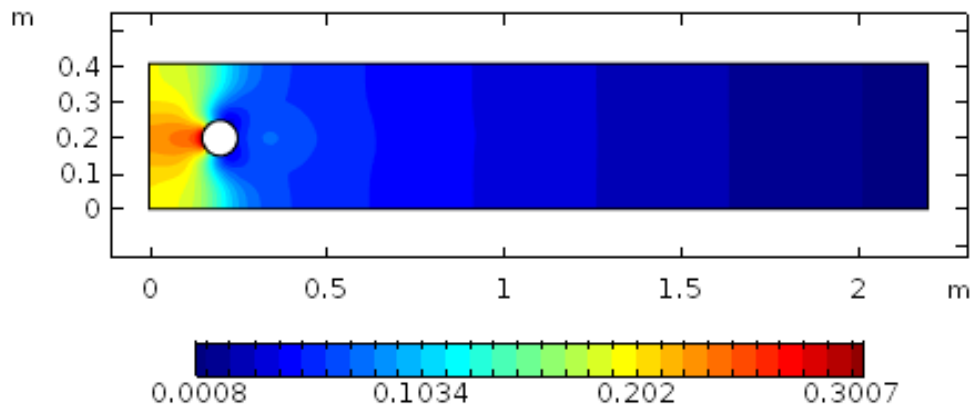


Fig. 10.25. Pressure plot when $n = 2$, $U_{\max} = 0.3$ and $Re = 10$.

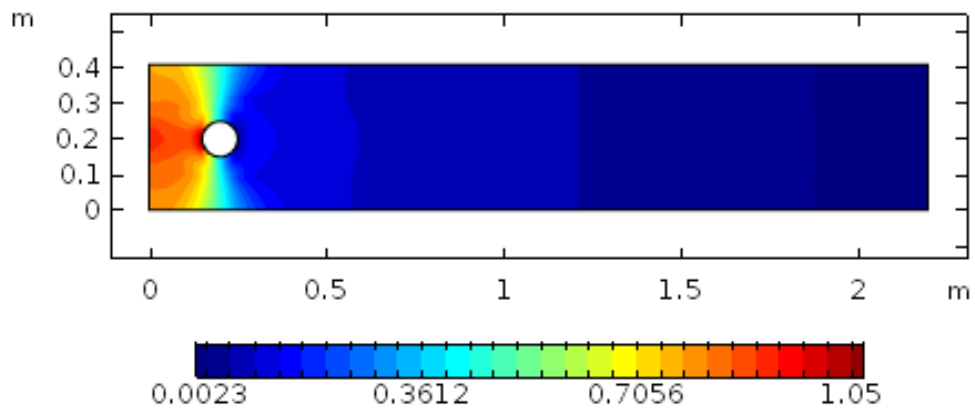


Fig. 10.26. Pressure plot when $n = 3$, $U_{\max} = 0.3$ and $Re = 5$.

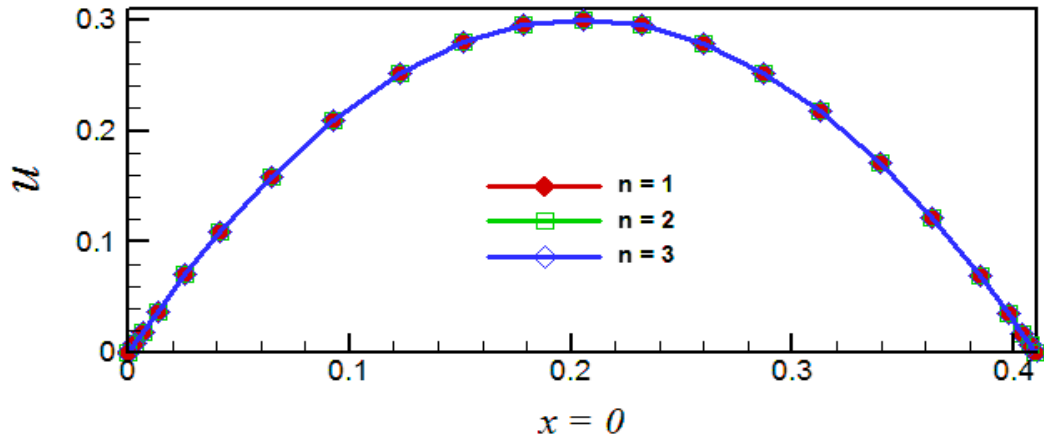


Fig. 10.27. Line graph of Power law parabolic velocity profile at location $x = 0$.

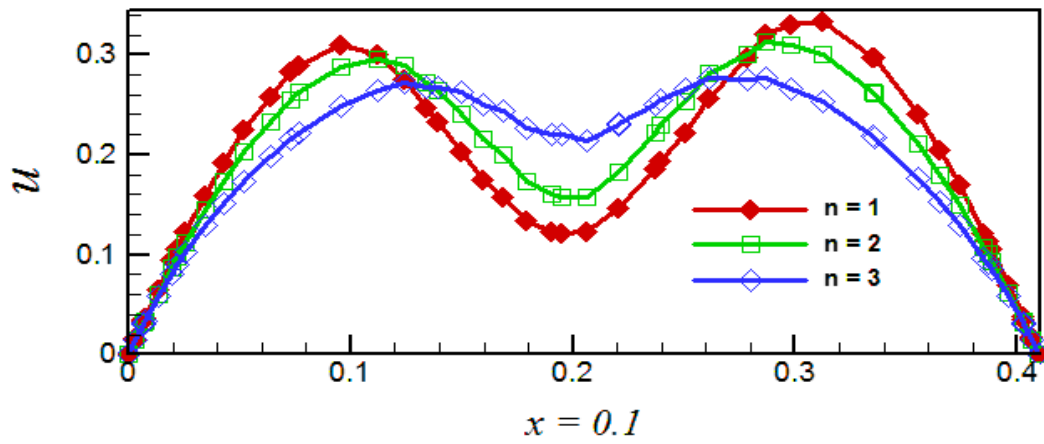


Fig. 10.28. Line graph of Power law parabolic velocity profile at location $x = 0.1$.

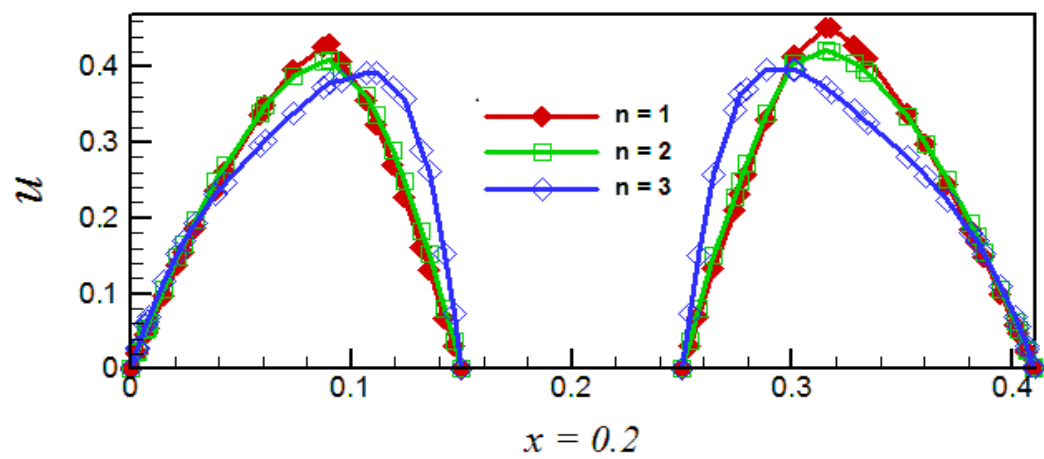


Fig. 10.29. Line graph of Power law parabolic velocity profile at location $x = 0.2$.

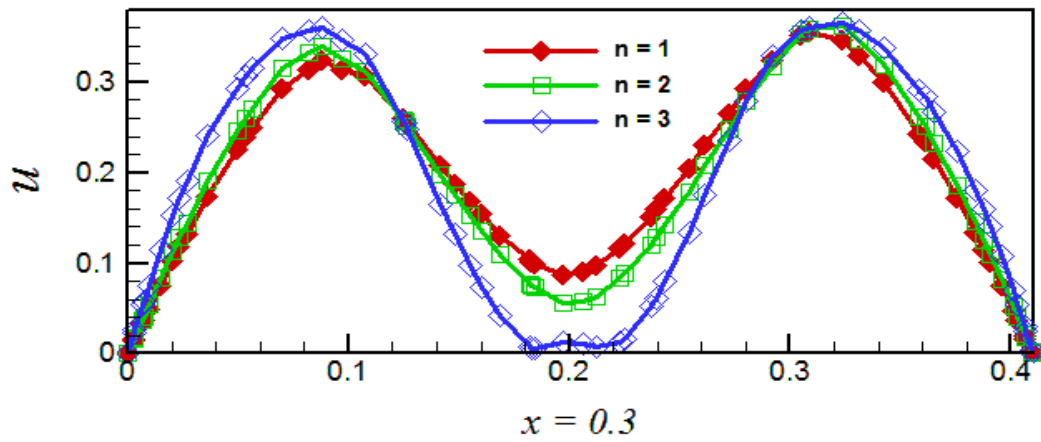


Fig. 10.30. Line graph of Power law parabolic velocity profile at location $x = 0.3$.

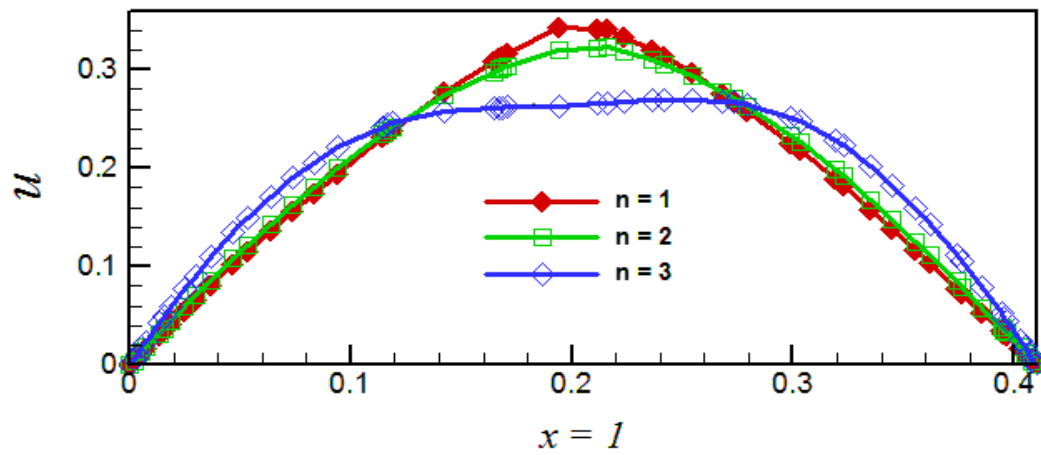


Fig. 10.31. Line graph of Power law parabolic velocity profile at location $x = 1$.

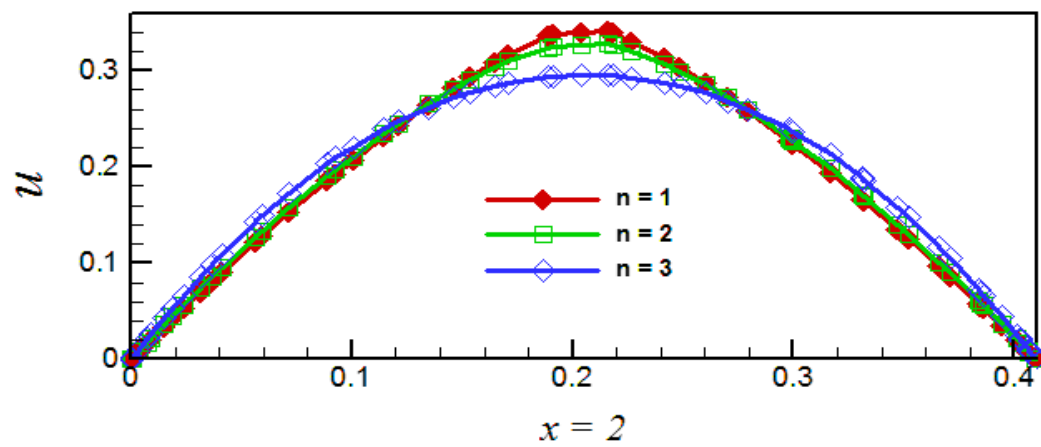


Fig. 10.32. Line graph of Power law parabolic velocity profile at location $x = 2$.

Table 10.7: Numerical values of drag and lift coefficients when

$$U_{\max} = 0.3 \text{ with mesh level-1.}$$

| Refinement Level-1 | n | | |
|-----------------------|-----|--------|-----------|
| | 1.5 | 9.5964 | -0.028461 |
| | 2 | 16.949 | 0.32324 |
| | 2.5 | 33.442 | 0.71828 |
| | 3 | 70.466 | 0.88759 |
| | 3.5 | 152.18 | 0.94013 |
| | 4 | 331.47 | 0.74999 |
| | 4.5 | 725.43 | -0.25092 |
| | 5 | 1590.0 | -3.726 |

Table 10.8: Numerical values of drag and lift coefficients when

$$U_{\max} = 0.3 \text{ with mesh level-2.}$$

| Refinement Level-2 | n | C_D | C_L |
|-----------------------|-----|--------|-----------|
| | 1.5 | 9.4436 | -0.087989 |
| | 2 | 17.247 | 0.48552 |
| | 2.5 | 35.164 | 1.0113 |
| | 3 | 76.097 | 1.5356 |
| | 3.5 | 168.57 | 2.2438 |
| | 4 | 377.29 | 3.6031 |
| | 4.5 | 847.32 | 6.3893 |
| | 5 | 1909.2 | 12.495 |

Table 10.9: Numerical values of drag and lift coefficients when

$$U_{\max} = 0.3 \text{ with mesh level-3.}$$

| Refinement Level-3 | n | C_D | C_L |
|-----------------------|-----|--------|----------|
| | 1.5 | 9.6406 | 0.059579 |
| | 2 | 17.793 | 0.45586 |
| | 2.5 | 36.889 | 0.93759 |
| | 3 | 81.234 | 1.3414 |
| | 3.5 | 182.80 | 1.9091 |
| | 4 | 416.40 | 2.9291 |
| | 4.5 | 953.04 | 4.7585 |
| | 5 | 2189.0 | 8.0252 |

Table 10.10: Numerical values of drag and lift coefficients when

$$U_{\max} = 0.3 \text{ with mesh level-4.}$$

| Refinement Level-4 | n | C_D | C_L |
|-----------------------|-----|--------|----------|
| | 1.5 | 9.5856 | 0.093698 |
| | 2 | 17.816 | 0.53352 |
| | 2.5 | 37.158 | 1.0750 |
| | 3 | 82.334 | 1.6323 |
| | 3.5 | 186.86 | 2.5035 |
| | 4 | 427.67 | 4.1503 |
| | 4.5 | 984.07 | 7.4840 |
| | 5 | 2271.8 | 14.380 |

Table 10.11: Numerical values of drag and lift coefficients when

$$U_{\max} = 0.3 \text{ with mesh level-5.}$$

| Refinement Level-5 | n | C_D | C_L |
|-----------------------|-----|--------|---------|
| | 1.5 | 9.6397 | 0.10608 |
| | 2 | 17.933 | 0.51939 |
| | 2.5 | 37.368 | 1.0307 |
| | 3 | 83.067 | 1.5209 |
| | 3.5 | 189.35 | 2.2469 |
| | 4 | 435.61 | 3.5628 |
| | 4.5 | 1008.2 | 6.1400 |
| | 5 | 2342.2 | 11.302 |

Table 10.12: Numerical values of drag and lift coefficients when

$$U_{\max} = 0.3 \text{ with mesh level-6.}$$

| Refinement Level-6 | n | C_D | C_L |
|-----------------------|-----|--------|---------|
| | 1.5 | 9.6322 | 0.13090 |
| | 2 | 17.963 | 0.54648 |
| | 2.5 | 37.562 | 1.0735 |
| | 3 | 83.741 | 1.5967 |
| | 3.5 | 191.41 | 2.3953 |
| | 4 | 441.24 | 3.8662 |
| | 4.5 | 1023.5 | 6.7791 |
| | 5 | 2385.1 | 12.625 |

Table 10.13: Numerical values of drag and lift coefficients when

$$U_{\max} = 0.3 \text{ with mesh level-7.}$$

| Refinement Level-7 | n | C_D | C_L |
|-----------------------|-----|--------|---------|
| | 1.5 | 9.6395 | 0.12978 |
| | 2 | 17.975 | 0.54648 |
| | 2.5 | 37.701 | 1.0784 |
| | 3 | 84.221 | 1.6043 |
| | 3.5 | 192.90 | 2.3863 |
| | 4 | 446.44 | 3.8645 |
| | 4.5 | 1039.3 | 6.8143 |
| | 5 | 2432.4 | 12.816 |

Table 10.14: Numerical values of drag and lift coefficients when

$$U_{\max} = 0.3 \text{ with mesh level-8.}$$

| Refinement Level-8 | n | C_D | C_L |
|-----------------------|-----|--------|---------|
| | 1.5 | 9.6408 | 0.13175 |
| | 2 | 17.994 | 0.54753 |
| | 2.5 | 37.724 | 1.0727 |
| | 3 | 84.291 | 1.5963 |
| | 3.5 | 193.32 | 2.4024 |
| | 4 | 447.49 | 3.9073 |
| | 4.5 | 1042.8 | 6.9203 |
| | 5 | 2443.4 | 13.049 |

Table 10.15: Numerical values of drag and lift coefficients for Newtonian fluid model

when $U_{\max} = 0.2$.

| Refinement levels | Newtonian case (n = 1) | |
|-------------------|------------------------|-----------|
| | C_D | C_L |
| 1 | 5.1671 | -0.055807 |
| 2 | 4.8794 | -0.038878 |
| 3 | 4.8317 | -0.057457 |
| 4 | 4.8014 | 0.0086052 |
| 5 | 4.8040 | 0.012904 |
| 6 | 4.7944 | 0.046508 |

Table 10.16: Numerical values of drag and lift coefficients for Newtonian fluid model

when $U_{\max} = 0.3$.

| Refinement levels | Newtonian case (n = 1) | |
|-------------------|------------------------|-----------|
| | C_D | C_L |
| 1 | 6.0207 | -0.099437 |
| 2 | 5.6119 | -0.10289 |
| 3 | 5.5796 | -0.091933 |
| 4 | 5.5892 | -0.050458 |
| 5 | 5.5930 | -0.038479 |
| 6 | 5.5863 | 0.020429 |
| 7 | 5.582 | 0.0084230 |
| 8 | 5.5811 | 0.010207 |

Table 10.17: DOFs statistics for various refinement levels.

| Refinement levels | DOFs | Refinement levels | DOFs |
|-------------------|------|-------------------|--------|
| 1 | 1680 | 5 | 10899 |
| 2 | 2694 | 6 | 19071 |
| 3 | 4131 | 7 | 43542 |
| 4 | 7533 | 8 | 102984 |

Tables. 10.7-10.14 offer the numerical values due to both the drag and lift coefficients when the Power law fluid model is considered towards channel of length 2.2 m with height 0.41 m. Both the drag and lift forces are generated due to placement of circular cylinder centered at (0.2, 0.2) m. The numerical values are evaluated for different values of Power law index that is $n = 1.5, 2, 2.5, 3, 3.5, 4, 4.5$ and 5 up-to 8-refinement levels subject to domain meshing of channel. Owing the level 8 values it is noticed that when we iterate Power law index namely, $n = 1.5, 2, 2.5, 3, 3.5, 4, 4.5$ and 5 the drag and lift coefficient values enhances significantly. Since the Power law fluid model is considered and it is well known fact that for $n = 1$ the Power law fluid model reduces to Newtonian case. Schaefer and Turek [140] consider Newtonian fluid flow in a channel having circular obstacle centred at (0.2, 0.2). The benchmark quantities are calculated in this attempt and the most reliable digits proposed for the drag and lift coefficients were $C_D = 5.579535$ and $C_L = 0.010618$ respectively. It is important to note that they consider parabolic profile at an inlet of channel. Table 10.15 reports the numerical values of drag and lift coefficients for linear (constant) profile at various refinement levels when $n = 1$. Table 10.16 reports the numerical data for both the drag and lift coefficients at various refinement levels when $n = 1$. It can be seen that a good agreement is found with Schaefer and Turek [140]. Especially at 8th refinement level.

10.7 Conclusion

The present attempt deals finite element analysis on non-Newtonian fluid flow in a channel when both the lower and upper walls with no slip condition. The right wall is specified with the Neumann condition. Two different velocity profiles of Power law fluid are initiated at an inlet namely, linear (constant) and parabolic velocity profile. The Power law fluid in each case strikes with an obstacle being placed within channel and the bifurcation of Power law fluid occurs around circular cylinder. The concluding observations are itemized as follows:

- The leading stagnation point region increases towards higher values of Power law index that is $n = 1, 2$ and 3 both for linear and parabolic profiles initiated at an inlet of Power law fluid.

- For $n = 1$ (Newtonian fluid) in the laminar flow zone, the Power law fluid velocity remarks significant magnitude of velocity as compared to iteration of Power law index $n = 2$ and 3 .
- For higher values of the Power law index that is $n = 1, 2$ and 3 the pressure in leading point region increases.
- Pressure singularities occur at an inlet in case of linear (constant) velocity profile of Power law fluid.
- Power law fluid with parabolic profile initiated at an inlet is more realistic approach than that of Power law fluid with linear (constant) profile.
- Both drag and lift coefficients are increasing functions of iteration in Power law index that is $n = 1.5, 2, 2.5, 3, 3.5, 4, 4.5$ and 5 .

Chapter 11

Object Dependent Optimization of Hydrodynamic Forces in Liquid Stream: Finite Element Analysis

11.1 Introduction

The present chapter reports the extended novelty of the hydrodynamics. To be more specific, the flowing fluid stream admitting Newton's law of viscosity is considered in a smooth rectangular channel. The various typical shaped cylinders are placed fixed in between rectangular channel as an obstacle. The shape of obstacles includes the triangle, square, hexagon, octagon and circle. The no-slip condition is carried at both the upper and lower walls of the channel. The right wall as an outlet is specified with the Neumann condition. The fluid is initiated at an inlet of the channel with the two different class of velocity profiles, namely the constant velocity profile and the parabolic profile. The whole physical designed is controlled mathematically in terms of Navier-Stokes equations. The solution is proposed with the finite element method and for the discretization of flow narrating equations the LBB-stable finite element pair is utilized along with a hybrid meshing scheme. The primitive variables namely, the velocity and pressure are reported for each obstacle. The line integration around the outer surface of the triangle, square, hexagon, octagon and circular cylinders is carried for the evaluation of hydrodynamic forces. The statistical data for such hydrodynamic forces is recorded up-to nine various refinement levels.

11.2 Problem Description

The rectangular channel having length 2.2m and height 0.41m is considered as a computational domain. The Newtonian fluid is taken in a rectangular channel. The boundary assumption includes the no-slip condition at both upper and lower walls that is the relative velocity of fluid particles and the lower/upper walls is zero. The right wall is treated as an outlet of the channel and it is carried with notable Neumann condition while

the left wall of the channel is considered as an inlet. The two different types of velocity profiles are considered with which the Newtonian fluid enters into the channel. The velocity supposition includes the constant velocity profile and the parabolic velocity profile. The incoming fluid strikes with the obstacles being placed fixed in a channel. The triangle, square, hexagon, octagon and circular shaped cylinders are taken as an obstacle in present work.

11.3 Mathematical Model

To investigate the fluid flow towards the triangle, square, hexagon, octagon and circular shaped cylinders as an obstacle being placed in between the rectangular channel, the most acceptable mathematical model named Navier-Stokes equations is considered. To attain the concluding flow narrating differential equations firstly one can initiate with the equation of continuity as follows:

$$\frac{\partial \rho(x, y, z, t)}{\partial t} + \vec{\nabla} \cdot (\rho(x, y, z, t) \vec{V}(x, y, z, t)) = 0, \quad (11.1)$$

and the momentum equation can be written as:

$$\rho(x, y, z, t) \frac{D\vec{V}(x, y, z, t)}{Dt} = -\vec{\nabla} p(x, y, z) + \mu \vec{\nabla}^2 \vec{V}(x, y, z, t) + \rho(x, y, z, t) \vec{B}, \quad (11.2)$$

to attain the dimensionless form of the Eq. (11. 2), the following setup is taken:

$$\vec{V}^* = D_m \vec{V}, \vec{V}^*(x, y, z, t) = \frac{\vec{V}(x, y, z, t)}{U_m}, \frac{\partial}{\partial t^*} = \frac{D_m}{U_m} \frac{\partial}{\partial t}, p^* = p \frac{1}{\rho U_m^2}, \vec{B}^* = \vec{B} \frac{D_m}{U_m^2}, \quad (11.3)$$

by use of Eq. (11.3) into Eq. (11.2), one can get

$$\frac{D\vec{V}^*(x, y, z, t)}{Dt^*} = -\vec{\nabla}^* p^*(x, y, z) + \frac{\mu}{\rho D_m U_m} \vec{\nabla}^{*2} \vec{V}^*(x, y, z, t) + \vec{B}^*, \quad (11.4)$$

here, $\frac{1}{\text{Re}} = \frac{\mu}{\rho D_m U_m}$ is termed as the Reynolds number. Further, by dropping “*” one can

render

$$\frac{D\vec{V}(x, y, z, t)}{Dt} = -\vec{\nabla} p(x, y, z) + \frac{1}{\text{Re}} \vec{\nabla}^2 \vec{V}(x, y, z, t) + \vec{B}, \quad (11.5)$$

here, \vec{V} is the velocity field, μ is viscosity, ρ is fluid density, p represents the pressure, \vec{B} is the body force. ∇ is the del operator, U_m be the reference velocity, D_m be the characteristic length and Re is the symbolic notation of Reynolds number. In the absence of body force ($\vec{B}=0$), and by considering two dimensional an incompressible steady fluid flow in a rectangular channel, the concluding mathematical flow narrating differential equations are:

$$\frac{\partial u}{\partial x} + \frac{\partial v}{\partial y} = 0, \quad (11.6)$$

$$Re \left(u \frac{\partial u}{\partial x} + v \frac{\partial u}{\partial y} \right) = -Re \frac{\partial p}{\partial x} + \frac{\partial^2 u}{\partial x^2} + \frac{\partial^2 u}{\partial y^2}, \quad (11.7)$$

$$Re \left(u \frac{\partial v}{\partial x} + v \frac{\partial v}{\partial y} \right) = -Re \frac{\partial p}{\partial y} + \frac{\partial^2 v}{\partial x^2} + \frac{\partial^2 v}{\partial y^2}. \quad (11.8)$$

The endpoint condition for constant velocity profile can be written as:

$$\begin{aligned} \text{Inlet boundary} \quad u &= U_c, v = 0, \\ \text{Outlet boundary} \quad \frac{\partial u}{\partial x} &= \frac{\partial v}{\partial x} = 0, \\ \text{Side walls} \quad u &= 0, v = 0. \end{aligned} \quad (11.9)$$

The mathematical endpoint expressions for the assumption of the parabolic velocity profile case can be summarized as follows:

$$\begin{aligned} \text{Inlet boundary} \quad u &= 4.U_{Max} y.(H - y), \quad v = 0, \\ \text{Outlet boundary} \quad \frac{\partial u}{\partial x} &= \frac{\partial v}{\partial x} = 0, \\ \text{Side walls} \quad u &= 0, v = 0. \end{aligned} \quad (11.10)$$

The fluid flow around an object produces both the lift and drag force. It is all about the position of object in a fluid because it is correct to say that the existence of drag force does not imply the existence of lift force. In present case the height of channel is selected 0.41m so that the obstacles becomes offset with center (0.2, 0.2)m and when fluid past the triangle, square, hexagon, octagon and circular shaped obstacles, both the drag and lift forces will appear. To investigate these benchmark quantities, the dimensionless expression for the lift and drag coefficients are written as follows:

$$L_f = \frac{2L_F}{\rho(U_{\text{mean}})^2 D_m}, \quad (11.11)$$

$$D_f = \frac{2D_F}{\rho(U_{\text{mean}})^2 D_m}, \quad (11.12)$$

the symbolic notation for the lift coefficient is L_f and D_f is the symbolic notation for the drag coefficient, whereas U_{mean} , L_F and D_F denotes mean velocity, lift force and drag force respectively.

11.4 Computational Scheme

The Eq. (11.1) represents the equation of continuity while the Eq. (11.2) is Lagrangian form of Navier-Stokes equation. To achieve dimensionless form, the setup provided in Eq. (11.3) is utilized and the ultimate dimensionless form of the Eq. (11.2) is written in Eq. (11.5). Using the assumption of time independent and two dimensional incompressible flow of Newtonian fluid in the rectangular channel leads to Eq. (11.6), Eq. (11.7) and Eq. (11.8). To be more specific, the Eq. (11.6) is two dimensional continuity equation. In the absence of body force, the two dimensional incompressible mathematical exercise subject to Eq. (11.5) reduces to Eq. (11.7) and Eq. (11.8) as x -component and y -component respectively. The mathematical expression for the case of constant velocity profile assumption is given in Eq. (11.9) while the Eq. (11.10) own the mathematical form for the assumption of parabolic velocity profile. The attention is to find the solution of Eqs. (11.6)-(11.10) case wise. Since the differential system provided in Eqs. (11.6)-(11.10) is highly nonlinear therefore to find exact solution seems not possible. Therefore, we have used finite element method to report better approximations. The finite element simulation is known as finite element analysis (FEA). The FEA is one of the prominent directory adopted by researchers to examine real life phenomena like thermal transport and fluid flow field. The Eqs. (11.6)-(11.10) for both the velocities assumptions namely, the linear velocity profile and the parabolic velocity profile, are solved against each obstacle. The primitive variables which includes the velocity and the pressure are evaluated for each case. To evaluate the accurate values of the lift and drag coefficients towards triangle, square, hexagon, octagon and circle, the fine meshing around each obstacle is carried. To offer broader frame the simulations are recorded for extremely coarse meshing (level-1),

extra coarse meshing (level-2), courser meshing (level-3), coarse meshing (level-4), normal meshing (level-5), fine meshing (level-6), finer meshing (level-7), extra fine meshing (level-8), and extremely fine meshing (level-9). The adopted parametric values for the case of constant velocity profile is as follows: $U_{mean} = U_c = 2/7$, $\mu = 0.001$, and $\rho = 1$. To fix the Reynolds number $Re = 20$, for both triangle and square obstacle the characteristic length is selected $D_m = 0.07$ while for hexagon, octagon and circular obstacle it is selected as $D_m = 0.1$. The adopted values for the case of parabolic velocity profile are $\rho = 1$, $\mu = 0.001$, and for fixing Reynolds number $Re = 20$, the mean inflow velocity is taken as a reference velocity $U_{mean} = \frac{2}{3}U_{Max} = 2/7$, where $U_{Max} = 3/7$, is the maximum inflow velocity of the parabolic profile for both triangle and square obstacle with characteristic length $D_m = 0.07$. For hexagon, octagon and circle with characteristic length $D_m = 0.1$, the mean inflow velocity is considered as a reference velocity $U_{mean} = \frac{2}{3}U_{Max} = 0.2$, where $U_{Max} = 0.3$, is the maximum inflow velocity of the parabolic profile.

11.5 Analysis

The flow around triangle, square, hexagon, octagon and circular shaped obstacles in a rectangular domain is investigated and discussed case-wise namely, OBSTACLE -I, OBSTACLE -II, OBSTACLE -III, OBSTACLE -IV and OBSTACLE -V.

11.5.1 OBSTACLE-I

In this case the triangle shaped cylinder is consider as an obstacle being placed towards ongoing Newtonian fluid in a rectangular channel. The vertices of triangle are selected as follows: (0.165, 0.165), (0.235, 0.165) and (0.165, 0.235). The boundary assumption for computational domain can be written as:

| | | |
|------------------------|--|---------|
| Inlet boundary | $u = U_c = 2/7$ or $4.U_{Max} \cdot y(H - y), v = 0,$ | (11.13) |
| Outlet boundary | $\frac{\partial u}{\partial x} = \frac{\partial v}{\partial x} = 0,$ | |
| Channel side walls | $u = 0, v = 0,$ | |
| Triangle outer surface | $u = 0, v = 0.$ | |

The Eq. (11. 13) represents the assumption of both the constant and parabolic velocity profiles. To examine the flow field properties the FEM is used and the outcomes are recorded for nine various refinement levels. Figs. 11.1-11.9 and Tables 11.1-11.3 provided the finite element simulation for triangle obstacle. In detail, Fig. 11.1 is domain discretization of rectangular channel and termed as extremely coarse meshing (level-1). In this level the computational domain consists of 1005 domain elements (DEs) and 113 boundary elements (BEs). The Fig. 11.2 shows the normal meshing (level-5) for rectangular channel having triangle shaped cylinder as an obstacle. The discretization contains 7544 DEs and 406 BEs. The extreme fine meshing is provided in Fig. 11.3 and it consist of 132202 DEs and 2062 BEs. Further, the detail of meshing statistics against each level for channel with triangle obstacle is provided in Table. 11.1. Fig. 11.4 is velocity plot when the Reynolds number is taken fixed of value $Re = 20$ and the flow is initiated with constant velocity profile at an inlet of channel. It is seen that the incoming fluid strikes with triangle obstacle and the speedy bifurcation occurs. The velocity of fluid increases due to collision with triangle obstacle. It can be seen that the velocity of particles with both upper and lower walls of channel seems absurd. The corresponding pressure distribution is given with the help of Fig. 11.5. One can see that the pressure is maximum at left face of triangle. The stagnation point exists at right face where the pressure seems maximum. The assumption of no-slip condition at both upper and lower walls with constant velocity entrances of fluid leads to maximum pressure at (0, 0) and (0, 0.41). The Fig. 11.6 and Fig. 11.7 are plotted when the fluid is initiated with the parabolic velocity profile. Particularly, Fig. 11.6 reports the velocity distribution for the fixed value of Reynolds number $Re = 20$. It is observed that the Newtonian fluid strikes with triangle and creates stagnation point region at left face of obstacle. The fluid bifurcation happens around triangle obstacle. The fluid gain momentum after striking with obstacle and obstacle disturbance can be observed up-to length of channel $x = 1$. The corresponding pressure distribution for parabolic velocity profile being initiated at an inlet of channel is given by means of Fig. 11.7. Fig.

11.8 reports the line graph study of u -velocity at various position of channel for the first case that is the fluid enters into channel with linear velocity $U_c = 2/7 = 0.28$. Such assumption is graphically testified at the position $x = 0.0$. The significant bifurcation occurs for the channel length $x = 0.1$. One can see from Fig. 11. 8, at $x = 0.3$, the fluid just left the obstacle and travels with uniform distribution at both upper and lower half of channel. At $x = 2.0$ it can be seen that the fluid attain the bulk motion down the stream. It is important to note that initially the fluid is initiated with constant velocity profile so there should be a constant profile at an outlet of channel but we achieved parabolic view. This happens due to non-compatible assumptions which includes; the zero velocity of both upper and lower walls; the relative velocity of walls and fluid particles should be zero that is the no-slip assumption at upper and lower walls; the constant velocity with which fluid enters into channel. When fluid enters into channel with constant profile the walls offer resistance to flow due to no-slip condition and hence maximum pressure is observed at an inlet of channel with corner points that is $(0, 0)$ and $(0, 0.41)$. Such corners points are termed as pressure singularities. Fig. 11.9 offers the line graph study of u -velocity for the case of parabolic velocity profile. The graphical justification for the parabolic velocity profile being assumed at inlet of channel can be seen at $x = 0.0$. Later, the significant bifurcation can be observed at $x = 0.1$ and $x = 0.3$. The velocity line graph at channel of length $x = 2.0$ shows that the fluid retrace its profile. This happens due to selection of parabolic velocity profile at an inlet of channel because with this assumption the pressure singularities got eliminated. The striking of fluid with triangle shaped obstacle give birth to two benchmark quantities namely, the drag coefficient and the lift coefficient. These benchmark quantities are evaluated by performing line integration around the outer surface of triangle. Particularly, Table. 11.2 offer the values of both the drag and lift coefficient for the constant velocity profile while Table. 11.3 report the values of both the drag and the lift coefficient for the case of parabolic velocity profile. Both results are carried at fixed value of Reynolds number $Re = 20$. For the case of the constant velocity profile the most refined value of drag coefficient is 2.9253 and lift coefficient is 0.23208. For the parabolic velocity profile at level-9, the refined value of drag coefficient is 6.0074 and lift coefficient is -0.69112.

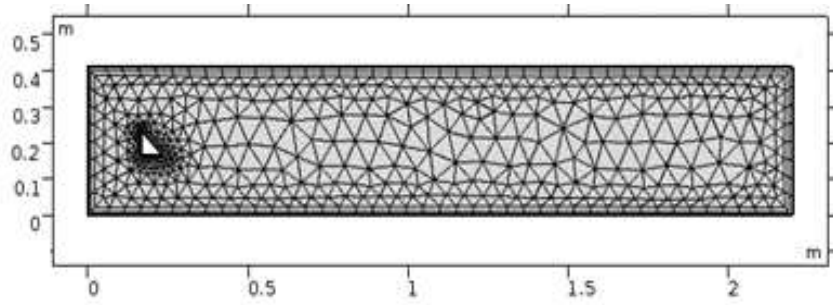


Fig. 11.1. Extremely coarse meshing when triangle is taken as an obstacle.

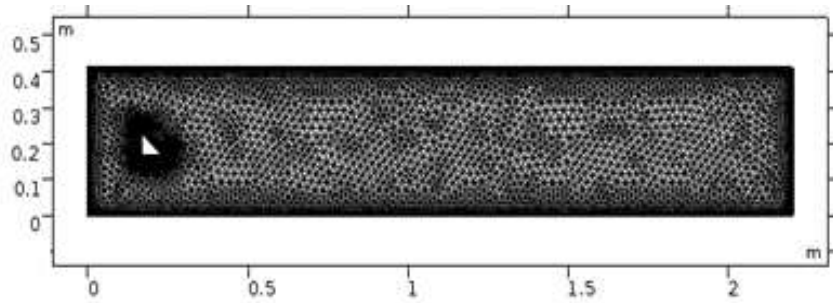


Fig. 11.2. Normal meshing when triangle is taken as an obstacle.

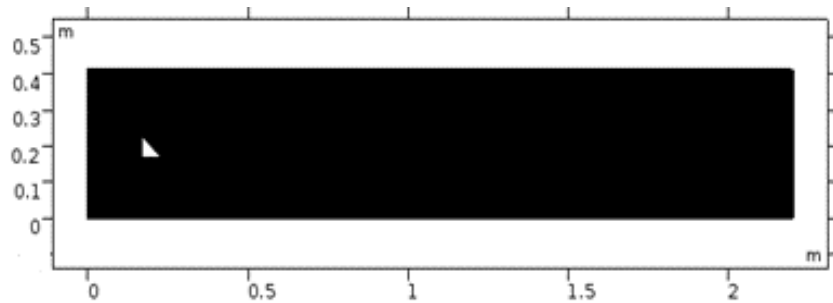


Fig. 11.3. Extremely fine meshing when triangle is taken as an obstacle.

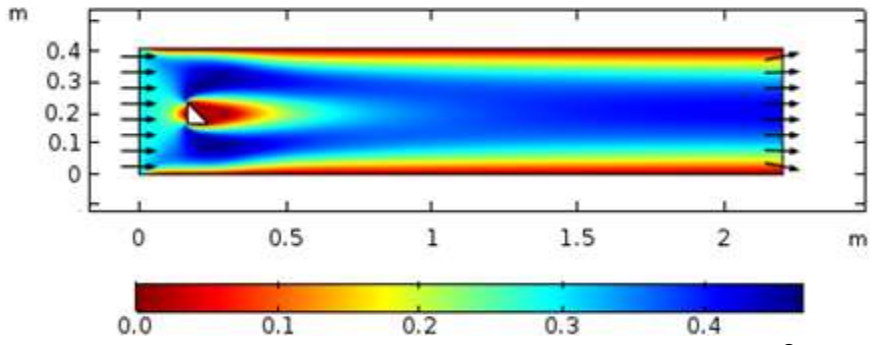


Fig. 11.4. Velocity plot for triangle obstacle when $D_m = 0.07$, $U_c = \frac{2}{7}$ and $Re = 20$.

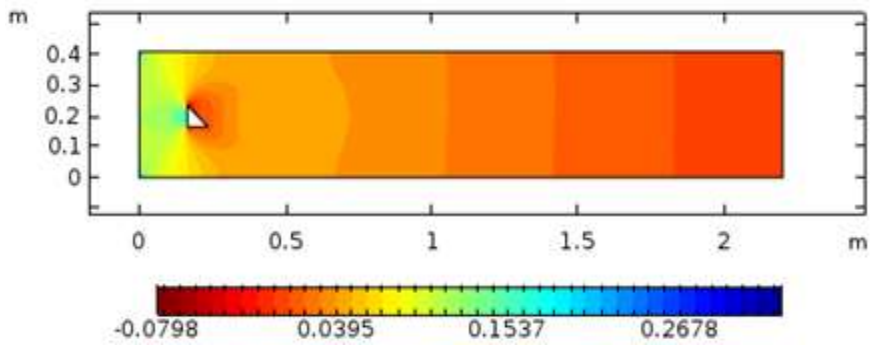


Fig. 11.5. Pressure plot for triangle obstacle when $D_m = 0.07$, $U_c = \frac{2}{7}$ and $Re = 20$.

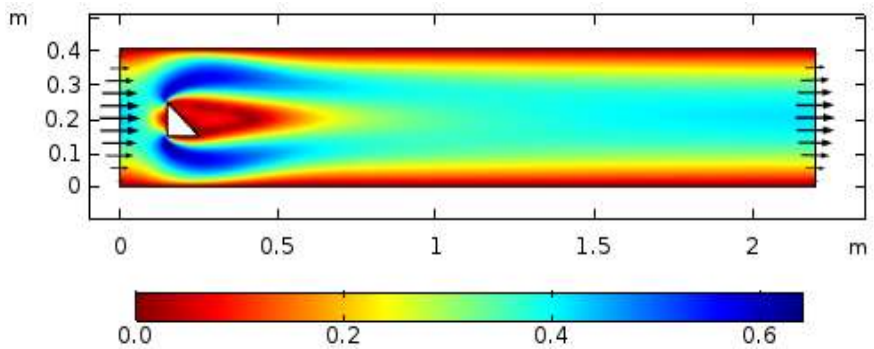


Fig. 11.6. Velocity plot for triangle obstacle when $D_m = 0.07$, $U_{Max} = \frac{3}{7}$ and $Re = 20$.

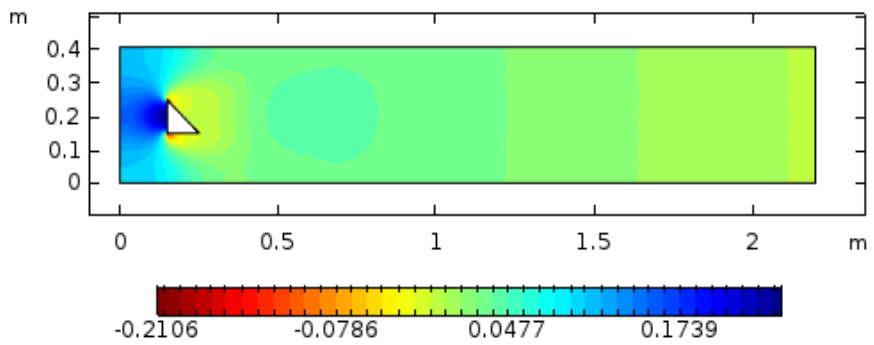


Fig. 11.7. Pressure plot for triangle obstacle when $D_m = 0.07$, $U_{Max} = \frac{3}{7}$ and $Re = 20$.

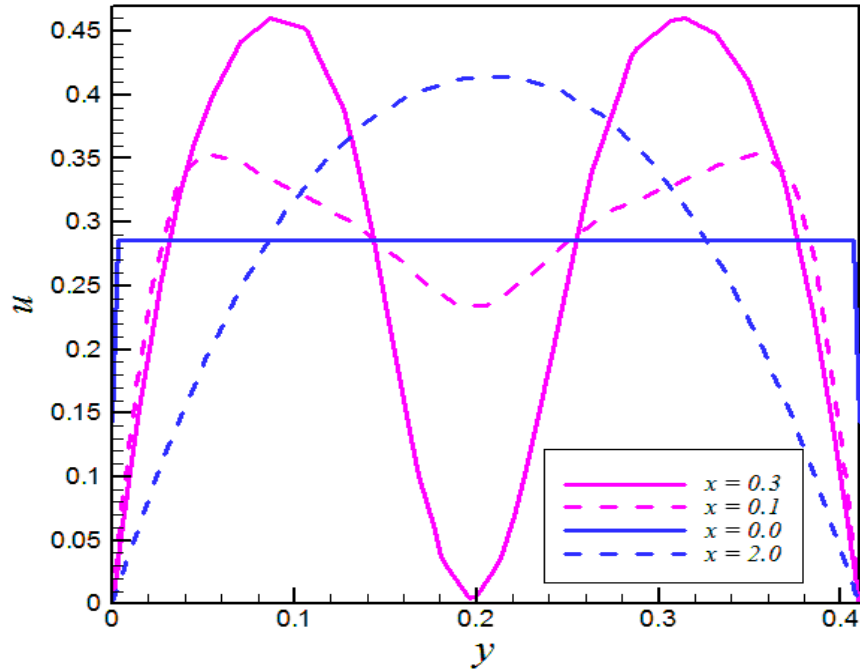


Fig. 11.8. Velocity line graphs at various position of channel having triangle obstacle and $D_m = 0.07$, $U_c = \frac{2}{7}$ and $Re = 20$.

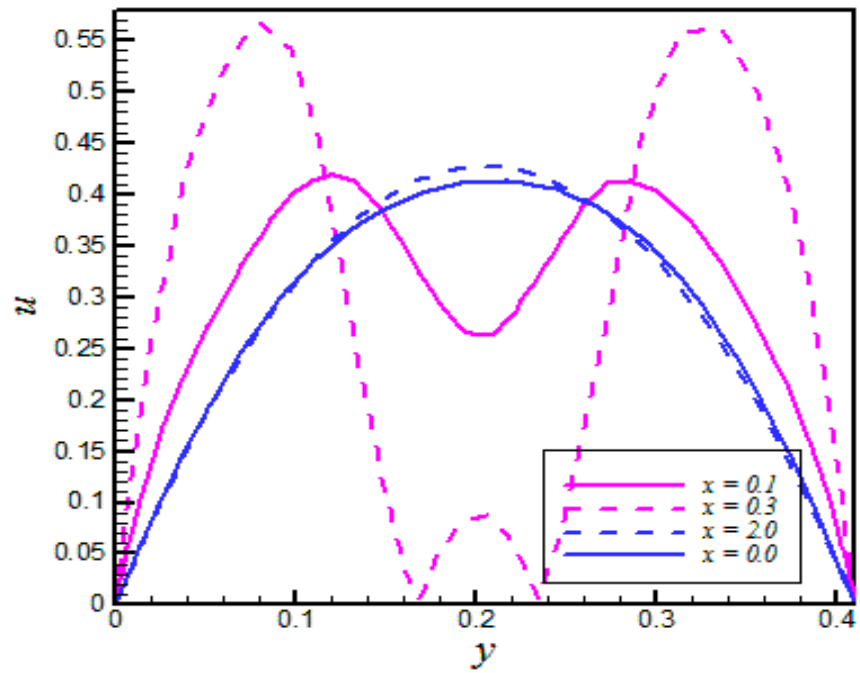


Fig. 11.9. Velocity line graphs at various position of channel having triangle obstacle and $D_m = 0.07$, $U_{Max} = \frac{3}{7}$ and $Re = 20$.

11.5.2 OBSTACLE-II

The square shaped cylinder is taken as an obstacle towards incoming fluid flow in a channel. In two dimensional frame, (0.165, 0.235), (0.165, 0.165), (0.235, 0.165) and (0.235, 0.235) are the vertices of square in rectangular channel of length 2.2 m and height 0.41m. The endpoint assumptions for both the constant and parabolic velocity profiles are as follows:

$$\begin{array}{ll}
 \text{Inlet boundary} & u = U_c = 2/7 \text{ or } 4.U_{Max} \cdot y(H - y), v = 0, \\
 \text{Outlet boundary} & \frac{\partial u}{\partial x} = \frac{\partial v}{\partial x} = 0, \\
 \text{Channel side walls} & u = 0, v = 0, \\
 \text{Square outer surface} & u = 0, v = 0.
 \end{array} \tag{11.14}$$

The solution is obtained by means of finite element method and the outcomes in this direction are shared with the help of Figs. 10-18 and Tables. 4-6. In detail, the Fig. 10 provides the extremely coarse meshing of rectangular channel having square as an obstacle. In this level the geometry is discretized into 1020 DEs and 116 BEs. The normal meshing for present case is shown in Fig. 11.11 and it contains 7702 DEs and 416 BEs. For better approximation the extremely fine meshing is performed and shown in Fig. 11.12 and it contains 132928 DEs and 2102 BEs. The summary of nine various meshing scheme for the channel with square shaped obstacle is presented in Table. 11.4. Fig. 11.13 shows the velocity distribution for the fixed value of Reynolds number $Re = 20$ when fluid is initiated with constant velocity profile. The fluid strikes with left face of square and the bifurcation occurs. It can be noticed that the stagnation point appears at left face of obstacle. The corresponding pressure distribution is shared in Fig. 11.14. One can see that the pressure appears maximum at left face of obstacle and at the corner points of channel that is (0, 0) and (0, 0.41). Later, the pressure varies linearly down the stream in the channel. The points (0, 0) and (0, 0.41) are termed as pressure singularities and they appeared due to non-compatible choice of assumption at walls, and the fluid velocity at an inlet. Fig. 11.15 and Fig. 11.16 are plotted when the fluid flow is initiated with parabolic profile towards square obstacle in a channel. From Fig. 11.15 it is seen that the velocity of fluid near the walls is zero and after collision with obstacle the fluid velocity increases significantly. From Fig. 11.16 it is observed that the pressure is maximum at left face of square obstacle and the pressure singularities are eliminated. The line graph of u -velocity for both the

constant and parabolic profiles is examined. To be more specific, Fig. 11.17 provides the line graph study of u -velocity when the fluid is initiated with constant velocity profile at an inlet of channel. At position $x = 0.0$, the assumption is justified that is the constant velocity. It can be seen that at $x = 0.1$ the fluid bifurcate significantly. At $x = 0.2$ the fluid distribution is uniform towards upper and lower part of square obstacle and at this stage fluid velocity reflects higher value. The u -velocity examination is performed at position $x = 1.0$ and it is noticed that the fluid velocity cannot reshaped its initial constant velocity profile due to appearing of pressure singularities. Fig. 11.18 provides the u -velocity line graphs for the case of parabolic velocity profile. Fig. 11.18 contains evaluation at various position of channel which includes $x = 0.0, 0.1, 0.2$ and 2 . The initial assumption of parabolic velocity profile can be seen at $x = 0.0$ and the fluid deformation is observed at $x = 0.1$. The symmetric distribution of fluid towards square obstacle is seen at $x = 0.2$. The u -velocity examination is performed at $x = 2.0$ and one can easily seen that the fluid velocity recovers its initial assumption of parabolic velocity profile. The line integration is performed around the boundary of square obstacle and both the drag and the lift coefficients are evaluated. Particularly, Table 11.5 provides both the drag and lift coefficient values at nine meshed levels for the case of the constant velocity profile. The most trustful value of drag coefficient is 3.0686 and lift coefficient is 0.034400. Table 6 contains the statistics for drag and lift coefficients when the fluid is initiated with the parabolic velocity profile. The most refined values are obtained for simulation at an extremely fine meshing level. Accordingly, the drag coefficient is 3.7945 and the left coefficient is 0.0086561.

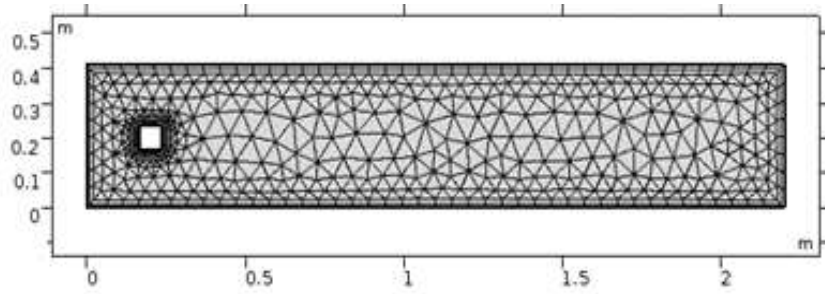


Fig. 11.10. Extremely coarse meshing when square is taken as an obstacle.

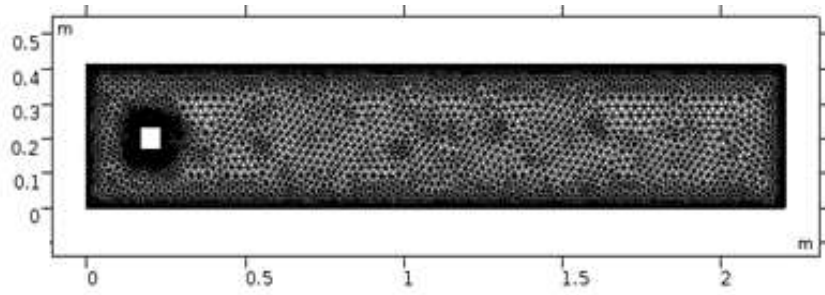


Fig. 11.11. Normal meshing when square is taken as an obstacle.

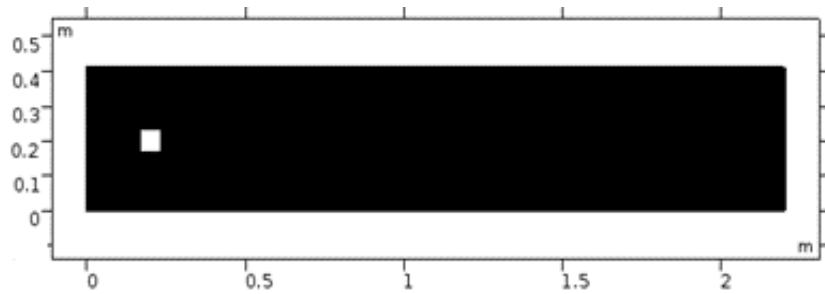


Fig. 11.12. Extremely fine meshing when square is taken as an obstacle.

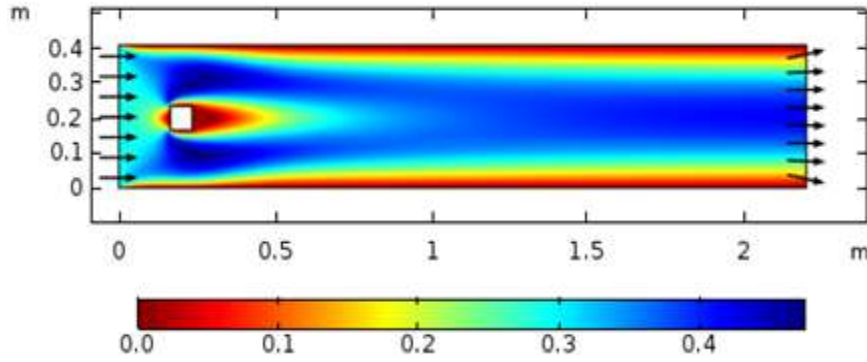


Fig. 11.13. Velocity plot for square obstacle when $D_m = 0.07$, $U_c = \frac{2}{7}$ and $Re = 20$.

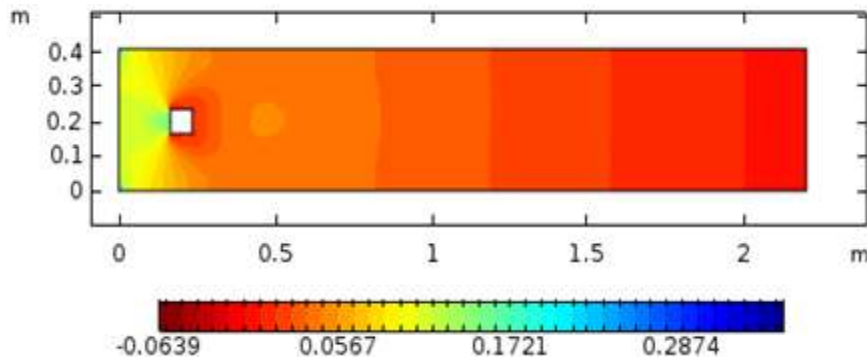


Fig. 11.14. Pressure plot for square obstacle when $D_m = 0.07$, $U_c = \frac{2}{7}$ and $Re = 20$.

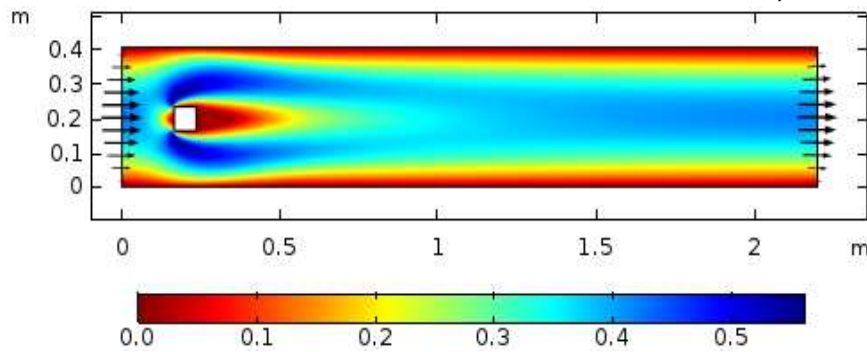


Fig. 11.15. Velocity plot for square obstacle when $D_m = 0.07$, $U_{Max} = \frac{3}{7}$ and $Re = 20$.

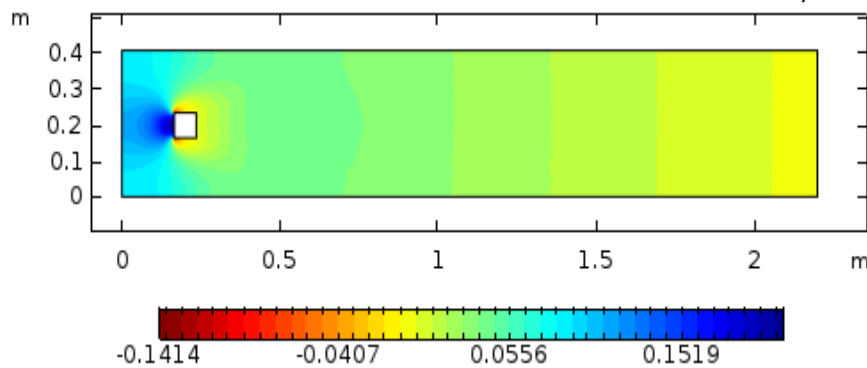


Fig. 11.16. Pressure plot for square obstacle when $D_m = 0.07$, $U_{Max} = \frac{3}{7}$ and $Re = 20$.

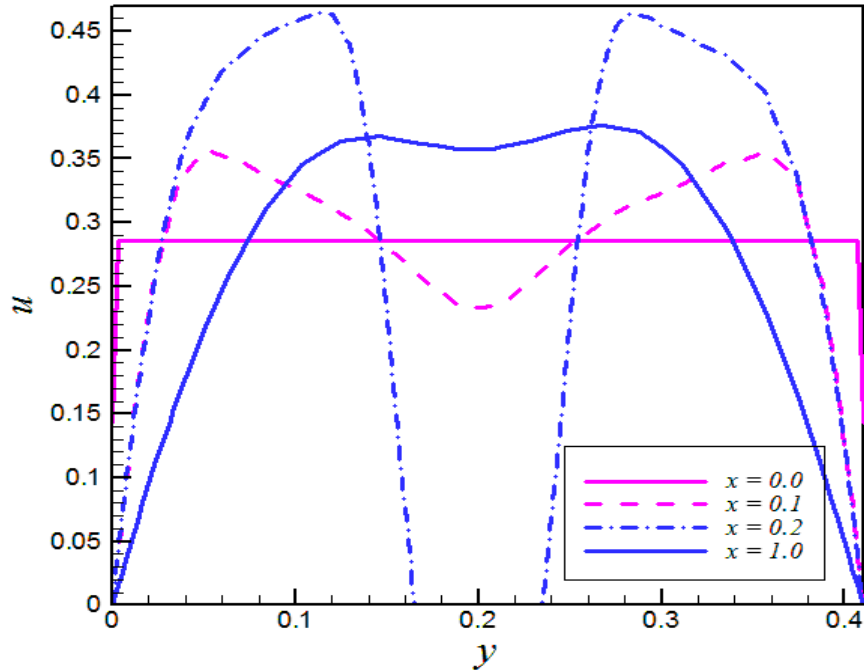


Fig. 11.17. Velocity line graphs at various position of channel having square obstacle with $D_m = 0.07$, $U_c = \frac{2}{7}$ and $Re = 20$.

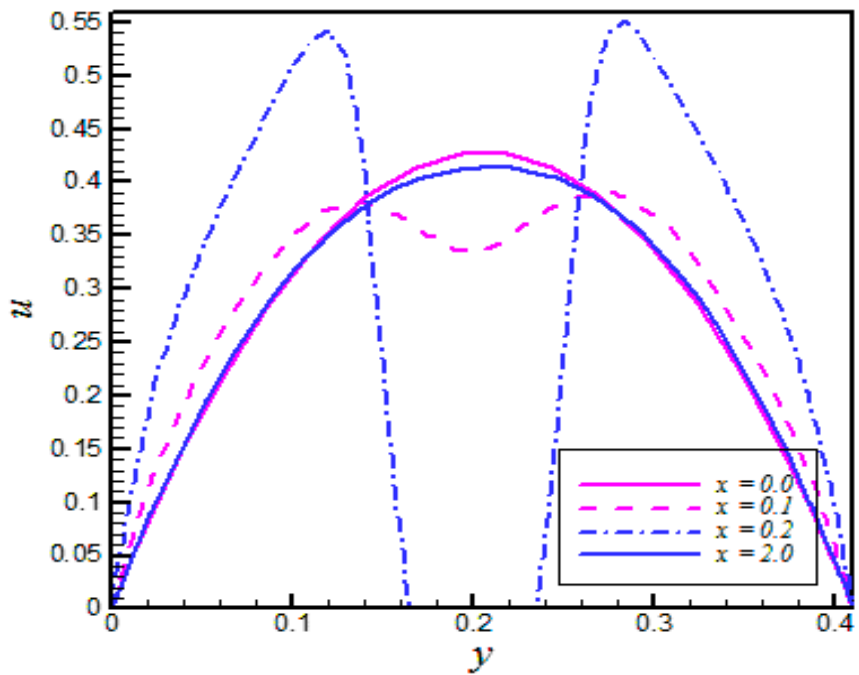


Fig. 11.18. Velocity line graphs at various position of channel having square obstacle with $D_m = 0.07$, $U_{Max} = \frac{3}{7}$ and $Re = 20$.

11.5.3 OBSTACLE-III

The channel with length 2.2m and height 0.41m is considered a computational domain. The hexagon shaped obstacle is placed fixed in between channel with vertices (0.2, 0.25), (0.165, 0.235), (0.165, 0.165), (0.2, 0.15), (0.235, 0.165), and (0.235, 0.235). For the present case the boundary conditions in terms of mathematical form can be written as:

$$\begin{aligned}
 \text{Inlet boundary} & \quad u = U_c = 0.2 \text{ or } 4.U_{Max}.y(H - y), v = 0, & (11.15) \\
 \text{Outlet boundary} & \quad \frac{\partial u}{\partial x} = \frac{\partial v}{\partial x} = 0, \\
 \text{Channel side walls} & \quad u = 0, v = 0, \\
 \text{Hexagon outer surface} & \quad u = 0, v = 0.
 \end{aligned}$$

For hexagon shaped obstacle the flow narrating differential system that is Eqs. (11.6)-(11.8) along with Eq. (11.15) is solved by using finite element method and the ultimate outcomes are presented with help of Figs. 11.19-11.27 and Tables 11.7-11.9. Figs. 11.19-11.21 are meshing structure of geometry of the problem. To be more specific, Fig. 11.19 shows the extreme coarse meshing of rectangular channel having hexagon shaped obstacle. This level contains 1010 DEs and 108 BEs. The level-5 also known as normal meshing is presented in Fig. 11.20. It is improved meshing with respect to extremely coarse meshing. The whole geometry is discretized into 7698 DEs and 388 BEs. Fig. 11.21 is extremely fine meshing of rectangular channel having hexagon as an obstacle. In this level, the geometry is discretized at best and contains 132430 domain elements and 2108 boundary elements. Rest of meshing statistics for other levels is summarized in Table 11.7. For fixing Reynolds number $Re = 20$, the simulation is performed for the constant velocity profile initiated at inlet of channel. The velocity and pressure snapshots are provided in Fig. 11.22 and Fig. 11.23 respectively. From, Fig. 11.22 it is noticed that the stagnation point appears at left face of hexagon obstacle and here the pressure seems maximum. Further, from Fig. 11.23, it is noticed that the pressure is maximum at corner points of channel (0, 0) and (0, 0.41) while the pressure varies linearly towards down the stream in channel. Fig. 11.24 and Fig. 11.25 are plotted for the case of parabolic velocity profile being initiated at an inlet of channel along with hexagon obstacle. Particularly, Fig. 11.24 is velocity snapshot at Reynolds number $Re = 20$ and Fig. 11.25 shows the pressure distribution. From Fig. 11.24 one can see that the significant disturbance in fluid due to hexagon obstacle travels up-to $x = 0.9$. Later, the fluid bifurcation disappears and fluid

moves uniformly towards outlet. From, Fig. 11.25 one can noticed that the pressure singularities are eliminated due to considering of parabolic velocity profile. The pressure is maximum at left face of the hexagon obstacle and varies linearly towards the outlet of channel. The line graph study is performed for both the constant and parabolic velocities and offered in Fig. 11.26 and Fig. 11.27. Particularly, Fig. 11.26 reports the u -velocity line graph examination when fluid enters in a rectangular channel with constant velocity. The line graph of constant velocity assumption can be seen at $x = 0.0$. The deformation of fluid about hexagon is observed at position $x = 0.1$. The fluid distribution is symmetric at position $x = 0.2$. At this position the fluid moves with higher velocity and hence the momentum increases due to collision of fluid with hexagon obstacle. The velocity curve at $x = 1.0$ reflects that as yet the fluid cannot reshape the initial velocity being initiated at inlet. Fig. 11.27 reports the line graph view of u -velocity for the case of parabolic velocity profile. The variation in u -velocity is reported for the positions $x = 0.0, 0.1, 0.2$ and 2.0 . The line graph view of the parabolic velocity profile can be seen at $x = 0.0$ while the bifurcation can be observed at $x = 0.1$. The symmetric distribution in a channel can be noticed at $x = 0.2$. The hexagon obstacle disturbance reduces and fluid reshaped its initial assumption of parabolic velocity profile at position $x = 2.0$. The line integration is performed at outer surface of hexagon and both the lift and drag coefficients are evaluated. Table 11.8 provides the statistical data of drag and lift coefficients at nine refinement levels for the constant velocity assumption. The most purified value is recorded at extremely fine level that is level -9. The drag coefficient is noticed 4.5619 and lift coefficient is 0.039569. Table 9 reports the drag and lift coefficient values at nine different refinement levels for the parabolic velocity assumption. It is noticed that at level-9, the drag coefficient value is 5.3844 and the lift coefficient value is 0.0093881.

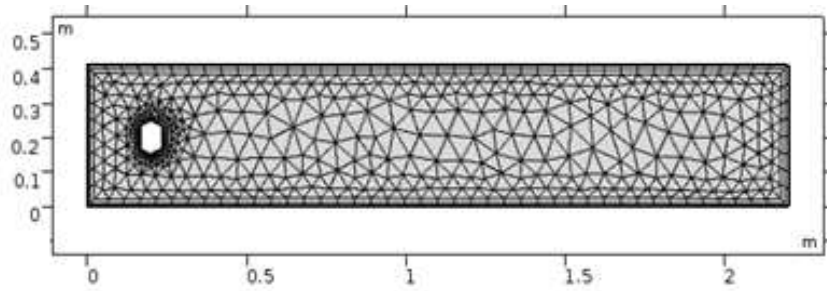


Fig. 11.19. Extremely coarse meshing when hexagon is taken as an obstacle.

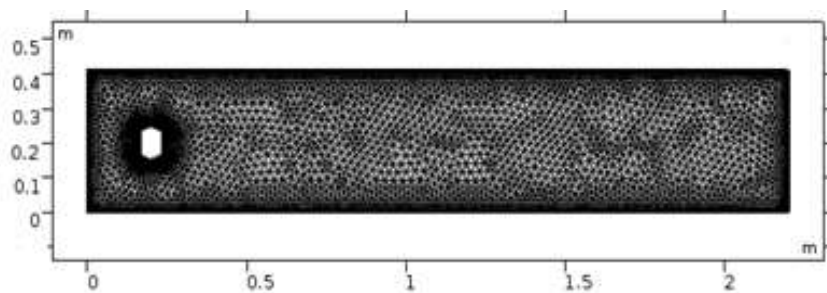


Fig. 11.20. Normal meshing when hexagon is taken as an obstacle.

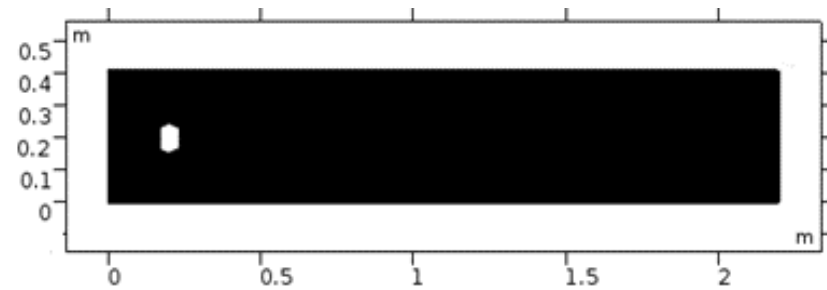


Fig. 11.21. Extremely fine meshing when hexagon is taken as an obstacle.

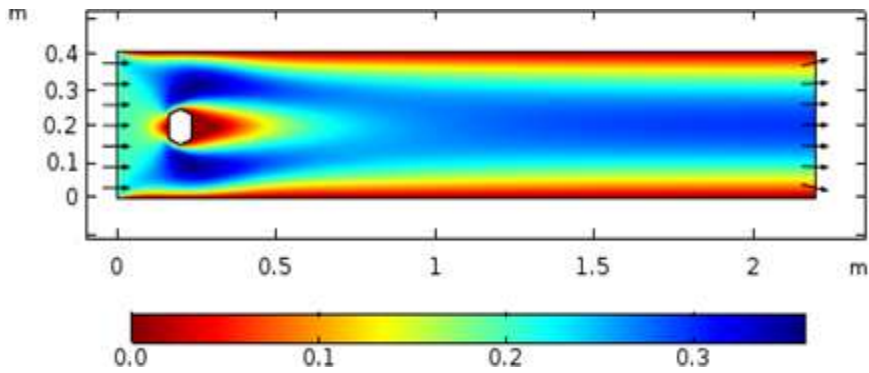


Fig. 11.22. Velocity plot for hexagon obstacle when $D_m = 0.1, U_c = 0.2$ and $Re = 20$.

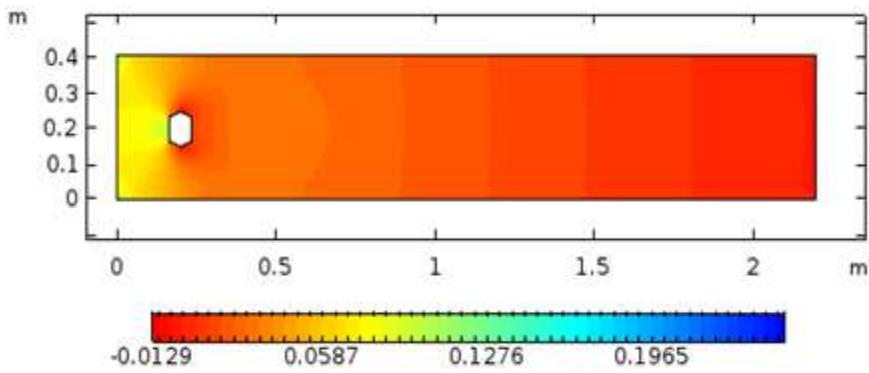


Fig. 11.23. Pressure plot for hexagon obstacle when $D_m = 0.1, U_c = 0.2$ and $Re = 20$.

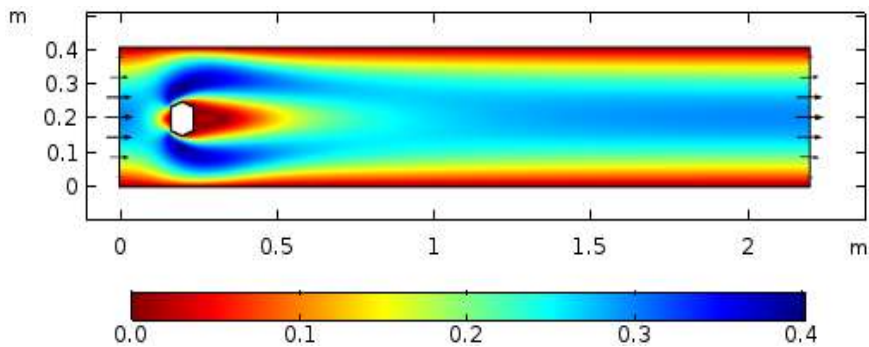


Fig. 11.24. Velocity plot for hexagon obstacle when $D_m = 0.1, U_{Max} = 0.3$ and $Re = 20$.

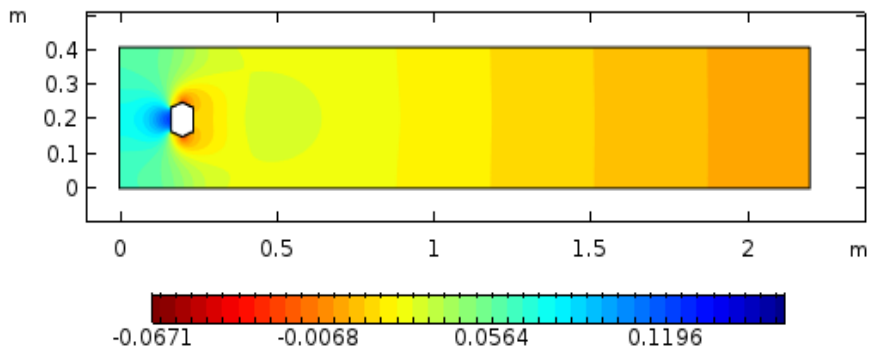


Fig. 11.25. Pressure plot for hexagon obstacle when $D_m = 0.1, U_{Max} = 0.3$ and $Re = 20$.

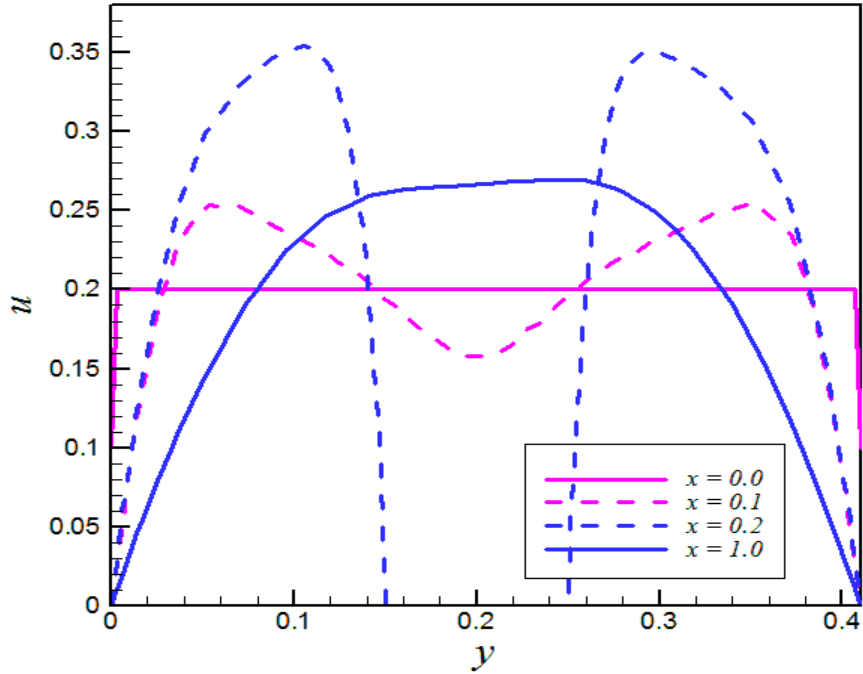


Fig. 11.26. Velocity line graphs at various position of channel having hexagon obstacle with $D_m = 0.1$, $U_c = 0.2$ and $Re = 20$.

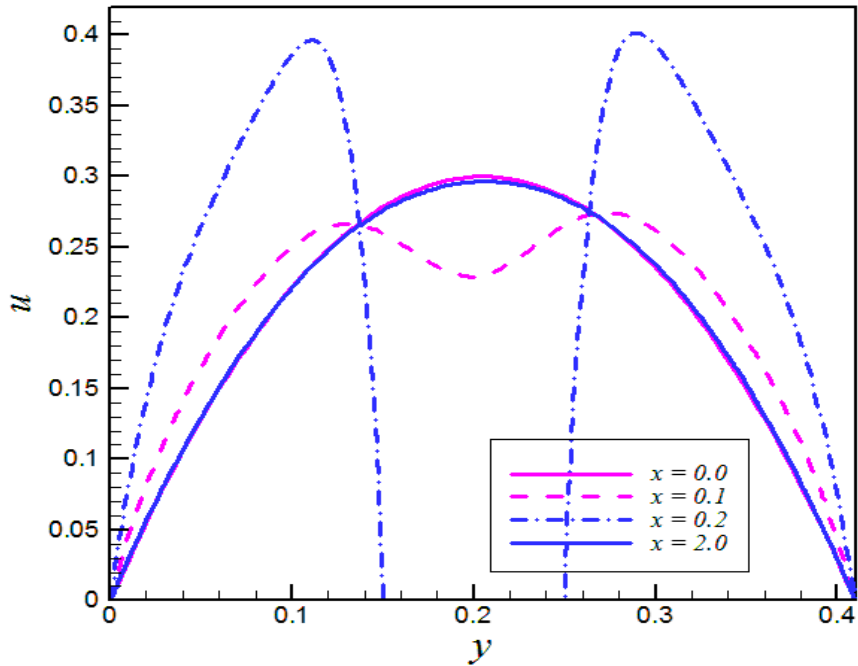


Fig. 11.27. Velocity line graphs at various position of channel having hexagon obstacle with $D_m = 0.1$, $U_{Max} = 0.3$ and $Re = 20$.

11.5.4 OBSTACLE-IV

The octagon obstacle is placed fixed in between channel with vertices (0.2, 0.25), (0.165, 0.235), (0.15, 0.2), (0.165, 0.165), (0.2, 0.15), (0.235, 0.165), (0.25, 0.2), and (0.235, 0.235). The viscous fluid is taken with constant and parabolic velocity profiles at an inlet and the complete mathematical notation for the present case can be written as:

$$\begin{array}{ll}
 \text{Inlet boundary} & u = U_c = 0.2 \text{ or } 4.U_{Max}.y(H - y), v = 0, \\
 \text{Outlet boundary} & \frac{\partial u}{\partial x} = \frac{\partial v}{\partial x} = 0, \\
 \text{Channel side walls} & u = 0, v = 0, \\
 \text{Octagon outer surface} & u = 0, v = 0.
 \end{array} \tag{11.16}$$

To examine the fluid flow towards channel having octagon shaped cylinder as an obstacle, solved the differential system Eqs. (11.6)-(11.8) along with Eq. (11.16) is solved by using finite element method. The solution in this direction is offered by means of Figs. 11.28-11.36 and Tables 11.10-11.12. The pre-processing stage involved in finite element is discretization. Therefore, the computational domain for the present case is discretized up-to nine refinement levels. Table 11.10 provides the complete statistics in this regard. The first level named extremely coarse level divides computational into 878 domain elements and 108 boundary elements. The geometric illustration for extremely coarse meshing is given in Fig. 11.28. The meshing is improved up-to 6738 domain elements and 388 boundary elements. Such level is termed as normal meshing and the geometric illustration in this direction is offered as Fig. 11.29. For better solution of fluid flow around octagon obstacle, the improved meshing is performed which includes the 125748 domain elements and 2010 boundary elements. This level is termed as extremely fine meshing. The Fig. 11.30 is provided in this regard. The meshing statistics for all levels is summarized in Table 11.10. The results presented in Fig. 11.31 and Fig. 11.32 are for the case of constant velocity profile. Particularly, Fig. 11.31 reports the velocity distribution for fluid flow around octagon shaped obstacle. The corresponding pressure distribution is given in Fig. 11.32. From both figures one can conclude that the stagnation point appears on left face of octagon where the pressure seems high. For octagon shaped obstacle the pressure singularities appears at corners of channel namely, (0, 0) and (0, 0.41) when the constant velocity profile is assumed. Fig. 11.33 and Fig. 11.34 depicts the velocity and pressure distribution respectively, when the fluid is initiated with parabolic velocity profile at an

inlet. The pressure singularities disappears due to choice of parabolic velocity profile. For better insight the velocity line graphs are plotted for both the constant and parabolic velocity profiles. To be more specific, Fig. 35 is the line graph study of u -velocity at various position of channel namely, $x = 0, 0.1, 0.2$ and 2 . It can be observed that the at an inlet $x = 0.0$ one has constant velocity profile while at $x = 0.1$ the fluid bifurcation occurs due to octagon obstacle being place towards ongoing viscous fluid. The u -velocity line graph $x = 2$ indicates that the fluid cannot reshaped the constant velocity profile at an outlet. The line graph study of u -velocity for the parabolic velocity assumption is performed at different position of channel namely, $x = 0.0, 0.1, 0.3$ and 2 . The Fig. 11.36 is evident in this direction. The parabolic velocity profile can be see at $x = 0.0$. The significant bifurcation occurs at $x = 0.1$ while the symmetric distribution in both upper and lower part of channel about octagon shaped obstacle can be seen at $x = 0.3$. The line graph at $x = 2.0$ reflects that fluid retrace the parabolic velocity profile at an outlet of channel. The fluid flow around octagon obstacle produces drag and lift forces on an obstacle. To evaluate the strength of these forces, the line integration around the outer surface of an octagon is performed and the observation in this direction is provided by way of Table 11.11 and Table 11.12. Particularly, Table 11.11 offers both the drag and lift coefficient values at nine various refinement levels for the case of constant velocity profile. The most accurate value of drag and lift coefficient is 4.5372 and 0.042178 respectively. Table 11.12 reports the value of drag and lift coefficient for the case parabolic velocity profile at nine different meshing levels. The level nine is extreme fine meshing and therefore the purified value of drag coefficient is 5.3294 and lift coefficient is 0.0058913.

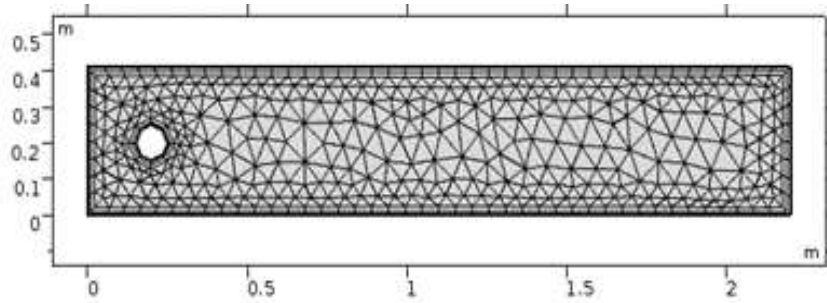


Fig. 11.28. Extremely coarse meshing when octagon is taken as an obstacle.

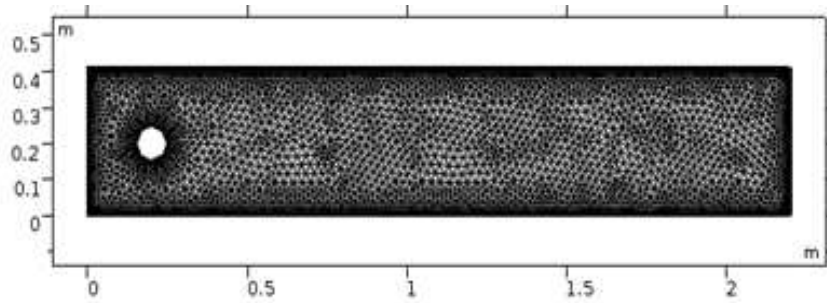


Fig. 11.29. Normal meshing when octagon is taken as an obstacle.

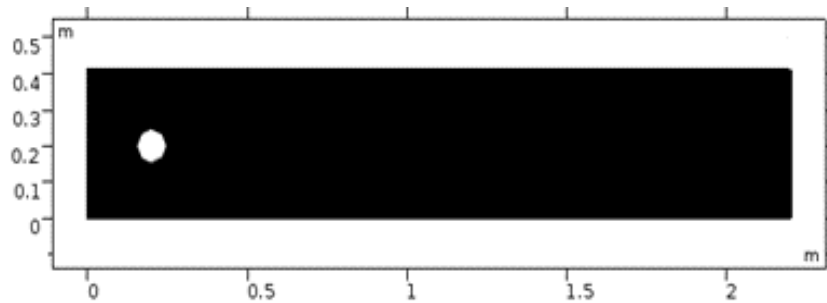


Fig. 11.30. Extremely fine meshing when octagon is taken as an obstacle.

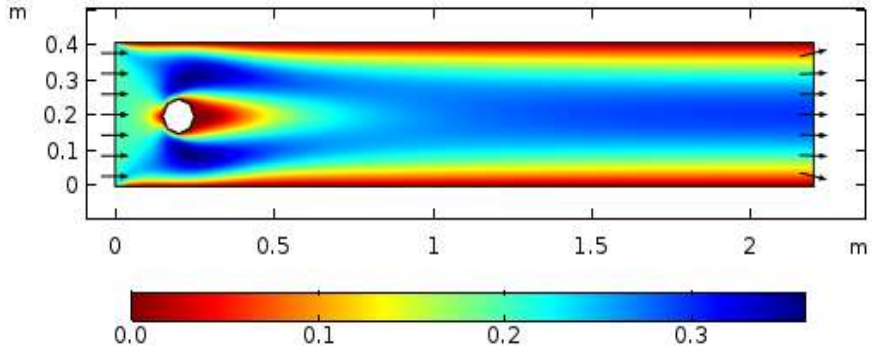


Fig. 11.31. Velocity plot for octagon obstacle when $D_m = 0.1, U_c = 0.2$ and $Re = 20$.

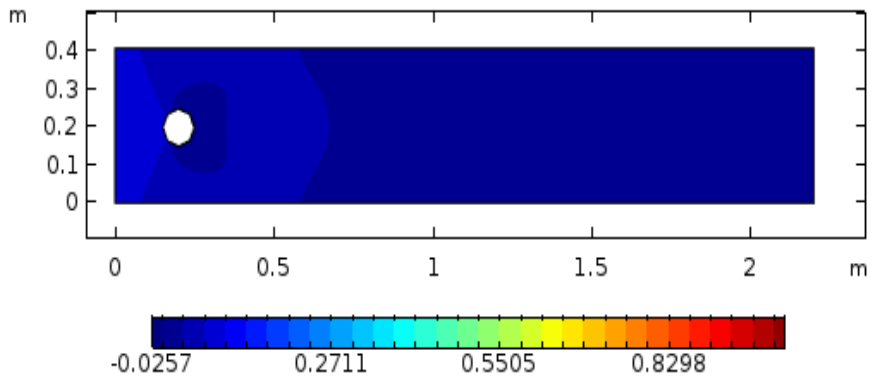


Fig. 11.32. Pressure plot for octagon obstacle when $D_m = 0.1, U_c = 0.2$ and $Re = 20$.

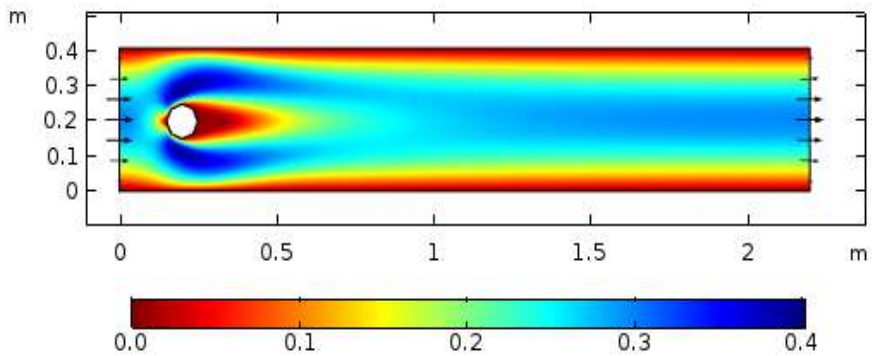


Fig. 11.33. Velocity plot for octagon obstacle when $D_m = 0.1, U_{Max} = 0.3$ and $Re = 20$.

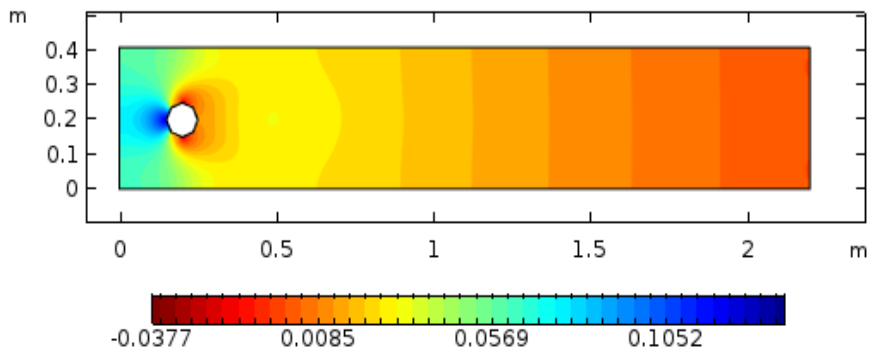


Fig. 11.34. Pressure plot for octagon obstacle when $D_m = 0.1, U_{Max} = 0.3$ and $Re = 20$.

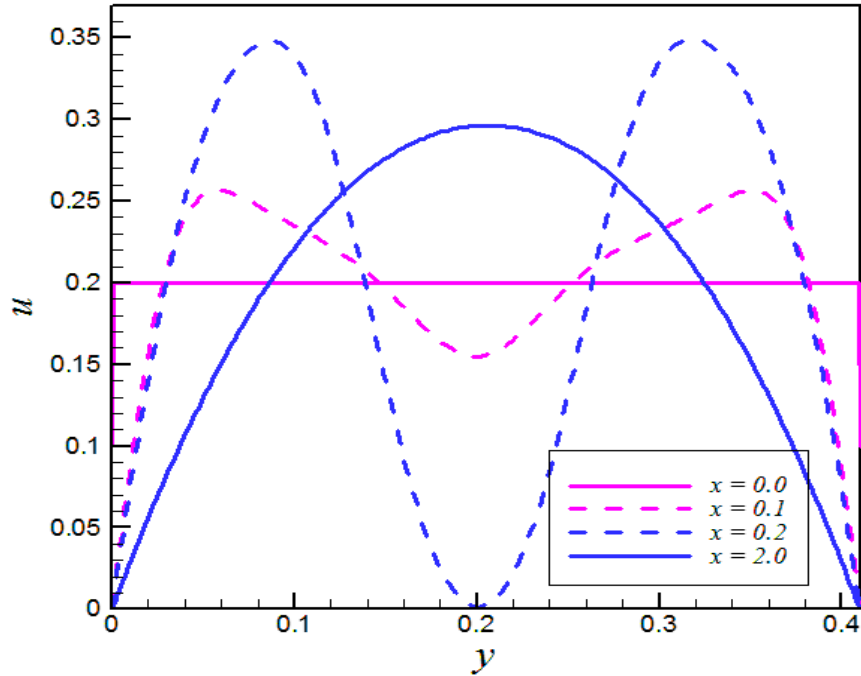


Fig. 11.35. Velocity line graphs at various position of channel having octagon obstacle with $D_m = 0.1$, $U_c = 0.2$ and $Re = 20$.

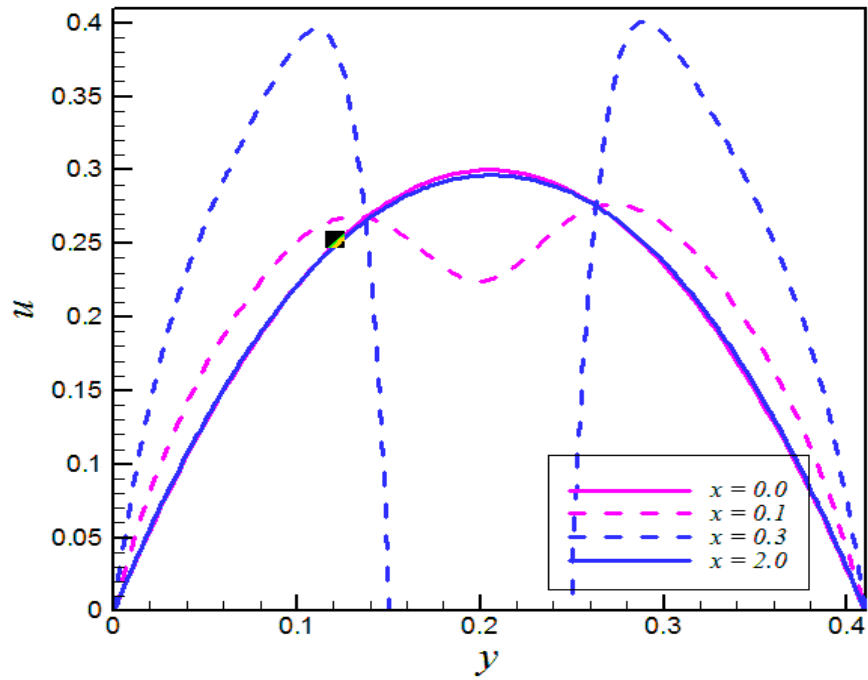


Fig. 11.36. Velocity line graphs at various position of channel having octagon obstacle with $D_m = 0.1$, $U_{Max} = 0.3$ and $Re = 20$.

11.5.5 OBSTACLE-V

The circular shaped cylinder is placed fixed in between channel as an obstacle towards ongoing Newtonian fluid. The channel is carried with length 2.2m and height 0.41m. The circle is taken with radius 0.05m along with the center (0.2, 0.2)m. The assumption remains same that is the both upper and lower walls are at no-slip condition. The fluid flow is taken with both constant and parabolic velocity profiles at an inlet of channel while the outlet of channel is specified with Neumann condition. For solution the nine different meshing schemes are carried and the statistics in this regard is offered in Table 11.13. In detail, the channel is discretized with 882 DEs and 108 BEs. Such level is called extremely coarse meshing. The second level is known by an extra coarse meshing and this level admits 1512 DEs and 160 BEs. The third level is known as coarser meshing and it consists of 2422 DEs and 206 BEs. The coarse meshing is called the level fourth and it consists of 4522 DEs and 306 BEs. The level five is known by normal meshing and in this level the channel is uniformly meshed with 6722 DEs and 388 BEs. The level six is termed as fine meshing and in such case the rectangular channel is discretized into 12162 DEs and 484 BEs. The level seven named as finer meshing. The channel at this stage is managed with 28244 DEs and 1040 BEs. The extra fine level is eight one and it consists of 69592 DEs and 2014 BEs. The level nine is called as extremely fine meshing. It consists of 125658 DEs and 2014 BEs. The whole discretization is also summarized in Table 11.13. The velocity snap shot for linear velocity profile case is given in Fig. 11.37 and the corresponding pressure distribution is reported in Fig. 11.38. The velocity distribution for parabolic case is shared with the help of Fig. 11.39 and the corresponding pressure distribution is given as Fig. 11.40. To examine the drag and lift forces experienced by circular shaped obstacle we have performed line integration around circumference of circle. Table 11.14 offers the drag and lift coefficient data for the case of constant velocity profile. Such values are collected at nine various meshed levels. The most accurate outcomes are noticed at extremely fine meshing level. The drag coefficient at this level is recorded 4.7944 and the lift coefficient is noticed 0.045508. Table 11.15 contains values of drag and lift coefficient for the case of parabolic velocity profile. The statistics is provided up-to nine different mesh levels. The level-9 simulation includes the drag coefficient 5.5811 and lift coefficient 0.010207.

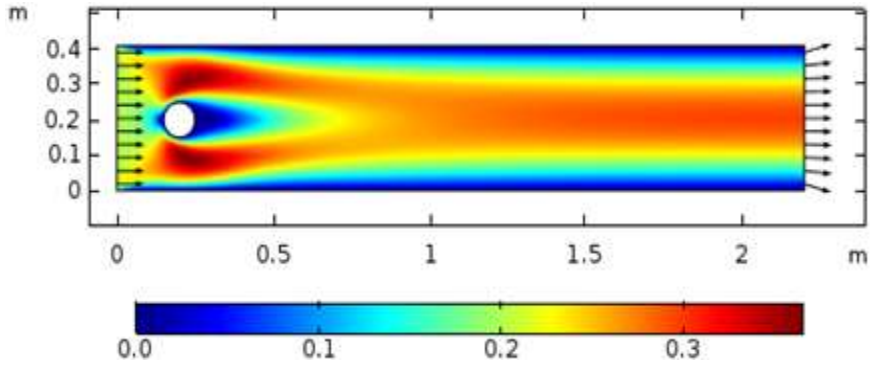


Fig. 11.37. Velocity plot for circular obstacle when $U_c = 0.2$ and $Re = 20$.

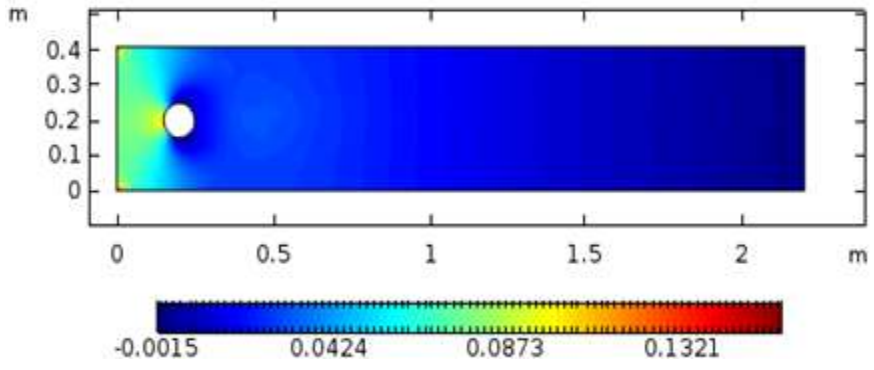


Fig. 11.38. Pressure plot for circular obstacle when $U_c = 0.2$ and $Re = 20$.

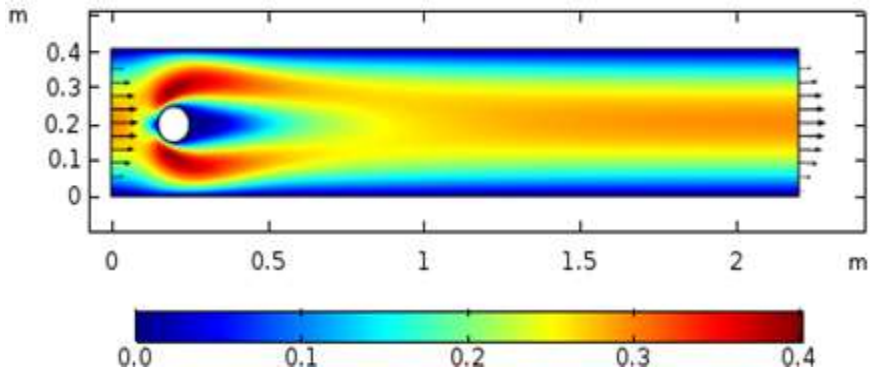


Fig. 11.39. Velocity plot for circular obstacle when $U_{Max} = 0.3$ and $Re = 20$.

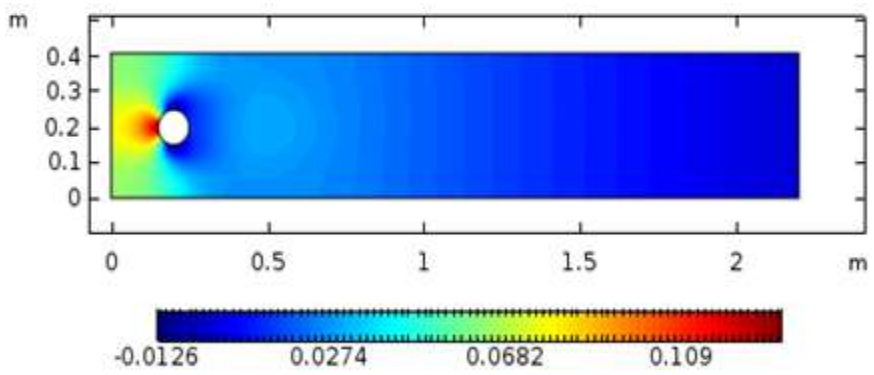


Fig. 11.40. Pressure plot for circular obstacle when $U_{Max} = 0.3$ and $Re = 20$.

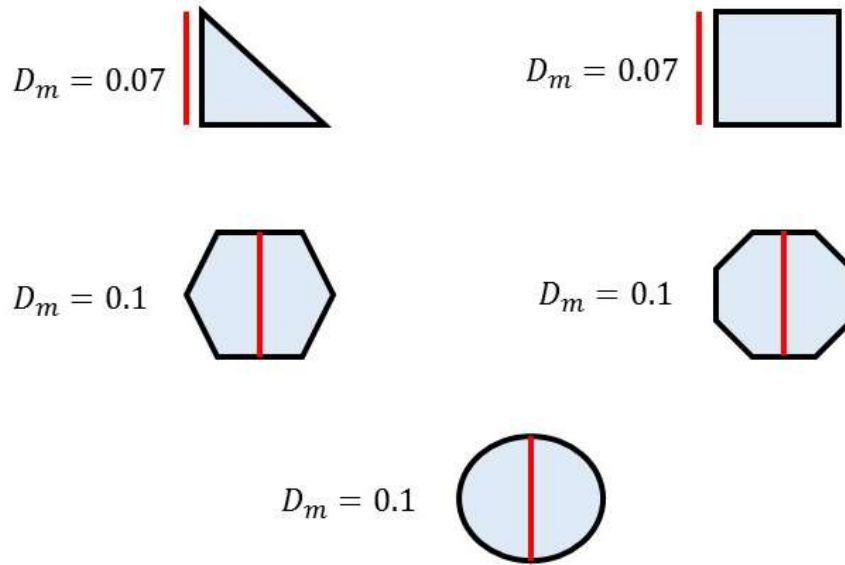


Fig. 11.41. Geometric illustration of obstacles.

11.6 Results benchmarking

The benchmark problem subject to flow around obstacle in rectangular channel was given by Schäfer et al. [140]. In this problem they considered the height of channel 0.41m and 2.2m. The simulation for circular obstacle being placed fixed in between channel at centre (0.2, 0.2)m was performed by fixing the value of Reynolds number $Re = 20$. They offered the value of drag coefficient $D_f = 5.579535$ and lift coefficient $L_f = 0.010618$ as a reliable values when the fluid is initiated with the parabolic velocity profile at an inlet of channel. Here, we commercially optimized the values of drag and lift coefficients by considering the various shapes of obstacles namely, triangle, square, hexagon, octagon and circle. Further, we consider both the constant and parabolic velocity profiles case-wise at an inlet of channel. Owing the parabolic velocity profile, it is noticed that the drag coefficient for triangle obstacle is $D_f = 6.0074$ and lift coefficient is $L_f = -0.69112$. For the square obstacle case the drag coefficient is $D_f = 3.7945$ and lift coefficient is $L_f = 0.0086561$. When hexagon is taken as an obstacle, the values of drag and lift coefficients are noticed $D_f = 5.3844$ and $L_f = 0.0093881$ respectively. Further, when we take octagon shaped obstacle the observed drag coefficient is noticed $D_f = 5.3294$ and

lift coefficient is $L_f = 0.0058913$. Since, we have used finite element method commercially, therefore to validate our drag and lift coefficient values for triangle, square, hexagon and octagon as an obstacles towards ongoing fluid in between rectangular channel having height 0.41m and length 2.2m, we have considered circular shaped obstacle with same constraints being used in Ref. [140]. We have noticed that for circular shaped obstacle the value of drag coefficient is $D_f = 5.5811$ and lift coefficient is $L_f = 0.010207$. These values are in a close agreement with the values proposed by Schäfer et al. [140] that is $D_f = 5.579535$ and $L_f = 0.010618$. It is important to note that in present analysis to retain $Re = 20$ the perpendicular side of triangle and side length of square are taken as characteristic length with numeric value $D_m = 0.07$ while for hexagon, octagon and circle it is taken $D_m = 0.1$. The characteristic length description for each obstacle is also given in Fig. 11.41.

Table. 11.1. Statistics for DEs and BEs when triangle is taken obstacle.

| Mesh level | Domain elements | Boundary elements |
|------------|-----------------|-------------------|
| 1 | 1005 | 113 |
| 2 | 1689 | 167 |
| 3 | 2629 | 213 |
| 4 | 4853 | 315 |
| 5 | 7544 | 406 |
| 6 | 13548 | 508 |
| 7 | 31197 | 1073 |
| 8 | 74240 | 2062 |
| 9 | 132202 | 2062 |

Table. 11.2. Statistics for both drag and lift coefficients when triangle is taken obstacle with $D_m = 0.07$, $U_c = \frac{2}{7}$ and $Re = 20$ (constant velocity profile case).

| Mesh level | Drag coefficient (D_f) | Lift coefficient (L_f) |
|------------|----------------------------|----------------------------|
| 1 | 3.1750 | 0.26966 |
| 2 | 3.1096 | 0.27194 |
| 3 | 3.0436 | 0.23533 |
| 4 | 2.9753 | 0.23676 |
| 5 | 2.9572 | 0.23338 |
| 6 | 2.9449 | 0.22834 |
| 7 | 2.9319 | 0.23194 |
| 8 | 2.9269 | 0.23313 |
| 9 | 2.9253 | 0.23208 |

Table. 11.3. Statistics for both drag and lift coefficients when triangle is taken obstacle with $D_m = 0.07$, $U_{Max} = \frac{3}{7}$ and $Re = 20$ (parabolic velocity profile case).

| Mesh level | Drag coefficient (D_f) | Lift coefficient (L_f) |
|------------|----------------------------|----------------------------|
| 1 | 6.3821 | -0.29744 |
| 2 | 6.2656 | -0.38954 |
| 3 | 6.1337 | -0.66866 |
| 4 | 6.0820 | -0.67412 |
| 5 | 6.0535 | -0.69019 |
| 6 | 6.0361 | -0.68980 |
| 7 | 6.0152 | -0.69074 |
| 8 | 6.0080 | -0.68856 |
| 9 | 6.0074 | -0.69112 |

Table. 11.4. Statistics for DEs and BEs when square is taken obstacle.

| Mesh level | Domain elements | Boundary elements |
|------------|-----------------|-------------------|
| 1 | 1020 | 116 |
| 2 | 1716 | 172 |
| 3 | 2696 | 218 |
| 4 | 4938 | 322 |
| 5 | 7702 | 416 |
| 6 | 13696 | 520 |
| 7 | 31816 | 1096 |
| 8 | 75368 | 2102 |
| 9 | 132928 | 2102 |

Table. 11.5. Statistics for both drag and lift coefficients when square is taken obstacle with

$$D_m = 0.07, U_c = \frac{2}{7} \text{ and } Re = 20 \text{ (constant velocity profile).}$$

| Mesh level | Drag coefficient (D_f) | Lift coefficient (L_f) |
|------------|----------------------------|----------------------------|
| 1 | 3.3490 | 0.12121 |
| 2 | 3.2529 | 0.041828 |
| 3 | 3.1646 | 0.040822 |
| 4 | 3.1145 | 0.025501 |
| 5 | 3.0958 | 0.030957 |
| 6 | 3.0857 | 0.033826 |
| 7 | 3.0743 | 0.033211 |
| 8 | 3.0699 | 0.034143 |
| 9 | 3.0686 | 0.034400 |

Table. 11.6. Statistics for both drag and lift coefficients when square is taken obstacle with

$$D_m = 0.07, U_{Max} = \frac{3}{7} \text{ and } Re = 20 \text{ (parabolic velocity profile).}$$

| Mesh level | Drag coefficient (D_f) | Lift coefficient (L_f) |
|------------|----------------------------|----------------------------|
| 1 | 4.0847 | 0.12126 |
| 2 | 3.9819 | 0.031317 |
| 3 | 3.8822 | 0.012820 |
| 4 | 3.8374 | -0.0085030 |
| 5 | 3.8226 | 0.0044956 |
| 6 | 3.8127 | 0.0063199 |
| 7 | 3.7989 | 0.0060534 |
| 8 | 3.7950 | 0.0081053 |
| 9 | 3.7945 | 0.0086561 |

Table. 11.7. Statistics for DEs and BEs when hexagon is taken obstacle.

| Mesh level | Domain elements | Boundary elements |
|------------|-----------------|-------------------|
| 1 | 1010 | 108 |
| 2 | 1726 | 160 |
| 3 | 2686 | 206 |
| 4 | 4956 | 306 |
| 5 | 7698 | 388 |
| 6 | 13708 | 484 |
| 7 | 31496 | 1040 |
| 8 | 75402 | 2108 |
| 9 | 132430 | 2108 |

Table. 11.8. Statistics for both drag and lift coefficients when hexagon is taken obstacle with $D_m = 0.1$, $U_c = 0.2$ and $Re = 20$ (constant velocity profile case).

| Mesh level | Drag coefficient (D_f) | Lift coefficient (L_f) |
|------------|----------------------------|----------------------------|
| 1 | 4.7449 | 0.017025 |
| 2 | 4.7008 | -0.0014085 |
| 3 | 4.6374 | 0.024829 |
| 4 | 4.5978 | 0.016693 |
| 5 | 4.5882 | 0.034250 |
| 6 | 4.5791 | 0.037992 |
| 7 | 4.5696 | 0.038859 |
| 8 | 4.5639 | 0.039698 |
| 9 | 4.5619 | 0.039569 |

Table. 11.9. Statistics for both drag and lift coefficients when hexagon is taken obstacle with $D_m = 0.1$, $U_{Max} = 0.3$ and $Re = 20$ (parabolic velocity profile case).

| Mesh level | Drag coefficient (D_f) | Lift coefficient (L_f) |
|------------|----------------------------|----------------------------|
| 1 | 5.4908 | -0.033100 |
| 2 | 5.4549 | -0.052569 |
| 3 | 5.3968 | -0.013332 |
| 4 | 5.4002 | -0.023184 |
| 5 | 5.4021 | -0.0020708 |
| 6 | 5.3983 | -0.0073047 |
| 7 | 5.3902 | 0.0080837 |
| 8 | 5.3851 | 0.0094143 |
| 9 | 5.3844 | 0.0093881 |

Table. 11.10. Statistics for DEs and BEs when octagon is taken obstacle.

| Mesh level | Domain elements | Boundary elements |
|------------|-----------------|-------------------|
| 1 | 878 | 108 |
| 2 | 1442 | 156 |
| 3 | 2296 | 206 |
| 4 | 4296 | 298 |
| 5 | 6738 | 388 |
| 6 | 12184 | 488 |
| 7 | 28522 | 1036 |
| 8 | 69382 | 2010 |
| 9 | 125748 | 2010 |

Table. 11.11. Statistics for both drag and lift coefficients when octagon is taken obstacle and $D_m = 0.1, U_c = 0.2$ and $Re = 20$ (constant velocity profile case).

| Mesh level | Drag coefficient (D_f) | Lift coefficient (L_f) |
|------------|----------------------------|----------------------------|
| 1 | 5.1739 | -0.069273 |
| 2 | 5.1376 | 0.026477 |
| 3 | 4.6817 | -0.032702 |
| 4 | 4.6266 | 0.018584 |
| 5 | 4.5851 | 0.0088819 |
| 6 | 4.5683 | 0.030466 |
| 7 | 4.5511 | 0.037610 |
| 8 | 4.5394 | 0.042764 |
| 9 | 4.5372 | 0.042178 |

Table. 11.12. Statistics for both drag and lift coefficients when octagon is taken obstacle and $D_m = 0.1, U_{Max} = 0.3$ and $Re = 20$ (parabolic velocity profile case).

| Mesh level | Drag coefficient (D_f) | Lift coefficient (L_f) |
|------------|----------------------------|----------------------------|
| 1 | 5.8833 | -0.097363 |
| 2 | 5.9483 | 0.024889 |
| 3 | 5.4218 | -0.086903 |
| 4 | 5.4066 | -0.023445 |
| 5 | 5.3690 | -0.040017 |
| 6 | 5.3618 | -0.0084999 |
| 7 | 5.3434 | -5.8831E-4 |
| 8 | 5.3299 | 0.0067864 |
| 9 | 5.3294 | 0.0058913 |

Table. 11.13. Statistics for DEs and BEs when circle is taken obstacle.

| Mesh level | Domain elements | Boundary elements |
|------------|-----------------|-------------------|
| 1 | 882 | 108 |
| 2 | 1512 | 160 |
| 3 | 2422 | 206 |
| 4 | 4522 | 306 |
| 5 | 6722 | 388 |
| 6 | 12162 | 484 |
| 7 | 28244 | 1040 |
| 8 | 69592 | 2014 |
| 9 | 125658 | 2014 |

Table. 11.14. Statistics for both drag and lift coefficients when circle is taken obstacle and $U_c = 0.2$ and $Re = 20$ (constant velocity profile case).

| Mesh level | Drag coefficient (D_f) | Lift coefficient (L_f) |
|------------|----------------------------|----------------------------|
| 1 | 5.1671 | -0.055807 |
| 2 | 4.8794 | -0.038878 |
| 3 | 4.8317 | -0.057457 |
| 4 | 4.8197 | -0.036253 |
| 5 | 4.8014 | 0.0086052 |
| 6 | 4.8040 | 0.012904 |
| 7 | 4.8005 | 0.046219 |
| 8 | 4.7965 | 0.045115 |
| 9 | 4.7944 | 0.045508 |

Table. 11.15. Statistics for both drag and lift coefficients when circle is taken obstacle and $U_{Max} = 0.3$ and $Re = 20$ (parabolic velocity profile case).

| Mesh level | Drag coefficient (D_f) | Lift coefficient (L_f) |
|------------|----------------------------|----------------------------|
| 1 | 6.0207 | -0.099437 |
| 2 | 5.6119 | -0.102890 |
| 3 | 5.5788 | -0.133150 |
| 4 | 5.5796 | -0.091933 |
| 5 | 5.5892 | 0.050458 |
| 6 | 5.5930 | 0.038479 |
| 7 | 5.5863 | 0.010429 |
| 8 | 5.5812 | 0.010423 |
| 9 | 5.5811 | 0.010207 |

11.7 Conclusion

The rectangular domain with the constraints $\Omega = [0, 2.2] \times [0, 0.41]$ m is considered as a computational domain. The fluid holding Newton's law of viscosity is taken in a channel. Both the upper and lower walls of the channel are at rest and the relative velocity of fluid particles and both walls is zero. The right wall of the channel is specified with Neumann condition. Five different shapes of cylinders are taken as an obstacle in between channel towards incoming fluid flow from an inlet. The obstacle shapes includes triangle, square, hexagon, octagon and circle. The analysis is performed for both the constant and parabolic velocity profiles with which the fluid flow has initiated an inlet of channel. The physical design is controlled mathematically in terms of Navier-Stokes equations. The finite element method is adopted to examine the flow field in the channel along with typical obstacles. Later, the drag and lift forces experienced by each obstacle are evaluated by performing the line integration around the outer surface of obstacles. For the assumption of a constant velocity profile for each obstacle, the pressure singularities are observed at corner points of the channel. Due to these singularities, one cannot recover the constant velocity profile at an outlet of channel. Such singularities can be eliminated by assuming the parabolic velocity profile at an inlet of the channel for each obstacle. Therefore, for the flow in a channel having both upper and lower walls at no-slip condition, the most realistic approach is to assume the parabolic velocity profile an inlet rather than to move-on with a constant velocity profile. Further, the compatibility of choice of velocity is independent of geometric illustration of an obstacle. Furthermore, both the drag and lift coefficients are found object dependent. To the best of our knowledge no reference data for triangle, square, hexagon and octagon shaped obstacles is available in the literature with the present proposed constraints. The optimized path from triangle to circular shaped obstacle could serve as reference values for the upcoming studies.

Thesis General Concluding Remarks

The prime findings of present thesis is itemized as follows:

- The fluid velocities subject to tangent hyperbolic, Eyring-Powell, Casson and Williamson models are found increasing function of curvature parameter.
- The fluid temperature subject to tangent hyperbolic, Eyring-Powell, Casson and Williamson models reflects decline values towards thermal stratification parameter.
- The fluid concentration subject to tangent hyperbolic, Eyring-Powell, Casson and Williamson models shows an inverse variation towards solutal stratification parameter.
- The surface quantities which includes Nusselt number and Skin friction coefficient are enriched for cylindrical surface as compared to flat surface.
- For flow in a channel the most realistic approach is to assume the parabolic velocity profile at an inlet rather than to move-on with a constant velocity profile.
- The compatibility of choice of velocity profile is independent of geometric illustration of installed obstacle towards ongoing fluid stream.
- Both drag and lift forces experienced by installed obstacles are increasing function of Power law index.

Bibliography

1. De Waele, A. "Viscometry and plastometry, Oil and Color Chem." *Assoc. J* 6, no. 33 (1923): e88.
2. Ostwald, Wolfgang. "On the Speed Function of Viscosity-Dispersed Systems." *Colloid & Polymer Science* 36, no. 2 (1925): 99-117.
3. Carreau, Pierre J. "Rheological equations from molecular network theories." *Transactions of the Society of Rheology* 16, no. 1 (1972): 99-127.
4. Yasuda, Kenji. "Investigation of the analogies between viscometric and linear viscoelastic properties of polystyrene fluids." PhD diss., Massachusetts Institute of Technology, 1979.
5. Cross, Malcolm M. "Rheology of non-Newtonian fluids: a new flow equation for pseudoplastic systems." *Journal of colloid science* 20, no. 5 (1965): 417-437.
6. Sisko, A. W. "The flow of lubricating greases." *Industrial & Engineering Chemistry* 50, no. 12 (1958): 1789-1792.
7. Eyring, Henry. "Viscosity, plasticity, and diffusion as examples of absolute reaction rates." *The Journal of chemical physics* 4, no. 4 (1936): 283-291.
8. Ree, Francis, Taikyue Ree, and Henry Eyring. "Relaxation theory of transport problems in condensed systems." *Industrial & Engineering Chemistry* 50, no. 7 (1958): 1036-1040.
9. Barus, Carl. "Isothermals, isopiestic and isometrics relative to viscosity." *American journal of science* 266 (1893): 87-96.
10. Matsuhisa, Seikichi, and R. Byron Bird. "Analytical and numerical solutions for laminar flow of the non-Newtonian ellis fluid." *AIChE Journal* 11, no. 4 (1965): 588-595.
11. Seely, Gilbert R. "Non-Newtonian viscosity of polybutadiene solutions." *AIChE Journal* 10, no. 1 (1964): 56-60.
12. Bingham, Eugene Cook. *Fluidity and plasticity*. Vol. 2. McGraw-Hill, 1922.
13. Herschel, Winslow H., and Ronald Bulkley. "Konsistenzmessungen von gummi-benzollösungen." *Colloid & Polymer Science* 39, no. 4 (1926): 291-300.
14. Waqas, Muhammad, Muhammad Farooq, Muhammad Ijaz Khan, Ahmed Alsaedi, Tasawar Hayat, and Tabassum Yasmeen. "Magnetohydrodynamic (MHD) mixed convection flow of micropolar liquid due to nonlinear stretched sheet with convective condition." *International Journal of Heat and Mass Transfer* 102 (2016): 766-772.
15. Cattaneo–Christov heat flux in the flow of variable thermal conductivity Eyring–Powell fluid." *Results in Physics* 7 (2017): 446-450.
16. Tamoor, M., M. Waqas, M. Ijaz Khan, Ahmed Alsaedi, and T. Hayat. "Magnetohydrodynamic flow of Casson fluid over a stretching cylinder." *Results in Physics* 7 (2017): 498-502.

17. Awais, M., M. Y. Malik, S. Bilal, T. Salahuddin, and Arif Hussain. "Magnetohydrodynamic (MHD) flow of Sisko fluid near the axisymmetric stagnation point towards a stretching cylinder." *Results in Physics* 7 (2017): 49-56.
18. Khan, Muhammad Imran, Tasawar Hayat, Muhammad Ijaz Khan, and Ahmed Alsaedi. "A modified homogeneous-heterogeneous reactions for MHD stagnation flow with viscous dissipation and Joule heating." *International Journal of Heat and Mass Transfer* 113 (2017): 310-317.
19. Hayat, Tasawar, Muhammad Ijaz Khan, Muhammad Waqas, and Ahmed Alsaedi. "On Cattaneo–Christov heat flux in the flow of variable thermal conductivity Eyring–Powell fluid." *Results in Physics* 7 (2017): 446-450.
20. Akbar, Noreen Sher, S. Nadeem, R. Ul Haq, and Z. H. Khan. "Numerical solutions of Magnetohydrodynamic boundary layer flow of tangent hyperbolic fluid towards a stretching sheet." *Indian journal of Physics* 87, no. 11 (2013): 1121-1124.
21. Naseer, Muhammad, Muhammad Yousaf Malik, Sohail Nadeem, and Abdul Rehman. "The boundary layer flow of hyperbolic tangent fluid over a vertical exponentially stretching cylinder." *Alexandria engineering journal* 53, no. 3 (2014): 747-750.
22. Hayat, Tasawar, Sajid Qayyum, Ahmed Alsaedi, and Sabir Ali Shehzad. "Nonlinear thermal radiation aspects in stagnation point flow of tangent hyperbolic nanofluid with double diffusive convection." *Journal of Molecular Liquids* 223 (2016): 969-978.
23. Powell, Richard E., and Henry Eyring. "Mechanisms for the relaxation theory of viscosity." *Nature* 154, no. 3909 (1944): 427.
24. Yoon, H. K., and A. J. Ghajar. "A note on the Powell-Eyring fluid model." *International communications in heat and mass transfer* 14, no. 4 (1987): 381-390.
25. Patel, Manisha, and M. G. Timol. "Numerical treatment of Powell–Eyring fluid flow using method of satisfaction of asymptotic boundary conditions (MSABC)." *Applied Numerical Mathematics* 59, no. 10 (2009): 2584-2592.
26. Javed, Tariq, Nasir Ali, Zaheer Abbas, and Muhammad Sajid. "Flow of an Eyring-Powell non-Newtonian fluid over a stretching sheet." *Chemical Engineering Communications* 200, no. 3 (2013): 327-336.
27. Roşca, Alin V., and Ioan Pop. "Flow and heat transfer of Powell–Eyring fluid over a shrinking surface in a parallel free stream." *International Journal of Heat and Mass Transfer* 71 (2014): 321-327.
28. Malik, M. Y., A. Hussain, and S. Nadeem. "Boundary layer flow of an Eyring–Powell model fluid due to a stretching cylinder with variable viscosity." *Scientia Iranica* 20, no. 2 (2013): 313-321.
29. Hayat, T., Numra Gull, M. Farooq, and B. Ahmad. "Thermal radiation effect in MHD flow of Powell—Eyring nanofluid induced by a stretching cylinder." *Journal of Aerospace Engineering* 29, no. 1 (2015): 04015011.

30. Rehman, Khalil Ur, M. Y. Malik, T. Salahuddin, and M. Naseer. "Dual stratified mixed convection flow of Eyring-Powell fluid over an inclined stretching cylinder with heat generation/absorption effect." *AIP Advances* 6, no. 7 (2016): 075112.
31. Rehman, Abdul, Sallauddin Achakzia, Sohail Nadeem, and Saleem Iqbal. "Stagnation point flow of Eyring Powell fluid in a vertical cylinder with heat transfer." *Journal of Power Technologies* 96, no. 1 (2016): 57-62.
32. Rahimi, J., D. D. Ganji, M. Khaki, and Kh Hosseinzadeh. "Solution of the boundary layer flow of an Eyring-Powell non-Newtonian fluid over a linear stretching sheet by collocation method." *Alexandria Engineering Journal* 56, no. 4 (2017): 621-627.
33. Mustafa, M., T. Hayat, I. Pop, and A. Aziz. "Unsteady boundary layer flow of a Casson fluid due to an impulsively started moving flat plate." *Heat Transfer—Asian Research* 40, no. 6 (2011): 563-576.
34. Nadeem, S., Rizwan Ul Haq, and C. Lee. "MHD flow of a Casson fluid over an exponentially shrinking sheet." *Scientia Iranica* 19, no. 6 (2012): 1550-1553.
35. Mustafa, Meraj, Tasawar Hayat, Pop Ioan, and Awatif Hendi. "Stagnation-point flow and heat transfer of a Casson fluid towards a stretching sheet." *Zeitschrift für Naturforschung A* 67, no. 1-2 (2012): 70-76.
36. Mukhopadhyay, Swati, Prativa Ranjan De, Krishnendu Bhattacharyya, and G. C. Layek. "Casson fluid flow over an unsteady stretching surface." *Ain Shams Engineering Journal* 4, no. 4 (2013): 933-938.
37. Mukhopadhyay, Swati. "Casson fluid flow and heat transfer over a nonlinearly stretching surface." *Chinese Physics B* 22, no. 7 (2013): 074701.
38. Mukhopadhyay, Swati, Iswar Chandra Moindal, and Tasawar Hayat. "MHD boundary layer flow of Casson fluid passing through an exponentially stretching permeable surface with thermal radiation." *Chinese Physics B* 23, no. 10 (2014): 104701.
39. Mahanta, G., and S. Shaw. "3D Casson fluid flow past a porous linearly stretching sheet with convective boundary condition." *Alexandria Engineering Journal* 54, no. 3 (2015): 653-659.
40. Mustafa, M., and Junaid Ahmad Khan. "Model for flow of Casson nanofluid past a non-linearly stretching sheet considering magnetic field effects." *AIP Advances* 5, no. 7 (2015): 077148.
41. Das, M., R. Mahato, and R. Nandkeolyar. "Newtonian heating effect on unsteady hydromagnetic Casson fluid flow past a flat plate with heat and mass transfer." *Alexandria Engineering Journal* 54, no. 4 (2015): 871-879.
42. Ramesh, K., and M. Devakar. "Some analytical solutions for flows of Casson fluid with slip boundary conditions." *Ain Shams Engineering Journal* 6, no. 3 (2015): 967-975.
43. Animasaun, I. L., E. A. Adebile, and A. I. Fagbade. "Casson fluid flow with variable thermo-physical property along exponentially stretching sheet with suction and exponentially decaying internal heat generation using the homotopy analysis method." *Journal of the Nigerian Mathematical Society* 35, no. 1 (2016): 1-17.

44. Raju, C. S. K., N. Sandeep, V. Sugunamma, M. Jayachandra Babu, and JV Ramana Reddy. "Heat and mass transfer in magnetohydrodynamic Casson fluid over an exponentially permeable stretching surface." *Engineering Science and Technology, an International Journal* 19, no. 1 (2016): 45-52.
45. Sandeep, Naramgari, Olubode Kolade Koriko, and Isaac Lare Animasaun. "Modified kinematic viscosity model for 3D-Casson fluid flow within boundary layer formed on a surface at absolute zero." *Journal of Molecular Liquids* 221 (2016): 1197-1206.
46. Qing, Jia, Muhammad Bhatti, Munawwar Abbas, Mohammad Rashidi, and Mohamed Ali. "Entropy generation on MHD Casson nanofluid flow over a porous stretching/shrinking surface." *Entropy* 18, no. 4 (2016): 123.
47. Ali, M. E., and N. Sandeep. "Cattaneo-Christov model for radiative heat transfer of magnetohydrodynamic Casson-ferrofluid: a numerical study." *Results in physics* 7 (2017): 21-30.
48. Williamson, R. Vo. "The flow of pseudoplastic materials." *Industrial & Engineering Chemistry* 21, no. 11 (1929): 1108-1111.
49. Lyubimov, D. V., and A. V. Perminov. "Motion of a thin oblique layer of a pseudoplastic fluid." *Journal of Engineering Physics and Thermophysics* 75, no. 4 (2002): 920-924.
50. Dapra, Irene, and Giambattista Scarpi. "Perturbation solution for pulsatile flow of a non-Newtonian Williamson fluid in a rock fracture." *International Journal of Rock Mechanics and Mining Sciences* 44, no. 2 (2007): 271-278.
51. Nadeem, S., and Safia Akram. "Peristaltic flow of a Williamson fluid in an asymmetric channel." *Communications in Nonlinear Science and Numerical Simulation* 15, no. 7 (2010): 1705-1716.
52. Vajravelu, K., S. Sreenadh, K. Rajanikanth, and Changhoon Lee. "Peristaltic transport of a Williamson fluid in asymmetric channels with permeable walls." *Nonlinear Analysis: Real World Applications* 13, no. 6 (2012): 2804-2822.
53. Nadeem, S., S. T. Hussain, and Changhoon Lee. "Flow of a Williamson fluid over a stretching sheet." *Brazilian journal of chemical engineering* 30, no. 3 (2013): 619-625.
54. Nadeem, S., and S. T. Hussain. "Flow and heat transfer analysis of Williamson nanofluid." *Applied Nanoscience* 4, no. 8 (2014): 1005-1012.
55. Akbar, Noreen Sher, S. U. Rahman, R. Ellahi, and S. Nadeem. "Blood flow study of Williamson fluid through stenosed arteries with permeable walls." *The European Physical Journal Plus* 129, no. 11 (2014): 256.
56. Zehra, Iffat, Malik Muhammad Yousaf, and Sohail Nadeem. "Numerical solutions of Williamson fluid with pressure dependent viscosity." *Results in Physics* 5 (2015): 20-25.
57. Hayat, T., Anum Shafiq, and A. Alsaedi. "Hydromagnetic boundary layer flow of Williamson fluid in the presence of thermal radiation and Ohmic dissipation." *Alexandria Engineering Journal* 55, no. 3 (2016): 2229-2240.

58. Malik, M. Y., M. Bibi, Farzana Khan, and T. Salahuddin. "Numerical solution of Williamson fluid flow past a stretching cylinder and heat transfer with variable thermal conductivity and heat generation/absorption." *AIP Advances* 6, no. 3 (2016): 035101.
59. Krishnamurthy, M. R., B. C. Prasannakumara, B. J. Giresha, and Rama Subba Reddy Gorla. "Effect of chemical reaction on MHD boundary layer flow and melting heat transfer of Williamson nanofluid in porous medium." *Engineering Science and Technology, an International Journal* 19, no. 1 (2016): 53-61.
60. Eldabe, N. T., M. A. Elogail, S. M. Elshaboury, and Alfaisal A. Hasan. "Hall effects on the peristaltic transport of Williamson fluid through a porous medium with heat and mass transfer." *Applied Mathematical Modelling* 40, no. 1 (2016): 315-328.
61. Hayat, T., Gulnaz Bashir, M. Waqas, and A. Alsaedi. "MHD 2D flow of Williamson nanofluid over a nonlinear variable thicked surface with melting heat transfer." *Journal of Molecular Liquids* 223 (2016): 836-844.
62. Bhatti, Muhammad Mubashir, and Mohammad Mehdi Rashidi. "Effects of thermo-diffusion and thermal radiation on Williamson nanofluid over a porous shrinking/stretching sheet." *Journal of Molecular Liquids* 221 (2016): 567-573.
63. Ahmad, Kartini, Zahir Hanouf, and Anuar Ishak. "MHD Casson nanofluid flow past a wedge with Newtonian heating." *The European Physical Journal Plus* 132, no. 2 (2017): 87.
64. Kumaran, G., and N. Sandeep. "Thermophoresis and Brownian moment effects on parabolic flow of MHD Casson and Williamson fluids with cross diffusion." *Journal of Molecular Liquids* 233 (2017): 262-269.
65. Ramzan, M., M. Bilal, and Jae Dong Chung. "MHD stagnation point Cattaneo–Christov heat flux in Williamson fluid flow with homogeneous–heterogeneous reactions and convective boundary condition—A numerical approach." *Journal of Molecular Liquids* 225 (2017): 856-862.
66. Liepmann, H. W. "Hydromagnetic Effects in Couette and Stokes Flow." In *Plasma in a Magnetic Field*, p. 117. 1958.
67. Wendl, Michael C. "General solution for the Couette flow profile." *Physical Review E* 60, no. 5 (1999): 6192.
68. Jalaal, M., M. G. Nejad, P. Jalili, Mehdi Esmaeilpour, H. Bararnia, E. Ghasemi, Soheil Soleimani, Davood Domiri Ganji, and S. M. Moghimi. "Homotopy perturbation method for motion of a spherical solid particle in plane couette fluid flow." *Computers & Mathematics with Applications* 61, no. 8 (2011): 2267-2270.
69. Hatami, M., M. Sheikholeslami, and G. Domairry. "High accuracy analysis for motion of a spherical particle in plane Couette fluid flow by multi-step differential transformation method." *Powder Technology* 260 (2014): 59-67.
70. Ellahi, R., E. Shivanian, S. Abbasbandy, and T. Hayat. "Numerical study of magnetohydrodynamics generalized Couette flow of Eyring-Powell fluid with heat

- transfer and slip condition." *International Journal of Numerical Methods for Heat & Fluid Flow* 26, no. 5 (2016): 1433-1445.
71. Danish, Mohammad, Shashi Kumar, and Surendra Kumar. "Exact analytical solutions for the Poiseuille and Couette–Poiseuille flow of third grade fluid between parallel plates." *Communications in Nonlinear Science and Numerical Simulation* 17, no. 3 (2012): 1089-1097.
 72. Mucha, Piotr B., and Tomasz Piasecki. "Compressible perturbation of Poiseuille type flow." *Journal de Mathematiques Pures et Appliquées* 102, no. 2 (2014): 338-363.
 73. Zhang, Yongbin. "Poiseuille flow in a nano channel for different wall surface patterns." *International Journal of Heat and Mass Transfer* 95 (2016): 243-248.
 74. Damianou, Yiolanda, and Georgios C. Georgiou. "On Poiseuille flows of a Bingham plastic with pressure-dependent rheological parameters." *Journal of Non-Newtonian Fluid Mechanics* 250 (2017): 1-7.
 75. Kyritsi-Yiallourou, Sophia, and Georgios C. Georgiou. "Newtonian Poiseuille flow in ducts of annular-sector cross-sections with Navier slip." *European Journal of Mechanics-B/Fluids* 72 (2018): 87-102.
 76. Liu, R., Z. Ding, and K. X. Hu. "Stabilities in plane Poiseuille flow of Herschel–Bulkley fluid." *Journal of Non-Newtonian Fluid Mechanics* 251 (2018): 132-144.
 77. Williamson, Charles HK. "Vortex dynamics in the cylinder wake." *Annual review of fluid mechanics* 28, no. 1 (1996): 477-539.
 78. Rajani, B. N., A. Kandasamy, and Sekhar Majumdar. "Numerical simulation of laminar flow past a circular cylinder." *Applied Mathematical Modelling* 33, no. 3 (2009): 1228-1247.
 79. Kanaris, Nicolas, Dimokratis Grigoriadis, and Stavros Kassinos. "Three dimensional flow around a circular cylinder confined in a plane channel." *Physics of Fluids* 23, no. 6 (2011): 064106.
 80. Hussain, Shafqat, Friedhelm Schieweck, and Stefan Turek. "An efficient and stable finite element solver of higher order in space and time for nonstationary incompressible flow." *International Journal for Numerical Methods in Fluids* 73, no. 11 (2013): 927-952.
 81. Andersson, H. I., K. H. Bech, and B. S. Dandapat. "Magnetohydrodynamic flow of a power-law fluid over a stretching sheet." *International Journal of Non-Linear Mechanics* 27, no. 6 (1992): 929-936.
 82. Hassanien, I. A., A. A. Abdullah, and R. S. R. Gorla. "Flow and heat transfer in a power-law fluid over a nonisothermal stretching sheet." *Mathematical and Computer Modelling* 28, no. 9 (1998): 105-116.
 83. Chen, Chien-Hsin. "Heat transfer in a power-law fluid film over a unsteady stretching sheet." *Heat and Mass Transfer* 39, no. 8-9 (2003): 791-796.
 84. Cortell, Rafael. "A note on magnetohydrodynamic flow of a power-law fluid over a stretching sheet." *Applied Mathematics and Computation* 168, no. 1 (2005): 557-566.

85. Chen, Chien-Hsin. "Effects of magnetic field and suction/injection on convection heat transfer of non-Newtonian power-law fluids past a power-law stretched sheet with surface heat flux." *International Journal of Thermal Sciences* 47, no. 7 (2008): 954-961.
86. Abel, M. Subhas, P. S. Datti, and N. Mahesha. "Flow and heat transfer in a power-law fluid over a stretching sheet with variable thermal conductivity and non-uniform heat source." *International Journal of Heat and Mass Transfer* 52, no. 11-12 (2009): 2902-2913.
87. Nadeem, S., Noreen Sher Akbar, Awatif A. Hendi, and Tasawar Hayat. "Power law fluid model for blood flow through a tapered artery with a stenosis." *Applied Mathematics and Computation* 217, no. 17 (2011): 7108-7116.
88. Postelnicu, A., and Ioan Pop. "Falkner–Skan boundary layer flow of a power-law fluid past a stretching wedge." *Applied Mathematics and Computation* 217, no. 9 (2011): 4359-4368.
89. Yang, K. T., J. L. Novotny, and Y. S. Cheng. "Laminar free convection from a nonisothermal plate immersed in a temperature stratified medium." *International journal of Heat and Mass transfer* 15, no. 5 (1972): 1097-1109.
90. Jaluria, Yogesh, and Benjamin Gebhart. "Stability and transition of buoyancy-induced flows in a stratified medium." *Journal of Fluid Mechanics* 66, no. 3 (1974): 593-612.
91. Chen, C. C., and R. Eichhorn. "Natural convection from a vertical surface to a thermally stratified fluid." *Journal of Heat Transfer* 98, no. 3 (1976): 446-451.
92. Ishak, Anuar, Roslinda Nazar, and Ioan Pop. "Mixed convection boundary layer flow adjacent to a vertical surface embedded in a stable stratified medium." *International Journal of Heat and Mass Transfer* 51, no. 13-14 (2008): 3693-3695.
93. Narayana, PA Lakshmi, P. V. S. N. Murthy, P. V. S. S. R. Krishna, and Adrian Postelnicu. "Free convective heat and mass transfer in a doubly stratified porous medium saturated with a power-law fluid." *International journal of Fluid mechanics Research* 36, no. 6 (2009).
94. Chang, Cheng-Long, and Zong-Yi Lee. "Free convection on a vertical plate with uniform and constant heat flux in a thermally stratified micropolar fluid." *Mechanics Research Communications* 35, no. 6 (2008): 421-427.
95. Cheng, Ching-Yang. "Combined heat and mass transfer in natural convection flow from a vertical wavy surface in a power-law fluid saturated porous medium with thermal and mass stratification." *International Communications in Heat and Mass Transfer* 36, no. 4 (2009): 351-356.
96. Mukhopadhyay, Swati, and Anuar Ishak. "Mixed convection flow along a stretching cylinder in a thermally stratified medium." *Journal of Applied Mathematics* 2012 (2012). <http://dx.doi.org/10.1155/2012/491695>.

97. Ibrahim, Wubshet, and O. D. Makinde. "The effect of double stratification on boundary-layer flow and heat transfer of nanofluid over a vertical plate." *Computers & Fluids* 86 (2013): 433-441.
98. Srinivasacharya, D., and Mendu Upendar. "Effect of double stratification on MHD free convection in a micropolar fluid." *Journal of the Egyptian Mathematical Society* 21, no. 3 (2013): 370-378.
99. Hayat, T., Tariq Hussain, S. A. Shehzad, and A. Alsaedi. "Thermal and concentration stratifications effects in radiative flow of Jeffrey fluid over a stretching sheet." *Plos one* 9, no. 10 (2014): e107858.
100. Choi, Stephen US, and Jeffrey A. Eastman. Enhancing thermal conductivity of fluids with nanoparticles. No. ANL/MSD/CP-84938; CONF-951135-29. Argonne National Lab., IL (United States), 1995.
101. Choi, S. U. S., Z. G. Zhang, Wu Yu, F. E. Lockwood, and E. A. Grulke. "Anomalous thermal conductivity enhancement in nanotube suspensions." *Applied physics letters* 79, no. 14 (2001): 2252-2254.
102. Maiga, Sidi El Becaye, Samy Joseph Palm, Cong Tam Nguyen, Gilles Roy, and Nicolas Galanis. "Heat transfer enhancement by using nanofluids in forced convection flows." *International Journal of Heat and Fluid Flow* 26, no. 4 (2005): 530-546.
103. Kang, Hyun Uk, Sung Hyun Kim, and Je Myung Oh. "Estimation of thermal conductivity of nanofluid using experimental effective particle volume." *Experimental Heat Transfer* 19, no. 3 (2006): 181-191.
104. Buongiorno, Jacopo. "Convective transport in nanofluids." *Journal of Heat Transfer* 128, no. 3 (2006): 240-250.
105. Wang, Xiang-Qi, and Arun S. Mujumdar. "A review on nanofluids-part I: theoretical and numerical investigations." *Brazilian Journal of Chemical Engineering* 25, no. 4 (2008): 613-630.
106. Khan, W. A., and I. Pop. "Boundary-layer flow of a nanofluid past a stretching sheet." *International journal of heat and mass transfer* 53, no. 11 (2010): 2477-2483.
107. Hussain, Tariq, Sabir Ali Shehzad, Tasawar Hayat, Ahmed Alsaedi, Falleh Al-Solamy, and Muhammad Ramzan. "Radiative hydromagnetic flow of Jeffrey nanofluid by an exponentially stretching sheet." *Plos One* 9, no. 8 (2014): e103719.
108. Hayat, Tasawar, Arsalan Aziz, Taseer Muhammad, and Bashir Ahmad. "Influence of magnetic field in three-dimensional flow of couple stress nanofluid over a nonlinearly stretching surface with convective condition." *PloS one* 10, no. 12 (2015): e0145332.
109. Pang, Changwei, Jae Won Lee, and Yong Tae Kang. "Review on combined heat and mass transfer characteristics in nanofluids." *International Journal of Thermal Sciences* 87 (2015): 49-67.

110. Sarkar, Jahar, Pradyumna Ghosh, and Arjumand Adil. "A review on hybrid nanofluids: recent research, development and applications." *Renewable and Sustainable Energy Reviews* 43 (2015): 164-177.
111. Bahiraei, Mehdi, and Morteza Hangi. "Flow and heat transfer characteristics of magnetic nanofluids: a review." *Journal of Magnetism and Magnetic Materials* 374 (2015): 125-138.
112. Ramzan, M., and M. Bilal. "Three-dimensional flow of an elastico-viscous nanofluid with chemical reaction and magnetic field effects." *Journal of Molecular Liquids* 215 (2016): 212-220.
113. Hussanan, Abid, Ilyas Khan, Hasmawani Hashim, Muhammad Khairul Anuar Mohamed, Nazila Ishak, Norhafizah Md Sarif, and Mohd Zuki Salleh. "Unsteady Mhd flow of some nanofluids past an accelerated vertical plate embedded in a porous medium." *J. Teknol.* 78, no. 2 (2016): 121-126.
114. Dogonchi, A. S., and D. D. Ganji. "Investigation of MHD nanofluid flow and heat transfer in a stretching/shrinking convergent/divergent channel considering thermal radiation." *Journal of Molecular Liquids* 220 (2016): 592-603.
115. Khan, Masood, and Muhammad Azam. "Unsteady heat and mass transfer mechanisms in MHD Carreau nanofluid flow." *Journal of Molecular Liquids* 225 (2017): 554-562.
116. Pavlov, K. B. "Magnetohydrodynamic flow of an incompressible viscous fluid caused by deformation of a plane surface." *Magnitnaya Gidrodinamika* 4, no. 1 (1974): 146-147.
117. Ishak, Anuar, Roslinda Nazar, and Ioan Pop. "Magnetohydrodynamic (MHD) flow and heat transfer due to a stretching cylinder." *Energy Conversion and Management* 49, no. 11 (2008): 3265-3269.
118. Singh, Gurminder, and Oluwole Daniel Makinde. "Computational dynamics of MHD free convection flow along an inclined plate with Newtonian heating in the presence of volumetric heat generation." *Chemical Engineering Communications* 199, no. 9 (2012): 1144-1154.
119. Singh, Gurminder, and O. D. Makinde. "MHD slip flow of viscous fluid over an isothermal reactive stretching sheet." *Annals of the Faculty of Engineering Hunedoara* 11, no. 2 (2013): 41.
120. Singh, G. U. R. M. I. N. D. E. R., and Oluwole Daniel Makinde. "Axisymmetric slip flow on a vertical cylinder with heat transfer." *Sains Malaysiana* 43, no. 3 (2014): 483-489.
121. Das, S., R. N. Jana, and O. D. Makinde. "MHD boundary layer slip flow and heat transfer of nanofluid past a vertical stretching sheet with non-uniform heat generation/absorption." *International Journal of Nanoscience* 13, no. 03 (2014): 1450019.
122. Mukhopadhyay, Swati. "MHD boundary layer slip flow along a stretching

- cylinder." *Ain Shams Engineering Journal* 4, no. 2 (2013): 317-324.
123. Mukhopadhyay, Swati. "MHD boundary layer slip flow along a stretching cylinder." *Ain Shams Engineering Journal* 4, no. 2 (2013): 317-324.
 124. Qasim, Muhammad, Zafar Hayat Khan, Waqar Ahmad Khan, and Inayat Ali Shah. "MHD boundary layer slip flow and heat transfer of ferrofluid along a stretching cylinder with prescribed heat flux." *PloS one* 9, no. 1 (2014): e83930.
 125. Wang, C. Y. "Free convection on a vertical stretching surface." *ZAMM-Journal of Applied Mathematics and Mechanics/Zeitschrift für Angewandte Mathematik und Mechanik* 69, no. 11 (1989): 418-420.
 126. Gorla, Rama Subba Reddy, and Ibrahim Sidawi. "Free convection on a vertical stretching surface with suction and blowing." *Applied Scientific Research* 52, no. 3 (1994): 247-257.
 127. Khan, W. A., and I. Pop. "Boundary-layer flow of a nanofluid past a stretching sheet." *International journal of heat and mass transfer* 53, no. 11-12 (2010): 2477-2483.
 128. Hussain, Arif, M. Y. Malik, T. Salahuddin, S. Bilal, and M. Awais. "Combined effects of viscous dissipation and Joule heating on MHD Sisko nanofluid over a stretching cylinder." *Journal of Molecular Liquids* 231 (2017): 341-352.
 129. Rehman, Khali Ur, Abid Ali Khan, M. Y. Malik, and Arif Hussain. "Numerical study of a thermally stratified flow of a tangent hyperbolic fluid induced by a stretching cylindrical surface." *The European Physical Journal Plus* 132, no. 9 (2017): 389.
 130. Akbar, Noreen Sher, Abdelhalim Ebaid, and Z. H. Khan. "Numerical analysis of magnetic field effects on Eyring-Powell fluid flow towards a stretching sheet." *Journal of Magnetism and Magnetic Materials* 382 (2015): 355-358.
 131. Fathizadeh, M., M. Madani, Yasir Khan, Naeem Faraz, Ahmet Yıldırım, and Serap Tutkun. "An effective modification of the homotopy perturbation method for mhd viscous flow over a stretching sheet." *Journal of King Saud University-Science* 25, no. 2 (2013): 107-113.
 132. Ishak, Anuar Mohd, and Roslinda Mohd Nazar. "Laminar boundary layer flow along a stretching cylinder." *European Journal of Scientific Research* 36, no. 1 (2009): 22-29.
 133. Grubka, L. J., and K. M. Bobba. "Heat transfer characteristics of a continuous, stretching surface with variable temperature." *Journal of Heat Transfer* 107, no. 1 (1985): 248-250.
 134. Bidin, Biliana, and Roslinda Nazar. "Numerical solution of the boundary layer flow over an exponentially stretching sheet with thermal radiation." *European journal of scientific research* 33, no. 4 (2009): 710-717.
 135. Mukhopadhyay, Swati. "MHD boundary layer flow and heat transfer over an exponentially stretching sheet embedded in a thermally stratified medium." *Alexandria Engineering Journal* 52, no. 3 (2013): 259-265.

136. Rehman, Khalil Ur, Aqeela Qaiser, M. Y. Malik, and U. Ali. "Numerical communication for MHD thermally stratified dual convection flow of Casson fluid yields by stretching cylinder." *Chinese Journal of Physics* 55, no. 4 (2017): 1605-1614.
137. Bilal, S., Khalil Ur Rehman, and M. Y. Malik. "Numerical investigation of thermally stratified Williamson fluid flow over a cylindrical surface via Keller box method." *Results in physics* 7 (2017): 690-696.
138. Bang, Hyochoong, and Young W. Kwon. *The finite element method using MATLAB*. CRC press, 2000.
139. Brezzi, Franco, and Michel Fortin. *Mixed and hybrid finite element methods*. Vol. 15. Springer Science & Business Media, 2012.
140. Schäfer, Michael, Stefan Turek, Franz Durst, Egon Krause, and Rolf Rannacher. "Benchmark computations of laminar flow around a cylinder." In *Flow simulation with high-performance computers II*, pp. 547-566. Vieweg+ Teubner Verlag, 1996.